Atomic Layer Etching of Metal Oxides

and Atomic Layer Deposition of Metal Fluorides

by

Younghee Lee

B.S., Seoul National University, l999

M.S., Seoul National University, 2001

A thesis submitted to the

Faculty of the Graduate School of the

University of Colorado in partial fulfillment

of the requirement for the degree of

Doctor of Philosophy

Department of Chemistry and Biochemistry

2015

This thesis entitled:

Atomic Layer Etching of Metal Oxides and Atomic Layer Deposition of Metal Fluorides

written by Younghee Lee

has been approved for the Department of Chemistry and Biochemistry

_____

Professor Steven M. George

_____

Professor Carl A. Koval

Date_____

The final copy of this thesis has been examined by the signatories, and we

find that both the content and the form meet acceptable presentation standards

of scholarly work in the above mentioned discipline.

Lee, Younghee (Ph.D., Chemistry)

Atomic Layer Etching of Metal Oxides and Atomic Layer Deposition of Metal Fluorides

Thesis directed by Professor Steven M. George

Atomic control of thin film growth and removal is essential for semiconductor processing. Atomic layer deposition (ALD) is a thin film deposition technique that is based on self-limiting surface reactions that deposit thin conformal films with atomic scale precision. The ALD of metal fluorides has been limited by the difficulty of handling the hydrogen fluoride (HF) precursor that is necessary for metal fluoride film growth. The use of HF-pyridine as an HF reservoir has allowed the development of metal fluoride ALD processes such as AlF_3, LiF, lithium ion conducting $(AlF_3)(LiF)_x$ alloy, ZrF_4, HfF_4, MnF_2, MgF_2, and ZnF_2. AlF_3 ALD was studied using trimethylaluminum (TMA) and HF at temperatures from 150-300°C by *in situ* techniques such as quartz crystal microbalance (QCM), quadrupole mass spectrometry (QMS) and Fourier transform infrared (FTIR) spectroscopy. *Ex situ* characterization of the films was conducted using X-ray reflectivity (XRR) and spectroscopic ellipsometry (SE), grazing incidence X-ray diffraction (GIXRD), X-ray photoelectron spectroscopy (XPS), and Rutherford backscattering spectrometry (RBS). These high quality metal fluoride ALD films will be useful for many applications such as optical coatings and Lewis acid catalysts.

”Reverse ALD”, i.e. atomic layer etching (ALE), is a film removal technique that is able to remove thin films with atomic level control. Current ALE processes based on halogen adsorption and ion-enhancement are inherently directional processes that lead to an anisotropic removal of material. New thermal approaches for Al_2O_3 and HfO_2 ALE were demonstrated using $Sn(acac)_2$ and HF as the reactants. *In situ* and *ex situ* studies showed that thermal ALE of Al_2O_3 and HfO_2 is possible at temperatures from 150-250°C. In the proposed reaction

mechanism, the HF reactant fluorinates the metal oxide surfaces to form the corresponding metal fluoride and H_2O as reaction products. The $Sn(acac)_2$ reactant induces a ligand exchange reaction to produce volatile $SnF(acac)$ and $Al(acac)_3$ or $Hf(acac)_4$. This etching approach based on fluorination and ligand exchange is general and can be applied to other metal oxides, as well as metal nitrides, metal phosphides, metal arsenides and elemental metals. Thermally driven ALE processes will provide an important tool for isotropically etching materials at the atomic scale.

"We discovered something today."

John Bardeen (1908-1991)

ACKNOWLEDGEMENTS

CONTENTS

CHAPTER

TABLES

FIGURES

CHAPTER 1

INTRODUCTION

1.1 Atomic Layer Deposition

Atomic layer deposition (ALD) is a film growth method based on sequential, self-limiting surface reactions.[1] Because of its self-limiting nature, a very conformal continuous thin film can be grown with atomic layer control.[1] A typical ALD reaction consists of two sequential half reactions. Figure 1-1 shows a schematic for a general ALD process. During the first half sequence, gas molecule (A) reacts with the surface of the substrate to form a new surface saturated by (A). A purge step removes excess (A) molecules. During the second sequence, gas molecule (B) reacts with the surface formed by (A) to produce another surface terminated by (B). A purge step removes excess (B) molecules. As this ALD reaction is repeated, a thin film is deposited.
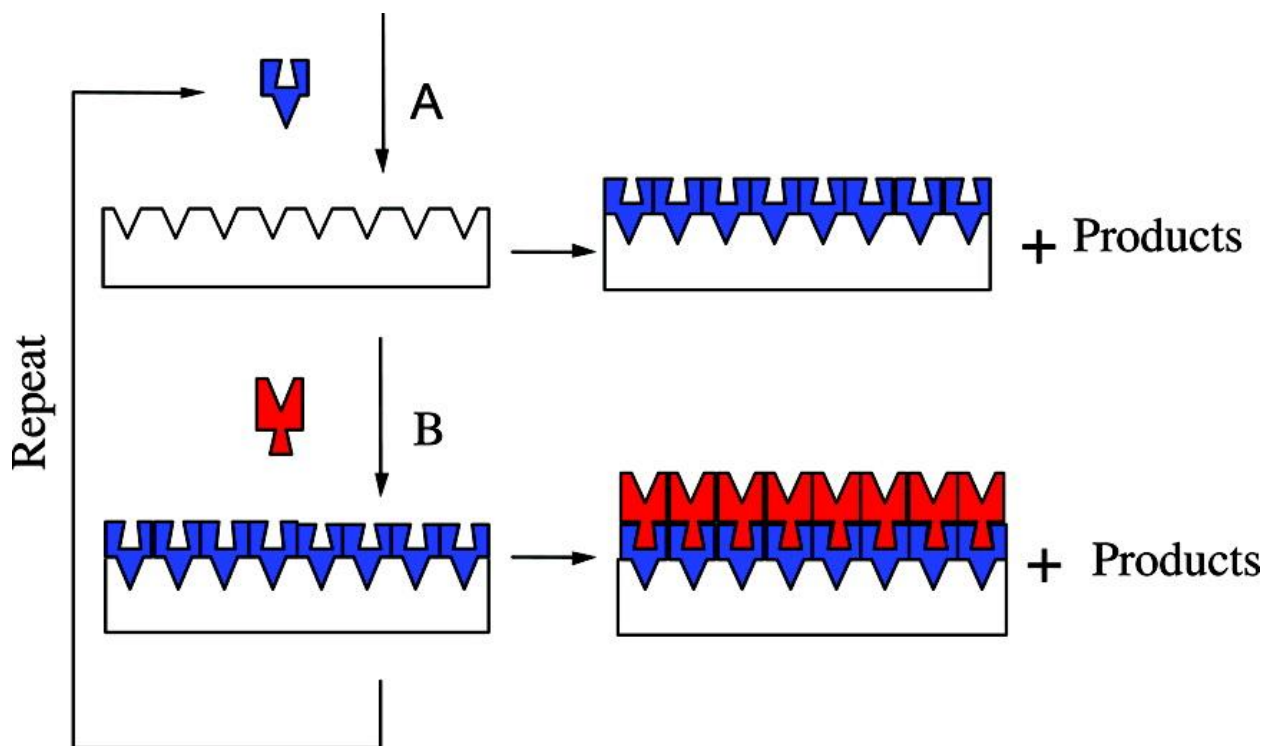
Figure 1-1. Schematic of the general ALD process based on sequential, self-limiting surface reactions (Ref. 1).

The Al_2O_3 ALD reaction using trimethylaluminum (TMA) and H_2O is the most well established ALD process. A schematic of the surface chemistry for Al_2O_3 ALD using TMA and H_2O is shown in Figure 1-2. In reaction A, there is a hydroxylated surface that is produced after several Al_2O_3 ALD cycles on the initial substrate. When TMA molecules are exposed to react with –OH groups on the surface, Al-CH_3 bonds are formed and methane molecules are produced as a reaction byproduct. In the second reaction B, H_2O molecules are brought into the surface to convert Al-CH_3 bonds into Al-OH bonds. This Al_2O_3 ALD reaction repeats until the ALD reaction stops and a certain Al_2O_3 ALD thickness is achieved.

The overall reaction for Al_2O_3 ALD is very exothermic. HSC chemistry shows that the formation of Al_2O_3 from the reaction between TMA and H_2O is very favorable having $\Delta H =$ -376 kcal/(2 mol. Al) or -188 kcal/(1 mol. Al) at 0°C.[2]

$$2Al(CH_3)_3 + 3H_2O \rightarrow Al_2O_3 + 6CH_4 \qquad \Delta H = \text{-376 kcal} \qquad (1)$$

This reaction is very favorable due to the formation of strong Al-O bond. ALD reactions are typically accomplished using thermal chemistry. However, plasma ALD is sometimes employed to enhance the surface reactions.[3]

ALD process can grow very conformal Al_2O_3 ALD films on high aspect ratio structures. A conformal Al_2O_3 ALD film can be grown on a Si wafer with a trench structure.[4] An Al_2O_3 ALD film can be coated on nanoparticles conformally using a rotary reactor.[5] The thin films grown by ALD are continuous and pinhole free. These conformal films are key for applications such as high-k dielectrics in semiconductor devices[6,7] or as protective coatings in Li ion batteries.[8,9]
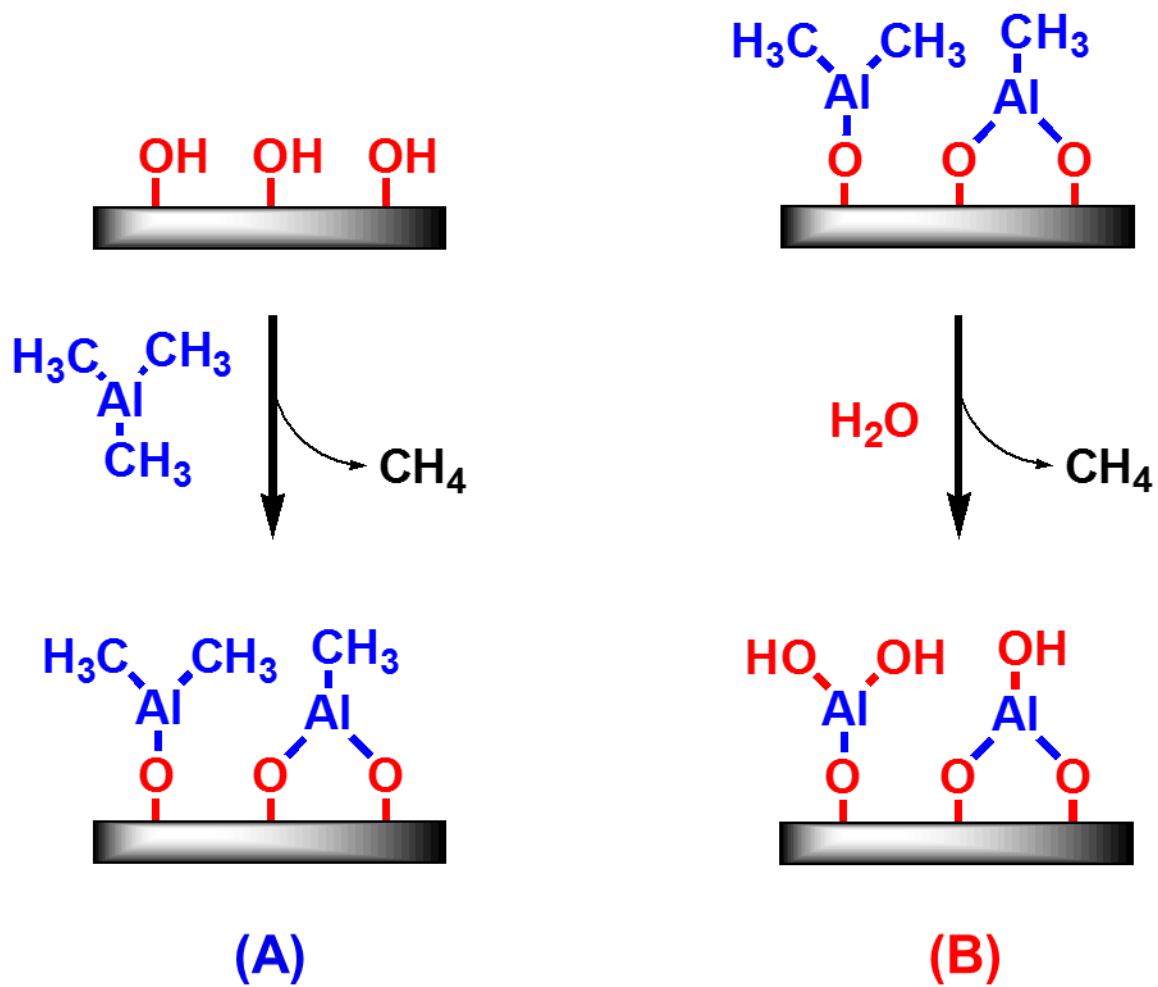
Figure 1-2. Schematic of surface chemistry for Al_2O_3 ALD using TMA and H_2O as the reactants.

ALD films have been commercialized by the semiconductor industry. Figure 1-3 shows a TEM image of a single transistor from Intel's 45 nm technology.[10] Intel has applied HfO_2 ALD films as their high-k dielectric in 45 nm metal-oxide field effect transistor (MOSFET) in 2007.[10] The dielectric HfO_2 layer is located between the metal gate and the silicon. ALD of HfO_2 has replaced thermally grown SiO_2 to achieve higher performance with low cost.[10,11]

A wide range of materials from metal oxides to metals can be grown by ALD.[12] ALD of metal oxides, nitrides, and sulfides has been developed using H_2O, NH_3, and H_2S respectively.[12] ALD of metal fluorides has proven difficult because HF is not a benign reactant. Most of the metal fluoride ALD processes have avoided using HF.[12]

The overall reaction for AlF_3 ALD from TMA and HF is very exothermic. HSC chemistry shows that the formation of AlF_3 is very favorable having $\Delta H = -240$ kcal/(1 mol. Al) at 0°C.[2]

$$Al(CH_3)_3 + 3HF \rightarrow AlF_3 + 3CH_4 \qquad\qquad \Delta H = -240 \text{ kcal} \qquad\qquad (2)$$
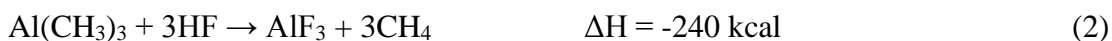
This AlF_3 formation reaction in equation 2 is an even more favorable than Al_2O_3 formation in equation 1 due to the formation of a very strong Al-F bond. Although this overall reaction is very thermochemically favorable, AlF_3 ALD has not been demonstrated until recently.[13,14]

A hydrogen fluoride-pyridine (HF-pyridine) solution comprised of 70% HF and 30% pyridine was employed as a fluorine precursor for the study of AlF_3 ALD.[13,14] HF-pyridine, known as Olah's reagent, is a commercially available precursor. Use of gaseous HF from HF-pyridine enables the safe handling of anhydrous HF. Because HF-pyridine is a liquid at room temperature and has an equilibrium with a small amount of gaseous HF, the problems of
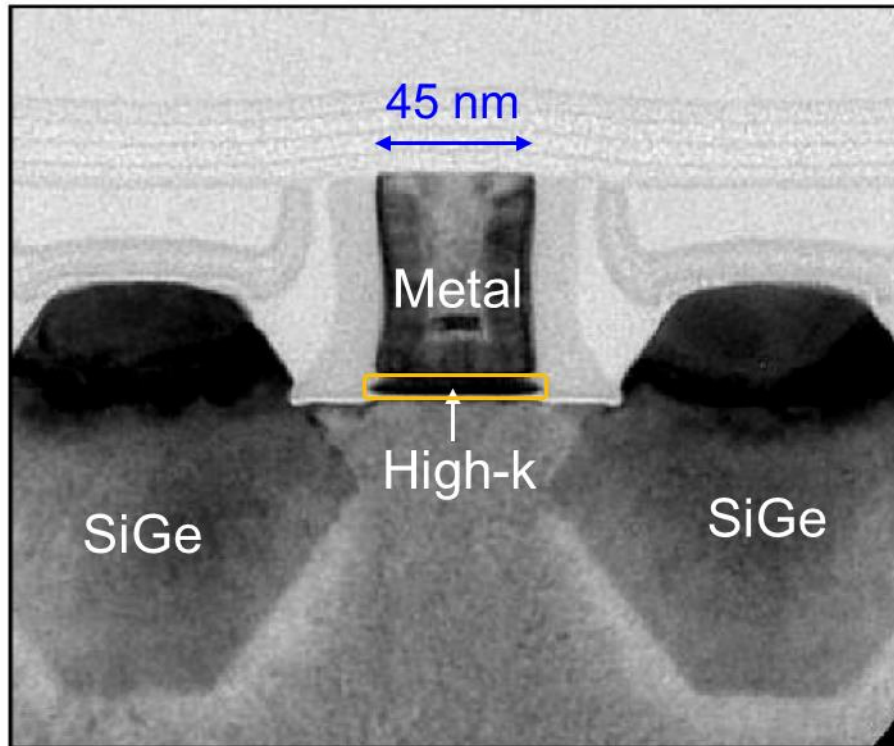
Figure 1-3.   Cross-sectional TEM image of Intel's MOSFET employing high-k gate dielectrics

grown by ALD (Ref. 10).

using HF from compressed gas cylinders can be avoided. With static exposures and no pumping on our ALD reactor, the vapor pressure of HF over the HF-pyridine solution was 90-100 Torr at room temperature. This pressure is approximately 1/8 of the vapor pressure of pure HF at room temperature.
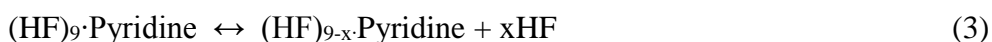
$$(HF)_9 \cdot Pyridine \; \leftrightarrow \; (HF)_{9-x} \cdot Pyridine + xHF \qquad\qquad (3)$$

The mass spectrometer measurements have revealed that HF is the dominant species in the vapor pressure of HF-pyridine. These results can be understood as a high boiling azeotrope.

The use of HF-pyridine as a convenient reservoir for anhydrous HF enabled the development for ALD process of many metal fluorides such as LiF, lithium ion conducting $(AlF_3)(LiF)_x$ alloy, ZrF_4, HfF_4, MnF_2, MgF_2, and ZnF_2. The metal precursors utilized for these processes include metal alkyls, cyclopentadienyls, alkylamides, silylamides, and alkoxides. These precursors, listed in order of increasing reactivity, have been employed for ALD of metal oxides. Various metal precursors employed for the demonstration of metal fluorides ALD are summarized in Table 1-1. The molecular structures of various metal precursors are illustrated in Figure 1-4. ALD of many other metal fluorides can also be developed using HF from HF-pyridine solution.

One question someone may ask is whether metal β -diketonates will work as ALD precursors for metal fluoride ALD. Metal β-diketonates are not typically used for ALD reactions even though they tend to have decent vapor pressures. Because of the strong bond between the metal and the oxygens in a β -diketonate ligand, metal β -diketonates are not usually reactive to H_2O to form metal oxides. A plasma or a strong oxidant such as ozone is frequently required to enhance the surface reaction.

Various Metal Precursor	Acronym
Trimethylaluminum	TMA
Diethylzinc	DEZ
Bis(ethylcyclopentadienyl) manganese	$Mn(EtCp)_2$
Bis(ethylcyclopentadienyl) magnesium	$Mg(EtCp)_2$
Tetrakis(dimethylamido) hafnium	TDMAH
Tetrakis(ethylmethylamido) zirconium	TEMAZ
Lithium hexamethyldisilazide	LiHMDS
Zirconium *tert*-butoxide	ZTB
Tin acetylacetonate	$Sn(acac)_2$

Table 1-1.   Various metal precursors used for metal fluorides ALD.
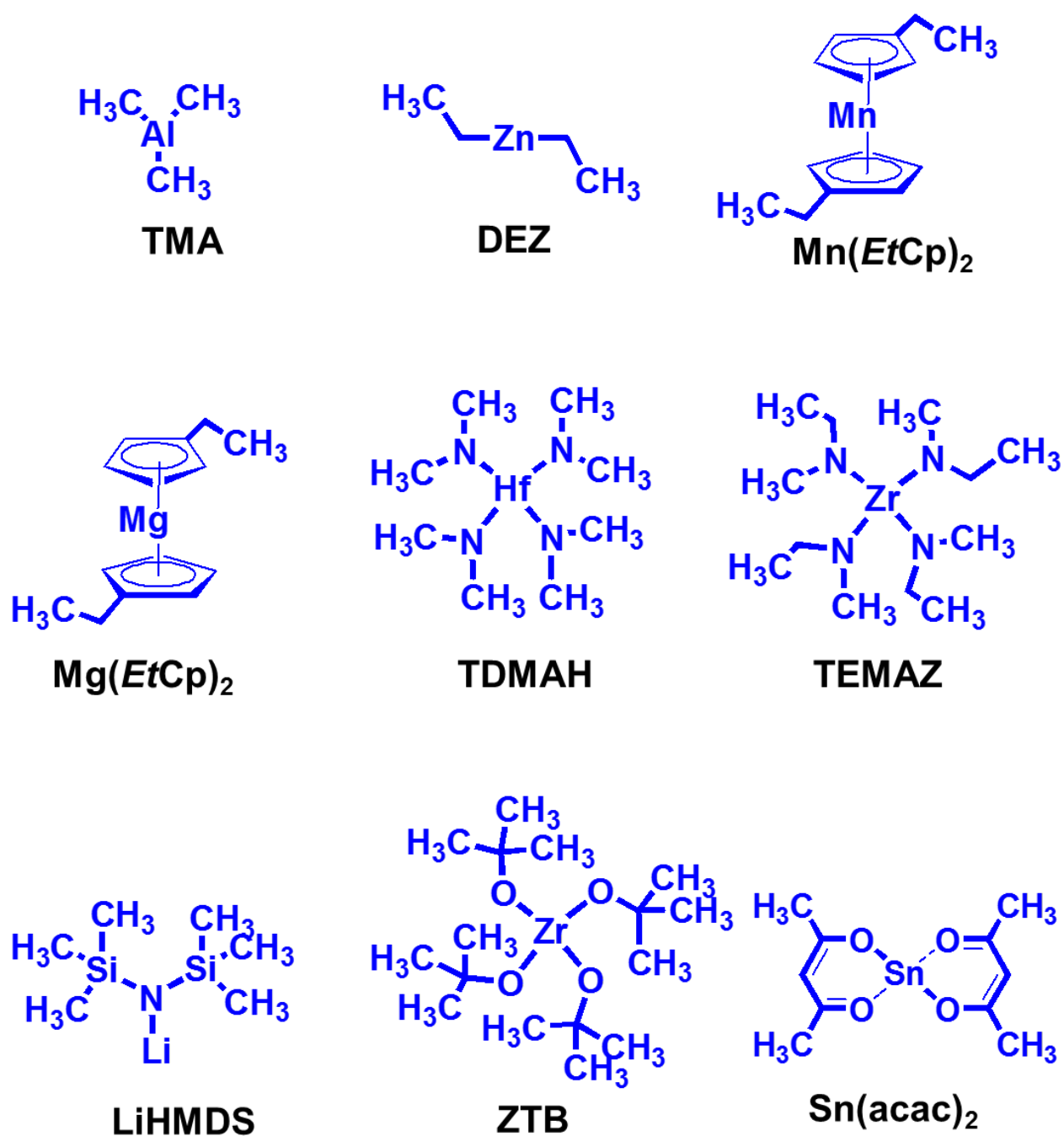
Figure 1-4. Molecular structures of various metal precursors such as metal alkyls (TMA & DEZ), cyclopentadienyls (Mn(*Et*Cp)$_2$ & Mg(*Et*Cp)$_2$), alkylamides (TDMAH & DEMAZ), silyamides (LiHMDS), alkoxides (ZTB), and β-diketonates (Sn(acac)$_2$). Molecular structures omitted CH$_2$ and CH for clarity.

HF, however, is very interesting molecule and may interact differently with metal β-diketonates than H_2O. HF is a weak Brønsted acid in solution and is able to provide a proton. HF can act differently in the gas phase or on the surface, emphasizing the Lewis basicity of HF due to an electron-rich fluorine. Therefore, the reactivity between metal β-diketonates and HF is not straightforward.

Tin(II) acetylacetonate ($Sn(acac)_2$) is a commercially available metal β-diketonate precursor. It is a liquid at room temperature and has a good vapor pressure at ~100°C, which is also shown in Figure 1-4. $Sn(acac)_2$ was utilized as the tin precursor for the demonstration of SnS ALD.[15]

Reactivity between $Sn(acac)_2$ amd HF would produce SnF_2 ALD films. SnF_2 is stable at atmospheric pressures, which is necessary for *ex situ* characterization. While other fluorides have possible applications such as optical coatings, Lewis acid catalysts, and solid state electrolytes, SnF_2 is not a very useful material except as an ingredient in more expensive toothpastes (e.g., Crest Pro Health®) where is replaces the more common ingredient, sodium fluoride (NaF).

1.2 Atomic Layer Etching

Curiosity on the reactivity between $Sn(acac)_2$, a metal β-diketonate, and HF to grow SnF_2 ALD films led to the discovery of "thermal" atomic layer etching (ALE), which is a technology that the semiconductor industry has been desperately searching for.[16,17] This ALE process is based on sequential, self-limiting thermal reactions that enable an isotropic etching of material with atomic layer control.[18,19]

Moore's Law predicts that the number of transistors in a chip will be approximately doubled every 24 months.[20] To meet the requirements for the miniaturization of devices the devices will need to be designed three dimensionally. .[16,21] Figure 1-5a shows schematic of a planar field effect transistor (FET).[21] Basically, a FET is a switch. The charge carriers, either electrons or holes, travel from the source to the drain through the channel created by the field that is applied on the gate. As the feature size of the transistor gets smaller than 20 nm, the leakage current through this channel becomes a challenge.[21] To address this issue, the semiconductor industry has employed a three dimensional structure; e.g., the FinFET in 2012.[22] The FinFET illustrated in Figure 1-5b[21] takes its name from the shape of the narrow semiconductor structure that looks like the dorsal fin of a shark. By wrapping around the channel with a gate dielectric, the FinFET technology is able to turn on and off very effectively.[21,22] This FinFET technology has led to lower power consumption and higher performance while adding little cost.[22]

To make three dimensional structures such as the fin in the FinFET structure, an anisotropic dry etching process such as reactive ion etching (RIE) is typically employed. This RIE process is based on the Bosch process,[23] where the bottom of a Si substrate is etched by a SF_6 plasma while a thin polymeric layer is simultaneously deposited on the sidewalls by a C_4F_8 plasma. This plasma process can damage the Si substrate. A more precise and gentle process will be required for devices as with nanometer feature sizes.

The process of removing material at the atomic scale has been known for 25 years under different names such as atomic layer etching[24], digital etching[25] or layer-by-layer etching[26]. This processes are all based on energetic ion or neutral atom bombardment.
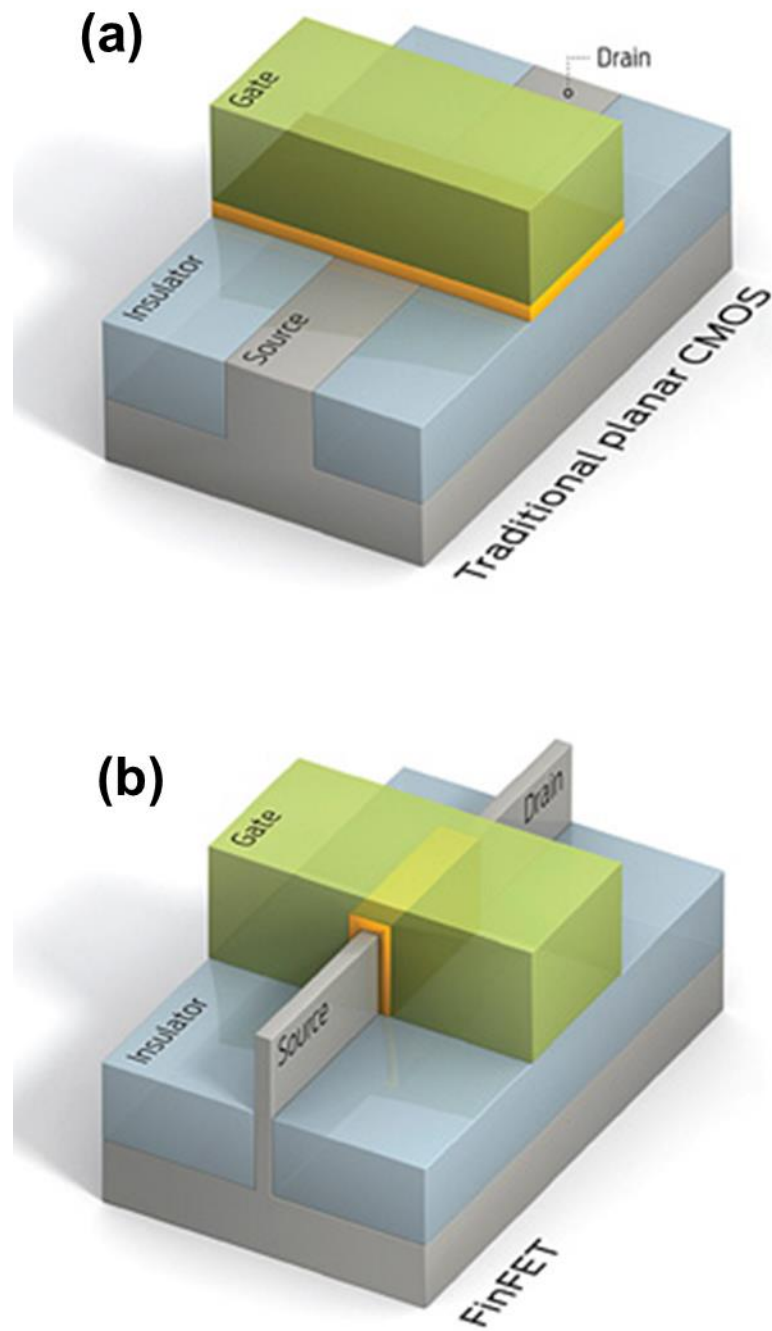
Figure 1-5. Schematic of (a) the planar FET and (b) FinFET. (ref 21)

These processes aim for anisotropic etching of semiconductors such as Si[25-27], Ge, [28,29] GaAs,[30] and InP.[31] ALE processes have been accomplished using either Cl or F adsorption that followed by the removal of surface species using Ar^+ ion or neutral Ar or Ne bombardment. The schematic of this process is shown in Figure 1-6[32].

The ALE of metal oxides such as Al_2O_3,[33] HfO_2,[34] ZrO_2,[35] and TiO_2 [36] and SiO_2[37,38] has been reported because the removal of the dielectric layer is needed to make contacts at the source and drain. Most reported ALE processes, including the first ALE patent,[24] are not based on the thermal processes. The process based on ion-enhanced removal of materials is inherently directional and leads to an anisotropic etching of the material. In contrast, most ALD processes are accomplished with thermal processes that result in conformal depositions. The first ALD patent by T. Suntola published in 1977 also used a thermal process.[39]

The comparison of an anisotropic etching with an isotropic etching is shown in Figure 1-7a and 1-7b. An isotropic etching of material is necessary to create three dimensional structures such as the Gate-All-Around (GAA) transistor.[17] Isotropic etching of the patterned area enables to undercut shown is Figure 1-7c. Currently, wet chemical techniques are the only available isotropic etch processes. Wet etching becomes more challenging when the size of the device approaches the nanometer scale due to capillary forces.[17] An isotropic dry etching with atomic layer control should be able to replace wet etching methods for nanoscale structures. Isotropic etching could also be employed to clean the sidewalls after plasma etching.[17] The ability to make the surface smooth by removing rough surfaces and defects would be very desirable in channels with nanometer size.[17] These aspects of isotropic etching could be accomplished by thermal ALE.
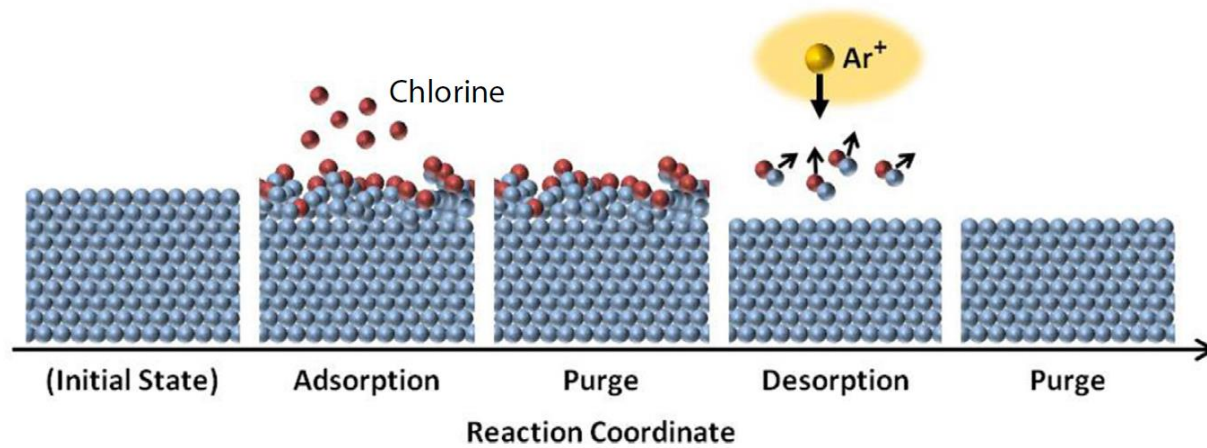
Figure 1-6. Schematic of the process steps in an ALE cycle for a silicon film etched by chlorine and argon. (ref. 32)
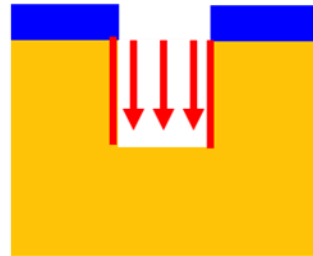
Figure 1-7. Schematic of (a) anisotropic etching; (b) isotropic etching; (c) Undercut etching by isotropic etching.
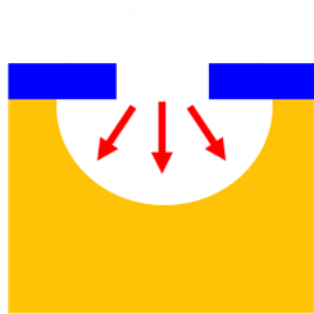
Turning around ALD surface chemistry is fundamentally difficult because ALD reactions are very exothermic. An alternative strategy for ALE needs to be developed. Thermal ALE is considered the reverse of ALD processes and has only been reported very recently (2015).[18,19]

Figure 1-8 shows the generic schematic of thermal Al_2O_3 ALE. A fluorination step conducted by HF exposure converts Al_2O_3 surface to an intermediate AlF_3 layer. A purge step removes an excess HF and H_2O produced from the surface. Subsequent ligand exchange reaction of AlF_3 proceeded by $Sn(acac)_2$ produces volatile etch products. A purge step removes these etch products such as $SnF(acac)$ and $Al(acac)_3$.

The overall proposed reaction can be expressed as:

$$Al_2O_3 + 6HF + 6Sn(acac)_2 \rightarrow 2Al(acac)_3 + 6SnF(acac) + 3H_2O \tag{4}$$
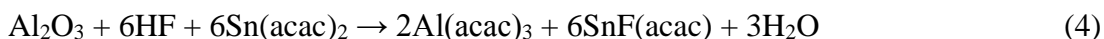
This Al_2O_3 ALE reaction based on fluorination and ligand exchange is general and could be expanded to ALE of other materials such as other metal oxides, as well as metal nitrides, metal phosphides, metal arsenides and elemental metals. Thermally driven ALE process will provide an important tool for an isotropic etching of materials at the atomic scale.

1.3 Outline of Remaining Chapters

Chapter 2 will demonstrate the ALD of AlF_3 using TMA and HF. HF-pyridine will be employed as a HF source. AlF_3 ALD will serve as a model system providing a basic understanding for ALD of many other metal fluorides. This work has been presented at *the 13th International Conference on Atomic Layer Deposition*, San Diego, California, July 28-31, 2013.
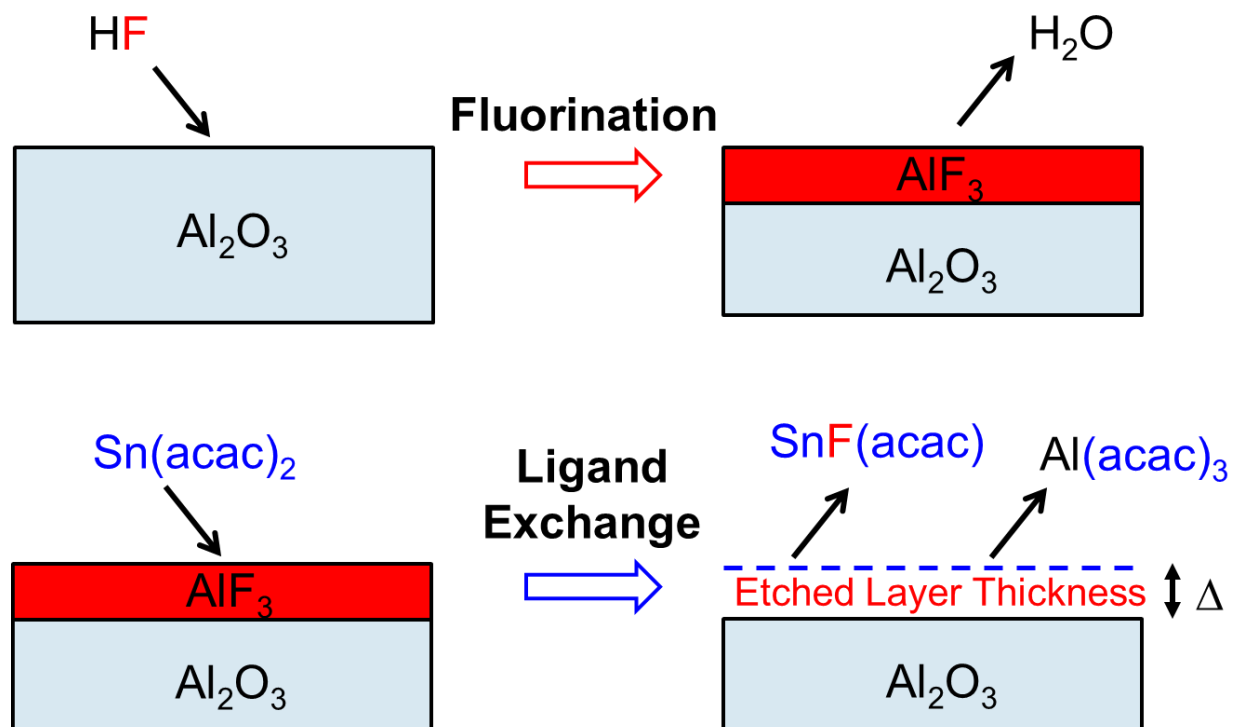
Figure 1-8. Generic schematic of the thermal Al_2O_3 ALE process etched by HF and $Sn(acac)_2$

This chapter, entitled "Atomic Layer Deposition of AlF$_3$ Using Trimethylaluminum and Hydrogen Fluoride" by Younghee Lee, Jaime W. DuMont, Andrew S. Cavanagh, and Steven M. George, has been submitted for publication in *Journal of Physical Chemistry C* 2015.

Chapter 3 will show ALD of LiF using lithium hexamethyldisilazide and hydrogen fluoride. This chapter will also show the development of lithium ion conducting (AlF$_3$)(LiF)$_x$ alloys by the combination of AlF$_3$ ALD and LiF ALD. This work has been presented at *the 14th International Conference on Atomic Layer Deposition*, Kyoto, Japan, June 15-18, 2014. This chapter, entitled "ALD of LiF and Lithium Ion Conducting (AlF$_3$)(LiF)$_x$ Alloys Using Trimethylaluminum, Lithium Hexamethyldisilazide and Hydrogen Fluoride" by Younghee Lee, Daniela M. Piper, Andrew S. Cavanagh, Matthias J. Young, Se-Hee Lee and Steven M. George, has been prepared for submission to a peer-reviewed journal.

Chapter 4 will review ALD of various metal fluorides such as ZrF$_4$, HfF$_4$, MnF$_2$, MgF$_2$, and ZnF$_2$. Different metal precursors including metal alkoxides, metal amides, and metal cyclopentadienyl will be employed to demonstrate the generality of an approach using HF derived from HF-pyridine as a F source. This work will be presented at *the 15th International Conference on Atomic Layer Deposition*, Portland, Oregon, June 28-July 1, 2015. This chapter, entitled "Atomic Layer Deposition of Metal Fluorides Using Various Metal Precursors and Hydrogen Fluoride" by Younghee Lee, Huaxing Sun, and Steven M. George, has been prepared for submission to a peer-reviewed journal.

Chapter 5 will demonstrate the ALE of Al$_2$O$_3$ using sequential, self-limiting, thermal reactions with Sn(acac)$_2$ and HF. This is the first report of a thermal ALE process. This chapter, entitled "Atomic Layer Etching of Al$_2$O$_3$ Using Sequential, Self-Limiting Thermal Reactions

with Sn(acac)$_2$ and HF" by Younghee Lee and Steven M. George, has been published in *ACS Nano* 2015, 9, 2061.

Chapter 6 will discuss the temperature dependence and the mechanism of the thermal ALE of Al$_2$O$_3$ using sequential reactions with Sn(acac)$_2$ and HF. This chapter entitled "Mechanism of Thermal Al$_2$O$_3$ Atomic Layer Etching Using Sequential Reactions with Sn(acac)$_2$ and HF" by Younghee Lee, Jaime W. DuMont and Steven M. George has been submitted for publication in *Chemistry of Materials* 2015.

Chapter 7 will describe the ALE of HfO$_2$ using sequential, self-limiting, thermal reactions with Sn(acac)$_2$ and HF. This chapter, entitled "Atomic Layer Etching of HfO$_2$ Using Sequential, Self-Limiting Thermal Reactions with Sn(acac)$_2$ and HF" by Younghee Lee, Jaime W. DuMont and Steven M. George, has been published in *ECS Journal of Solid State Science and Technology* 2015, 4, N5013. This paper is part of *JSS Focus Issue on Atomic Layer Etching and Cleaning*.

A provisional application for patent based on the thermal ALE has been filed.

1.4 References

(1)   George, S. M. *Chem. Rev.* **2010**, 110, 111.

(2)   HSC Chemistry; HSC Chemistry 5.1, Outokumpu Research Oy: Pori, Finland.

(3)   Profijt, H. B.; Potts, S. E.; van de Sanden, M. C. M.; Kessels, W. M. M. *J. Vac. Sci. Technol. A* **2011**, 29, 050801.

(4)   Ritala, M.; Leskela, M.; Dekker, J. P.; Mutsaers, C.; Soininen, P. J.; Skarp, J. *Chem. Vap. Deposition* **1999**, 5, 7.

(5)   McCormick, J. A.; Cloutier, B. L.; Weimer, A. W.; George, S. M. *J. Vac. Sci. Technol., A* **2007**, 25, 67.

(6)   Groner, M. D.; Elam, J. W.; Fabreguette, F. H.; George, S. M. *Thin Solid Films* **2002**, 413, 186.

(7)   Gusev, E. P.; Cabral, C.; Copel, M.; D'Emic, C.; Gribelyuk, M. *Microelectron. Eng*. **2003**, 69, 145.

(8)   Jung, Y. S.; Cavanagh, A. S.; Dillon, A. C.; Groner, M. D.; George, S. M.; Lee, S. H. *J. Electrochem. Soc.* **2010**, 157, A75.

(9)   Jung, Y. S.; Cavanagh, A. S.; Riley, L. A.; Kang, S. H.; Dillon, A. C.; Groner, M. D.; George, S. M.; Lee, S. H. *Adv. Mater.* **2010**, 22, 2172.

(10)   Mistry, K. et al. *2007 IEEE International Electron Devices Meeting, Vols 1 and 2* **2007**, 247.

(11)   Bohr, M. T.; Chau, R. S.; Ghani, T.; Mistry, K. *IEEE Spectrum* **2007**, 44, 29.

(12)   Miikkulainen, V.; Leskela, M.; Ritala, M.; Puurunen, R. L. *J. Appl. Phys.* **2013**, 113, 021301.

(13)   Lee, Y.; Cavanagh, A. S.; George, S. M. Atomic Layer Deposition of AlF_3 Using Trimethylaluminum and Hydrogen Fluoride-Pyridine, *Proceedings of the 13th International Conference on Atomic Layer Deposition, San Diego, California, July 28-31,* **2013**.

(14)   Lee, Y.; DuMont, J. W.; Cavanagh, A. S.; George, S. M. *Submitted to J. of Phys. Chem. C* **2015**.

(15)   Kim, J. Y.; George, S. M. *J. Phys. Chem. C* **2010**, 114, 17597.

(16)   Kuhn, K. J. *IEEE Trans. Electron Devices* **2012**, 59, 1813.

(17)   Carver, C. T.; Plombon, J. J.; Romero, P. E.; Suri, S.; Tronic, T. A.; Turkot Jr., R. B. *ECS J. Solid State Sci. Technol,* **2015**, 4, N5005.

(18)   Lee, Y.; George, S. M. *ACS Nano* **2015**, 9, 2061.

(19)   Lee, Y.; DuMont, J. W.; George, S. M. ECS *J. Solid State Sci. Technol.* **2015**, 4, N5013.

(20)   Moore, G. *Electron. Lett.* **1965**, 38.

(21)   Ahmed, K.; Schuegraf, K. *IEEE Spectrum* **2011**, 48, 50.

(22)   Auth, C. et al. *Symposium on VLSI Technology Digest of Technical Papers* **2012**.

(23)   Laermer, F.; Schilp, A. *U.S. Patent No. 5,501,893* **1996**.

(24)   Yoder, M. N. *U.S. Patent No. 4,756,794* **1987**.

(25)   Horiike, Y.; Tanaka, T.; Nakano, M.; Iseda, S.; Sakaue, H.; Nagata, A.; Shindo, H.; Miyazaki, S.; Hirose, M. *J. Vac. Sci. Technol., A* **1990**, 8, 1844.

(26)   Matsuura, T.; Murota, J.; Sawada, Y.; Ohmi, T. *Appl. Phys. Lett.* **1993**, 63, 2803.

(27)   Athavale, S. D.; Economou, D. J. *J. Vac. Sci. Technol., A* **1996**, 14, 3702.

(28)   Matsuura, T.; Sugiyama, T.; Murota, J. *Surf. Sci.* **1998**, 402, 202.

(29)   Sugiyama, T.; Matsuura, T.; Murota, J. *Appl. Surf. Sci.* **1997**, 112, 187.

(30)   Lim, W. S.; Park, S. D.; Park, B. J.; Yeom, G. Y. *Surf. Coat. Tech.* **2008**, 202, 5701.

(31)   Park, S. D.; Oh, C. K.; Bae, J. W.; Yeom, G. Y.; Kim, T. W.; Song, J. I.; Jang, J. H. *Appl. Phys. Lett.* **2006**, 89, 043109.

(32)   Lee, C. G. N.; Kanarik, K. J.; Gottscho, R. A. *J. Phys. D: Appl. Phys.* **2014**, 47.

(33)   Min, K. S.; Kang, S. H.; Kim, J. K.; Jhon, Y. I.; Jhon, M. S.; Yeom, G. Y. *Microelectron. Eng.* **2013**, 110, 457.

(34)   Park, J. B.; Lim, W. S.; Park, B. J.; Park, I. H.; Kim, Y. W.; Yeom, G. Y. *J. Phys. D Appl. Phys.* **2009**, 42, 055202.

(35)   Lim, W. S.; Park, J. B.; Park, J. Y.; Park, B. J.; Yeom, G. Y. *J. Nanosci. Nanotechnol.* **2009**, 9, 7379.

(36)   Park, J. B.; Lim, W. S.; Park, S. D.; Park, Y. J.; Yeom, G. Y. *J. Korean Phys. Soc.* **2009**, 54, 976.

(37)   Metzler, D.; Bruce, R. L.; Engelmann, S.; Joseph, E. A.; Oehrlein, G. S. *J. Vac. Sci. Technol. A* **2014**, 32, 020603.

(38)   Rauf, S.; Sparks, T.; Ventzek, P. L. G.; Smirnov, V. V.; Stengach, A. V.; Gaynullin, K. G.; Pavlovsky, V. A. *J. Appl. Phys.* **2007**, 101, 033308.

(39)   Suntola, T.; Antson, J. *U.S. Patent No. 4,058,430* **1977**.

CHAPTER 2

Atomic Layer Deposition of AlF₃ Using Trimethylaluminum and Hydrogen Fluoride

2.1. Introduction

AlF₃ is a dielectric material with a low refractive index[1-2] and wide band gap >10 eV.[3-4]

AlF₃ has high transmission at infrared (IR), ultraviolet (UV) and deep UV wavelengths.[1,5-7]

These properties make AlF₃ useful for optical coatings. Aluminum fluoride (AlF₃) has also been

demonstrated as an excellent protective film for Li ion batteries.[8-9] AlF₃ films enhance the

cycling stability of anode and cathode materials, and also improve the thermal stability by

suppressing exothermal side reactions.[8-10] In addition, AlF₃ is employed as heterogeneous

catalyst for the production of chlorofluorocarbons (CFCs) due to its strong Lewis acidity.[11-13]

AlF₃ films have been grown by physical vapor deposition techniques such as

sputtering,[14-15] thermal evaporation,[3,6,16] electron beam deposition,[1,5] and ion-assisted

deposition.[17-18] AlF₃ films have also been grown by atomic layer deposition (ALD). ALD is a

technique based on sequential, self-limiting surface reactions that deposits extremely conformal

and continuous thin films with atomic level control.[19] We initially reported AlF₃ ALD using

trimethylaluminum (TMA) and HF from a HF-pyridine solution.[20] AlF_3 ALD has also been demonstrated recently using a halide-halide exchange reaction with $AlCl_3$ and TiF_4.[21]

In this paper, the growth of AlF_3 ALD films using TMA and HF as the reactants was examined using *in situ* quartz crystal microbalance (QCM), quadrupole mass spectrometer (QMS) and Fourier transform infrared (FTIR) spectroscopy measurements. The reactions were performed at temperatures between 75 °C and 300 °C. The AlF_3 film thickness and density were determined with *ex situ* X-ray reflectivity (XRR). The AlF_3 film thickness and refractive index were measured with spectroscopic ellipsometry (SE). The structure of the AlF_3 films was examined with grazing incidence X-ray diffraction (GIXRD). The composition of the AlF_3 ALD film was also determined with X-ray photoelectron spectroscopy (XPS) and Rutherford backscattering spectrometry (RBS).

2.2. Experimental

2.2A. Viscous Flow Reactor with *in situ* QCM and QMS

The ALD reactions were performed in a viscous flow ALD reactor equipped with an *in situ* QCM and QMS at temperatures between 75 °C and 300 °C.[22-23] A mechanical pump (Pascal 2015SD, Alcatel) was used maintain vacuum conditions in the ALD reactor. Reactants were dosed into a N_2 carrier gas. A mass flow controllers (Type 1179A, MKS) supplied a constant N_2 carrier gas flow of 150 sccm. This N_2 gas flow resulted in a base pressure of ~1 Torr in the reactor. A PID temperature controller (2604, Eurotherm) kept the reactor at a fixed temperature within ± 0.04 °C. A bakeable capacitance manometer (Baratron 121A, MKS) monitored pressure change during reaction.

The AlF$_3$ ALD reactions were performed using TMA (97 %, Sigma-Aldrich), and HF-pyridine (70 wt% HF, Sigma-Aldrich) as the reactants. Use of gaseous HF from HF-pyridine enables the safe handling of anhydrous HF. HF-pyridine is a liquid at room temperature and is known as Olah's reagent.[24] HF-pyridine was transferred to a stainless steel bubbler in a dry N$_2$-filled glove bag. The HF-pyridine solution has an equilibrium with gaseous HF. Our mass spectrometer measurements have revealed that HF is the dominant species in the vapor pressure of HF-pyridine. With static exposures with no pumping in our ALD reactor, the vapor pressure HF over the HF-pyridine solution was 90-100 Torr at room temperature. Each AlF$_3$ ALD experiment was conducted on a fresh Al$_2$O$_3$ ALD film. The Al$_2$O$_3$ ALD films were prepared using TMA and H$_2$O (Chromasolv for HPLC, Sigma-Aldrich). The TMA, HF-pyridine, and H$_2$O precursors were held at room temperature.

A film deposition monitor (Maxtek TM-400, Inficon) was used to perform the *in situ* QCM measurements. The QCM sensors were polished, 6 MHz, AT-cut (Colorado Crystal Corp.) and RC-cut (Colnatec) quartz crystals with gold electrodes. The QCM sensor was secured in the bakeable single sensor head (BSH-150, Inficon) and sealed with high temperature epoxy (Epo-Tek H21D, Epoxy technology). Deposition on the back-side of the QCM sensor was prevented by flowing an additional 20 sccm of N$_2$ through the QCM housing.[22] This additional N$_2$ was supplied using a bellows-sealed metering valve (SS-4BMG, Swagelok).

Quadrupole mass spectrometry (QMS) was performed on the vapor phase species in the ALD reactor. Measurements were performed with a residual gas analyzer (RGA 200, Stanford Research Systems). The gases produced during the ALD reactions were sampled using an aperture with a diameter of 50 µm. The aperture separated the pressure of the ALD reactor at ~1 Torr from the pressure of the QMS region at ~1 $\times 10^{-7}$ Torr. To maintain these pressures with a

conductance between the two regions, the QMS region was differentially pumped with a turbomolecular pump (V70LP, Varian). A dual thoriated-iridium (ThO_2/Ir) filament was used for electron emission in the mass spectrometer. The ionization energy was 70 eV. A Faraday cup was used as the detector.

2.2B. Fourier Transform Infrared (FTIR) Spectroscopy

The *in situ* FTIR studies were performed in a reactor equipped with an FTIR spectrometer that has been described previously.[25] The reactor was pumped using a mechanical pump (TRIVAC D8B , Oerlikon Leybold Vacuum). The FTIR spectrometer (Nicolet 6700 FTIR, Thermo Scientific) utilized a liquid-N_2-cooled mercury cadmium telluride (MCT-B) detector. Dry, CO_2-free air was employed to purge the spectrometer, mirror, and detector setup. Each spectrum consisted of a total of 100 scans at 4 cm^{-1} resolution from 400 to 4000 cm^{-1}.

The transmission FTIR measurements were performed on high surface area SiO_2 nanoparticles (99.5%, US Research Nanomaterials) with an average diameter of 15-20 nm. The high surface area of these nanoparticles was needed to enhance the number of surface species in the infrared beam. The SiO_2 nanoparticles absorb infrared radiation between 400-650 cm^{-1}, 700-875 cm^{-1}, and 925- 1400 cm^{-1}. These absorption regions leave available windows to observe absorbance from the AlF_3 ALD film. Sample preparation involved pressing the SiO_2 nanoparticles into a tungsten grid support (Tech-Etch).[26-27] The tungsten grids had dimensions of 2×3 cm^2. Each grid was 50 μm thick with 100 grid lines per inch.

The tungsten grid was resistively heated using a DC power supply (6268B, 20V/ 20A, Hewlett-Packard). The voltage output of the power supply was controlled by a PID temperature controller (Love Controls 16B, Dwyer Instruments). A type K thermocouple was attached to the

bottom of the tungsten grid with epoxy (Ceramabond 571, Aremco) that attached and electrically isolated the thermocouple.

The AlF$_3$ ALD reactions were performed using sequential exposures of TMA (97 %, Sigma-Aldrich), and HF from HF-pyridine (70 wt% HF, Sigma-Aldrich). To achieve self-limiting behavior on the high surface area particle substrates, the AlF$_3$ ALD films were deposited using two consecutive TMA doses with exposure times of 2.0 s and two consecutive HF doses with exposure times of 2.0 s. These exposure times produced pressure transients of ~450 mTorr and ~500 mTorr above the base pressure for TMA and HF, respectively. A 180 s purge time was utilized after each reactant exposure.

Reactants were dosed into a flowing N$_2$ carrier gas stream. A mass flow controller supplied the constant N$_2$ carrier gas flow rate of 50 sccm. This N$_2$ gas flow resulted in a base pressure of ~0.650 Torr in the reactor. The TMA, HF-pyridine, and H$_2$O precursors were held at room temperature. Each AlF$_3$ ALD experiment was conducted on a fresh initial Al$_2$O$_3$ ALD film. The Al$_2$O$_3$ ALD films were prepared using 3 ALD cycles with TMA and H$_2$O (Chromasolv for HPLC, Sigma-Aldrich) as the reactants.

2.2C. *Ex situ* Film Characterization using XRR, XRD and SE

For *ex situ* measurements, boron-doped Si (100) wafers (p-type, Silicon Valley Microelectronics) were used as the substrates. The Si wafer was cleaved into 2.5 cm by 2.5 cm samples. These samples were cleaned with acetone, isopropanol, and deionized water and dried with N$_2$ gas.

The film thicknesses and the density were determined using *ex situ* XRR measurements. The XRR measurements were performed with a high resolution X-ray diffractometer (Bede D1, Jordan Valley Semiconductors) using a Cu Kα ($\lambda = 1.540$ Å) X-ray tube. The filament current was 35 mA and the voltage was 40 kV. The step size and acquisition time for all the XRR scans

were 10 arcsec and 5 s, respectively. The XRR scans were modeled with the Bede REFS software package (Bede REFS, Jordan Valley Semiconductors) to determine film thickness, surface roughness, and film density. The film structure was examined by grazing incidence X-ray diffraction (GIXRD) using the same X-ray diffractometer.

The film thicknesses and refractive index were measured using spectroscopic ellipsometry (SE). These measurements were performed using a spectroscopic ellipsometer (M-2000, J. A. Woollam) employing a spectral range from 240 to 1700 nm with an incidence angle of 75°. Measurement of Ψ and Δ were modeled with the CompleteEASE software package (CompleteEASE, J. A. Woollam) and a Sellmier model.[28] The Sellmeier model is commonly used for optically transparent films such as metal fluoride films.[28]

2.2D. X-ray Photoelectron Spectroscopy and Rutherford Backscattering Spectrum

The film composition was determined by X-ray photoelectron spectroscopy (XPS). The XPS instrument (PHI 5600, RBD Instruments) used a monochromatic Al Kα X-rays source (1486.6 eV). Survey scans were measured with a pass energy of 93.9 eV and a step size of 0.400 eV. Depth profiles were obtained using Ar ion sputtering. A pass energy of 58.7 eV and a step size was 0.250 eV was used for the depth profiling analysis. An electron beam neutralizer was employed at 17.8 mA. Data was collected with the Auger Scan software package (Auger Scan, RBD Instruments) and analyzed with the Casa XPS software package (Casa XPS, Casa Software).

The RBS analysis was performed in the Nanofabrication Center at the University of Minnesota. Glassy carbon plates (Type 2, 1 mm thick, Alfa Aesar) with dimensions of 1.2 cm by 1.2 cm were used as the substrates for RBS analysis. The glassy carbon substrates were cleaned with acetone, isopropanol, and deionized water and dried with N_2 gas. Initially, Al_2O_3 ALD films were deposited as an adhesion layer on the glassy carbon plates using 20 cycles of Al_2O_3 ALD. The AlF_3 films were then deposited using 800 cycles of AlF_3 ALD.

The incident 2 MeV beam of He$^+$ ions was integrated to 40 μC of total charge per point using an ion detector positioned at 165° relative to the incident ion beam. The backscattered ions were collected using a microchannel plate detection system. RBS spectra were acquired using a MAS 1700 pelletron tandem ion accelerator (5SDH) equipped with charge exchange RF plasma source (National Electrostatics Corporation) and RBS 400 analytical endstation (Charles Evans & Associates). The data was modeled using a QUARK software package.[29]

2.3. Results and Discussion

2.3A. Growth of AlF$_3$ Films

Figure 1 shows the QCM measurements of mass gain during 200 cycles of AlF$_3$ ALD at 150°C using TMA and HF. The initial layer on the QCM sensor was an Al$_2$O$_3$ ALD film grown with 200 cycles of Al$_2$O$_3$ ALD using TMA and H$_2$O as the reactants. The reaction sequence of one AlF$_3$ ALD cycle consisted of a 1 s dose of TMA, 30 s of N$_2$ purge, a 1 s dose of HF, and 30 s of N$_2$ purge. This reaction sequence is designated as (1-30-1-30). The TMA and HF doses produced pressure transients of 40 mTorr and 100 mTorr, respectively. The AlF$_3$ ALD growth is very linear with a mass gain per cycle (MGPC) of 31 ng/(cm^2 cycle). In addition, AlF$_3$ ALD nucleates nearly immediately on the initial Al$_2$O$_3$ ALD surface.

Figure 2 shows the mass gain during three sequential AlF$_3$ ALD cycles at 150°C using the reaction sequence (1-30-1-30). These three cycles were the 148th, 149th, and 150th AlF$_3$ ALD cycles in Figure 1. The mass gains are very distinct. The mass increase after the TMA exposure is $\Delta M_{TMA} = 22$ ng/(cm^2 cycle). The mass increase after the HF exposure is $\Delta M_{HF} = 9$ ng/(cm^2 cycle). The MGPC was 31 ng/(cm^2 cycle).
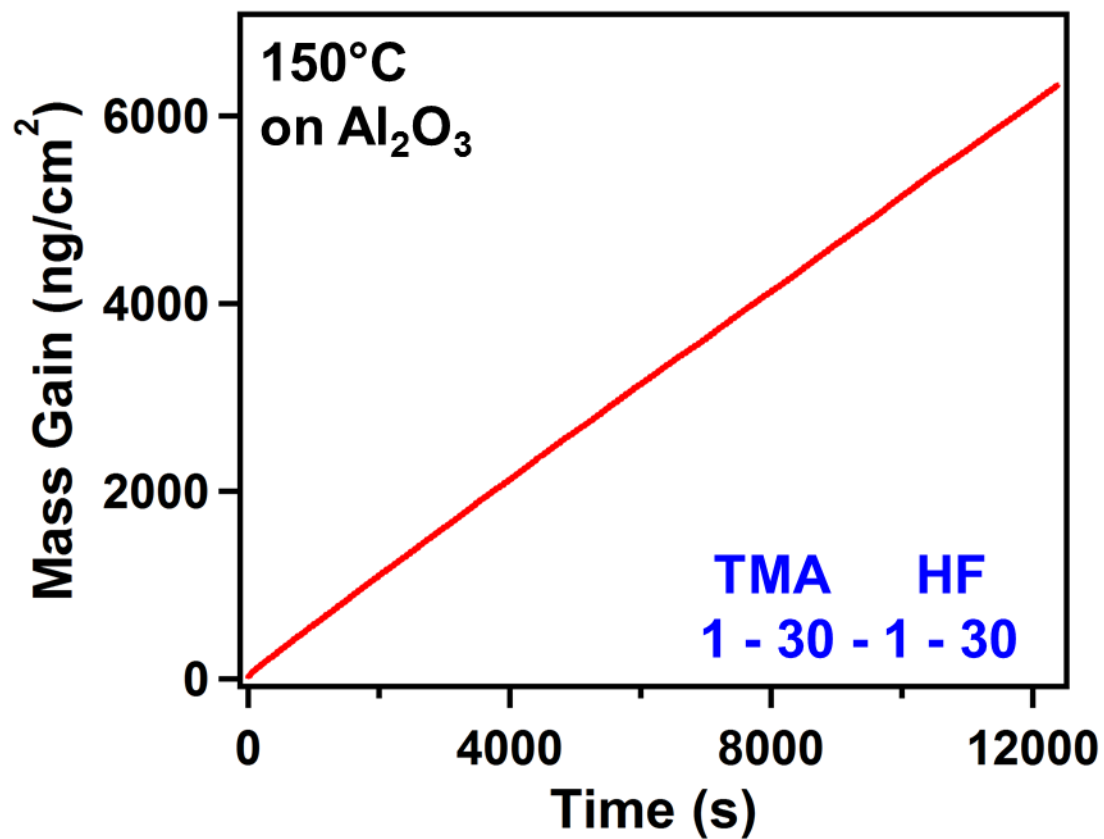
Figure 2-1. Mass gain versus time during 200 AlF$_3$ ALD cycles with TMA and HF as the

reactants on Al$_2$O$_3$ at 150 °C using the reaction sequence of (1-30-1-30).
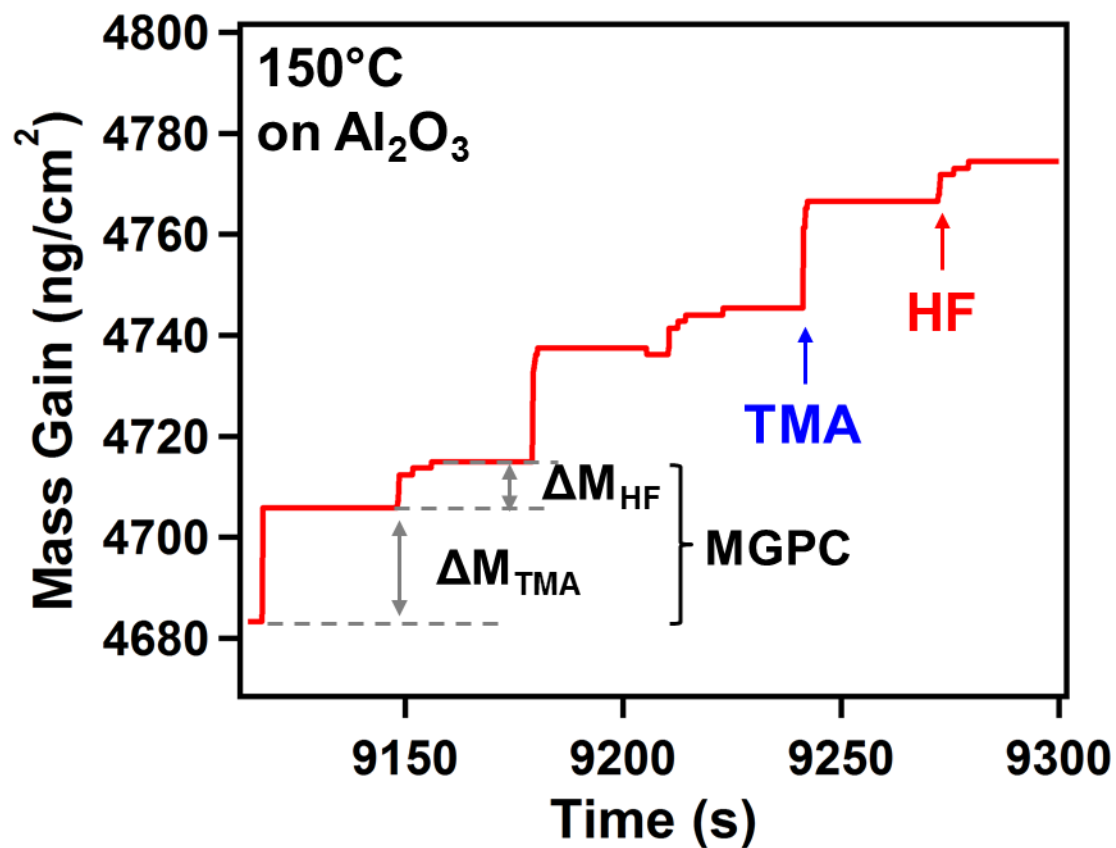
Figure 2-2. Enlargement of mass gain versus time for three sequential TMA and HF exposures during AlF$_3$ ALD in the steady-state, linear growth regime shown in Figure 2-1.

Figure 3 displays the MGPC and the ΔM_{TMA}/MGPC ratio during 200 cycles of AlF_3 ALD using a reaction sequence of (1-30-1-30). The MGPC is 31 ng/(cm^2 cycle) and consists of constant mass gains of ΔM_{TMA} = 22 ng/(cm^2 cycle) and ΔM_{HF} = 9 ng/(cm^2 cycle). Except for the first 3 AlF_3 ALD cycles, the ΔM_{TMA}/MGPC ratio is constant at 0.71. The MGPC and the ΔM_{TMA}/MGPC ratio were nearly independent of the purge time. Extended purge times of 120 s slightly decreased the MGPC to ~29 ng/(cm^2 cycle). However, the ΔM_{TMA}/MGPC ratio remained at 0.71. The ΔM_{TMA}/MGPC ratio will be used later to determine the reaction stoichiometry.

The self-limiting behavior of the TMA and HF reactions for AlF_3 ALD was also examined using *in situ* QCM experiments. Figure 4a and 4b show the mass gains during the TMA and HF exposures, respectively, at 150°C. For each of these exposures, the previous reactant exposure had reached saturation. Each minidose consisted of an exposure time of 0.5 s and a purge time of 30 s. Both reactions displayed self-limiting behavior. ΔM_{TMA} versus minidoses of TMA reached the plateau of ΔM_{TMA} = ~22 ng/(cm^2 cycle) after one minidose. Similarly, ΔM_{HF} versus minidoses of HF leveled off at ΔM_{HF} = ~9 ng/(cm^2 cycle) after one minidose.

Figure 5 displays the film thickness for 20, 50, 100, 200, 400, and 800 cycles of AlF_3 ALD on a Si wafer at 150°C as determined by *ex situ* XRR and SE analysis. The thickness measurements from XRR and SE were nearly identical. The AlF_3 ALD growth on the silicon wafers was linear with a growth rate of 1.0 Å /cycle at 150°C. The density of these AlF_3 ALD films obtained from XRR was 2.9 g /cm^3. This density is slightly less than the bulk density of 3.10 g /cm^3 for crystalline AlF_3.[30] The thickness variation between samples grown in the reactor at different spatial locations using 800 cycles of AlF_3 ALD revealed good spatial uniformity
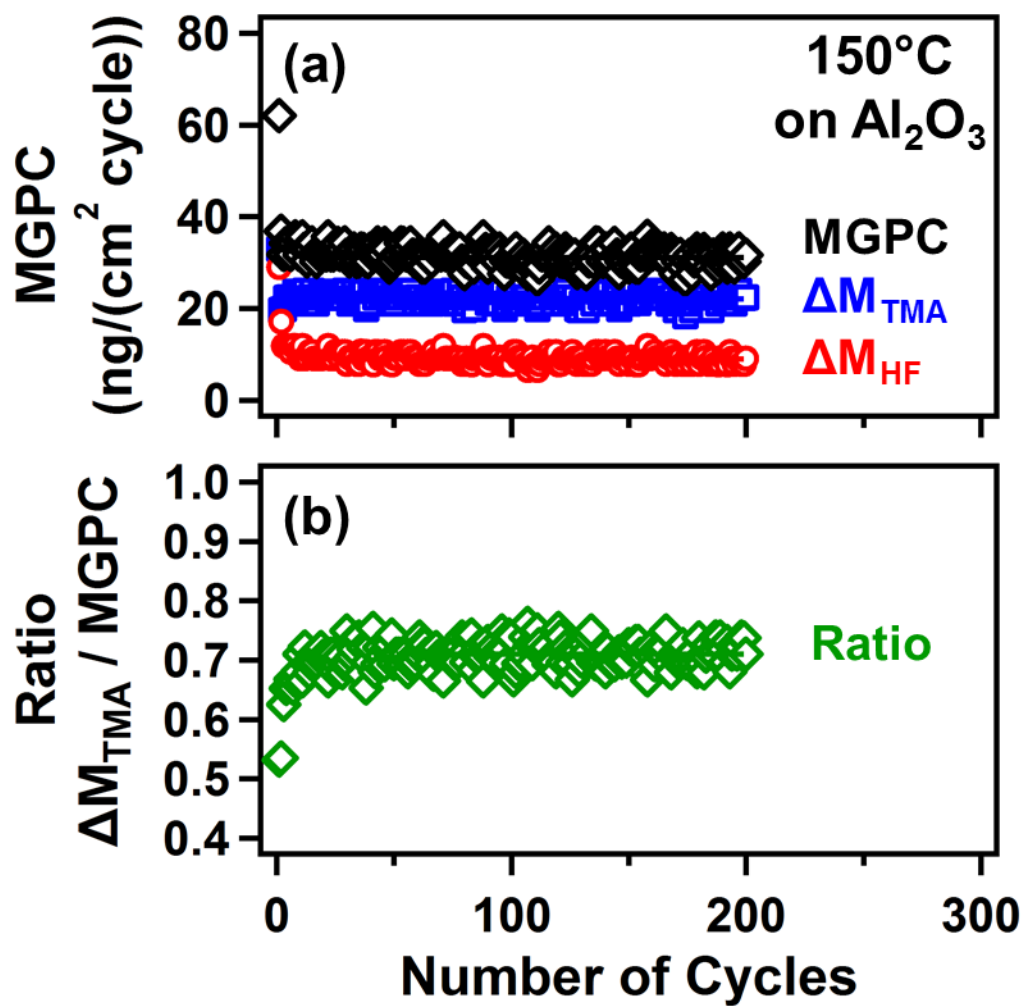
Figure 2-3. (a) MGPC, ΔM_{TMA}, and ΔM_{HF} and (b) M_{TMA}/MGPC ratio during 200 AlF_3 ALD

cycles with TMA and HF as the reactants on Al_2O_3 at 150 °C.
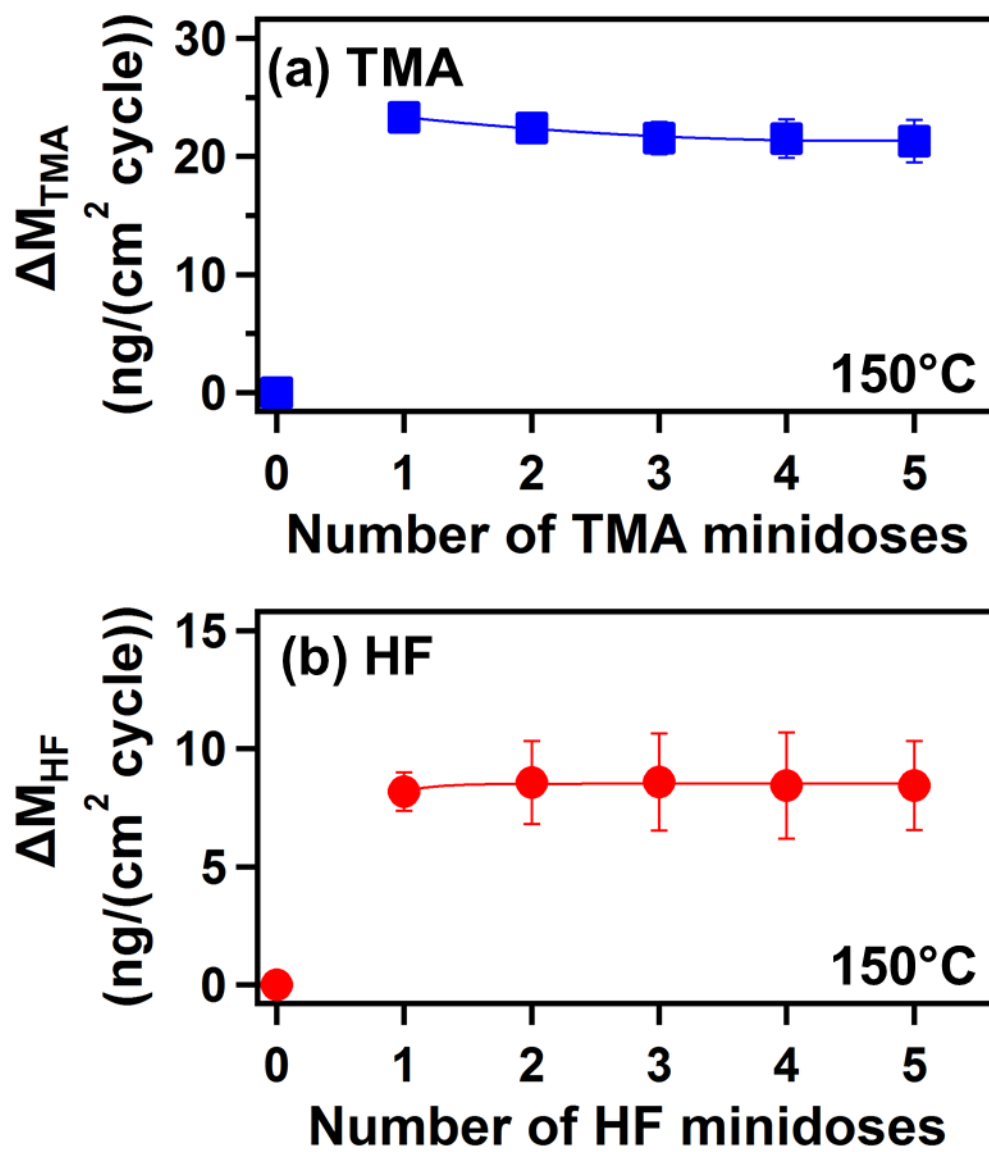
Figure 2-4. (a) ΔM_{TMA} versus versus number of TMA minidoses with the HF exposure fixed at 1.0 s. (b) ΔM_{HF} versus versus number of HF minidoses with the TMA exposure fixed at 1.0 s.
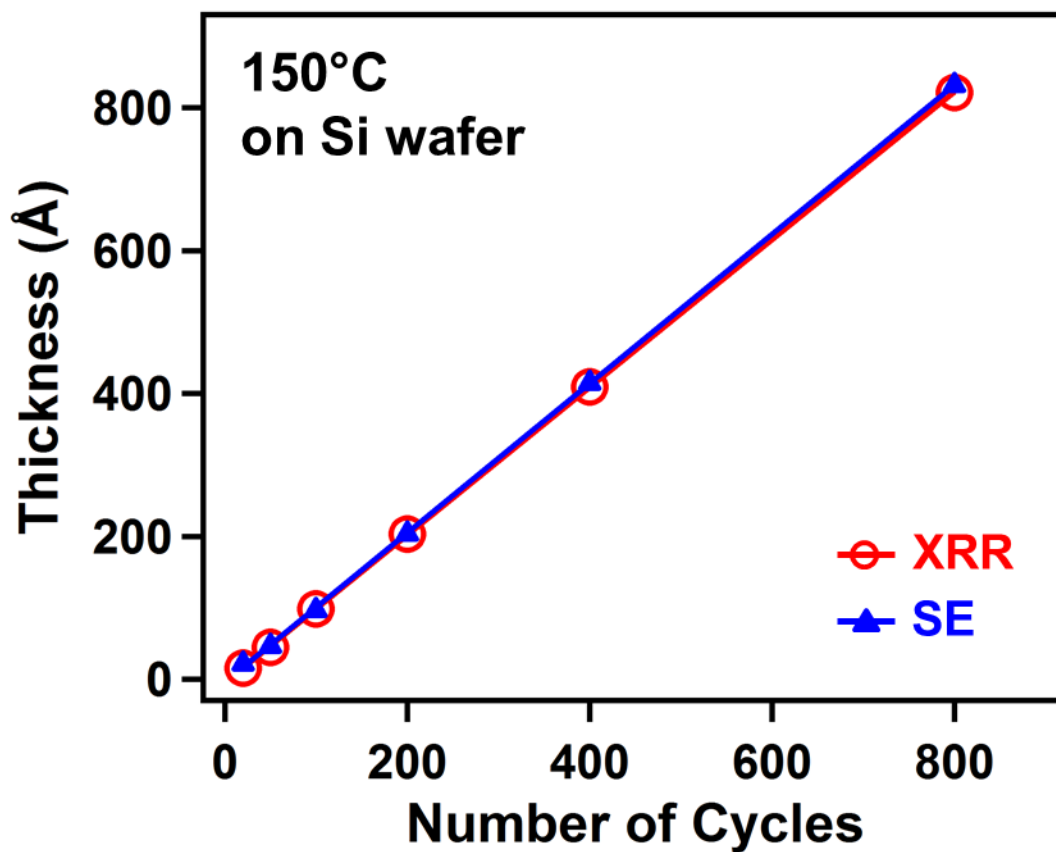
Figure 2-5. Film thickness versus number of cycles for 800 AlF$_3$ ALD cycles with TMA and

HF as the reactants on Si(100) at 150 ℃ determined by XRR and SE measurements.

within ±1% as measured by XRR analysis. The films grown using 800 cycles of AlF_3 ALD were very smooth with a surface roughness of 4 -5 Å .

The growth rate of 1.0 Å /cycle at 150℃ obtained by the XRR analysis can be compared with the MGPC of 31 ng/(cm^2 cycle) obtained by the QCM measurements. This comparison is possible using the density of 2.9 g/cm^3 obtained by XRR analysis. Using this density, the MGPC of 31 ng/(cm^2 cycle) is equivalent to a growth rate of 1.1 Å /cycle. There is excellent agreement between the AlF_3 ALD growth rates determined using QCM and XRR measurements.

Grazing incidence X-ray diffraction (GIXRD) analysis revealed that the AlF_3 ALD films were amorphous. The AlF_3 ALD films remain amorphous even after annealing at 500℃ in argon. The AlF_3 ALD films were also stable in air. The thickness, film density, and film roughness of AlF_3 films did not change after storage in atmosphere for one month.

Figure 6 reveals some of the gas phase species detected by the quadrupole mass spectrometer during AlF_3 ALD using sequential TMA and HF exposures. These mass spectrometry signals were recorded at the same time as the mass gains shown in Figure 2. The targeted gas phase species were the CH_4 reaction product at m/z=16, the HF reactant at m/z=20 and the pyridine species at m/z=52. Results are shown for three AlF_3 ALD cycles using the reaction sequence (1-30-1-30).

The mass signal at m/z = 16 in Figure 6 appears during both the TMA and HF exposures. This mass signal is assigned to CH_4 reaction product during the HF exposure. HF reacts with Al-CH_3* surface species to produce CH_4. TMA also reacts with HF on the surface to produce CH_4. In addition, some of the m/z=16 mass signal is also produced as a cracking fragment of TMA. Mass spectrometer analysis performed after the TMA reaction reached saturation showed that cracking of TMA could account for ~1/3 of the m/z=16 mass signal observed in Figure 6.
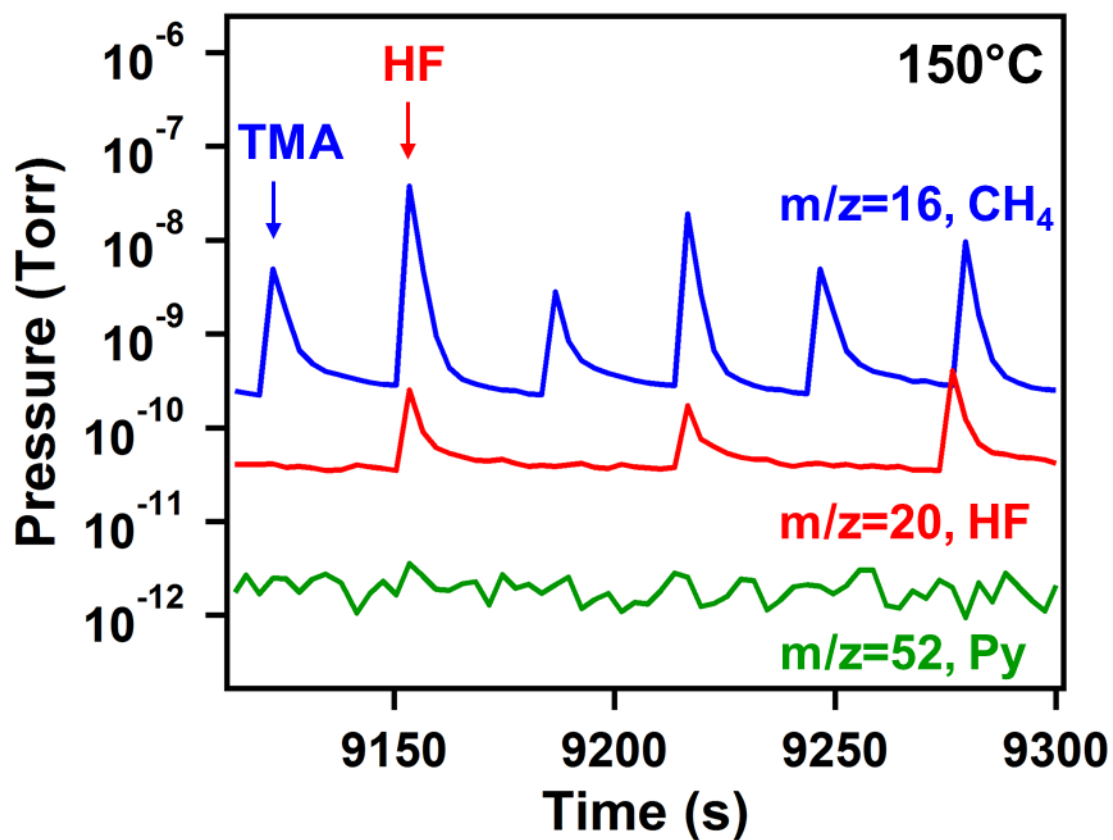
Figure 2-6. Mass spectrometer signals for m/z= 16, 20 and 52 for CH_4, HF and pyridine, respectively, during three AlF_3 ALD cycles at 150°C. These signals were recorded at the same time as the mass changes shown in Figure 2-2.

Figure 6 also indicates that a mass signal at m/z=20 is coincident only with the HF exposures. This mass signal is assigned to the HF reactant. The QMS does not detect a mass signal at m/z = 52 or m/z=79. These mass signals are the two largest mass cracking fragments for pyridine.[31] These results indicate that the HF-pyridine solution has a negligible pyridine vapor pressure. In contrast, the vapor pressure of pyridine at 20°C is ~15 Torr.[32] The negligible pyridine vapor pressure is consistent with the stabilization of pyridine with HF in a high boiling point azeotrope.[33] Additional experiments with pure pyridine solutions clearly showed substantial mass signals at m/z = 52 and m/z = 79.

Additional experiments examined the growth of AlF_3 ALD films at various substrate temperatures. Figure 7a shows the temperature dependence of the MGPC from *in situ* QCM measurements. The MGPC can be converted to the growth rate in Å /cycle using the film density of 2.9 g/cm^3 measured by XRR. These growth rates are shown in Figure 7b. In addition, Figure 7b also displays the growth rates determined from *ex situ* XRR and SE measurements. The agreement between the *in situ* and *ex situ* measurements of the growth rate is very good. A maximum growth rate of 1.5 Å / cycle was obtained at 100 °C. A summary of the temperature-dependent growth rates is given in Table 1.

Both Figure 7a and Figure7b show that the AlF_3 ALD growth rate decreases at higher temperatures. The progressive decrease in the AlF_3 ALD growth rate could be explained by the loss of surface species responsible for growth at higher temperature. A similar decrease in ALD growth rate was observed for the temperature dependence of Al_2O_3 ALD.[34] In addition, the AlF_3 ALD growth rate becomes negative at temperatures >250°C. At these higher temperatures, the TMA and HF exposures are able to etch the AlF_3 ALD films.
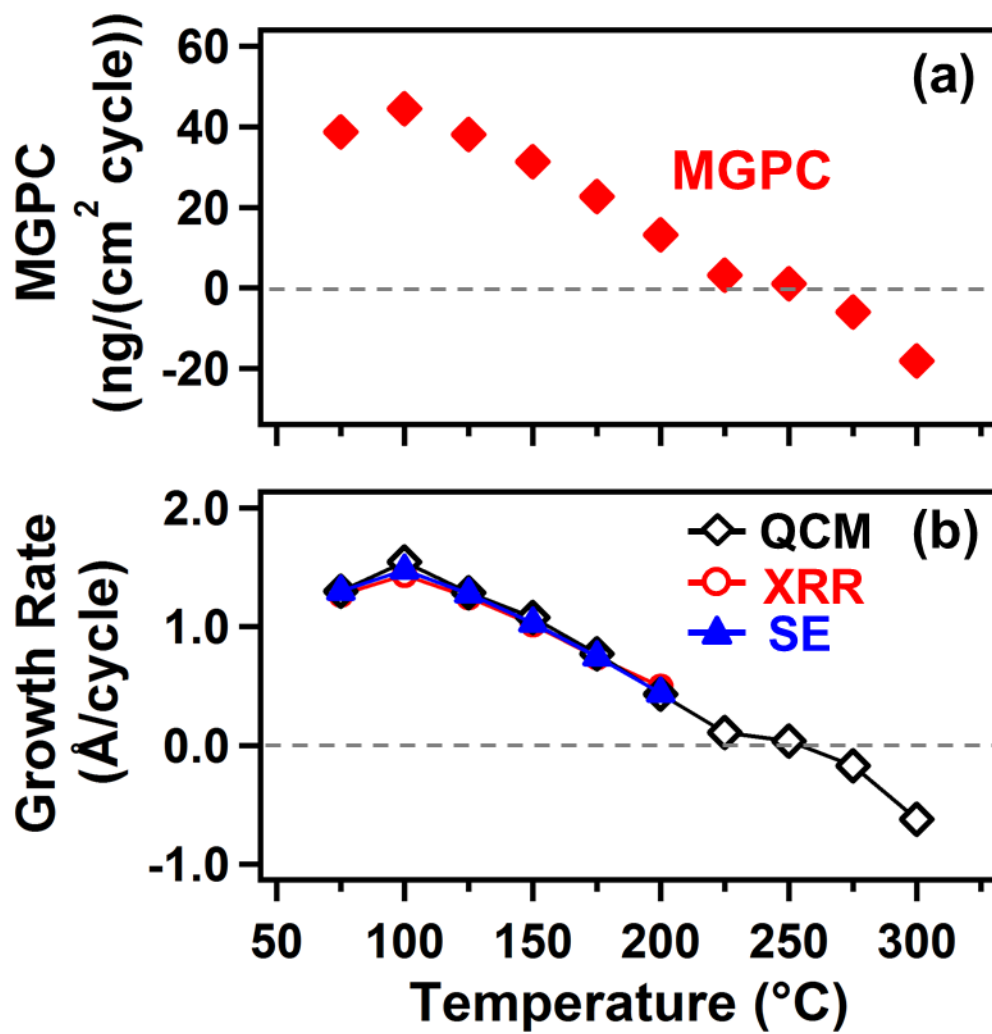
Figure 2-7.   (a) Mass gain per cycle (MGPC) and (b) growth rate versus reaction temperature

using reaction sequence of (1-30-1-30).

Temperature (°C)	MGPC	Growth Rate	ΔM_{TMA}	ΔM_{HF}	$\Delta M_{TMA}/$ MGPC	x
75	38.7	1.27	28.3	10.4	0.73	0.67
100	44.4	1.43	29.7	14.8	0.67	0.99
125	38.1	1.25	26.2	12.0	0.69	0.88
150	31.4	1.02	22.3	9.1	0.71	0.78
175	22.7	0.74	16.7	6.0	0.73	0.67
200	13.2	0.50	9.3	3.9	0.70	0.83

Table 2-1. ΔM_{TMA}, ΔM_{HF}, MGPC, $\Delta M_{TMA}/$MGPC, and x for AlF_3 ALD at different temperatures. ΔM_{TMA}, ΔM_{HF}, and MGPC are expressed in units of ng/(cm^2 cycle). Growth rate is expressed in unit of Å /cycle

The AlF$_3$ etching may occur by the reaction: AlF$_3$ + 2Al(CH$_3$)$_3$ $\rightarrow$ 3AlF(CH$_3$)$_2$. In this reaction, TMA accepts fluorine from AlF$_3$ to form AlF(CH$_3$)$_2$. The –CH$_3$ from TMA is transferred to the substrate and forms additional AlF(CH$_3$)$_2$. This etching process is related to the thermal atomic layer etching (ALE) for Al$_2$O$_3$ and HfO$_2$ films that has been observed using Sn(acac)$_2$ and HF reactants.[35-36] However, in this case, the etching of AlF$_3$ by TMA is not self-limiting. The AlF$_3$ etching rate at 250 and 300°C is dependent on the length of the TMA exposure. We will report AlF$_3$ ALE using Sn(acac)$_2$ and HF in a future publication.

2.3B. Nucleation and Reaction Mechanism for AlF$_3$ ALD

FTIR vibrational spectroscopy was used to monitor AlF$_3$ ALD and identify the surface species present during AlF$_3$ ALD. Figure 8 shows the growth of absorbance in the frequency range from 500-800 cm^{-1} during AlF$_3$ ALD cycles on Al$_2$O$_3$ ALD films on SiO$_2$ nanoparticles. This FTIR spectrum was referenced to the FTIR spectrum for the Al$_2$O$_3$ ALD film on the SiO$_2$ nanoparticles. The absorbance progressively increases versus number of AlF$_3$ ALD cycles. The growth of absorbance in the frequency range from 500-800 cm^{-1} is attributed to the Al-F stretching vibration in AlF$_3$. Earlier vibrational studies have observed the absorption of Al-F stretching vibrations in AlF$_3$ at 500-800 cm^{-1}.[16,37-39]

Figure 8 also monitors an absorbance loss at ~800-1050 cm^{-1} after the first AlF$_3$ ALD cycle. To explore this absorbance loss, FTIR spectra were recorded during nucleation after the first TMA exposure and first HF exposure during AlF$_3$ ALD. Figure 9 displays these FTIR spectra that were again referenced the FTIR spectrum for the Al$_2$O$_3$ ALD film on the Si nanoparticles. There is a slight absorbance loss at ~1000 cm^{-1} and absorbance gain at 650-850 cm^{-1} after the first TMA exposure. The slight absorbance loss at ~1000 cm^{-1} is attributed to the removal of an Al-OH vibrational feature on the initial Al$_2$O$_3$ ALD film. This loss has been
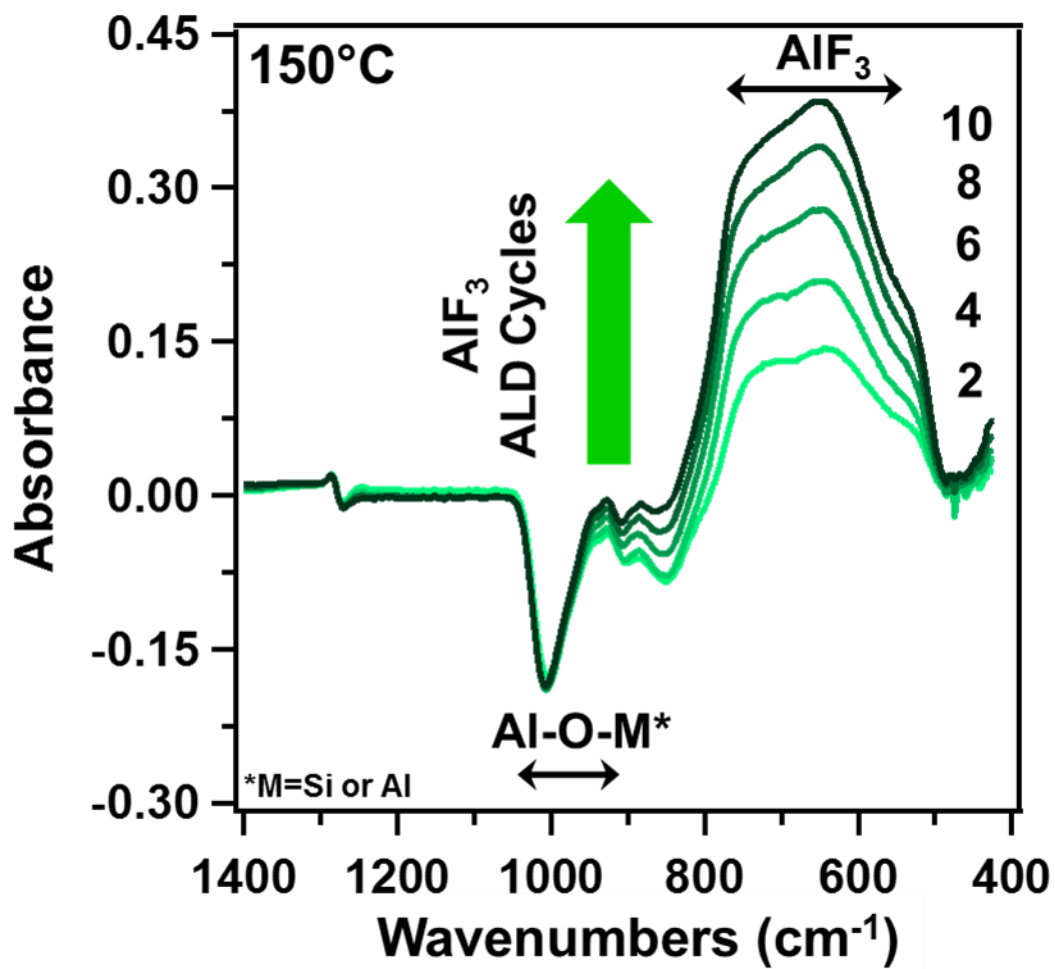
Figure 2-8.   FTIR spectra versus AlF$_3$ ALD cycles on initial Al$_2$O$_3$ surface. These spectra are

all referenced to the initial Al$_2$O$_3$ film on the SiO$_2$ nanoparticles.
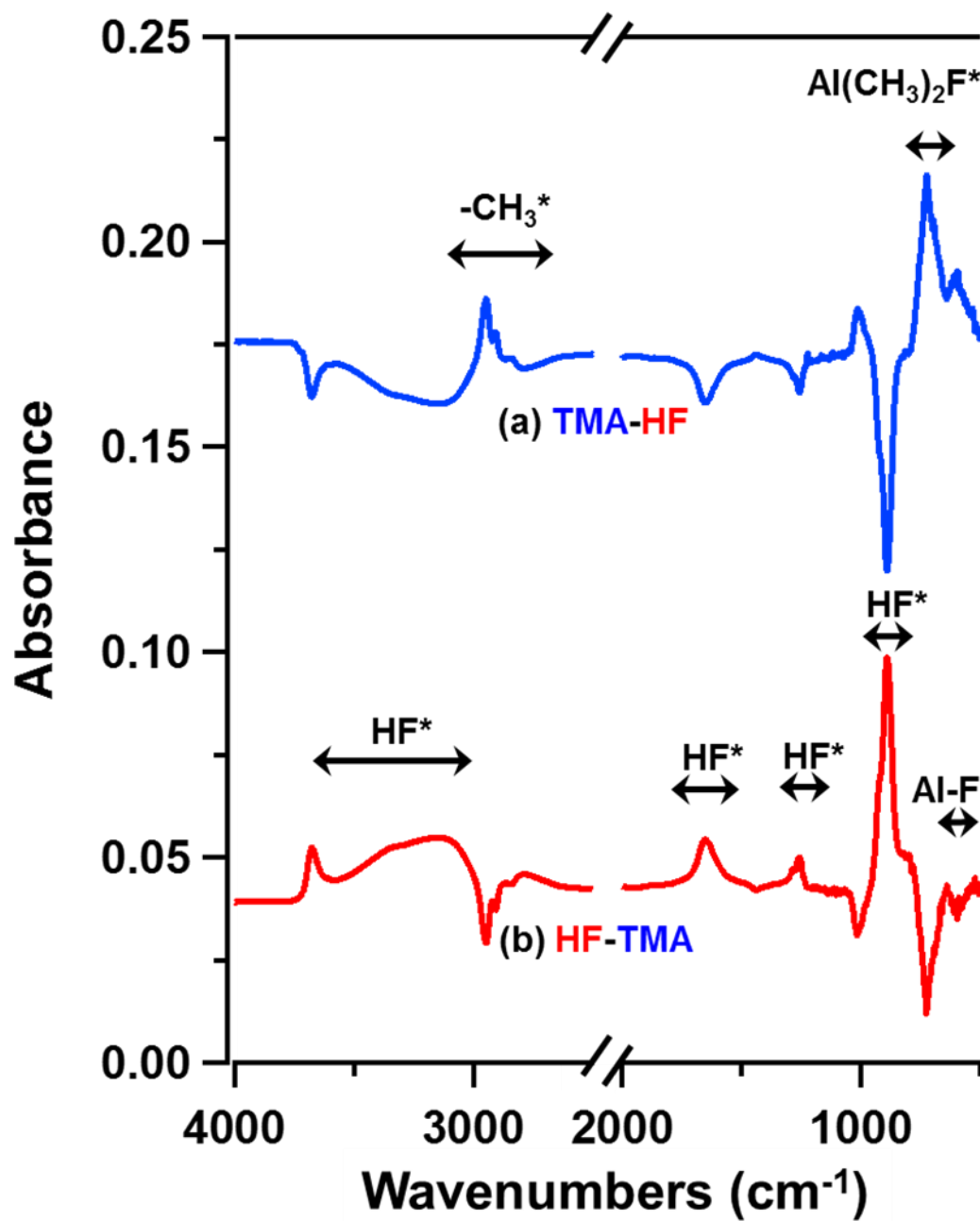
Figure 2-9. Difference FTIR spectra after (a) 1st TMA exposure on initial Al_2O_3 surface and (b) 1st HF exposure after 1st TMA exposure. The difference spectra are referenced to spectra recorded immediately prior to the TMA and HF exposures.

observed before during Al_2O_3 ALD growth.[40-41] The absorbance gain at 650-850 cm^{-1} is

attributed to the growth of more Al_2O_3 after the reaction of TMA with AlOH* surface species.

An absorbance loss also occurs between 800-1050 cm^{-1} after the first HF exposure. This

absorbance loss is in the range of the Al-O stretching vibrations in Al_2O_3 and results from the

loss of Al_2O_3. In addition, there is an absorbance gain at 500-800 cm^{-1}. This absorbance gain is

again attributed to the Al-F stretching vibration in AlF_3.[37-39] These absorbance losses and gains

are consistent with the conversion of Al_2O_3 to AlF_3 by the reaction $Al_2O_3 + 6HF \rightarrow 2AlF_3 +$

$3H_2O$. This reaction is thermochemically favorable and spontaneous with ΔG = -63 kcal at

150°C.[42]

The conversion of Al_2O_3 to AlF_3 only occurs during nucleation of AlF_3 ALD after the

first HF exposure. Figure 8 shows that the pronounced absorbance loss between 800-1050 cm^{-1}

remains fairly constant versus number of AlF_3 ALD cycles. There is a reduction of the

absorbance loss in the frequency range of 800-950 cm^{-1} with the number of AlF_3 ALD cycles.

The absorbance loss is progressively reduced by the growth of absorbance from the Al-F

stretching vibrations.

Figure 10 shows the FTIR difference spectra for two consecutive TMA and HF

exposures. These difference spectra are referenced to the spectra after the previous reactant

exposure. Figure 10a shows the difference spectrum after the TMA exposure referenced to the

spectrum after the previous HF exposure (TMA-HF). Figure 10a reveals absorbance gains for

vibrational features at ~650-600, 725, 1450, and ~2800-3000 cm^{-1}. These positive absorbance

features are all consistent with the vibrational features of molecular $(CH_3)_2AlF$.[43] The

absorbance features at 600-650, 725 and 1450 cm^{-1} are attributed to the Al-F stretching mode of

$(CH_3)_2AlF$, the CH_3 rocking mode and the CH_3 asymmetric deformation, respectively.[43] The

positive features between 2800 – 3000 cm^{-1} are consistent with the C-H stretches of $(CH_3)_2AlF$.[43]

The TMA exposure also results in negative features at 900, 1250, 1650 and ~3000- 3675

cm^{-1} that are attributed to the removal of HF surface species. The negative feature at 900 cm^{-1} is

attributed to an out-of-plane librational mode.[44] The features at 1250 and 1650 cm^{-1} are

attributed to the transverse and longitudinal vibrations of the FHF^- ion.[45] The absorbance features

at ~3000- 3675 cm^{-1} are attributed to the stretching vibrations of isolated and hydrogen-bonded

Al-(HF)* surface species absorbed on AlF_3 surfaces, respectively.[46]

Figure 10b displays the difference spectrum after the HF exposure referenced to the

spectrum after the previous TMA exposure (HF-TMA). Most of the absorbance features that

were added as a result of the previous TMA exposure are removed by the subsequent HF

exposure. Negative absorbance features at 725, 1450 and 2800-3000 cm^{-1} are consistent with the

removal of $(CH_3)_2AlF*$ surface species.[43] Positive absorbance features at 900, 1250, 1650 and

~3000- 3675 cm^{-1} also indicate that the HF reabsorbs to the surface. A positive absorbance

feature between 600 – 650 cm^{-1} indicates that Al-F species are also added during HF exposures.

This bulk AlF_3 vibrational mode grows steadily with the number of reaction cycles as shown in

Figure 8.

Based on the results from the QCM and FTIR measurements, Figure 11 presents a

schematic showing the proposed reaction mechanism. In reaction A, TMA molecules react with

HF molecules adsorbed on the surface to yield $AlF(CH_3)_2$ and CH_4 molecules as the reaction

products. The $AlF(CH_3)_2$ species remain adsorbed on the surface. In reaction B, HF converts

the adsorbed $AlF(CH_3)_2$ species to AlF_3. CH_4 is again a reaction product and additional HF

molecules may remain on the surface.
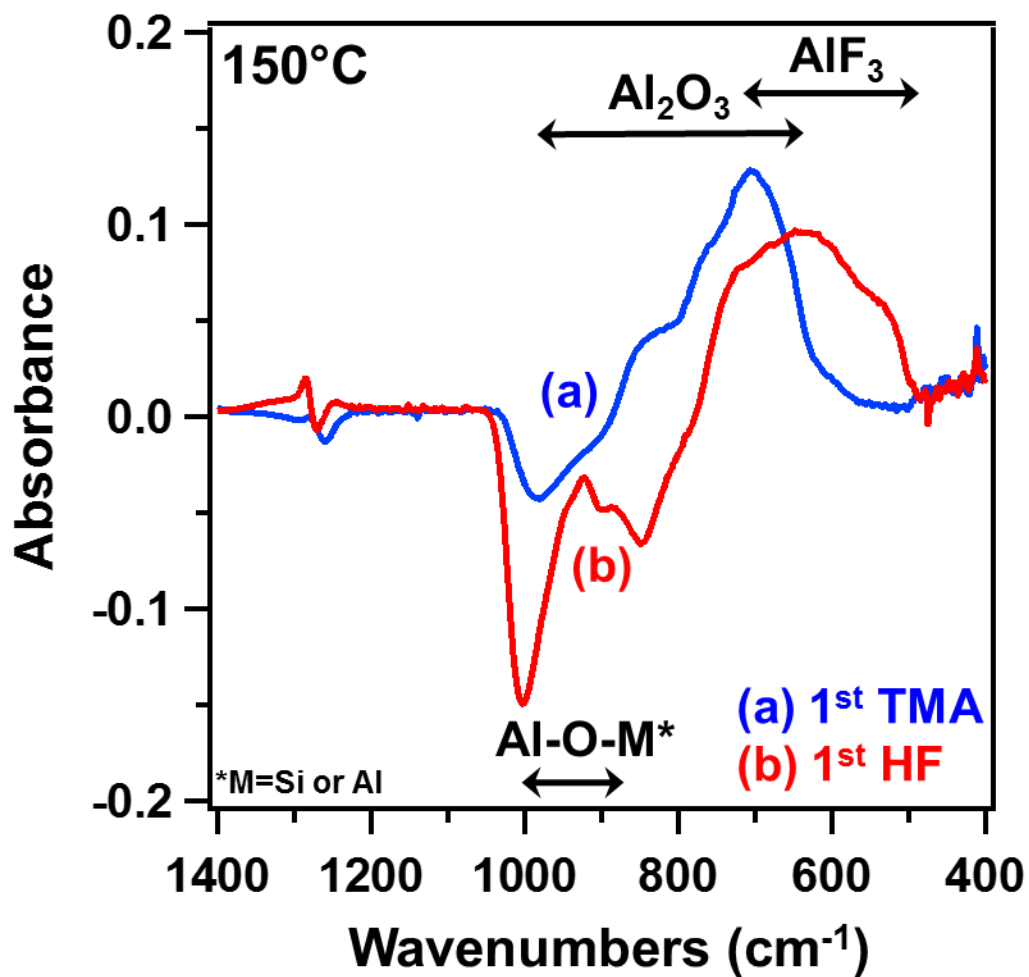
Figure 2-10. FTIR difference spectra during AlF_3 ALD. (a) Difference spectrum after the TMA exposure referenced to the spectrum after the previous HF exposure (TMA-HF) and (b) Difference spectrum after the HF exposure referenced to the spectrum after the previous TMA exposure (HF-TMA).
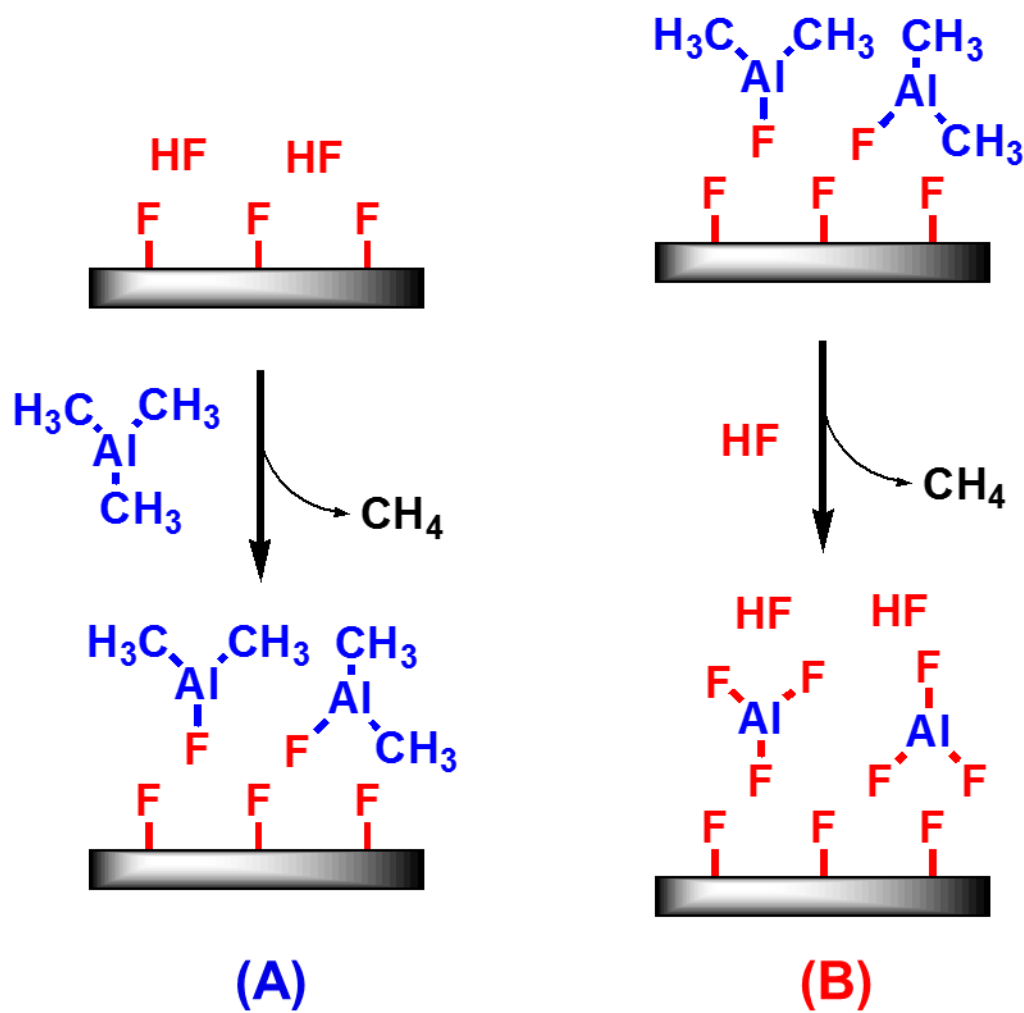
Figure 2-11. Proposed reaction mechanism for AlF$_3$ ALD using TMA and HF as the reactants.

The more general surface chemistry for AlF$_3$ ALD can be expressed by:

(A) AlF$_3$|xHF* + Al(CH$_3$)$_3$ $\rightarrow$ AlF$_3$|AlF$_x$(CH$_3$)$_{3-x}$* + xCH$_4$ (2)

(B) AlF$_3$|AlF$_x$(CH$_3$)$_{3-x}$* + 3HF $\rightarrow$ AlF$_3$|AlF$_3$|xHF* + (3-x)CH$_4$ (3)

The asterisks designate the surface species. The vertical lines distinguish the various surface species. The parameter x quantifies the number of HF molecules adsorbed on the surface relative to the number of AlF$_3$ species deposited during one AlF$_3$ ALD cycle. x=1 indicates one HF per AlF$_3$ on the surface as shown in Figure 11. x=1 is also consistent with AlF(CH$_3$)$_2$ as the adsorbed surface species in Figure 11.

Based on this surface chemistry, the ΔM_{TMA}/MGPC ratio can be determined by:

$$\frac{\Delta M_{TMA}}{MGPC} = \frac{\Delta M_{TMA}}{\Delta M_{TMA} + \Delta M_{HF}} = \frac{M_{TMA} - x \cdot M_{CH_4}}{M_{TMA} + 3M_{HF} - 3M_{CH_4}} = \frac{M_{TMA} - x \cdot M_{CH_4}}{M_{AlF_3}} \qquad (4)$$

In equation 4, M_{TMA}, M_{HF}, M_{CH4}, and M_{AlF3} are the molar masses of TMA, HF, CH$_4$, and AlF$_3$ respectively. The equation for x is:

$$x = \frac{1}{M_{CH_4}}[M_{TMA} - M_{AlF_3}(\frac{\Delta M_{TMA}}{MGPC})] = \frac{1}{16}[72.1 - 84(\frac{\Delta M_{TMA}}{MGPC})] \qquad (5)$$

The ΔM_{TMA}/MGPC ratio and x can be determined from the mass changes obtained by the QCM measurements. A ΔM_{TMA}/MGPC ratio of 0.71 was determined from the QCM measurements at 150°C shown in Figure 4b. This ratio of 0.71 is close to the ratio of 0.67 based on the proposed mechanism in Figure 11 where x=1.

The ratio varied slightly at the different reaction temperatures. The ΔM_{TMA}/MGPC ratios were 0.73, 0.67, 0.69, 0.71, 0.73 and 0.70 at 75, 100, 125, 150, 175 and 200°C, respectively. The corresponding x values were 0.67, 0.99, 0.88, 0.78, 0.67 and 0.83 at 75, 100, 125, 150, 175

and 200°C, respectively. These values are summarized in Table 1. An x value of x=0.99 or nearly x=1 is observed at 100°C. The maximum AlF_3 ALD growth rate of 1.43 Å /cycle is also measured at 100°C. x values <1 are consistent with a mixture of $AlF(CH_3)_2$ and $Al(CH_3)_3$ on the surface after the TMA exposure.

The mass changes measured during the QCM experiments support the existence of HF and $AlF(CH_3)_2$ species on the surface after the HF and TMA exposures. A binding interaction is expected between HF and the AlF_3 surface. Strong coordination of HF on α-AlF_3 and β-AlF_3 surfaces has been predicted with DFT calculations.[47-48] AlF_3 is a Lewis acid. The F in HF can act as a Lewis base. Together AlF_3 and HF have a strong Lewis acid-base interaction. TMA and $AlF(CH_3)_2$ are also Lewis acids. The F in Al-F* species on the surface can act as a Lewis base. A strong Lewis acid-base interaction is also expected between Al-F* and either TMA or $AlF(CH_3)_2$.

2.3C. *Ex situ* AlF_3 Film Characterization

Figure 12 shows an X-ray photoelectron spectroscopy (XPS) sputter depth profile of an AlF_3 ALD film. The film is almost entirely aluminum and fluorine after removal of the adventitious surface carbon. Oxygen impurities are detected at ~2 at%. The oxygen impurity may result from water that could be produced in the reaction of HF with metal oxide inside the stainless steel reactor. Carbon and nitrogen impurities are below the detection limit of XPS. The ratio between the calibrated aluminum and fluorine XPS signals is 1:2.4. The preferential sputtering of fluorine may explain the low fluorine signals.[17-18]

Figure 13 shows the Rutherford backscattering spectrum (RBS) of a film grown using 800 cycles of AlF_3 ALD. A glassy carbon substrate is used instead of a silicon wafer because
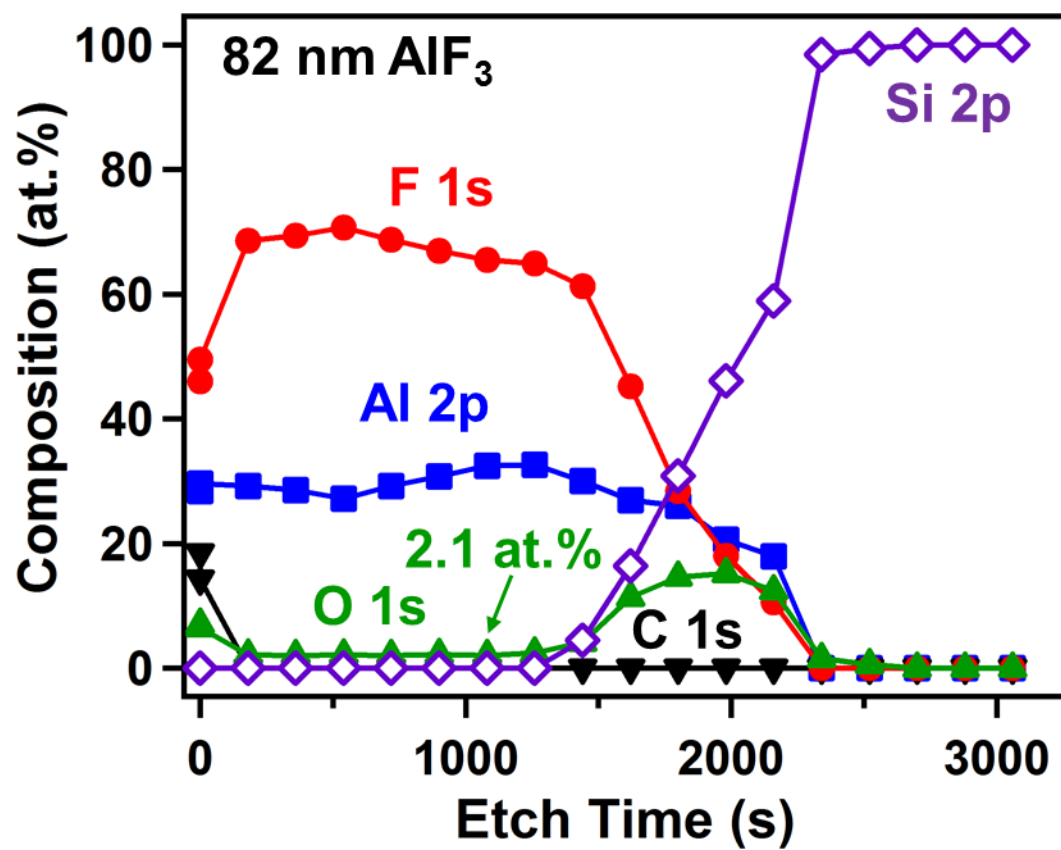
Figure 2-12. Sputter depth profile of AlF$_3$ film measured by X-ray photoelectron spectroscopy.
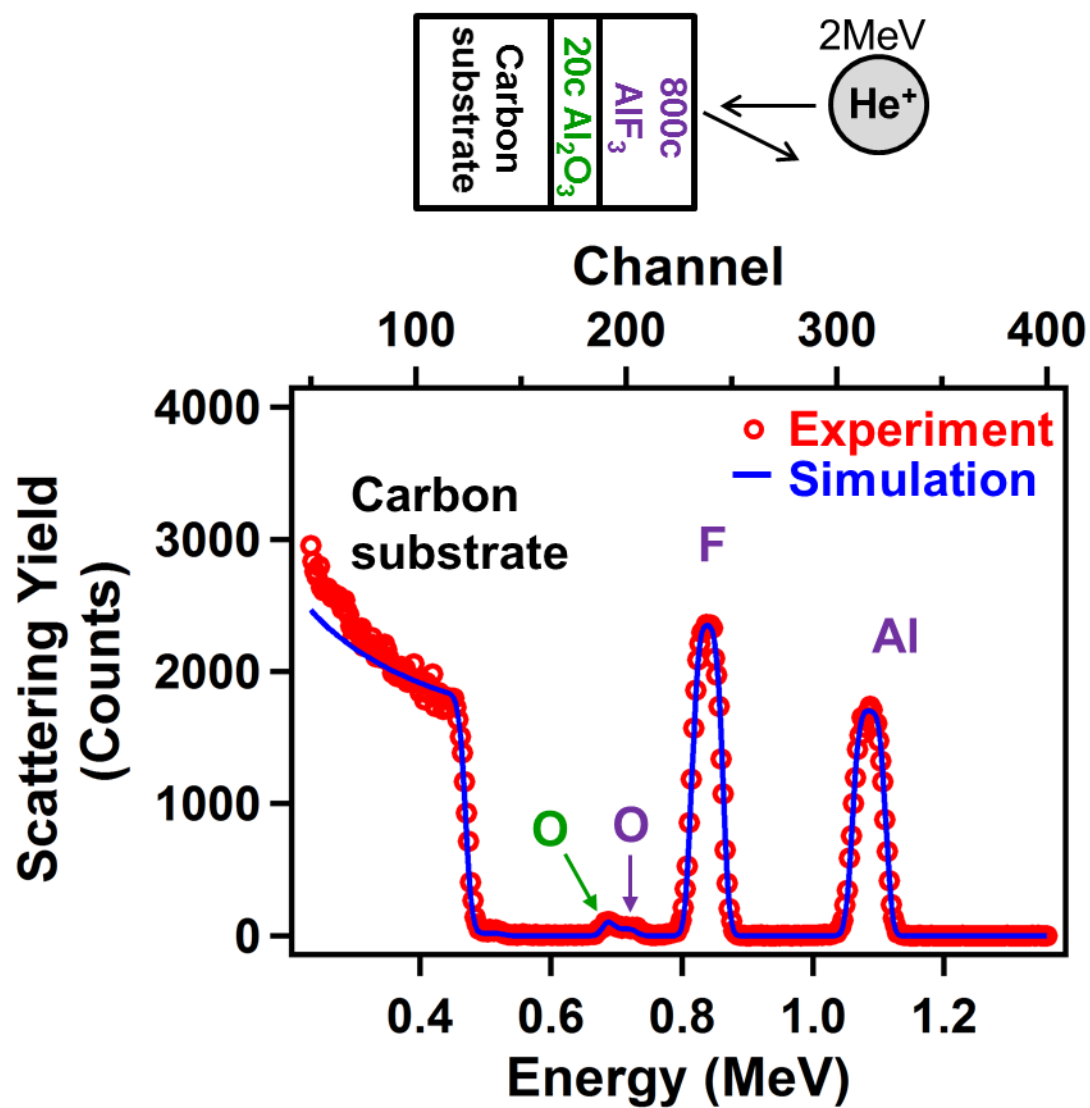
Figure 2-13. Rutherford backscattering spectrum of 800 cycles of AlF$_3$ ALD film on 20 cycles

of Al$_2$O$_3$ ALD film on carbon substrate.
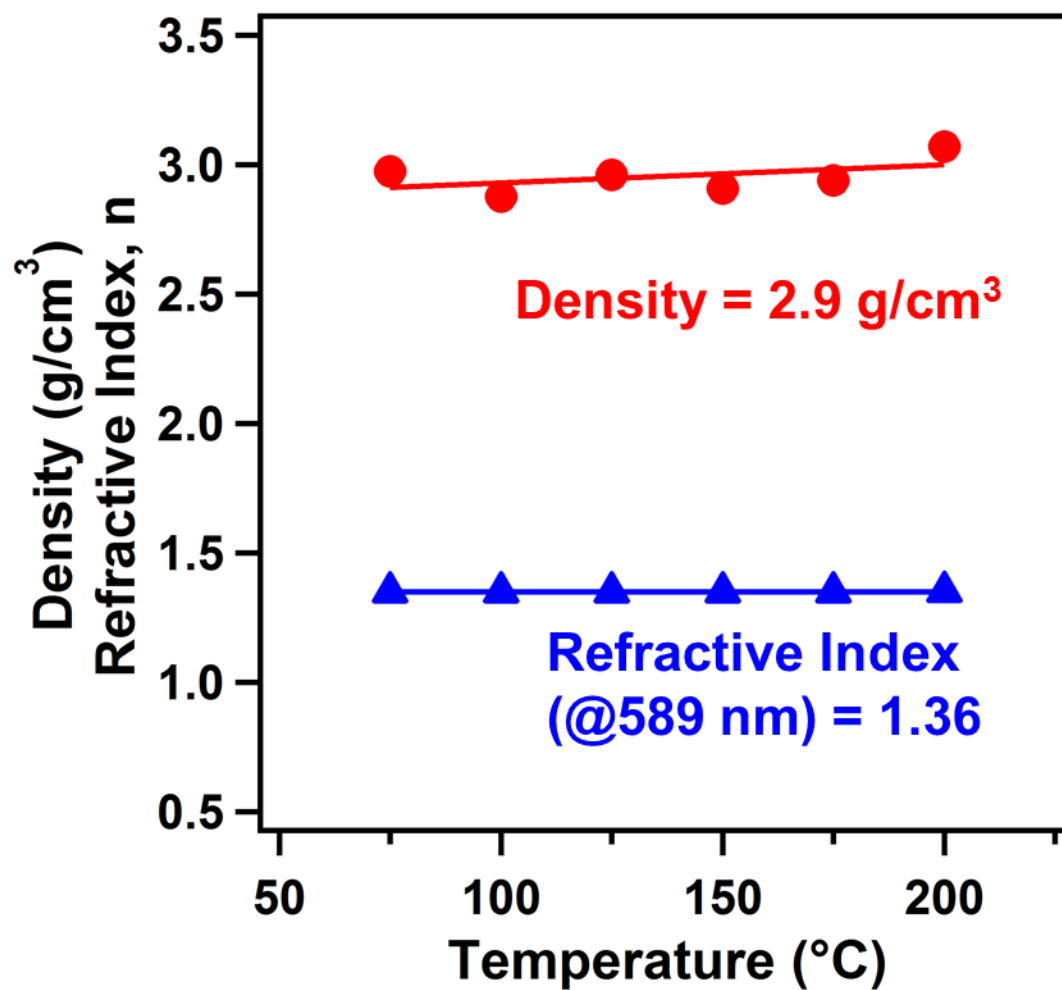
Figure 2-14. Density and refractive index for AlF$_3$ ALD films grown at various temperatures.

aluminum and silicon have similar atomic masses and overlapping RBS signals. An Al_2O_3 ALD film grown on the glassy carbon served as an adhesion layer. The RBS spectrum observed an aluminum peak at 1.1 MeV and a fluorine peak around 0.8 MeV. The aluminum to fluorine ratio is 1:2.85 based on the peak areas. This ratio is consistent with nearly stoichiometric AlF_3. Carbon or nitrogen is not observed in the film within the detection limits of RBS.

The film density and refractive index was also measured for AlF_3 films grown using 200 AlF_3 ALD cycles at different temperatures. These results are presented in Figure 14. The film density is nearly constant at 2.9 g/cm^3 at all reaction temperatures. This density is ~94 % of the bulk density of 3.1 g/cm^3 for crystalline AlF_3.[30] Refractive indices of the films grown at different reaction temperatures are also constant at n= 1.36. These refractive indices were measured by SE at 589 nm and were obtained using the Sellmeier model.

The measured refractive index of n=1.36 is consistent with n= 1.38 for bulk AlF_3 at 589 nm^2 and n= 1.36 at 600 nm for an AlF_3 film grown using the electron beam technique.[1] The extinction coefficient for the AlF_3 films is zero because the AlF_3 ALD film is transparent in the range between 240 nm and 1700 nm resulting from the wide band gap of > 10 eV for AlF_3.[3-4] The film roughness of 4 Å - 5 Å as measured by XRR is also nearly constant at all the reaction temperatures. This very smooth film is consistent with amorphous AlF_3 ALD films. AlF_3 film grown by other vacuum techniques have also displayed amorphous structure.[6,14,16,49]

2.4. Conclusions

AlF_3 ALD films were grown over a range of temperatures from 75°C to 300°C using TMA and HF from HF-pyridine as the reactants. The AlF_3 ALD was examined using *in situ*

quartz crystal microbalance (QCM), quadrupole mass spectrometer (QMS) and Fourier transform infrared (FTIR) spectroscopy. The maximum mass gain per cycle (MGPC) for AlF_3 ALD of 44 ng/(cm^2 cycle) occurred at 100°C. The MGPC then decreased progressively at higher temperatures. The MGPC became negative at T> 250°C. At these higher temperatures, the TMA and HF were able to etch the underlying AlF_3 films.

FTIR measurements observed an absorbance increase at 500-800 cm^{-1} during AlF_3 ALD. This absorbance increase was attributed to the Al-F stretching vibrations. The FTIR analysis also monitored the nucleation of AlF_3 ALD on Al_2O_3 substrates. The first HF exposure was able to convert Al_2O_3 to AlF_3. The FTIR spectra also revealed $AlF(CH_3)_2$ and HF species on the surface after the TMA and HF exposures, respectively. In addition, mass spectrometry measurements demonstrated that HF is the main gaseous species in equilibrium with the HF-pyridine solution.

Ex situ X-ray reflectivity (XRR) and spectroscopic ellipsometry (SE) measurements were also employed to measure the AlF_3 ALD film thicknesses. The AlF_3 ALD growth rate measured by XRR and SE was 1.43 Å /cycle at 100°C. XPS and RBS measurements showed that the AlF_3 ALD films were nearly stoichiometric AlF_3 with an oxygen impurity of only ~2 at%. AlF_3 ALD may be useful for a number of applications such as ultraviolet optical films, protective coatings for the electrodes of Li ion batteries and Lewis acid catalytic films.

2.5. Acknowledgements

2.6. References

(1)   Pellicori, S. F.; Colton, E. Fluoride Compounds for Ir Coatings, *Thin Solid Films* **1992**, *209*, 109-115.

(2)   Staritzky, E.; Asprey, L. B. Aluminum Trifluoride, Alf3, *Anal Chem* **1957**, *29*, 984-984.

(3)   Barriere, A. S.; Lachter, A. Optical-Transitions in Disordered Thin-Films of Ionic Compounds MgF2 and AiF3 as a Function of Their Conditions of Preparation, *Appl Optics* **1977**, *16*, 2865-2871.

(4)   Konig, D.; Scholz, R.; Zahn, D. R. T.; Ebest, G. Band diagram of the AlF3/SiO2/Si system, *J Appl Phys* **2005**, *97*,

(5)   Bridou, F.; Cuniot-Ponsard, M.; Desvignes, J. M.; Richter, M.; Kroth, U.; Gottwald, A. Experimental determination of optical constants of MgF2 and AlF3 thin films in the vacuum ultra-violet wavelength region (60-124 nm), and its application to optical designs, *Opt Commun* **2010**, *283*, 1351-1358.

(6)   Lee, C. C.; Liu, M. C.; Kaneko, M.; Nakahira, K.; Takano, Y. Characterization of AlF3 thin films at 193 nm by thermal evaporation, *Appl Optics* **2005**, *44*, 7333-7338.

(7)   Niisaka, S.; Saito, T.; Saito, J.; Tanaka, A.; Matsumoto, A.; Otani, M.; Biro, R.; Ouchi, C.; Hasegawa, M.; Suzuki, Y.; Sone, K. Development of optical coatings for 157-nm lithography. I. Coating materials, *Appl Optics* **2002**, *41*, 3242-3247.

(8)   Sun, Y. K.; Lee, M. J.; Yoon, C. S.; Hassoun, J.; Amine, K.; Scrosati, B. The Role of AlF3 Coatings in Improving Electrochemical Cycling of Li-Enriched Nickel-Manganese Oxide Electrodes for Li-Ion Batteries, *Adv Mater* **2012**, *24*, 1192-1196.

(9)   Ding, F.; Xu, W.; Choi, D. W.; Wang, W.; Li, X. L.; Engelhard, M. H.; Chen, X. L.; Yang, Z. G.; Zhang, J. G. Enhanced performance of graphite anode materials by AlF3 coating for lithium-ion batteries, *J Mater Chem* **2012**, *22*, 12745-12751.

(10)   Myung, S. T.; Lee, K. S.; Yoon, C. S.; Sun, Y. K.; Amine, K.; Yashiro, H. Effect of AlF3 Coating on rhermal Behavior of Chemically Delithiated Li-0.35[Ni1/3Co1/3Mn1/3]O-2, *J Phys Chem C* **2010**, *114*, 4710-4718.

(11)   Herron, N.; Farneth, W. E. The design and synthesis of heterogeneous catalyst systems, *Adv Mater* **1996**, *8*, 959-968.

(12)   Kemnitz, E.; Gross, U.; Rudiger, S.; Shekar, C. S. Amorphous metal fluorides with extraordinary high surface areas, *Angew Chem Int Edit* **2003**, *42*, 4251-4254.

(13)   Kemnitz, E.; Menz, D. H. Fluorinated metal oxides and metal fluorides as heterogeneous catalysts, *Prog Solid State Ch* **1998**, *26*, 97-153.

(14)   Taki, Y. Film structure and optical constants of magnetron-sputtered fluoride films for deep ultraviolet lithography, *Vacuum* **2004**, *74*, 431-435.

(15)   Iwahori, K.; Furuta, M.; Taki, Y.; Yamamura, T.; Tanaka, A. Optical properties of fluoride thin films deposited by RF magnetron sputtering, *Appl Optics* **2006**, *45*, 4598-4602.

(16)   Heitmann, W. VACUUM EVAPORATED FILMS OF ALUMINUM FLUORIDE, *Thin Solid Films* **1970**, *5*, 61-&.

(17)   Schink, H.; Kolbe, J.; Zimmermann, F.; Ristau, D.; Welling, H., "Reactive ion-beam-sputtering of fluoride coatings for the UV/VUV range", at Proc. SPIE June 1, 1991.

(18)   Targove, J. D.; Bovard, B. G.; Lingg, L. J.; Macleod, H. A. Densification of Aluminum Fluoride Thin-Films by Ion-Assisted Deposition, *Thin Solid Films* **1988**, *159*, L57-L59.

(19)   George, S. M. Atomic Layer Deposition: An Overview, *Chem Rev* **2010**, *110*, 111-131.

(20)   Lee, Y.; Cavanagh, A. S.; George, S. M. *Atomic Layer Deposition of AlF₃ Using Trimethylaluminum and Hydrogen Fluoride-Pyridine, Proceedings of the 13th International Conference on Atomic Layer Deposition, San Diego, California, July 28-31, 2013.*

(21)   Mäntymäki, M.; Heikkilä, M. J.; Puukilainen, E.; Mizohata, K.; Marchand, B.; Räisänen, J.; Ritala, M.; Leskelä, M. Atomic Layer Deposition of AlF₃ Thin Films Using Halide Precursors *Chem. Mater.* **2014**, *27*, 604-611.

(22)   Elam, J. W.; Groner, M. D.; George, S. M. Viscous flow reactor with quartz crystal microbalance for thin film growth by atomic layer deposition, *Rev Sci Instrum* **2002**, *73*, 2981-2987.

(23)   Lee, Y.; Yoon, B.; Cavanagh, A. S.; George, S. M. Molecular Layer Deposition of Aluminum Alkoxide Polymer Films Using Trimethylaluminum and Glycidol, *Langmuir* **2011**, *27*, 15155-15164.

(24)   Olah, G. A.; Nojima, M.; Kerekes, I. Synthetic Methods and Reactions .2. Hydrofluorination of Alkenes, Cyclopropane and Alkynes with (Trialkylamine) Reagents, *Synthesis-Stuttgart* **1973**, 779-780.

(25)   DuMont, J. W.; George, S. M. Pyrolysis of Alucone Molecular Layer Deposition Films Studied Using In Situ Transmission Fourier Transform Infrared Spectroscopy, *Journal of Physical Chemistry C (In Press)* **2015**,

(26)   Ballinger, T. H.; Wong, J. C. S.; Yates, J. T. Transmission Infrared-Spectroscopy of High Area Solid-Surfaces - A Useful Method for Sample Preparation, *Langmuir* **1992**, *8*, 1676-1678.

(27)   Ferguson, J. D.; Weimer, A. W.; George, S. M. Atomic layer deposition of ultrathin and conformal Al2O3 films on BN particles, *Thin Solid Films* **2000**, *371*, 95-104.

(28)   D. Shannon, R.; Shannon, R. C.; Medenbach, O.; Fischer, R. X. Refractive Index and Dispersion of Fluorides and Oxides, *Journal of Physical and Chemical Reference Data* **2002**, *31*, 931-970.

(29)   Lennard, W. N., QUARK ver. 1.3, 2001 http://www.physics.uwo.ca/~wlennard.

(30)   *CRC Handbook of Chemistry and Physics*; 85th ed.; Lide, D. R., Ed.; CRC Press: Boca Raton, FL, 2005.

(31)   Linstrom, P. J.; Mallard, W. G. *NIST Chemistry WebBook, NIST Standard Reference Database Number 69, National Institute of Standards and Technology, Gaithersburg MD, 20899 (http://webbook.nist.gov).*

(32)   van der Meulen, P. A.; Mann, R. F. The Vapor Pressure of Pyridine, *J. Am. Chem. Soc.* **1931**, *53*, 451-453.

(33)   Atkins, P. W. *Physical Chemistry, 5th Edition*; Oxford University Press: Oxford 1994.

(34)   Ott, A. W.; Klaus, J. W.; Johnson, J. M.; George, S. M. Al3O3 thin film growth on Si(100) using binary reaction sequence chemistry, *Thin Solid Films* **1997**, *292*, 135-144.

(35)   Lee, Y.; DuMont, J. W.; George, S. M. Atomic Layer Etching of HfO2 Using Sequential, Self-Limiting Thermal Reactions with Sn(acac)2 and HF, *J. Solid State Sci. Technol. (In Press)* **2015**,

(36)   Lee, Y.; George, S. M. Atomic Layer Etching of Al2O3 Using Sequential, Self-Limiting Thermal Reactions with Sn(acac)2 and HF, *ACS Nano* **2015**, *9*, 2061-2070.

(37)   Gross, U.; Ruediger, S.; Kemnitz, E.; Brzezinka, K.-W.; Mukhopadhyay, S.; Bailey, C.; Wander, A.; Harrison, N. Vibrational analysis study of aluminum trifluoride phases, *J. Phys. Chem. A* **2007**, *111*, 5813-5819.

(38)   Koenig, R.; Scholz, G.; Scheurell, K.; Heidemann, D.; Buchem, I.; Unger, W. E. S.; Kemnitz, E. Spectroscopic characterization of crystalline AlF3 phases, *J. Fluorine Chem.* **2010**, *131*, 91-97.

(39)   Utkin, A. N.; Girichev, G. V.; Giricheva, N. I.; Khaustov, S. V. STRUCTURE AND VIBRATIONAL FREQUENCIES OF ALUMINUM TRIFLUORIDE AND GALLIUM TRIFLUORIDE, *J. Struct. Chem.* **1986**, *27*, 212-215.

(40)   Ferguson, J. D.; Weimer, A. W.; George, S. M. Atomic layer deposition of Al2O3 films on polyethylene particles, *Chem Mater* **2004**, *16*, 5602-5609.

(41)   Goldstein, D. N.; McCormick, J. A.; George, S. M. Al_2O_3 Atomic Layer Deposition with Trimethylaluminum and Ozone Studied by in Situ Transmission FTIR Spectroscopy and Quadrupole Mass Spectrometry, *J Phys Chem C* **2008**, *112*, 19530-19539.

(42)   *HSC Chemistry*; HSC Chemistry 5.1, Outokumpu Research Oy: Pori, Finland.

(43)   Weidlein, J.; Krieg, V. VIBRATIONAL SPECTRA OF DIMETHYL AND DIETHYL ALUMINUM FLUORIDE, *Journal of Organometallic Chemistry* **1968**, *11*, 9-&.

(44)   Giguere, P. A.; Zengin, N. SPECTRE INFRAROUGE DE HF A LETAT CRISTALLIN, *Canadian Journal of Chemistry-Revue Canadienne De Chimie* **1958**, *36*, 1013-1019.

(45)   Buslov, D. K.; Sushko, N. I.; Yukhnevich, G. V. The IR spectrum of liquid hydrogen fluoride, *Journal of Optical Technology* **2003**, *70*, 28-30.

(46)   Ayotte, P.; Hebert, M.; Marchand, P. Why is hydrofluoric acid a weak acid?, *Journal of Chemical Physics* **2005**, *123*,

(47)   Bailey, C. L.; Wander, A.; Mukhopadhyay, S.; Searle, B. G.; Harrison, N. M. Adsorption of HF and HCl on the beta-AlF(3) (100) surface, *Phys Chem Chem Phys* **2008**, *10*, 2918-2924.

(48)   Bailey, C. L.; Mukhopadhyay, S.; Wander, A.; Searle, B. G.; Harrison, N. M. Structure and Stability of alpha-AlF3 Surfaces, *J Phys Chem C* **2009**, *113*, 4976-4983.

(49)   Pulker, H. K. CHARACTERIZATION OF OPTICAL THIN-FILMS, *Appl Optics* **1979**, *18*, 1969-1977.

CHAPTER 3

Atomic Layer Deposition of LiF and Lithium Ion Conducting (AlF₃)(LiF)ₓ Alloys Using Trimethylaluminum, Lithium Hexamethyldisilazide and Hydrogen Fluoride

3.1. Introduction

LiF is an important material for lithium ion batteries due to its role in solid electrolyte interface (SEI) layer.[1,2] At 13.6 eV,[3] LiF has one of the largest bandgaps of any known material, which leads to its transparency in deep ultraviolet, making it appealing for optical coatings.[4] LiF has also been widely employed in the electron injection layer of organic light-emitting diodes (OLED)[5,6] to reduce the work function of Al cathode.[7]

LiF films have been grown by physical vapor deposition methods such as thermal evaporation[8-13] , sputtering[14,15], electron beam deposition[16,17], pulsed laser deposition.[18,19] Atomic layer deposition (ALD) of LiF was demonstrated using TiF₄ as F precursor recently.[20] LiF and metal fluorides can form alloys having high ionic conductivity.[8,21-23] For example, (AlF₃)(LiF)ₓ alloys grown by thermal evaporation can serve as a solid state electrolytes because their ionic conductivities are ~10^6 S/cm.[8,21,22] Lithium ion conducting films are very important as solid state electrolytes and protective coatings for lithium ion batteries.

ALD is a film growth technique based on sequential, self-limiting surface reactions, which enables subnananometer control of conformal thin films.[24] ALD of metal oxides, nitrides, and sulfides has been developed using H_2O, NH_3, and H_2S respectively.[25] ALD of metal fluorides has proven difficult because HF is not a benign reactant.[26] Most ALD of metal fluorides has been performed using alternative F precursors rather than HF.[26-29]

HF-pyridine that consists of 70% HF and 30% pyridine has been employed as a F precursor for AlF_3 ALD.[30] HF-pyridine is a liquid at room temperature, which enables the safe handling of HF not using a pressurized cylinder of HF.[31] HF-pyridine serves as a reservoir for anhydrous HF forming equilibrium mixture between stable $(HF)_{9-x}$-pyridine complex and small amount of gaseous xHF.

The growth of LiF ALD film and reaction mechanism using LiHMDS and HF are examined by *in situ* techniques, such as quartz crystal microbalance (QCM) and quadrupole mass spectrometer (QMS) at reaction temperatures between 125°C and 250°C. The growth of $(AlF_3)(LiF)_x$ alloy film and reaction mechanism are also examined by the combination of AlF_3 and LIF ALD. The film properties such as refractive index and film density are studied by *ex situ* techniques such as X-ray reflectivity (XRR) and spectroscopic ellipsometry (SE)

Crystalline LiF and $(AlF_3)(LiF)_x$ alloy films grown at 150°C were confirmed by grazing incidence X-ray diffraction (GIXRD). This dense film with a low refractive index is important for optical coatings. X-ray photoelectron spectroscopy (XPS) confirmed that the film consisted of Li and F or Al, Li, and F. Inductively coupled plasma mass spectrometry (ICP-MS) and ionic chromatography revealed atomic ratio of the LiF film of Li:F=1:1.1 and $(AlF_3)(LiF)_x$ alloy film of Al:Li:F=1:2.7: 5.4 for $(AlF_3)(LiF)_x$ alloy film. Lithium ion conductivity for $(AlF_3)(LiF)_x$ alloy film was measured as $\sigma = 7.5 \times 10^{-6}$ S/cm.

3.2. Experimental section

3.2A. Viscous Flow Reactor Equipped with *in situ* QCM and QMS Measurements

The ALD reactions were performed in the viscous flow reactor equipped with an *in situ* quartz crystal microbalance (QCM) and a quadrupole mass spectrometer (QMS) at temperatures between 125°C and 250°C[32,33]. A film deposition monitor (Maxtek TM-400, Inficon) monitored *in situ* QCM experiments. The QCM sensor with quartz crystal (polished and gold coated AT-cut, 6MHz, Colorado Crystal Corp.) was placed in the bakeable single sensor head (BSH-150, Inficon) and sealed with high temperature epoxy (Epo-Tek H21D, Epoxy technology). A PID temperature controller (2604, Eurotherm) kept the reactor at a fixed temperature within ± 0.04 °C. A capacitance manometer (Baratron 121A, MKS) monitored pressure change during reaction.

Quadrupole mass spectrometry (QMS) was performed on the vapor phase species in the ALD reactor. Measurements were performed with a residual gas analyzer (RGA 200, Stanford Research Systems). The gases produced during ALD reaction were sampled via an aperture. The aperture separated two distinct pressure regions, the ALD reactor (~1 Torr) and the QMS region (~1 $\times$10-7 Torr). In order to maintain these pressures with an open conductance between the two regions, the QMS region was differentially pumped with a turbo molecular pump (V70LP, Varian). The aperture radius was 25 µm. A dual thoriated-iridium (ThO2/Ir) filament was used for electron emission in the mass spectrometer. The ionization energy was 70 eV. A Faraday cup was used as the detector.

The LiF ALD reactions were studied with LiHMDS (95%, Gelest) and HF-pyridine (70 wt% HF, Sigma-Aldrich). HF-pyridine was transferred to a stainless steel bubbler in a dry nitrogen-filled glove bag. Although HF-pyridine minimizes the risks from employing HF, the inhalation of fumes and the contact with skin should be avoided

The LiHMDS was transferred to stainless steel bubblers in a dry nitrogen-filled glove bag and maintained at 115°C. A mechanical pump (Pascal 2015SD, Alcatel) pumped the reactants with a nitrogen carrier gas. The mass flow controllers (Type 1179A, MKS) supplied a constant nitrogen carrier gas flow of 150 sccm. Deposition of back-side of the crystal was prevented from additional purge gas flow of 20 sccm supplied using a metering bellows-sealed valve (SS-4BMG, Swagelok) into the QCM housing. The total nitrogen gas flow of 170 sccm produced a base pressure of ~1 Torr in the reactor.

3.2B. X-ray reflectivity (XRR), grazing incidence X-ray diffraction (GIXRD), and spectroscopic ellipsometry (SE)

Boron doped Si (100) wafers (p-type, Silicon Valley Microelectronics) was used for the substrates for ALD deposition. The Si wafer was cleaved into ~2.5 cm by ~2.5 cm substrates. The substrates were cleaned with acetone, isopropanol, and deionized water and dried with nitrogen gas.

The film thicknesses and the density were analyzed by *ex situ* X-ray reflectivity (XRR). A high resolution X-ray diffractometer (Bede D1, Jordan Valley Semiconductors) using Cu Kα ($\lambda = 1.540$ Å) radiation recorded the XRR scans. The filament current in the X-ray tube was 35 mA and the voltage was 40 kV. A step size and an acquisition time used for all XRR scans were 10 arcsec and 5 s, respectively. The XRR scans were fit by modeling software (Bede REFS, Jordan Valley Semiconductors) to analyze film thickness, surface roughness, and film density.

The crystallinity was examined by grazing incidence X-ray diffraction (GIXRD) with the samples rotated at $\omega=0.5°$, a step size of $0.01°$, and a count time of 3s.

The film thicknesses and refractive index were also determined using reflective spectroscopic ellipsometry (SE). These measurements were performed using a spectroscopic ellipsometer (M-2000 , J. A. Woollam) employing a spectral range from 240 to 1700 nm with an incidence angle of 75 degree. The measurement of Ψ and Δ yielded the film thicknesses and refractive index using the control and analysis software (CompleteEASE, J. A. Woollam) with a Sellmier model.

3.2C. X-ray Photoelectron Spectroscopy (XPS), inductively coupled plasma mass spectrometry (ICP-MS), and ionic chromatography (IC)

The film composition was determined by X-ray photoelectron spectroscopy (XPS). X-ray photoelectron spectrometer (PHI 5600, RBD Instruments) used monochromatic Al Kα X-rays of 1486.6 eV. Survey scans of the sample surfaces were measured with a pass energy of 93.9 eV and a step size of 0.400 eV. A depth profile was measured using Ar ion sputtering. A pass energy of 58.7 eV and a step size was 0.250 eV was used for the depth profiling analysis. An electron beam neutralizer was employed at 17.8 mA. Data was obtained with the control program (Auger Scan, RBD Instruments) and analyzed by the software (CASA XPS, Casa Software).

For determination of stoichiometry of LiF and $(AlF_3)(LiF)_x$ alloy films, ICP-MS and IC were employed. LiF and AlF_3 have solubility of 0.134g and 0.50g in 100g of water respectively.[34] LiF and $(AlF_3)(LiF)_x$ alloy films on a silicon wafer were dissolved in DI water. Dissolution of 800 cycles of LiF ALD (~60µg) in 30 g of DI water yielded ~2ppm concentration. SE confirmed LiF film and $(AlF_3)(LiF)_x$ alloy films were dissolved completely. Lithium and

aluminum were analyzed by ICP-MS (SCIEX Elan DRC-e, Perkin Elmer). Fluorine cannot be analyzed by ICP-MS because it has a higher ionization energy than the argon used as medium. Analysis of F was performed with liquid ion chromatography system (Dionex Series 4500i, Thermo).

3.2D. Electrochemical impedance spectroscopy (EIS) measurements

Electrochemical impedance spectroscopy (EIS) was performed using the potentiostat (VMP3, Biologic). The AC impedance measurements were recorded using a signal with an amplitude of 5 mV and a frequency from 1 MHz to 10 mHz. EIS was conducted in symmetric coin-type form factor cells (Pred Materials) with an electrode area of 1.27 cm^2 in the following configuration: $(AlF_3)(LiF)_x$ alloy ALD film on Cu foil current collector / liquid electrolyte (EC/DEC 1M $LiPF_6$, Soulbrain) with the separator / $(AlF_3)(LiF)_x$ alloy ALD film on Cu foil current collector. Two thicknesses of $(AlF_3)(LiF)_x$ alloy ALD film were tested for a more accurate analysis of ionic conduction through the films.

3.3. Results and Discussion

3.3A. Growth of LiF Films

Figure 1 shows the plot of mass gain during 100 cycles of LiF ALD at 150°C using LiHMDS and HF monitored by quartz crystal microbalance (QCM). The reaction sequence of one ALD cycle consists of 1 s dose of LiHMDS, 30 s of nitrogen purge, 1 s dose of HF, and 30 s of nitrogen purge. This reaction sequence is denoted as (1-30-1-30). There is a very linear growth showing a mass gain per cycle (MGPC) of 12 ng/(cm^2 cycle). To measure the steady-state growth rate on a fully nucleated surface, ~300 cycles of LiF ALD was deposited on 200
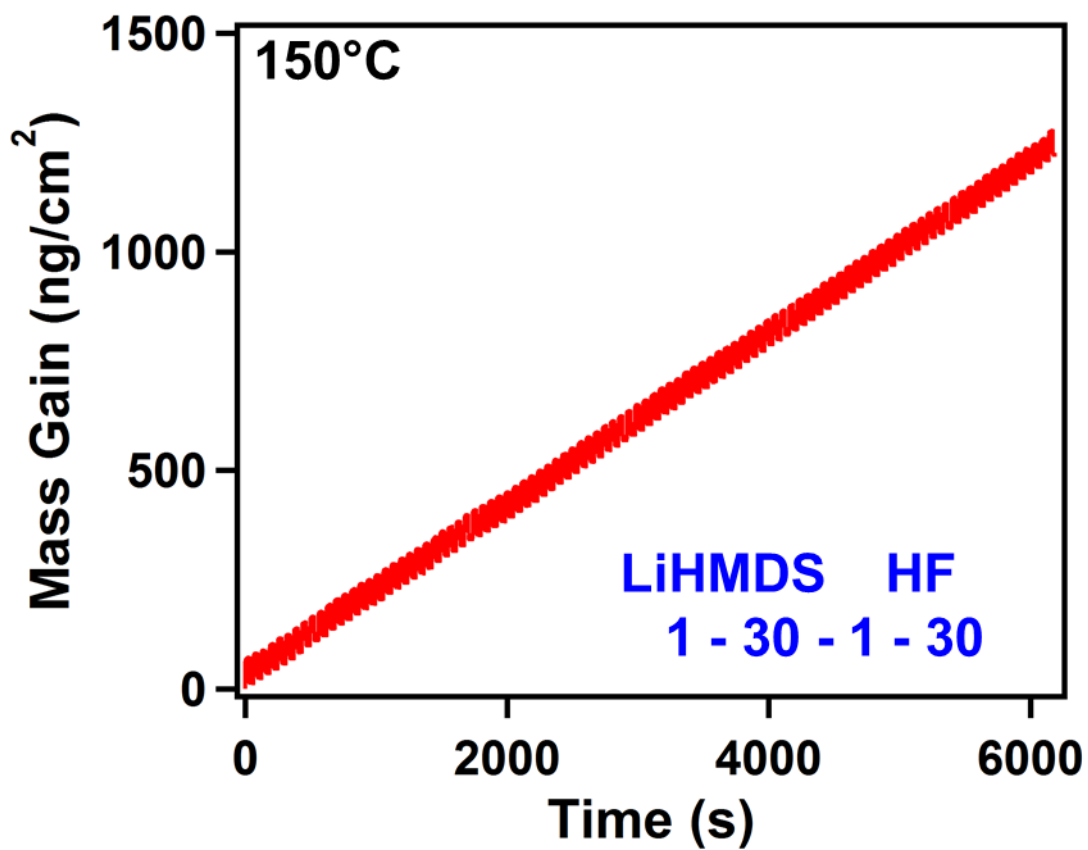
Figure 3-1.   Mass gain versus time during 100 cycles of LiHMDS and HF reaction at 150 °C

using the reaction sequence of (1-30-1-30).
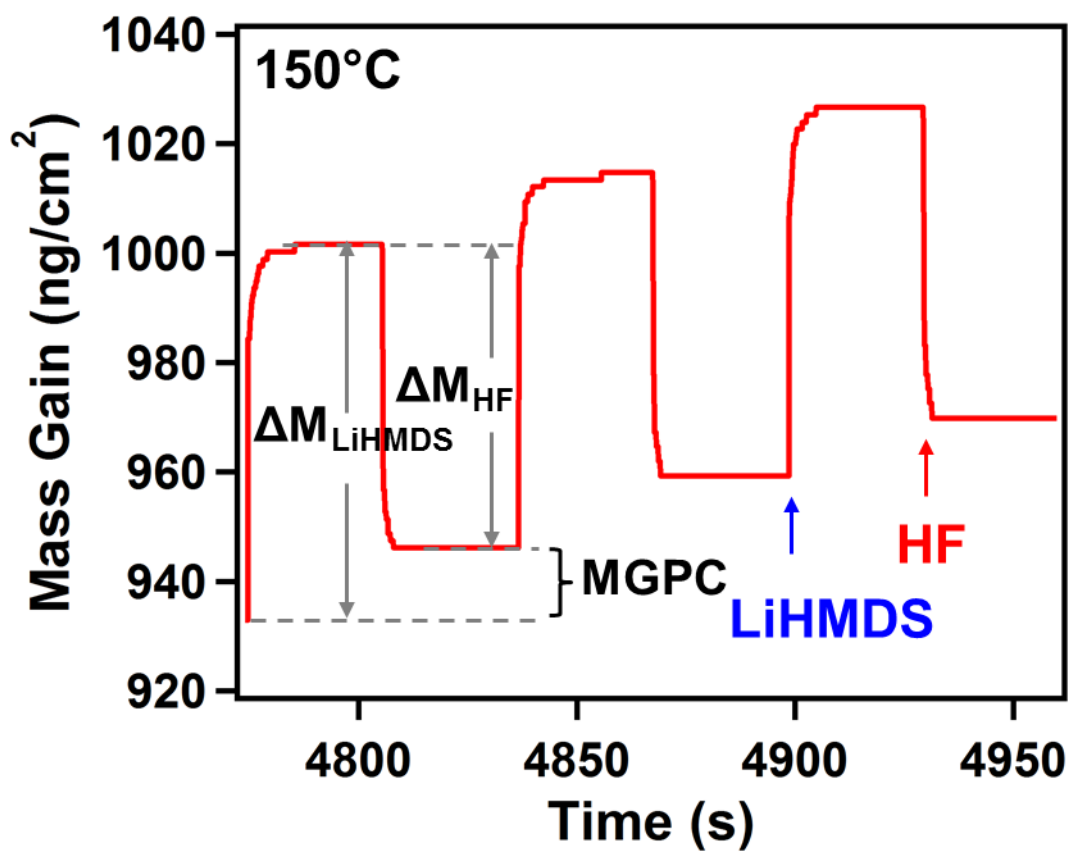
Figure 3-2. Enlargement of mass gain versus time for three sequential LiHMDS and HF

reactions in the steady-state, linear growth regime shown in Figure 3-1.

cycles of Al_2O_3 ALD before QCM measurements. This high number of nucleation cycles is probably due to the complicated reaction between LiF ALD and initial Al_2O_3 surface.

Figure 2 shows three sequential LiF ALD reactions recorded by QCM during 78th, 79th, and 80th cycles using the reaction sequence of (1-30-1-30). The mass increase after LiHMDS exposure is $\Delta M_{Li} = 67$ ng/(cm^2 cycle). Mass loss after HF exposure is $\Delta M_{HF} = -55$ ng/(cm^2 cycle). Steps for a large mass gain followed by a large mass loss indicate an absorption of a molecule with a high molecular weight during LiHMDS exposure followed by leaving a large ligand from the surface during HF exposure.

The self-limiting behavior LiF ALD was also examined by mass gain as function of number of minidoses of each reactant consisting of 0.5 s of dose and 30 s of purge at 150°C. Both reactants showed self-limiting reactions. ΔM_{Li} versus minidoses of LiHMDS reached the plateau of at $\Delta M_{Li} = \sim 67$ ng/(cm^2 cycle) using one 0.5 s of minidose Similarly, ΔM_{HF} versus minidoses of HF leveled off at $\Delta M_{HF} = \sim -55$ ng/(cm^2 cycle) using one 0.5 s of minidose.

Figure 3 displays the MGPC and the ratio of mass gain during the LiHMDS exposure to the total mass gain (ΔM_{Li}/MGPC) during 100 cycles. The MGPC of 12 ng/(cm^2 cycle) consists of $\Delta M_{Li} = 67$ ng/(cm^2 cycle) and $\Delta M_{HF} = -55$ ng/(cm^2 cycle). The ΔM_{Li}/MGPC ratio stays on the line of 5.6. This ratio can be used to determine the surface chemistry from the calculation using molar mass of each species.[33] This ratio of 5.6 will be discussed later.

Figure 4 reveals the species in the gas phase monitored during the same LiF reactions shown in Figure 2. Figure 4a-c show the mass spectrum obtained by quadrupole mass spectrometer (QMS). The hexamethydisilazane (HMDS) peak of m/z = 65 as a reaction byproduct does not appear during either LiHMDS or HF cycles as shown in Figure 4a. The HF peak of m/z = 20 appears during HF exposure shown in Figure4b. Figure 4c also shows an
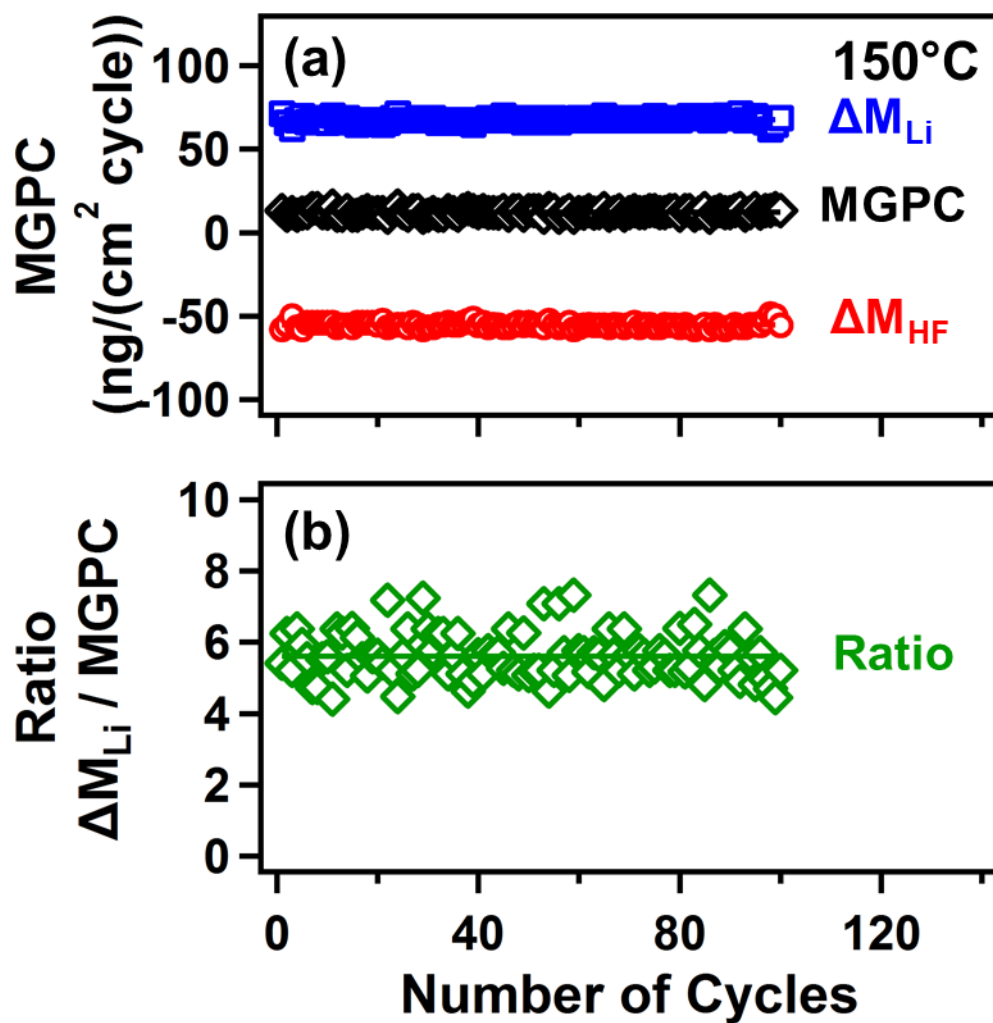
Figure 3-3. MGPC and ΔM_{Li}/MGPC ratio during 100 cycles of LiHMDS and HF reaction at 150 °C: (a) MGPC, ΔM_{Li}, and ΔM_{HF}; (b) M_{Li}/MGPC ratio.
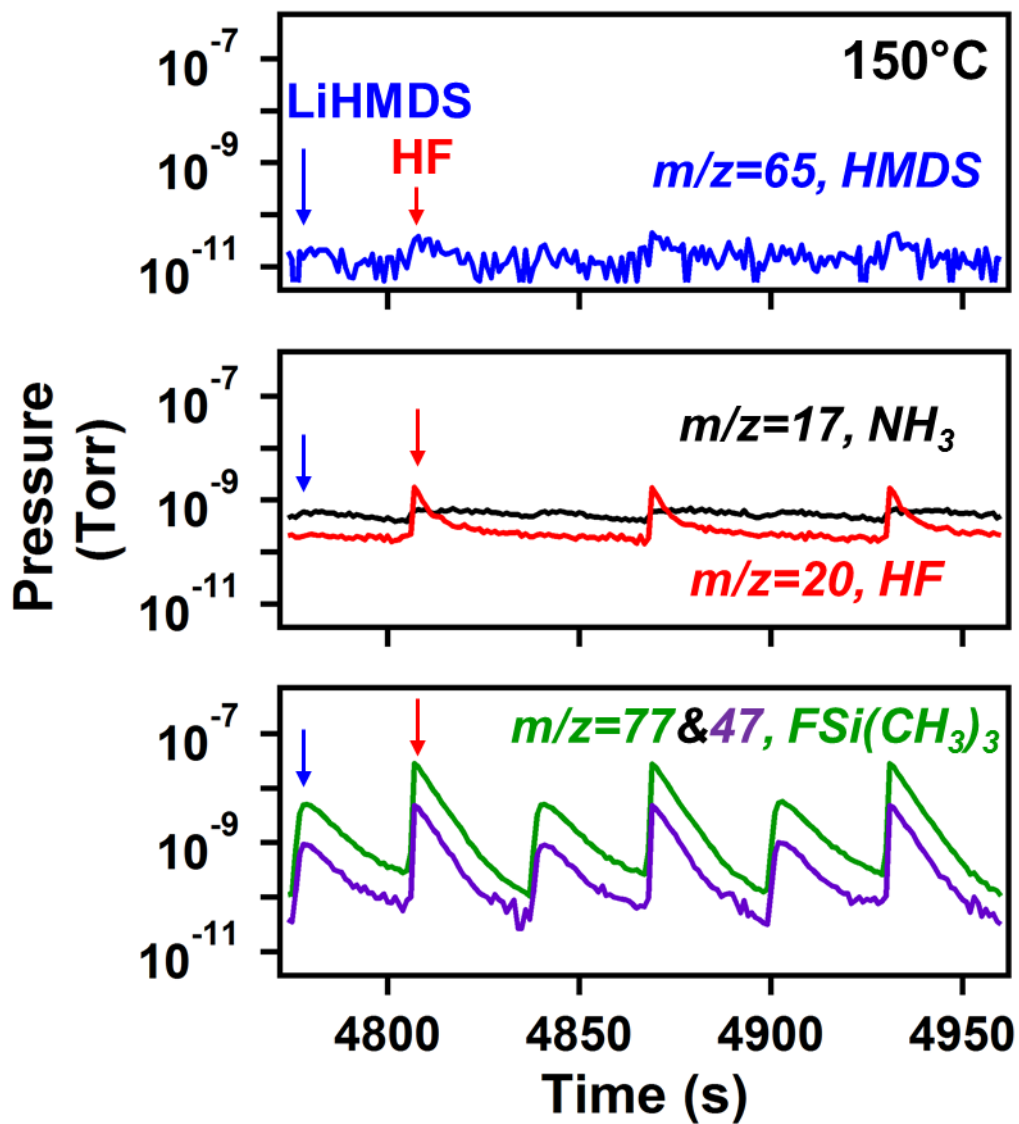
Figure 3-4. Mass spectrometer signals for (a) m/z= 65 for HMDS; (b) m/z= 17 for NH_3 and m/z=20 for HF; (c) m/z=77 and 47 for $FSi(CH)_3$ respectively, during three LiF ALD cycles at 150°C shown in Figure 3-2.

increased background signal of $> 10^{-10}$ Torr for NH_3 at m/z = 17 during LiF reaction. Before the

LiF reaction it was $<10^{-11}$ Torr. This increase may be due to some spillover from m/z=16.

Another possibility is that this significant increase of m/z = 17 may indicates strong interaction

between NH_3 and HF through acid-base interaction in the gas phase. Interestingly, QMS detects

peaks from $FSi(CH_3)_3$ of both m/z = 77 and m/z = 47 shown in Figure 4c. Formation of

$FSi(CH_3)_3$ suggests the decomposition of HMDS by HF into NH_3 and $FSi(CH_3)_3$. Formation of

$FSi(CH_3)_3$ between HMDS, $(CH_3)_3SiNHSi(CH_3)_3$, and F^- in the gas phase was previously studied

in the tube reactor with He flow by mass spectrometry.[35] Possible reaction pathways for these

species include:

$(CH_3)_3SiNHSi(CH_3)_3 + HF \rightarrow FSi(CH_3)_3 + (CH_3)_3SiNH_2$ (1a)

$(CH_3)_3SiNH_2 + HF \rightarrow FSi(CH_3)_3 + NH_3$ (1b)

$(CH_3)_3SiNHSi(CH_3)_3 + 2HF \rightarrow 2FSi(CH_3)_3 + NH_3$ (2)

The QMS did not observe peaks from $(CH_3)_3SiNH_2$, m/z = 89, 88, and 87. Absence of

$(CH_3)_3SiNH_2$ peaks and significant increase of NH_3 m/z=17 suggest HMDS decomposes

completely to two $FSi(CH_3)_3$ and one NH_3 by HF shown in equation 2

Figure 5 illustrates the proposed reaction mechanism. In reaction A, an initial surface of

LiF is assumed from several LiF ALD reactions. When LiHMDS molecules are exposed to the

surface, LiHMDS physisorbs on the surface. In reaction B, HF molecules are exposed to the

surface to break Li-HMDS to form Li-F. During this reaction HMDS on the surface can be

decomposed into two $FSi(CH_3)_3$ and NH_3 by HF molecules during HF exposure. The

assumption of LiHMDS adsorption on the surface during reaction A is based on the mass gain
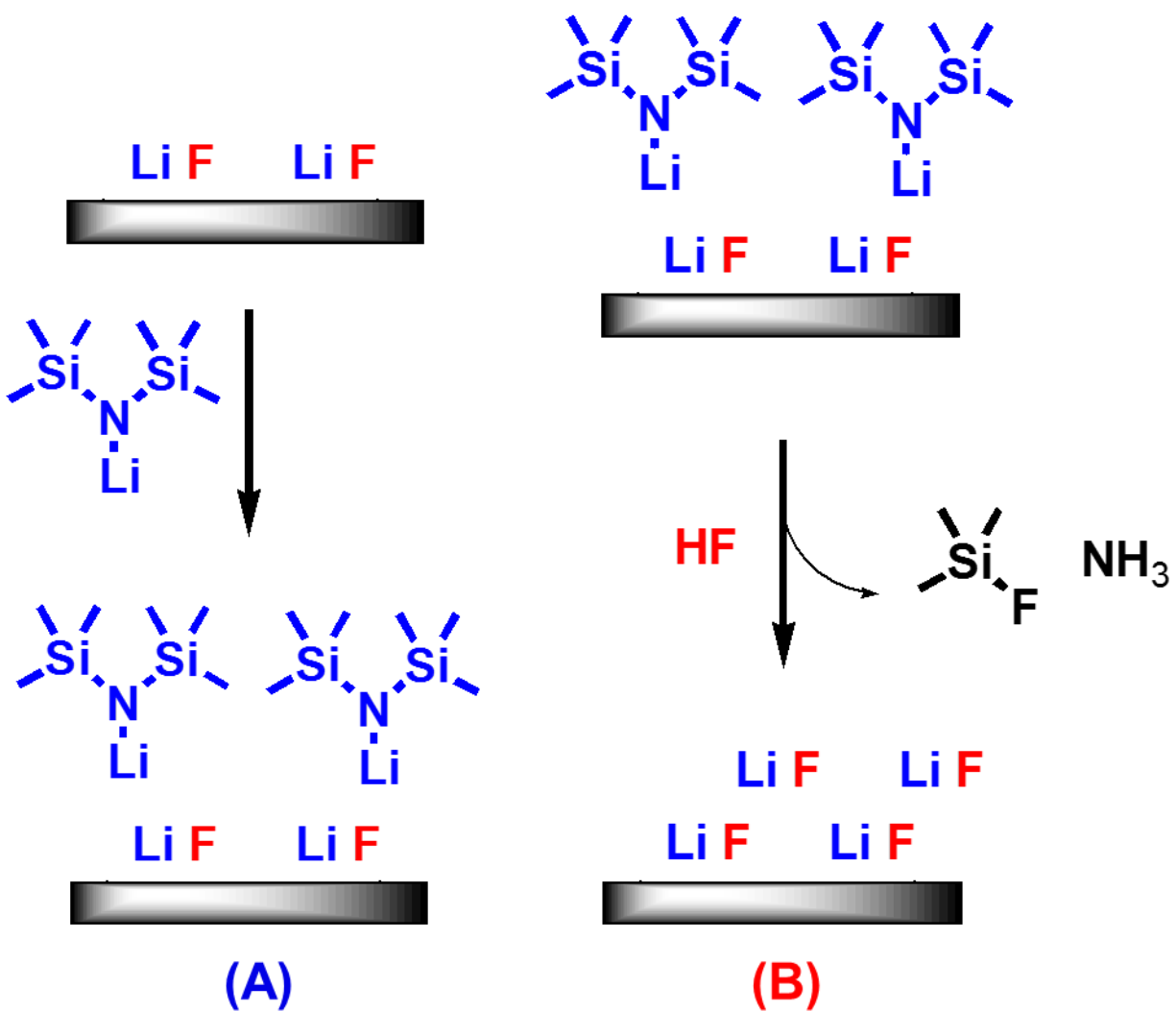
Figure 3-5. Proposed reaction mechanism of LiF ALD using LiHMDS and HF.

ratio during LiHMDS exposure obtained by QCM experiment. With the amount of HF present

on the surface for each LiF represented as "x", the surface chemistry can be expressed by

(A) $LiF|xHF^* + LiHMDS \rightarrow LiF|LiF_x(HMDS)_{1-x}^* + x \cdot (FSi(CH_3)_3 + 1/2NH_3)$ (3a)

(B) $LiF|LiF_x(HMDS)_{1-x}^* + 3HF \rightarrow LiF|LiF|x \cdot HF^* + (1-x) \cdot (FSi(CH_3)_3 + 1/2NH_3)$ (3b)
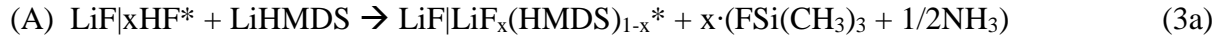
The ratio $\Delta M_{Li}/MGPC$ can be calculated from:

$$\frac{\Delta M_{Li}}{MGPC} = \frac{\Delta M_{Li}}{\Delta M_{Li} + \Delta M_{HF}} = \frac{M_{LiHMDS} - x \cdot (M_{HMDS})}{M_{LiF}} \quad (4)$$

where M_{LiHMDS}, M_{HMDS}, and M_{LiF} are the molar masses of LiHMDS, HMDS, and LiF,

respectively.

In the absence of HF on the surface (x = 0), the reaction should progress with only

LiHMDS adsorption on LiF surface. The $\Delta M_{Li}/MGPC$ ratio for x = 0 is 6.5 from equation 4.

The LiHMDS mass gain ratio of 5.6 from QCM experiment is close to the ratio of 6.5 based on

LiHMDS adsorption with no surface HF in Figure 5a. With the assumption of one HF per LiF

surface species(x = 1), the $\Delta M_{Li}/MGPC$ ratio is 0.23. This is much smaller than the LiHMDS

mass gain ratio of 5.6 from QCM experiments. In this case we should be able to see mass gain

instead of mass loss from HF adsorption in the reaction B, which we do not see. The ratio of 5.6

approximately corresponds to one HF molecule per seven LiF surface species, where x = 0.14.

The LiHMDS mass gain ratio, and therefore the amount of surface HF, was nearly constant

between 125°C° and 175°C. The ratio slightly increased to 6.8 at 200°C. This indicates

adsorption of HF on LiF surface may be prevented at higher reaction temperature of ~200°C,

however a negligible amount of HF is present at lower temperatures. This result is obviously

different from AlF$_3$ ALD which has always has a significant amount of HF on the AlF$_3$ surface.[30]

Adsorption of LiHMDS on LiF surface can be explained by strong interactions of Si in LiHMDS with F in LiF surface and N in LHMDS with Li in LiF. Stable Si-N-Li-F ring structures were reported in solution chemistry previously.[36-38]

The growth of LiF ALD film on the silicon wafer is relatively linear having the growth rate of 0.5-0.6 Å /cycle measured by X-ray reflectivity (XRR) and by spectroscopic ellipsometry (SE). The density of the films grown >400 cycles of LiF ALD measured by XRR is 2.6 g /cm^3. The bulk density of LiF is 2.64 g /cm.[3,34] The close agreement with the bulk LiF density suggests LiF ALD is crystalline. GIXRD confirmed the LiF film grown using 800 cycles of LiF ALD at 150°C was crystalline. LiF films grown by other vacuum techniques also show crystallinity.[10,20,39] Thin films prepared using 100 cycles and 200 cycles of ALD show 2.0 g /cm^3 and 2.5 g /cm^3 less dense films probably due to nucleation delay. The films grown using 800 cycles of LiF ALD have a roughness of 50 – 60 Å as modeled by XRR and SE. The growth rate calculated using a MGPC obtained by QCM experiment and the density measured by XRR yields 0.5 Å /cycle. The thickness, the film density, and film roughness of LiF film do not show noticeable changes after storage in atmosphere after one month. These results indicate LiF grown by ALD is not hygroscopic in the atmosphere. Refractive index were measured at the wavelength of 589 nm obtained by SE based on the Sellmeier model. The Sellmeier model is commonly used for optically transparent films such as metal fluoride films.[30,40] The extinction coefficient is zero because LiF ALD film are transparent in the range of between 240 nm and 1700 nm due to the wide band gap =13.6 eV.[3,13] This refractive index of 1.37 is achieved at 400 cycles of ALD. This refractive index of 1.37 is consistent with 1.39[4,10] at 590 nm for the bulk LiF[4,10], 1.39[10] at 600 nm for the film grown by thermal evaporation and 1.37–1.39[20] grown by ALD using Li(thmd) and TiF$_4$.

Figure 6 shows the temperature dependence of the MGPC and the growth rate. The MGPC obtained from QCM experiment at the different temperatures is shown in Figure 6a. This MGPC can be converted to the growth rate using the film density measured by XRR shown in Figure 6b. The growth rates calculated from the thickness of 400 cycles ALD measured by XRR and SE are shown in Figure 6b together. The calculation of growth rate using the thickness yields a different growth rate calculated from MGPC and density because the film growth suffers from nucleation delay. All the growth rates are in good agreement, with a maximum growth rate of 0.5–0.6 Å / cycle at 150 °C. The growth rate decreases at higher temperature, probably due to a decrease in LiHMDS adsorption. A slight decrease in the growth rate is also observed at the lower temperature of 125 °C.

3.3B. Growth of $(AlF_3)(LiF)_x$ Alloy Films

Figure 7 displays the plot of mass gain during 40 sequences of $(AlF_3)(LiF)_x$ alloy ALD at 150 °C monitored by QCM. One sequence $(AlF_3)(LiF)_x$ alloy ALD consists of AlF_3 subcycle and LiF ALD subcycle. This reaction sequence is denoted as (1-30-1-30)-(1-30-1-30). There is a very linear growth showing a mass gain per sequence (MGPS) of 22 ng/(cm^2 sequence). To measure the steady-state growth rate on a fully nucleated surface, ~200 sequence of $(AlF_3)(LiF)_x$ alloy film was deposited on 200 cycles of AlF_3 ALD before QCM measurements. This high number of nucleation cycles is probably due to the complicated reaction between AlF_3 ALD and LiF ALD.

Figure 8 shows three sequential $(AlF_3)(LiF)_x$ alloy ALD reactions recorded by QCM using the reaction sequence of (1-30-1-30)-(1-30-1-30). This alloy sequence consists of one AlF_3 subcycle and one LiF subcycle, which can be considered separately. The shape of mass
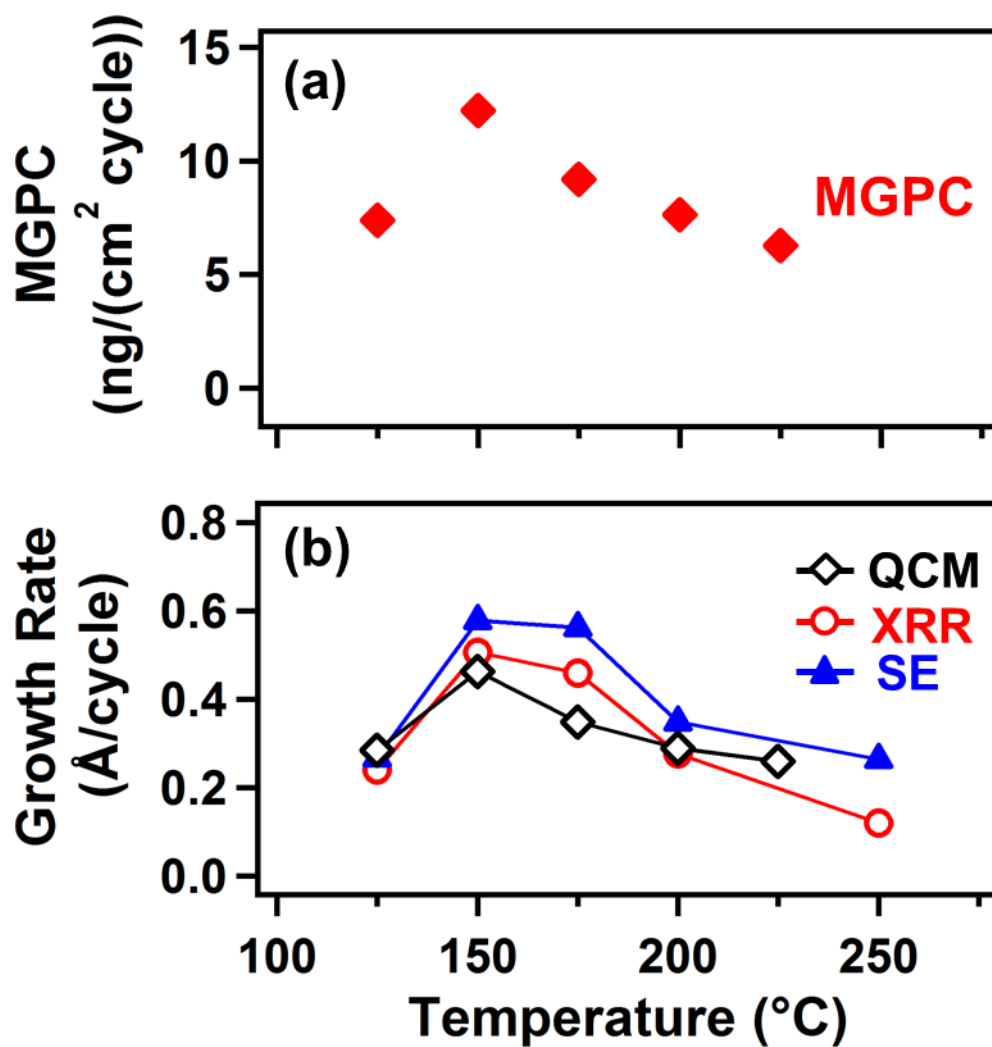
Figure 3-6. MGPC and growth rate versus reaction temperature using reaction sequence of (1-30-1-30): (a) MGPC; (b) Growth rate.

gain during AlF_3 subcycle is not the same as shown in AlF_3 ALD. There is no noticeable mass gain after HF exposure. The shape of mass change during LiF cycle is very similar to LiF ALD. The mass increase after AlF_3 subcycle is $\Delta M_{AlF3} = 12$ ng/(cm^2 cycle). The mass gain after LiF subcycle is $\Delta M_{LiF} = 10$ ng/(cm^2 cycle). Steps for a large mass gain followed by a large mass loss indicate an absorption of a molecule with a high molecular weight during LiHMDS exposure followed by leaving a large ligand from the surface during HF exposure.

Figure 9 displays the MGPS and the ratio of mass gain during AlF_3 subcycle to the total mass gain (ΔM_{AlF3}/MGPS) during 40 sequences. MGPS is the sum of mass changes during each fluoride subcycle. The MGPS of 22 ng/(cm^2 cycle) consists of $\Delta M_{AlF3} = 12$ ng/(cm^2 cycle) and $\Delta M_{LiF} = 10$ ng/(cm^2 cycle). The ΔM_{AlF3}/MGPS ratio stays on the line of 0.54. This ratio means that the alloy film consists of 54 wt. % of AlF_3 and 46% wt. % of LiF. This ratio can be used to determine the stoichiometry between Al and Li.

The molar mass of fluorides alloy is equal to the sum of molar mass of AlF_3 and the molar mass of LiF.

$$AlF_3 + x \cdot LiF \quad \rightarrow \quad (AlF_3)(LiF)_x \tag{5}$$
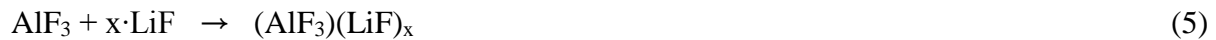
The ratio ΔM_{AlF3}/MGPS can be calculated from:

$$\text{Ratio} = \frac{\Delta M_{AlF3}}{\text{MGPS}} = \frac{\Delta M_{AlF3}}{\Delta M_{AlF3} + \Delta M_{LiF}} = \frac{M_{AlF3}}{M_{AlF3} + x M_{LiF}} \tag{6a}$$

$$0.54 = \frac{84}{84 + x26} \tag{6b}$$

where M_{AlF3} and M_{LiF} are the molar masses of AlF_3 and LiF, respectively.
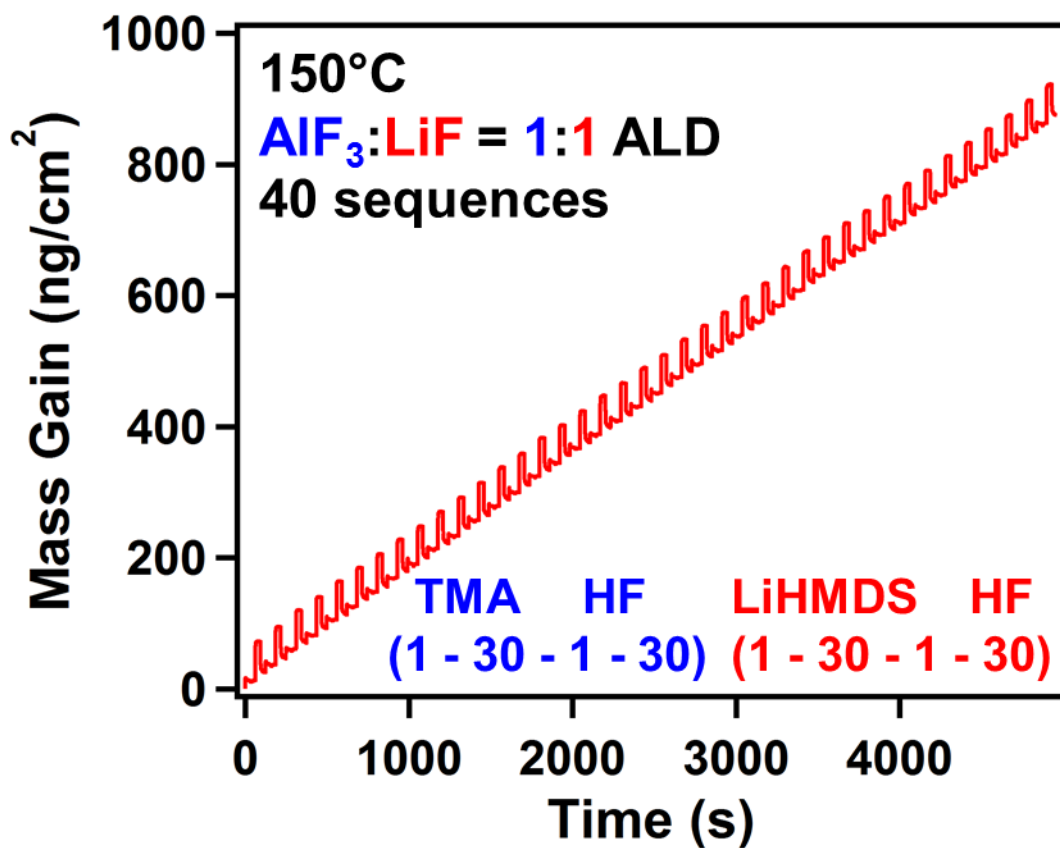
Figure 3-7. Mass gain versus time during 40 sequences of AlF$_3$:LiF= = 1:1 reaction at 150 ℃

using the reaction sequence of (1-30-1-30)-(1-30-1-30).
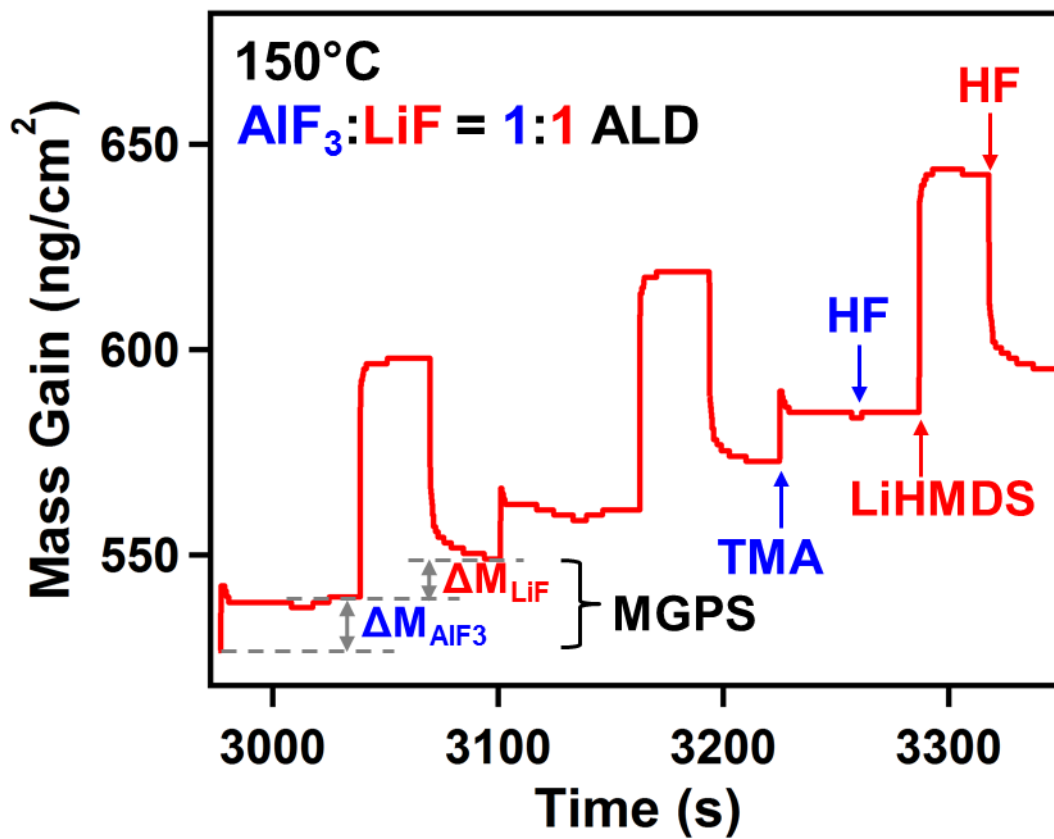
Figure 3-8.   Enlargement of mass gain versus time for three sequential TMA, HF, LiHMDS

and HF reactions in the steady-state, linear growth regime shown in Figure 3-7.
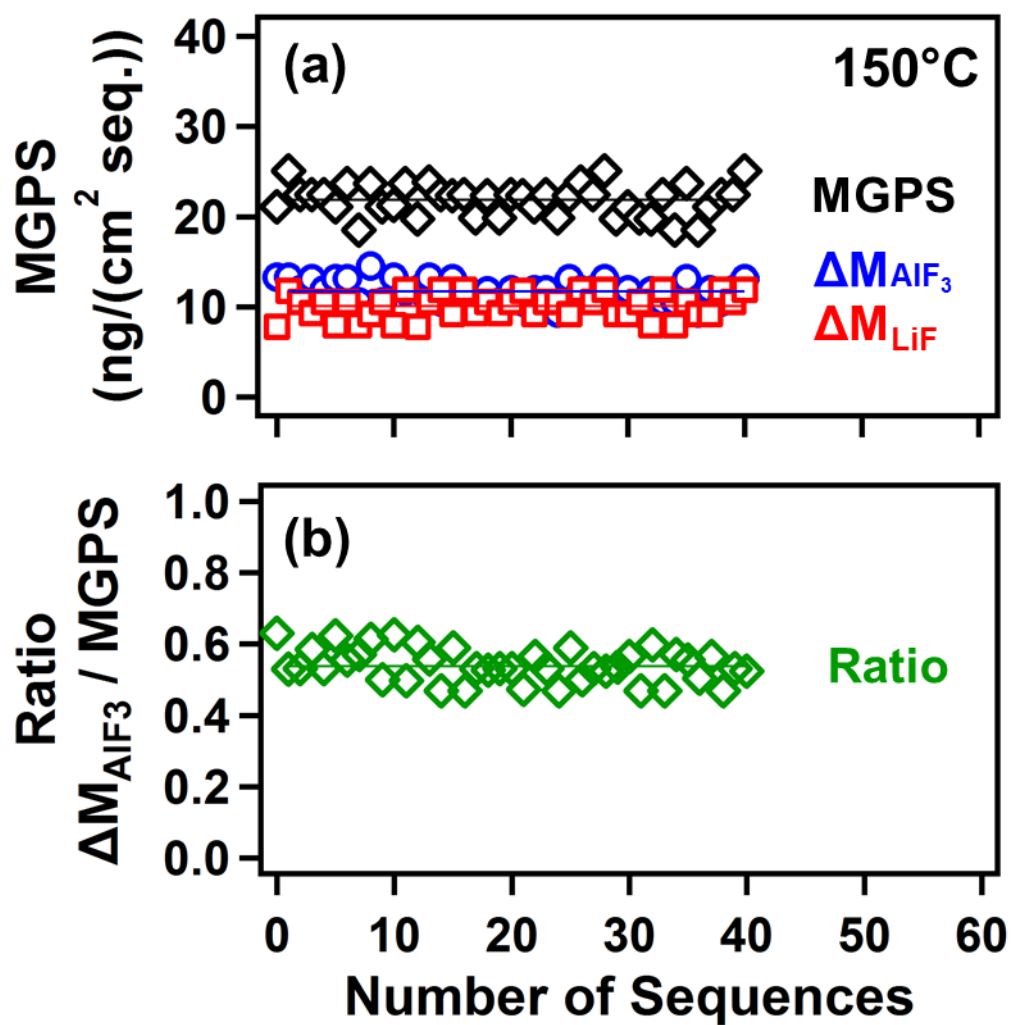
Figure 3-9. MGPS and ΔM_{AlF3}/MGPS ratio during 40 sequences of AlF_3:LiF= = 1:1 reaction at 150 °C: (a) MGPS, ΔM_{AlF3}/MGPS ratio ΔM_{AlF3}, and ΔM_{LiF}; (b) ΔM_{AlF3}/MGPS ratio.

The ratio and molar masses yields x=2.8. It is interesting that this stoichiometry, x=2.8 is very similar to the stoichiometry of only thermodynamically stable phase is Li_3AlF_6. ICP-MS determined x = 2.7 in this film, which is pretty consistent with QCM result.

Figure 10 reveals the species in the gas phase monitored during the same three sequential $(AlF_3)(LiF)_x$ alloy ALD reactions shown in Figure 8. Figure 10a-c show the mass spectrum obtained by quadrupole mass spectrometer (QMS). The methane (CH_4) peak of m/z = 16 as a reaction byproduct appear during AlF_3 subcycle either TMA or HF cycles as shown in Figure 10a. The HF peak of m/z = 20 appears during HF exposure either during AlF_3 or LiF subcycle shown in Figure 10b. QMS detects peaks from $FSi(CH_3)_3$ of both m/z = 77 and m/z = 47 due to the formation of $FSi(CH_3)_3$ shown in Figure 10c.

Figure 11 illustrates the proposed reaction mechanism for $(AlF_3)(LiF)_x$ alloy ALD reactions. In reaction A, an initial surface of $(AlF_3)(LiF)_x$ alloy film is assumed prepared by several $(AlF_3:LiF)=1:1$ ALD reactions. When TMA molecules are exposed to the surface, TMA adsorbs on the surface. In reaction B, HF molecules are exposed to the surface to form AlF3 and CH_4 as a byproduct. In reaction C, there is LiHMDS adsorption. And HF exposed in the reaction D form LiF and $FSi(CH_3)_3$ and ammonia as byproducts confirmed by QMS. Individual ratios during AlF_3 and LiF subcycles are consistent with the assumption of TMA and LiHMDS adsorption on the surface during reaction A and C based on the mass gain ratio obtained by QCM experiment.
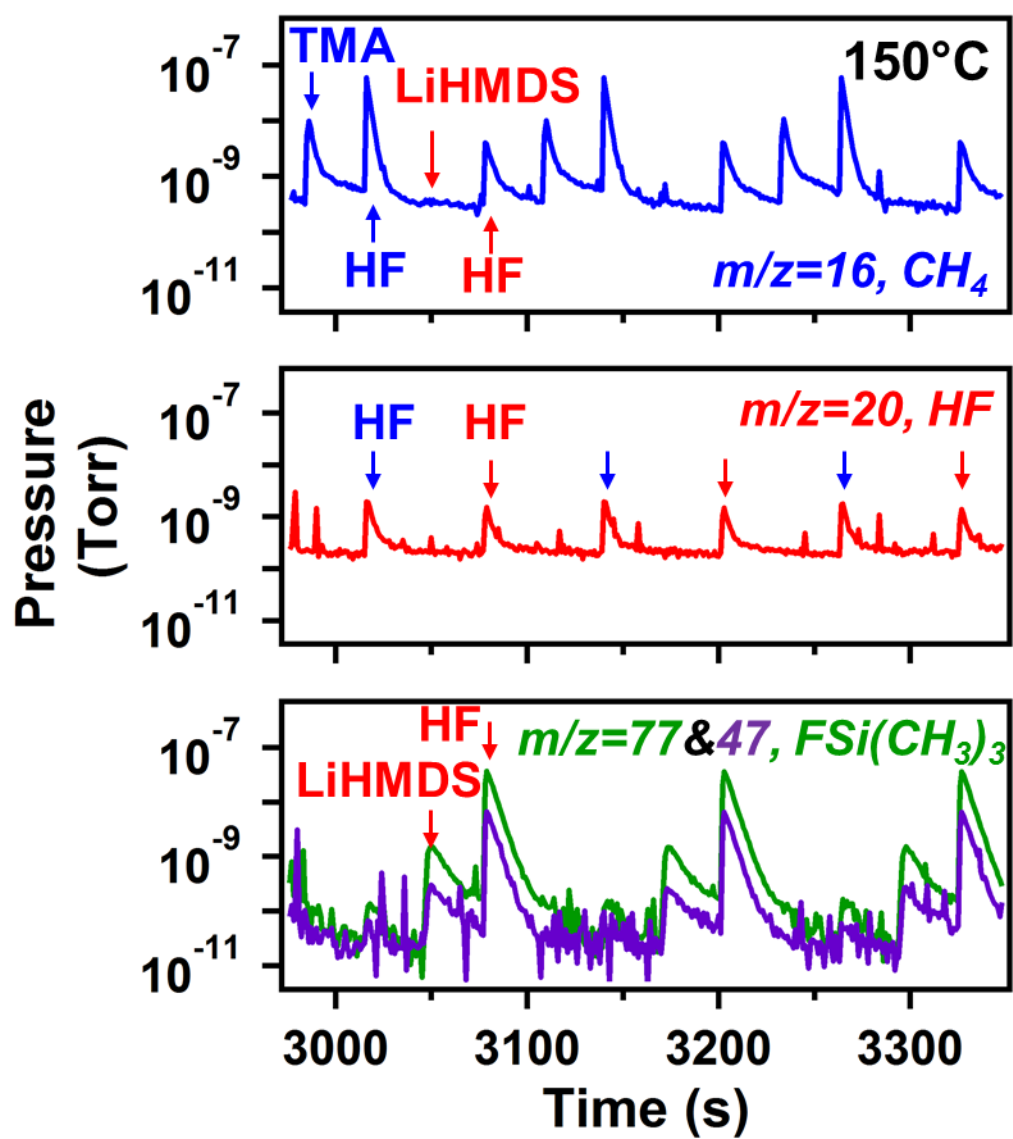
Figure 3-10. Mass spectrometer signals for (a) m/z= 16 for CH_4; (b) m/z= 20 for HF; (c)

m/z=77 and 47 for $FSi(CH)_3$, HF respectively, during 40 sequences of AlF_3:LiF=

= 1:1 reaction at 150 °C shown in Figure 3-7.
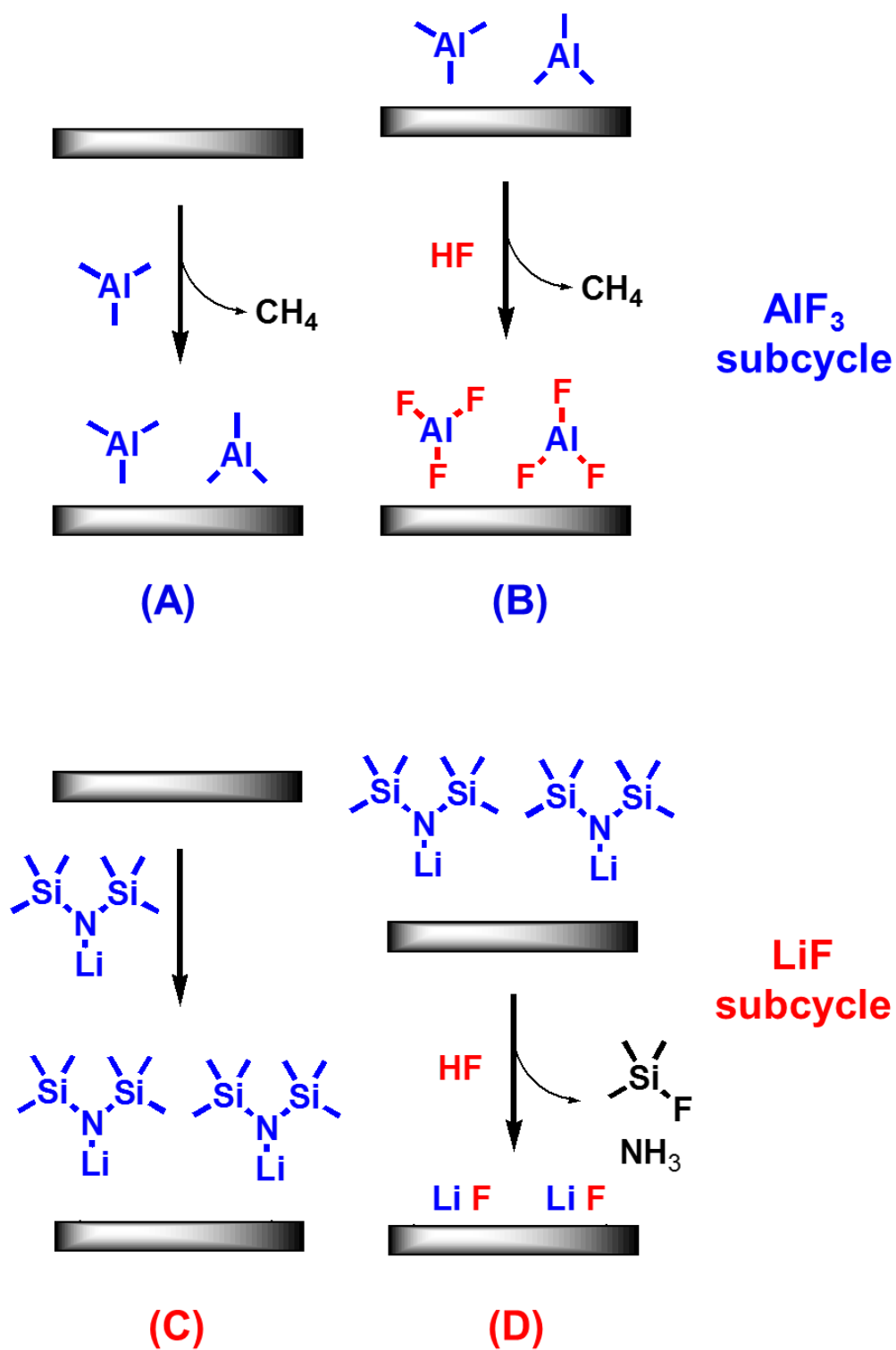
Figure 3-11. Proposed reaction mechanism of $(AlF_3)(LiF)_x$ alloy film consisting of AlF_3 ALD subcycle and LiF ALD subcycle.

3.3C. *Ex situ* Analysis of LiF and $(AlF_3)(LiF)_x$ Alloy Films

Figure 12 shows the plot of film thickness at the different number of sequences measured by XRR and SE. The plot of film thickness of $(AlF_3)(LiF)_x$ alloy ALD grown on silicon wafer at 50 100, 200, 400, 600, and 800 cycles. Growth of $(AlF_3)(LiF)_x$ alloy ALD film on the silicon wafer is linear having the growth rate of 0.9 Å /sequence measured by XRR and SE. The density of the films grown >200 sequences of $(AlF_3)(LiF)_x$ alloy ALD measured by XRR is 2.6 g /cm^3. Refractive index of the films is 1.36 measured by SE. The film density of the films closes to LiF ALD (2.6 g /cm^3.) rather than AlF_3 (2.9 g /cm^3) consistent with more LiF contents in alloys film. The thickness, the film density, and film roughness of alloy film do not show noticeable changes after storage in atmosphere after one month. These results indicate alloy grown by ALD is not hygroscopic in the atmosphere. Refractive indices were measured at the wavelength of 589 nm obtained by SE based on the Sellmeier model. This refractive index of 1.36 is achieved >200 sequences of ALD.

Figure 13a shows GIXRD of the films grown using 800 sequences of $(AlF_3)(LiF)_x$ alloy film at 150°C showing a crystalline peaks corresponding to Li_3AlF_6 phase. Alloy films grown using thermal evaporation and ALD was amorphous. GIXRD of LiF film is shown in Figure 13b as a comparison. Figure 13b shows GIXRD of the films grown using 800 cycles of LiF at 150°C showing a crystalline structure. (111), (200), and (220) peaks are observed. LiF grown using thermal evaporation and ALD were also crystalline.[10,20,39]

The depth profile of LiF and $(AlF_3)(LiF)_x$ alloy films obtained by X-ray photoelectron spectroscopy (XPS). The LiF film consists of lithium and fluorine after removal of adventitious surface carbon. The $(AlF_3)(LiF)_x$ alloy film consists of aluminum, lithium and fluorine after
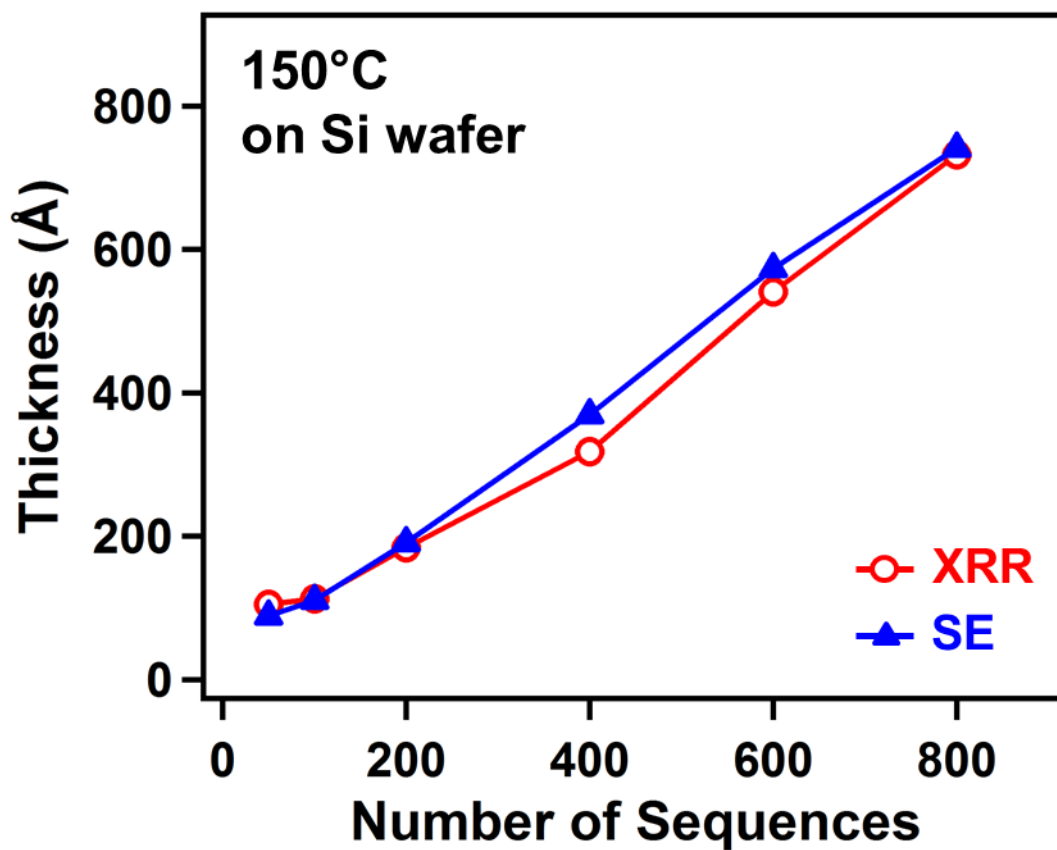
Figure 3-12. Film thickness versus number of sequences for AlF_3:LiF= = 1:1 reaction at

150 ℃ on Si (100) substrates determined by XRR and SE measurements.
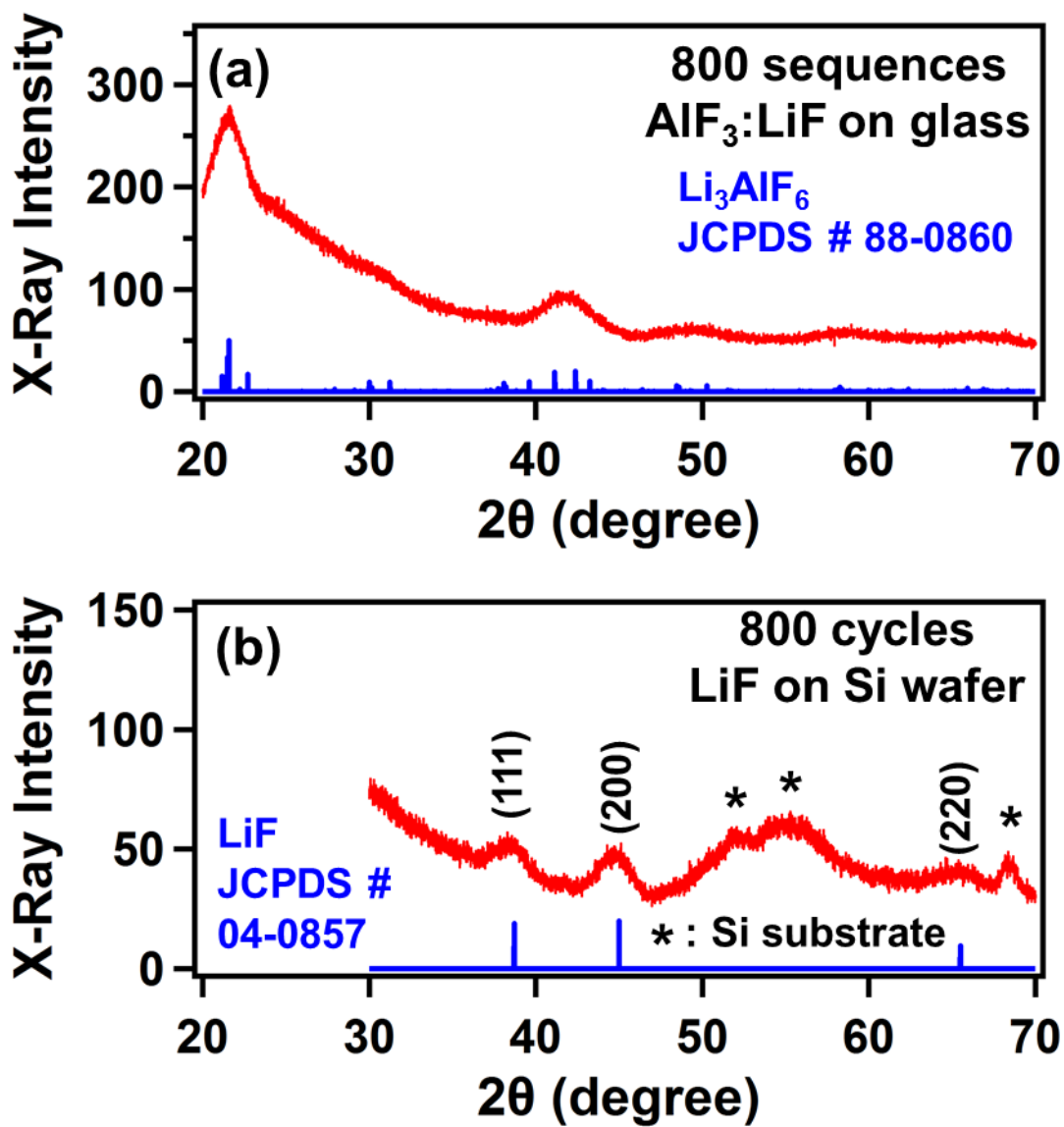
Figure 3-13. Grazing Incidence X-ray diffraction of (a) $(AlF_3)(LiF)_x$ alloy film; (b) LiF ALD film.

removal of adventitious surface carbon. Oxygen impurities are not detected for both films. Carbon, nitrogen, and silicon impurities are below the detection limit of XPS for both films. This absence of C, N, and Si in the film may be related with breakdown of HMDS ligand by HF shown in QMS experiments. The ratio between lithium and fluorine of LiF film is one to 0.73 that is quite off from stoichiometric LiF. The preferential sputtering of fluorine could explain why the measurements are off-stoichiometry.[30,41]

To determine the stoichiometry between lithium and fluorine, inductively coupled plasma mass spectrometry (ICP-MS) and ionic chromatography (IC) were performed. The LiF film grown using 800 cycles of ALD was dissolved in the DI water. Dissolution of LiF film was confirmed by SE. Lithium contents in LiF solution was measured by ICP-MS. ICP-MS can not analyze F because ionization energy of F is higher than argon that is used as medium. IC was employed to determine F contents in LiF solution. Atomic ratio of Li:F was determined as 1:1.1. ICP-MS and IC also determined $(AlF_3)(LiF)_x$ alloy film grown using 800 sequence of ALD. Atomic ratio of Al:Li:F=1:2.7:5.4 in this film, which is consistent with QCM result.

3.3D. Measurement of Ionic Conductivity of (AlF3)(LiF)x Alloy Films by EIS Using the Symmetric Coin Cell

Figure 14a shows the schematic of a typical coin cell. A coin cell consist of top and bottom cases and gasket between them to isolate negative and positive terminals. There are two working electrodes and the separator between them to prevent short circuit. There are also a spring and a stainless steel spacer for better contact. To measure ionic conductivity, two symmetric coin cells were prepared. The symmetric coin cell means two working electrodes are identical. The $(AlF_3)(LiF)_x$ fluorides alloy film on the copper foil are employed as working electrodes.
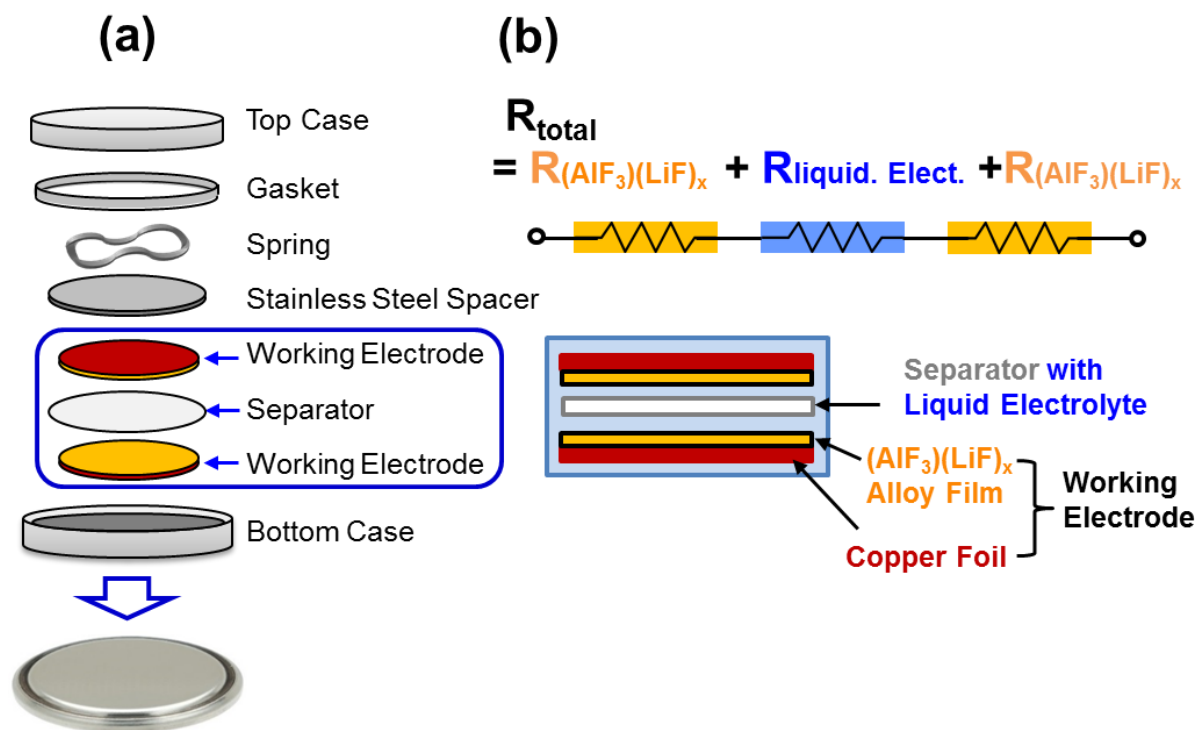
Figure 3-14. Schematic of symmetric coin cell and equivalent circuit

Figure 14b shows the schematic of the equivalent circuit of the symmetric coin cell. The total resistance of a coin cell consists of twice of resistance of fluorides alloy film and the resistance of liquid electrolytes.

$$\mathbf{R_{tot}= R_{(AlF3)(LiF)x} +R_{liquid\ elect.} + R_{(AlF3)(LiF)x} =2\times R_{(AlF3)(LiF)x} +R_{liquid\ elect.}} \qquad (7a)$$

Two coin cells with two different thicknesses of $(AlF_3)(LiF)_x$ alloy films were prepared for the measurement of the ionic conductivity of $(AlF_3)(LiF)_x$ alloy films. These two different thickness can exclude the possible issue of the contact resistance and the nucleation. Film thicknesses of 73 nm and 32 nm were prepared using 800 and 400 sequences measured on the Si wafer grown together by XRR.

The Nyquist plot measured by electrochemical impedance spectroscopy (EIS) shows two different x-intercepts in Figure 15a and figure 15b. The x-intercept represents the total resistance of the coin cell. The difference in resistances in Figure 15a and Figure 15b is due to the different thicknesses of two fluorides alloy films. The resistance of the liquid electrolyte is constant. And now there is two equations and two unknowns.

$$2\times R_{73nm} + R_{liq.elect.} = 4.45\ \Omega \qquad (7b)$$

$$2\times R_{32nm} + R_{liq.elect.} = 3.63\ \Omega \qquad (7c)$$

$$2\times(R_{73nm} - R_{32nm})= 0.82\ \Omega \qquad (8)$$

Ionic conductivity of 7.5×10^{-6} S/cm is obtained at room temperature using the thickness, the area and resistance of the film.

$$\mathbf{\sigma = \frac{t}{A\times R} = \frac{73\ nm\ -\ 32\ nm}{(1.33\ cm^2)\times(0.41\ \Omega)} = 7.5 \times 10^{-6}\ S/cm} \qquad (9)$$
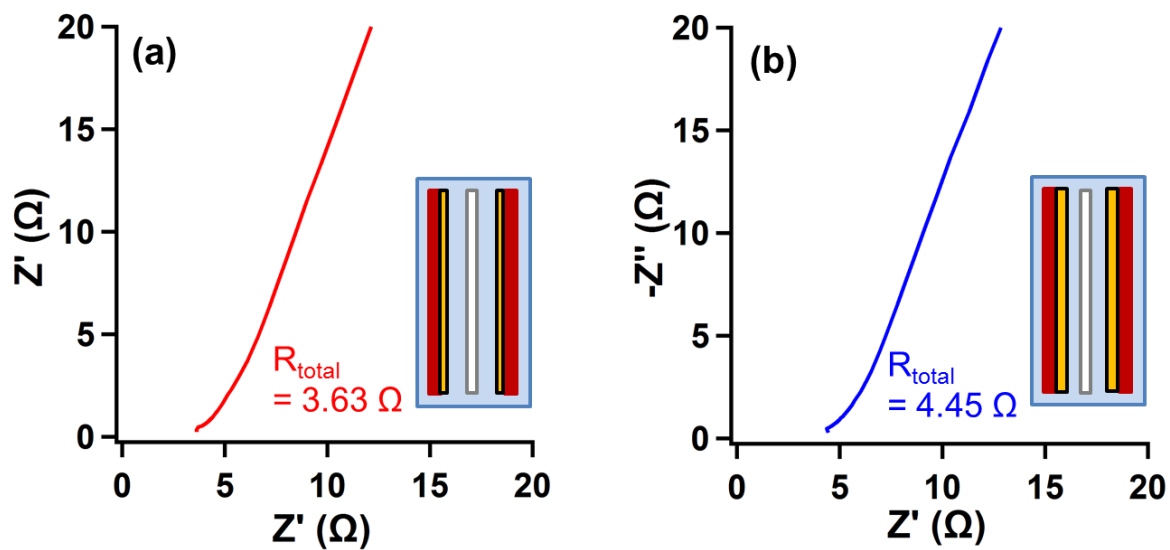
Figure 3-15. Total resistance of symmetric coin cell measured by electrochemical impedance spectroscopy (EIS) prepared using (a) 800 sequences of $(AlF_3)(LiF)_x$ alloy film; (b) 400 sequences $(AlF_3)(LiF)_x$ alloy film.

This ionic conductivity of 7.5×10^{-6} S/cm is slightly higher than the ionic conductivity of 1.0×10^{-6} S/cm for $AlLiF_4$ film grown by thermal evaporation.[8] The crystallinity of $(AlF_3)(LiF)_x$ alloy film grown by ALD may be responsible for this higher ionic conductivity. The fluorides allow film grown by thermal evaporation was amorphous.[8] This ionic conductivity of 7.5×10^{-6} S/cm of $(AlF_3)(LiF)_x$ alloy film also yields the conductivity of liquid electrolyte of 1.05×10^{-2} S/cm.

$$\sigma_{LE} = \frac{420\ \mu m}{(1.33\ cm^2)\times(2.99\ \Omega)} = 1.05\times10^{-2}\ S/cm$$

3.4. Conclusions

The ALD reactions of LiF using LiHMDS and HF were studied to understand the ALD film at the reaction temperatures between 125℃ and 250℃. The growth rate was $0.5-0.6$ A/cycle at 150℃. The reaction mechanism was LiHMDS adsorption. The ALD reactions of $(AlF_3)(LiF)_x$ alloy film using TMA, LiHMDS and HF were also studied to understand the ALD film at the reaction temperatures between 150℃. The growth rate was 0.9 A/sequence at 150℃. The reaction mechanism was TMA and LiHMDS adsorptions. XPS showed impurities such as carbon, oxygen, nitrogen, and silicon LiF and $(AlF_3)(LiF)_x$ alloy films were both below the detection limit of XPS. Grazing incidence X-ray diffraction (GIXRD) observed that LiF and $(AlF_3)(LiF)_x$ alloy film have crystalline structures. Inductively coupled plasma mass spectrometry (ICP-MS) and ionic chromatography revealed atomic ratio of Li:F=1:1.1 and Al:Li:F=1:2.7: 5.4 for $(AlF_3)(LiF)_x$ alloy film. EIS measurement revealed that lithium ion conductivity $(AlF_3)(LiF)_x$ alloy film was measured as $\sigma = 7.5\times10^{-6}$ S/cm.

3.5. Acknowledgements

3.6. References

(1)   Peled, E.; Golodnitsky, D.; Ardel, G. J. Electrochem. Soc. 1997, 144, L208.

(2)   Verma, P.; Maire, P.; Novak, P. Electrochim. Acta 2010, 55, 6332.

(3)   Roessler, D. M.; Walker, W. C. J. Phys. Chem. Solids 1967, 28, 1507.

(4)   Li, H. H. J. Phys. Chem. Ref. Data 1976, 5, 329.

(5)   Hung, L. S.; Tang, C. W.; Mason, M. G. Appl. Phys. Lett. 1997, 70, 152.

(6)   Jabbour, G. E.; Kippelen, B.; Armstrong, N. R.; Peyghambarian, N. Appl. Phys. Lett. 1998, 73, 1185.

(7)   Prada, S.; Martinez, U.; Pacchioni, G. Physical Review B 2008, 78.

(8)   Oi, T.; Miyauchi, K. Mater. Res. Bull. 1981, 16, 1281.

(9)   Schulz, L. G. J. Chem. Phys. 1949, 17, 1153.

(10)   Montereali, R. M.; Baldacchini, G.; Martelli, S.; Docarmo, L. C. S. Thin Solid Films 1991, 196, 75.

(11)   Smith, J. L.; Budenste.Pp J. Appl. Phys. 1969, 40, 3491.

(12)   Kim, H.; King, A. H. J. Mater. Res. 2008, 23, 452.

(13)   Lapianosmith, D. A.; Eklund, E. A.; Himpsel, F. J.; Terminello, L. J. Appl. Phys. Lett. 1991, 59, 2174.

(14)   Li, C. L.; Guo, X. X.; Gu, L.; Samuelis, D.; Maier, J. Adv. Funct. Mater. 2011, 21, 2901.

(15)   Li, C. L.; Gu, L.; Maier, J. Adv. Funct. Mater. 2012, 22, 1145.

(16)   Kumar, M.; Khan, S. A.; Rajput, P.; Singh, F.; Tripathi, A.; Avasthi, D. K.; Pandey, A. C. J. Appl. Phys. 2007, 102.

(17)   Kumar, M.; Rajput, P.; Khan, S. A.; Avasthi, D. K.; Pandey, A. C. Appl. Surf. Sci. 2010, 256, 2199.

(18)   Henley, S. J.; Ashfold, M. N. R.; Pearce, S. R. J. Appl. Surf. Sci. 2003, 217, 68.

(19)   Perea, A.; Gonzalo, J.; Afonso, C. N.; Martelli, S.; Montereali, R. M. Appl. Surf. Sci. 1999, 138, 533.

(20)   Mantymaki, M.; Hamalainen, J.; Puukilainen, E.; Munnik, F.; Ritala, M.; Leskela, M. Chem. Vap. Deposition 2013, 19, 111.

(21)   Oi, T., US4367267 1983.

(22)   Oi, T. Mater. Res. Bull. 1984, 19, 451.

(23)   Oi, T.; Miyauchi, K., Mater. Res. Bull. 1981, 16 1281-1289.

(24)   George, S. M. Chem. Rev. 2010, 110, 111.

(25)   Miikkulainen, V.; Leskela, M.; Ritala, M.; Puurunen, R. L. J. Appl. Phys. 2013, 113, 021301.

(26)   Ylilammi, M.; Rantaaho, T. J. Electrochem. Soc. 1994, 141, 1278.

(27)   Pilvi, T.; Hatanpaa, T.; Puukilainen, E.; Arstila, K.; Bischoff, M.; Kaiser, U.; Kaiser, N.; Leskela, M.; Ritala, M. J. Mater. Chem. 2007, 17, 5077.

(28)   Pilvi, T.; Puukilainen, E.; Kreissig, U.; Leskela, M.; Ritala, M. Chem. Mater. 2008, 20, 5023.

(29)   Putkonen, M.; Szeghalmi, A.; Pippel, E.; Knez, M. J. Mater. Chem. 2011, 21, 14461.

(30)   Lee, Y.; DuMont, J. W.; Cavanagh, A. S.; George, S. M. Submitted to Journal of Physical Chemistry C 2015.

(31)   Olah, G. A.; Nojima, M.; Kerekes, I. Synthesis-Stuttgart 1973, 779.

(32)   Elam, J. W.; Groner, M. D.; George, S. M. Rev. Sci. Instrum. 2002, 73, 2981.

(33)   Lee, Y.; Yoon, B.; Cavanagh, A. S.; George, S. M. Langmuir 2011, 27, 15155.

(34)   CRC Handbook of Chemistry and Physics; 85th ed.; Lide, D. R., Ed.; CRC Press: Boca Raton, FL, 2005.

(35)   Krouse, I. H.; Wenthold, P. G. J. Am. Soc. Mass Spectrom. 2005, 16, 697.

(36)   Stalke, D.; Keweloh, N.; Klingebiel, U.; Noltemeyer, M.; Sheldrick, G. M. Zeitschrift Fur Naturforschung Section B-a Journal of Chemical Sciences 1987, 42, 1237.

(37)   Dippel, K.; Klingebiel, U.; Sheldrick, G. M.; Stalke, D. Chemische Berichte-Recueil 1987, 120, 611.

(38)   Walter, S.; Klingebiel, U.; Noltemeyer, M. Chemische Berichte-Recueil 1992, 125, 783.

(39)   Mantymaki, M.; Hamalainen, J.; Puukilainen, E.; Sajavaara, T.; Ritala, M.; Leskela, M. Chem. Mater. 2013, 25, 1656.

(40)   D. Shannon, R.; Shannon, R. C.; Medenbach, O.; Fischer, R. X. J. Phys. Chem. Ref. Data 2002, 31, 931.

(41)   Targove, J. D.; Bovard, B. G.; Lingg, L. J.; Macleod, H. A. Thin Solid Films 1988, 159, L57.

CHAPTER 4

Atomic Layer Deposition of Metal Fluorides Using Various Metal Precursors and Hydrogen Fluoride

4.1. Introduction

Metal fluorides are important dielectric materials with a low refractive index and high transmission at ultraviolet (UV), deep UV and infrared (IR) wavelengths.[1-3] These properties of metal fluorides are useful for optical coatings. Metal fluorides are also employed as heterogeneous catalyst for the production of chlorofluorocarbons (CFCs) due to its strong Lewis acidity.[4-6]

Metal fluorides films have been grown by physical vapor deposition techniques such as sputtering,[7,8] thermal evaporation,[9-11] electron beam deposition,[1,12] and ion-assisted deposition.[13,14] Metal fluorides films have also been grown by atomic layer deposition (ALD). ALD is a technique based on sequential, self-limiting surface reactions that deposits extremely conformal and continuous thin films with atomic level control.[15]

Most ALD of metal fluorides has been performed using alternative F precursors rather than HF. The first report for metal fluoride ALD such as CaF_2, SrF_2, and ZnF_2 employed NH_4F

solid as F source.[16] NH₄F was delivered by sublimation at 80°C into the reactor and decomposed

to NH₃ and HF at the reaction temperatures between 260°C and 400°C.[16] ALD of MgF₂,[17,18]

LaF₃,[19] YF₃,[20] and LiF[21] has been demonstrated using either TiF₄ or TaF₅ as F source. The

ligand exchange between metal 2,2,6,6-tetramethyl-3,5-heptanedionate (M(tmhd)ₓ) and TiF₄ or

TaF₅ yields the metal fluoride (MFₓ) layer and volatile Ti(tmhd)₄ or Ta(tmhd)₅ as a byproduct.

Another approach has employed the plasma or the ozone ALD with hexafluoroacetylacetonate as

a fluorine source to grow MgF₂, CaF₂ and LaF₃ thin films.[22]

We initially reported ALD of AlF₃ using trimethylaluminum (TMA) and HF from a

HF-pyridine solution.[23,24] ALD of LiF, and (AlF₃)(LiF)ₓ alloy film alloy film was also reported

using lithium hexametyldisilazide (LiHMDS) using the same F precursor.[23,25]

In this paper, the growth of metal fluorides ALD films using HF derived from HF-

pyridine as F precursor. Various metal precursors such as tetrakis(ethylmethylamido) zirconium,

zirconium *tert*-butoxide, tetrakis(dimethylamido) hafnium, bis(ethylcyclopentadienyl)

manganese, bis(ethylcyclopentadienyl) magnesium, diethylzinc, TMA and LiHMDS are

employed for ALD of metal fluorides such as ZrF₄, HfF₄, MnF₂, MgF₂, ZnF₂, AlF₃, and LiF.

ALD of metal fluorides was examined using *in situ* quartz crystal microbalance (QCM) at

150 ℃. The thickness and density of metal fluoride films were determined with *ex situ* X-ray

reflectivity (XRR). The film thickness and refractive index were measured with spectroscopic

ellipsometry (SE). The composition of the metal fluorides ALD film was also determined with

X-ray photoelectron spectroscopy (XPS).

4.2. Experimental

4.2A. Viscous Flow Reactor with *in situ* QCM

The ALD reactions were performed in the viscous flow reactor equipped with an *in situ* quartz crystal microbalance (QCM) at 150°C.[26,27] A mechanical pump (Pascal 2015SD, Alcatel) was used maintain vacuum conditions in the ALD reactor. Reactants were dosed into a N_2 carrier gas. Mass flow controllers (Type 1179A, MKS) supplied a constant N_2 carrier gas flow of 150 sccm. This N_2 gas flow resulted in a base pressure of ~1 Torr in the reactor. A PID temperature controller (2604, Eurotherm) kept the reactor at a fixed temperature within ± 0.04 °C. A bakeable capacitance manometer (Baratron 121A, MKS) monitored pressure change during reaction.

The metal fluoride ALD reactions were performed using various metal precursors such as tetrakis(ethylmethylamido) zirconium (TEMAZ, 99.99%, Sigma Aldrich,), zirconium *tert*-butoxide (ZTB, 99%, Strem), tetrakis(dimethylamido) hafnium (TDMAH, 99.99%, Sigma Aldrich), bis(ethylcyclopentadienyl) manganese ($Mn(EtCp)_2$, 98%, Strem), bis(ethylcyclopentadienyl) magnesium ($Mg(EtCp)_2$, 98%, Strem), diethylzinc (DEZ, Zn 52.0 %, Sigma-Aldrich), trimethylaluminum (TMA, 97 %, Sigma-Aldrich) and lithium hexamethyldisilazide (LiHMDS, 95%, Gelest), and HF-pyridine (70 wt% HF, Sigma-Aldrich) as the reactants. The bubbler temperatures for TEMAZ, ZTB, TDMAH, $Mn(EtCp)_2$, $Mg(EtCp)_2$ and LiHMDS were held at 112, 65, 67, 100, 92, and 115°C and summarized in Table 1. Use of gaseous HF from HF-pyridine enables the safe handling of anhydrous HF. HF-pyridine is a liquid at room temperature and is known as Olah's reagent.[28] HF-pyridine was transferred to a stainless steel bubbler in a dry N_2-filled glove bag. The HF-pyridine solution has an equilibrium with gaseous HF. Our mass spectrometer measurements have revealed that HF is the dominant species in the vapor pressure of HF-pyridine. With static exposures with no pumping in our

Metal Fluorides	Metal Precursor	Acronym	Bubbler Tempeature (°C)
ZrF_4	Tetrakis(ethylmethylamido) zirconium	TEMAZ	112
ZrF_4	Zirconium *tert*-butoxide	ZTB	65
HfF_4	Tetrakis(dimethylamido) Hafnium	TDMAH	67
MnF_2	Bis(ethylcyclopentadienyl) Manganese	$Mn(EtCp)_2$	100
MgF_2	Bis(ethylcyclopentadienyl) Magnesium	$Mg(EtCp)_2$	90
ZnF_2	Diethylzinc	DEZ	RT
AlF_3	Trimethylaluminum	TMA	RT
LiF	Lithium hexamethyldisilazide	LiHMDS	115

Table 4-1.   Metal fluorides, metal precursors, acronym of metal precursors, and the bubbler temperature

ALD reactor, the vapor pressure HF over the HF-pyridine solution was 90-100 Torr at room temperature.

Each metal fluoride ALD experiment was conducted on a fresh metal oxide film grown by ALD at 150°C. The initial metal oxide ALD films were prepared using corresponding metal precursors and H_2O (Chromasolv for HPLC, Sigma-Aldrich). The TMA, DEZ, HF-pyridine, and H_2O precursors were held at room temperature.

A film deposition monitor (Maxtek TM-400, Inficon) was used to perform the *in situ* QCM measurements. The QCM sensors were polished, 6 MHz, AT-cut (Colorado Crystal Corp.) and RC-cut (Colnatec) quartz crystals with gold electrodes. The QCM sensor was secured in the bakeable single sensor head (BSH-150, Inficon) and sealed with high temperature epoxy (Epo-Tek H21D, Epoxy technology). Deposition on the back-side of the QCM sensor was prevented by flowing an additional 20 sccm of N_2 through the QCM housing.[26] This additional N_2 was supplied using a bellows-sealed metering valve (SS-4BMG, Swagelok).

4.2B. *Ex situ* Film Characterization using XRR, GIXRD, SE, and XPS

For *ex situ* measurements, boron-doped Si (100) wafers (p-type, Silicon Valley Microelectronics) were used as the substrates. The Si wafer was cleaved into 2.5 cm by 2.5 cm samples. These samples were cleaned with acetone, isopropanol, and deionized water and dried with N_2 gas.

The film thicknesses and the density were determined using *ex situ* XRR measurements. The XRR measurements were performed with a high resolution X-ray diffractometer (Bede D1, Jordan Valley Semiconductors) using a Cu Kα ($\lambda = 1.540$ Å) X-ray tube. The filament current was 35 mA and the voltage was 40 kV. The step size and acquisition time for all the XRR scans were 10 arcsec and 5 s, respectively. The XRR scans were modeled with the Bede REFS

software package (Bede REFS, Jordan Valley Semiconductors) to determine film thickness, surface roughness, and film density.

The film thicknesses and refractive index were measured using spectroscopic ellipsometry (SE). These measurements were performed using a spectroscopic ellipsometer (M-2000, J. A. Woollam) employing a spectral range from 240 to 1700 nm with an incidence angle of 75°. Measurement of Ψ and Δ were modeled with the CompleteEASE software package (CompleteEASE, J. A. Woollam) and a Sellmier model.[29] The Sellmeier model is commonly used for optically transparent films such as metal fluoride films.[29]

The film composition was determined by X-ray photoelectron spectroscopy (XPS). The XPS instrument (PHI 5600, RBD Instruments) used a monochromatic Al Kα X-rays source (1486.6 eV). Survey scans were measured with a pass energy of 93.9 eV and a step size of 0.400 eV. Depth profiles were obtained using Ar ion sputtering. A pass energy of 58.7 eV and a step size was 0.250 eV was used for the depth profiling analysis. An electron beam neutralizer was employed at 17.8 mA. Data was collected with the Auger Scan software package (Auger Scan, RBD Instruments) and analyzed with the Casa XPS software package (Casa XPS, Casa Software).

4.3. Results and Discussion

4.3A. Growth of ZrF₄ Films Using Tetrakis(ethylmethylamido)zirconium (TEMAZ) and HF

Figure 1a shows the QCM measurements of mass gain during 200 cycles of ZrF_4 ALD at 150°C using tetrakis(ethylmethylamido) zirconium (TEMAZ) and HF. The initial layer on the QCM sensor was a ZrO_2 ALD film grown with 200 cycles of ZrO ALD using TEMAZ and H_2O
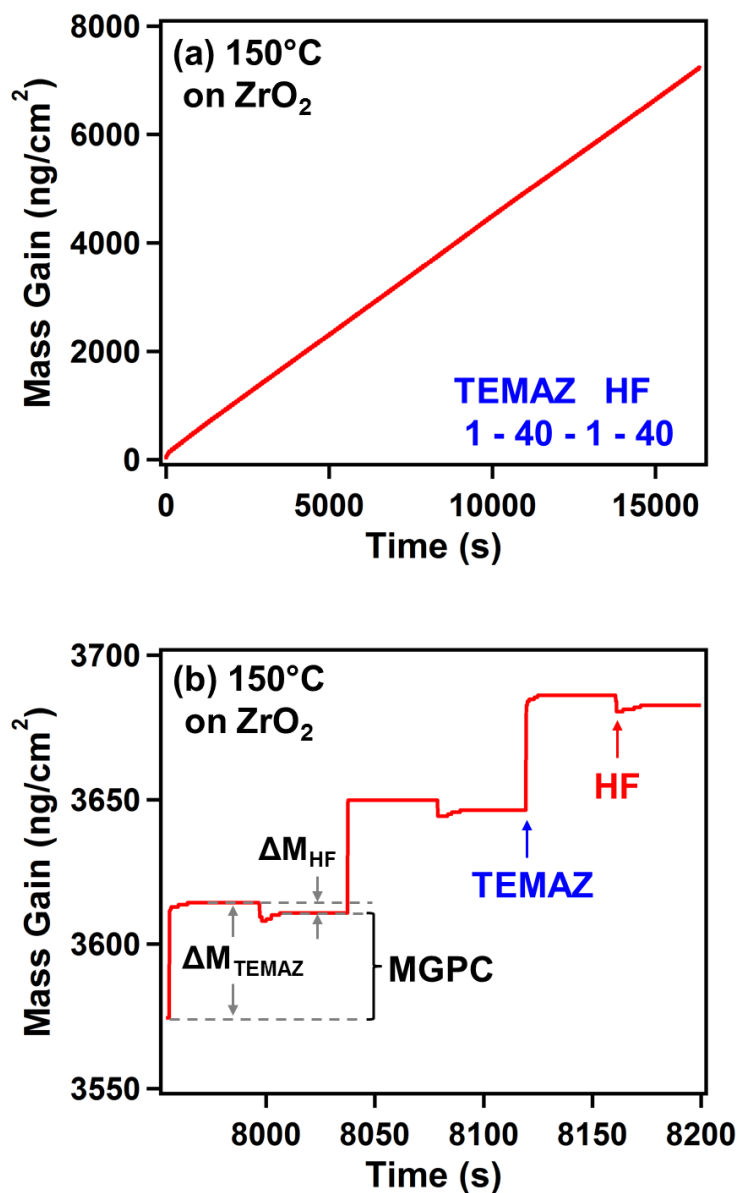
Figure 4-1. (a) Mass gain versus time during 200 ZrF_4 ALD cycles with TEMAZ and HF as

the reactants on ZrO_2 at 150 ℃ using the reaction sequence of (1-40-1-40);

(b) Enlargement of mass gain versus time for three sequential TEMAZ and HF

exposures during ZrF_4 ALD in the steady-state, linear growth regime.

as the reactants.[30] The reaction sequence of one ZrF_4 ALD cycle consisted of a 1 s dose of

TEMAZ, 40 s of N_2 purge, a 1 s dose of HF, and 40 s of N_2 purge. This reaction sequence is

designated as (1-40-1-40). The TEMAZ and HF doses produced pressure transients of 20 mTorr

and 100 mTorr, respectively. The ZrF_4 ALD growth is very linear with a mass gain per cycle

(MGPC) of 35.5 ng/(cm^2 cycle). In addition ZrF_4 ALD on Al_2O_3 initial surface showed nearly

identical results.

Figure 1b shows the mass gain during three sequential ZrF_4 ALD cycles at 150°C using

the reaction sequence (1-40-1-40). These three cycles were the 98th, 99th, and 100th ZrF_4 ALD

cycles in Figure 1a. The mass changes show very distinct steps. The mass increase after the

TEMAZ exposure is ΔM_{TEMAZ} = 39.2 ng/(cm^2 cycle). The mass change after the HF exposure is

ΔM_{HF} = -3.7 ng/(cm^2 cycle). The MGPC was 35.5 ng/(cm^2 cycle).   Figure 2 displays the MGPC

and the ΔM_{TEMAZ}/MGPC ratio during 200 cycles of ZrF_4 ALD using a reaction sequence of (1-

40-1-40). The MGPC is 35.5 ng/(cm^2 cycle) and consists of constant mass gains of ΔM_{TEMAZ} =

39.2 ng/(cm^2 cycle) and ΔM_{HF} = -3.7 ng/(cm^2 cycle). Except for the first 3 ZrF_4 ALD cycles, the

ΔM_{TMA}/MGPC ratio is constant at 1.1. ZrF_4 ALD nucleates nearly immediately on the initial

ZrO_2 ALD surface. The MGPC and the ΔM_{TEMAZ}/MGPC ratio were nearly independent of the

purge time. Extended purge times of 120 s slightly decreased the MGPC to ~33 ng/(cm^2 cycle).

However, the ΔM_{TEMAZ}/MGPC ratio remained at ~1.1. The ΔM_{TEMAZ}/MGPC ratio was

summarized in Table 2. This ratio will be used later to determine the reaction stoichiometry.

The self-limiting behavior of the TEMAZ and HF reactions for ZrF_4 ALD was also

examined using *in situ* QCM experiments. Figure 3a and 3b show the mass gains during the

TEMAZ and HF exposures, respectively, at 150°C. For each of these exposures, the previous

reactant exposure had reached saturation. Each minidose consisted of an exposure time of 0.5 s
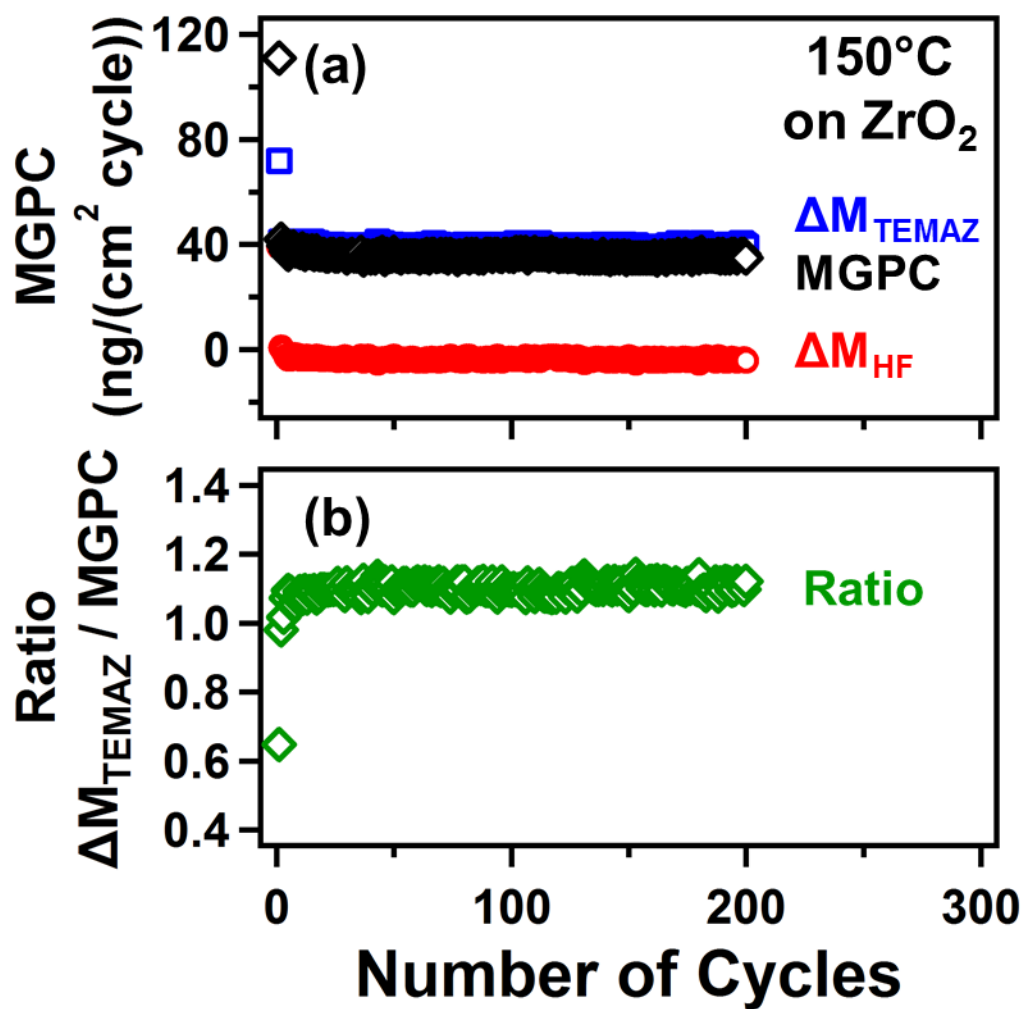
Figure 4-2. (a) MGPC, ΔM_{TEMAZ}, and ΔM_{HF} and (b) M_{TEMAZ}/MGPC ratio during 200 ZrF_4

ALD cycles with TEMAZ and HF as the reactants on ZrO_2 at 150 °C.

Metal Fluorides	Metal Precursor	MGPC (ng/(cm^2 cycle))	Ratio at 150°C	X : # of HF on MF$_y$
ZrF$_4$	TEMAZ	35.5	1.10	2.4
ZrF$_4$	ZTB	29.8	1.41	2.0
HfF$_4$	TDMAH	57.2	1.02	2.2
MnF$_2$	Mn(EtCp)$_2$	15.6	2.61	0
MgF$_2$	Mg(EtCp)$_2$	12.3	3.22	0.12
ZnF$_2$	DEZ	33.5	1.24	-0.02
AlF$_3$	TMA	31.4	0.71	0.78
LiF	(LiHMDS)	12.2	5.61	0.14

Table 4-2. Metal fluorides, Metal fluorides, acronym of metal precursors, MGPC, and number

of HF on metal fluoride.
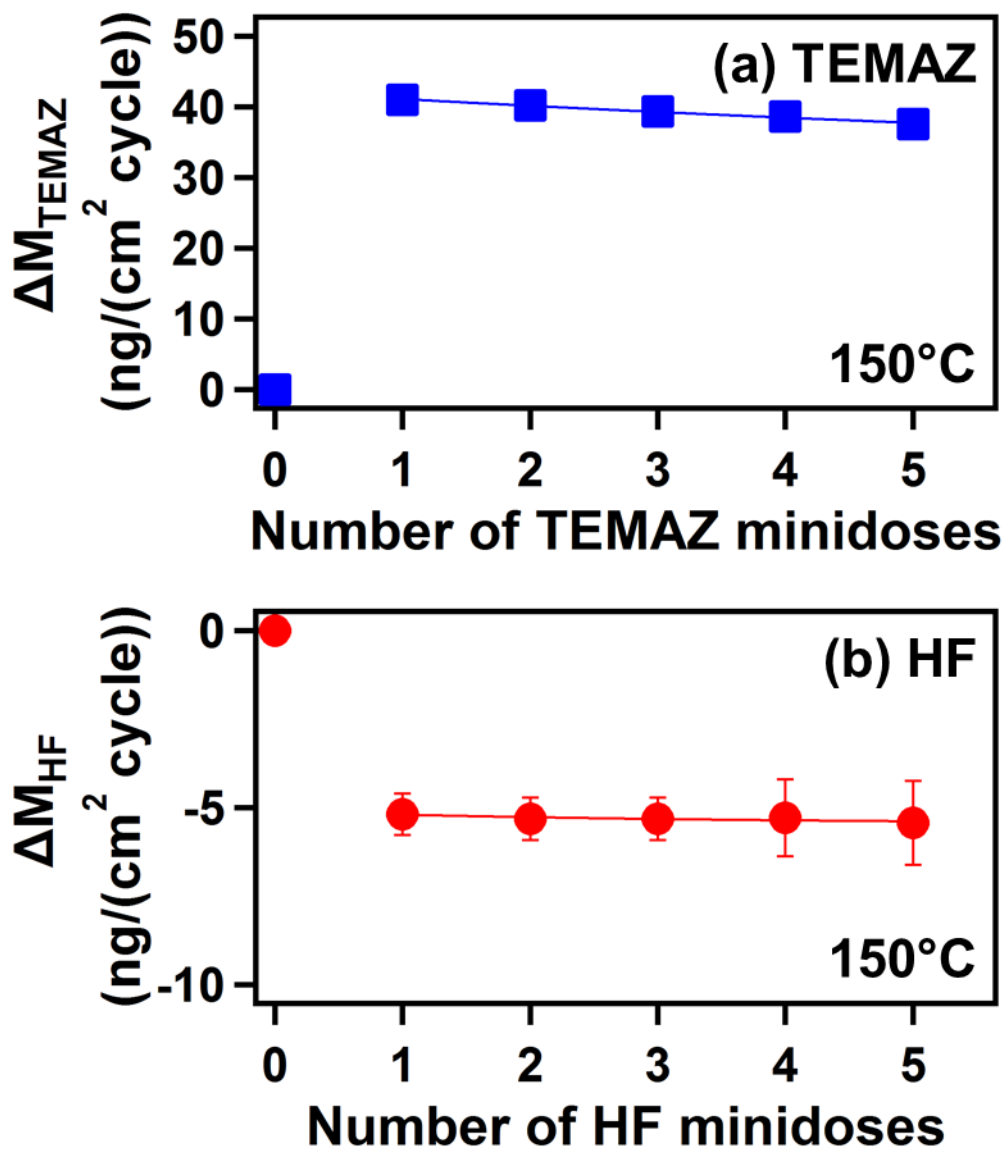
Figure 4-3. (a) ΔM_{TEMAZ} versus versus number of TEMAZ minidoses with the HF exposure

fixed at 1.0 s. (b) ΔM_{HF} versus versus number of HF minidoses with the TEMAZ

exposure fixed at 1.0 s.

and a purge time of 40 s. Both reactions displayed self-limiting behavior. ΔM_{TEMAZ} versus minidoses of TEMAZ reached the plateau of $\Delta M_{TEMAZ} = \sim 40 ng/(cm^2$ cycle) after one minidose. Similarly, ΔM_{HF} versus minidoses of HF leveled off at $\Delta M_{HF} = \sim 5$ ng/(cm^2 cycle) after one minidose.

The growth rates determined from *ex situ* XRR and SE measurements. ZrF$_4$ film was grown on Si wafer using 400 cycles of TEMAZ and HF reaction at 150℃. XRR and SE measured the film thickness of ZrF$_4$ ALD as 342 Å and 337 Å respectively. These thicknesses were consistent with 0.86 Å / cycle and 0.84 Å / cycle. The MGPC 35.5 ng/(cm^2 cycle) obtained by *in situ* QCM can be converted to the growth rate in Å /cycle using the film density. XRR also measured the film has density of 4.1 g/cm^3. This converted growth rate was 0.87 Å / cycle. The agreement between the *in situ* and *ex situ* measurements of the growth rate is very good. This density of 4.1 g/cm^3 is ~93 % of the bulk density of 4.43 g /cm^3 for crystalline ZrF$_4$.[31] The surface roughness was measured as 4 Å by XRR. SE determined the refractive index of 1.55 at 589 nm and were obtained using the Sellmeier model. The measured refractive index of n=1.55 is consistent with amorphous ZrF$_4$ n=1.56[32] at 633 nm, crystalline ZrF$_4$ n=1.59 [32], n=1.62[1], for e-beam grown ZrF$_4$ film at 600 nm. The ZrF$_4$ ALD films were also stable in air. The thickness, film density, and film roughness of ZrF$_4$ films did not change after storage in atmosphere for one month.

4.3B. Growth of ZrF$_4$ Films Using Zirconium *tert*-butoxide (ZTB) and HF

Figure 4a shows the QCM measurements of mass gain during 200 cycles of ZrF$_4$ ALD at 150℃ using zirconium *tert*-butoxide (ZTB) and HF. The initial layer on the QCM sensor was a ZrO$_2$ ALD film grown with 200 cycles of ZrO ALD using ZTB and H$_2$O as the reactants.[33] The
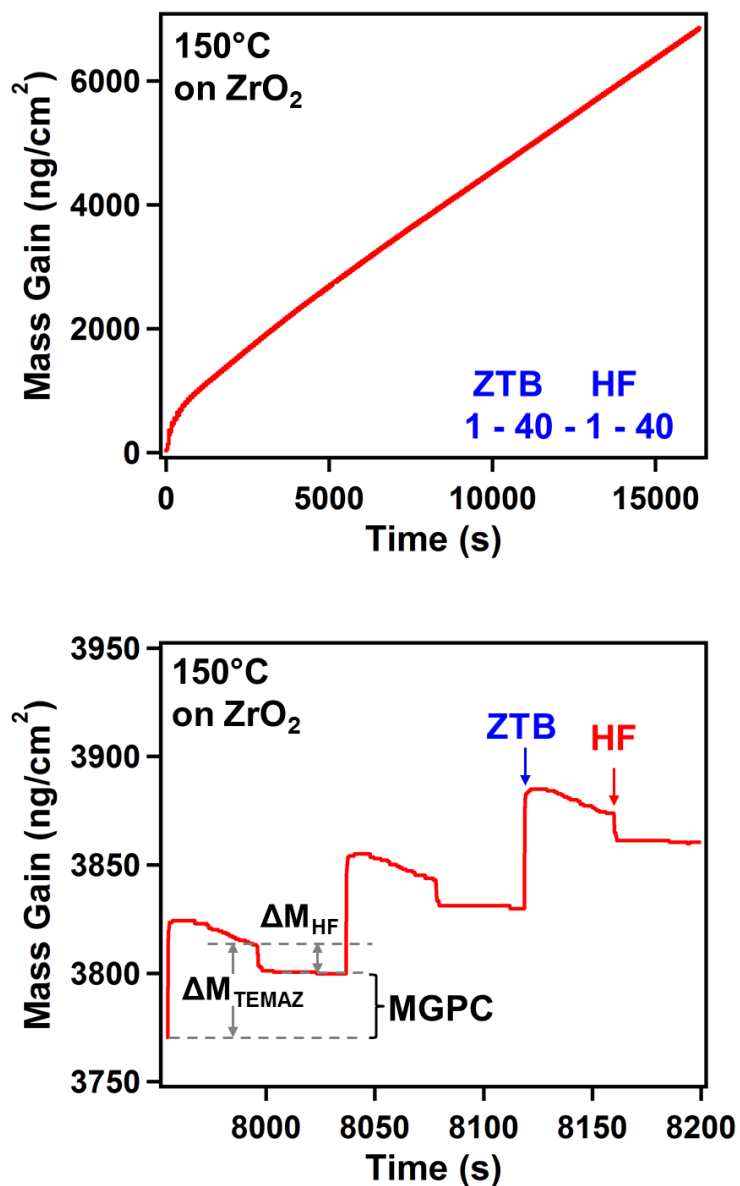
Figure 4-4. (a) Mass gain versus time during 200 ZrF$_4$ ALD cycles with ZTB and HF as the reactants on ZrO$_2$ at 150 °C using the reaction sequence of (1-40-1-40); (b) Enlargement of mass gain versus time for three sequential ZTB and HF exposures during ZrF$_4$ ALD in the steady-state, linear growth regime.

reaction sequence was (1-40-1-40). The ZTB and HF doses produced pressure transients of 5 mTorr and 100 mTorr, respectively. The ZrF_4 ALD growth is very linear with a mass gain per cycle (MGPC) of 29.8 ng/(cm^2 cycle). There is a nucleation periods of ~12 cycles. In addition ZrF_4 ALD on Al_2O_3 initial surface showed similar results. Figure 4b shows the mass gain during three sequential ZrF_4 ALD cycles at 150°C using ZTB by the reaction sequence (1-40-1-40).

These three cycles were the 98th, 99th, and 100th ZrF_4 ALD cycles in Figure 4a. The mass changes shows very distinct steps. The mass increase after the ZTB exposure is ΔM_{ZTB} = 42.0 ng/(cm^2 cycle). The mass change after the HF exposure is ΔM_{HF} = -12.2 ng/(cm^2 cycle). The MGPC was 29.8 ng/(cm^2 cycle). ΔM_{ZTB}/MGPC ratio averaged from 100-200 cycles of ZrF_4 ALD using a reaction sequence of (1-40-1-40) was ~1.4.

The growth rates determined from *ex situ* XRR and SE measurements. ZrF_4 film was grown on Si wafer using 400 cycles of ZTB and HF reaction at 150°C. XRR and SE measured the film thickness of ZrF_4 ALD as 252 Å and 249 Å respectively. These thicknesses were consistent with 0.63 Å / cycle and 0.62 Å / cycle. The MGPC of 29.8 ng/(cm^2 cycle) obtained by *in situ* QCM can be converted to the growth rate in Å /cycle using the film density. XRR also measured the film has density of 4.7 g/cm^3. This converted growth rate was 0.63 Å / cycle. The agreement between the *in situ* and *ex situ* measurements of the growth rate is very good. This density of 4.7 g/cm^3 is 106 % of the bulk density of 4.43 g /cm^3 for crystalline ZrF_4.[31] The surface roughness was measured as 4 Å by XRR. SE determined the refractive index of 1.62 at 589 nm and were obtained using the Sellmeier model. The measured refractive index of n=1.55 is consistent with n=1.56[32] for amorphous ZrF_4 at 633 nm, n=1.59[32] for crystalline ZrF_4 at 600 nm, and n=1.62[1] at 600 nm for ZrF_4 film grown by e-beam. The ZrF_4

ALD films were also stable in air. The thickness, film density, and film roughness of ZrF$_4$ films did not change after storage in atmosphere for one month.

4.3C. Growth of HfF$_4$ Films Using Tetrakis(dimethylamido)hafnium (TEMAH) and HF

Figure 5a shows the QCM measurements of mass gain during 200 cycles of HfF$_4$ ALD at 150°C using Tetrakis(dimethylamido) hafnium (TDMAH) and HF. The initial layer on the QCM sensor was a HfO$_2$ ALD film grown with 200 cycles of HfO$_2$ ALD using TDMAH and H$_2$O as the reactants.[30] The reaction sequence was (1-40-1-40). Figure 5b shows the mass gain during three sequential HfF$_4$ ALD cycles at 150°C using the reaction sequence (1-40-1-40). These three cycles were the 98th, 99th, and 100th HfF$_4$ ALD cycles in Figure 5a. The mass changes shows very distinct steps. The mass increase after the TDMAH exposure is ΔM_{TDMAH} = 58.4 ng/(cm^2 cycle). The mass change after the HF exposure is ΔM_{HF} = -1.2 ng/(cm^2 cycle). The MGPC was 57.2 ng/(cm^2 cycle). ΔM_{TDMAH}/MGPC ratio averaged from 100-200 cycles of HfF$_4$ ALD using a reaction sequence of (1-40-1-40) was 1.0. The growth rate for HfF$_4$ decreases at higher temperatures. The progressive decrease in the HfF$_4$ ALD growth rate could be explained by the loss of surface species responsible for growth at higher temperature.

The growth rates determined from *ex situ* XRR and SE measurements. HfF$_4$ film was grown on Si wafer using 400 cycles of TDMAH and HF reaction at 150°C. XRR and SE measured the film thickness of HfF$_4$ ALD as 320 Å and 339 Å respectively. These thicknesses were consistent with 0.80 Å / cycle and 0.85 Å / cycle. The MGPC 57.2 ng/(cm^2 cycle) obtained by *in situ* QCM can be converted to the growth rate in Å /cycle using the film density. XRR also measured the film has density of 6.8 g/cm^3. This converted growth rate was 0.84 Å / cycle. The agreement between the *in situ* and *ex situ* measurements of the growth rate is very good. This
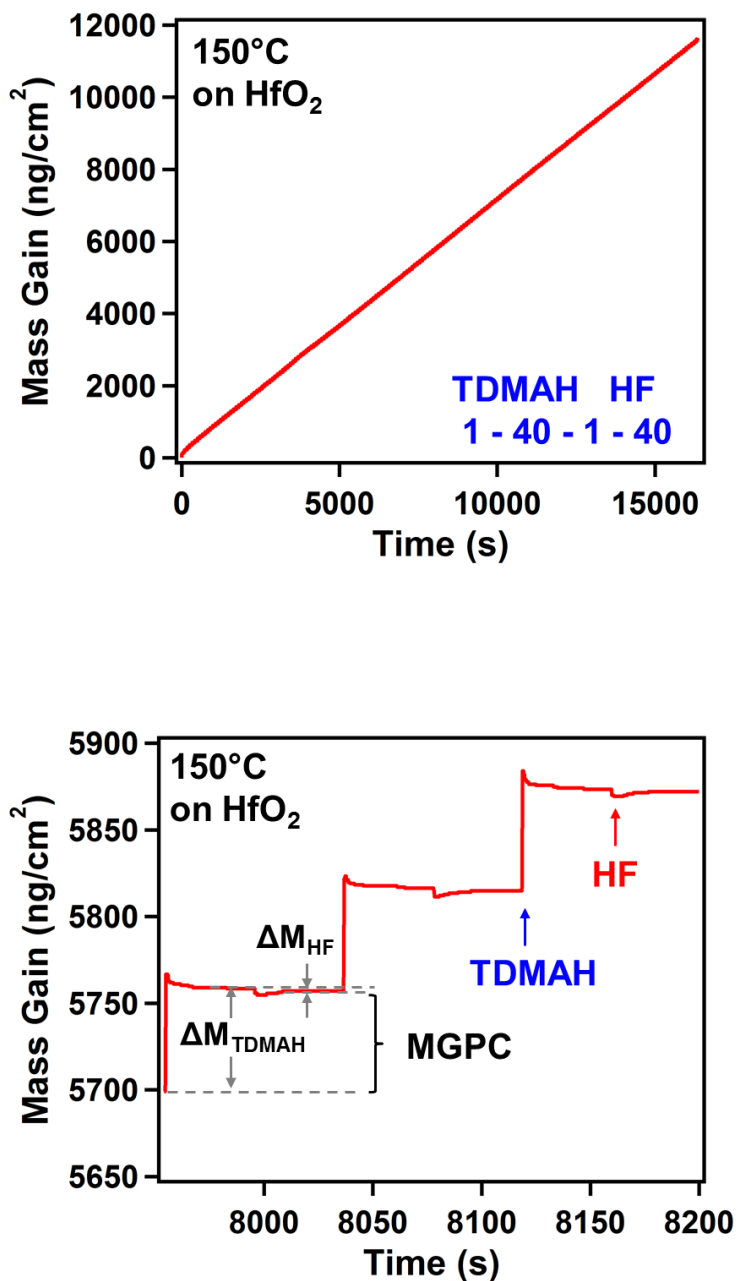
Figure 4-5. (a) Mass gain versus time during 200 HfF_4 ALD cycles with TDMAH and HF as the reactants on HfO_2 at 150 °C using the reaction sequence of (1-40-1-40); (b) Enlargement of mass gain versus time for three sequential TDMAH and HF exposures during HfF_4 ALD in the steady-state, linear growth regime.

density of 6.8 g/cm^3 is ~96 % of the bulk density of 7.1 g /cm^3 for crystalline HfF$_4$.[31] The

surface roughness was measured as 5 Å by XRR. SE determined the refractive index of 1.55 at

589 nm and were obtained using the Sellmeier model. The measured refractive index of n=1.55

is consistent with e-beam evaporated HfF$_4$ n=1.57 at 600 nm [2] sputtered HfF$_4$ film n=1.59[34] at

600 nm n=1.62,[1] for e-beam grown HfF$_4$ film at 600 nm. The HfF$_4$ ALD films were also stable

in air. The thickness, film density, and film roughness of HfF$_4$ films did not change after storage

in atmosphere for one month.

4.3D. Growth of MnF$_2$ Films Using Bis(ethylcyclopentadienyl)manganese (Mn(EtCp)$_2$) and HF

Figure 6a shows the QCM measurements of mass gain during 200 cycles of MnF$_2$ ALD

at 150°C using Bis(ethylcyclopentadienyl) manganese (Mn(EtCp)$_2$) and HF. The initial layer on

the QCM sensor was a MnO ALD film grown with 200 cycles of MnO ALD using Mn(EtCp)$_2$

and H$_2$O as the reactants. [35] The reaction sequence was (1-40-1-40). Nucleation over ~40 cycles

was observed. Figure 6b shows the mass gain during three sequential MnF$_2$ ALD cycles at

150°C using the reaction sequence (1-40-1-40). These three cycles were the 98th, 99th, and

100th MnF$_2$ ALD cycles in Figure 6a. The mass changes shows very distinct steps. The mass

increase after the Mn(EtCp)$_2$ exposure is $\Delta M_{Mn(EtCp)2}$ = 40.8 ng/(cm^2 cycle). The mass loss after

the HF exposure is ΔM_{HF} = -25.2 ng/(cm^2 cycle). The MGPC was 15.6 ng/(cm^2 cycle).

$\Delta M_{Mn(EtCp)2}$/MGPC ratio averaged from 100-200 cycles of MnF$_2$ ALD using a reaction sequence

of (1-40-1-40) was 2.6.

The growth rates determined from *ex situ* XRR and SE measurements. MnF$_2$ film was
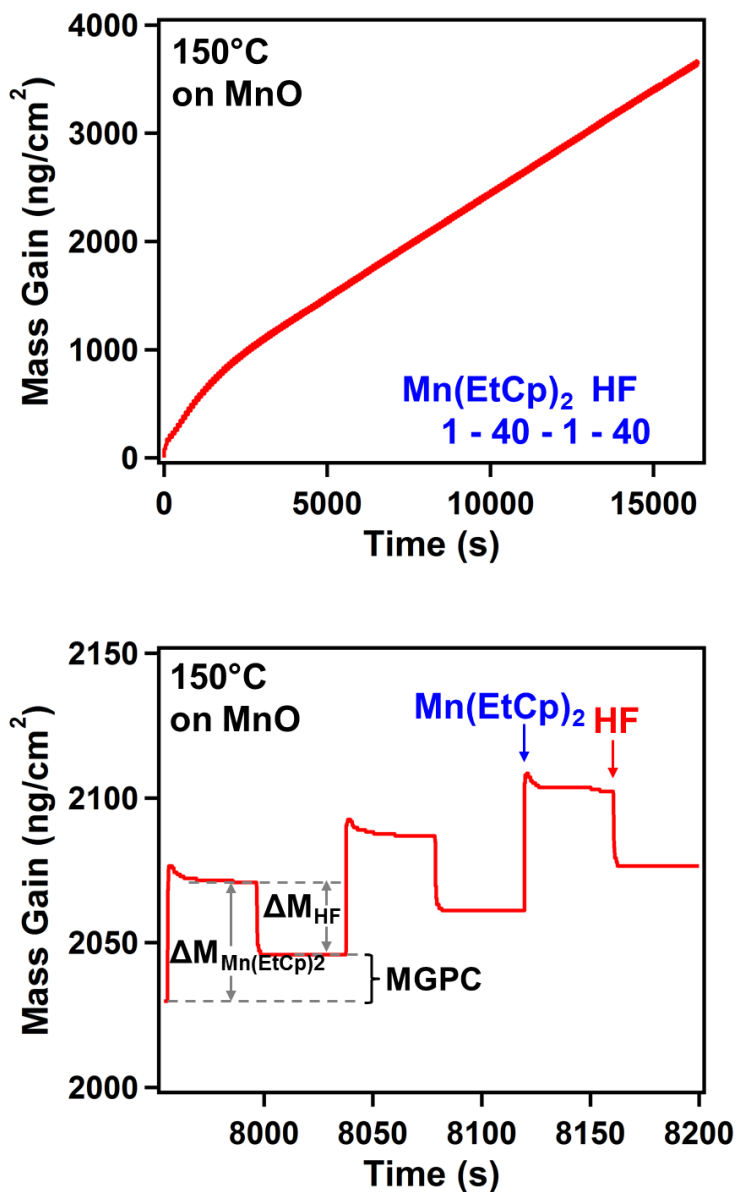
Figure 4-6. (a) Mass gain versus time during 200 MnF$_2$ ALD cycles with Mn(EtCp)$_2$ and HF as the reactants on MnO at 150 °C using the reaction sequence of (1-40-1-40); (b) Enlargement of mass gain versus time for three sequential Mn(EtCp)$_2$ and HF exposures during MnF$_2$ ALD in the steady-state, linear growth regime.

grown on Si wafer using 400 cycles of Mn(EtCp)$_2$ and HF reaction at 150°C. XRR and SE

measured the film thickness of MnF$_2$ ALD as 172 Å and 179 Å respectively. These thicknesses

were consistent with 0.43 Å / cycle and 0.45 Å / cycle. The MGPC 15.6 ng/(cm^2 cycle) obtained

by *in situ* QCM can be converted to the growth rate in Å /cycle using the film density. XRR also

measured the film has density of 3.8 g/cm^3. This converted growth rate was 0.41 Å / cycle. The

agreement between the *in situ* and *ex situ* measurements of the growth rate is very good. This

density of 3.8 g/cm^3 is ~95 % of the bulk density of 3.98 g /cm^3 for crystalline MnF$_2$.[31] The

surface roughness was measured as 26 Å by XRR. This high surface roughness suggests the

MnF$_2$ ALD film is crystalline. SE determined the refractive index of 1.50 at 589 nm and were

obtained using the Sellmeier model. The measured refractive index of n=1.50 is consistent with

the refractive index n=1.47-1.50 for MnF$_2$[36] at 589nm. The MnF$_2$ ALD films were also stable in

air. The thickness, film density, and film roughness of MnF$_2$ films did not change after storage

in atmosphere for one month.

4.3E. Growth of MgF$_2$ Using Films Bis(ethylcyclopentadienyl)magnesium (Mg(EtCp)$_2$) and HF

Figure 7a shows the QCM measurements of mass gain during 200 cycles of MgF$_2$ ALD at

150°C using Bis(ethylcyclopentadienyl) manganese (Mg(EtCp)$_2$) and HF. The initial layer on the

QCM sensor was a MgO ALD film grown with 200 cycles of MgO ALD using Mg(EtCp)$_2$ and

H$_2$O as the reactants.[37] The reaction sequence was (1-40-1-40). Figure 7b shows the mass gain

during three sequential MgF$_2$ ALD cycles at 150°C using the reaction sequence (1-40-1-40). These

three cycles were the 98th, 99th, and 100th MgF$_2$ ALD cycles in Figure 7a. The mass changes
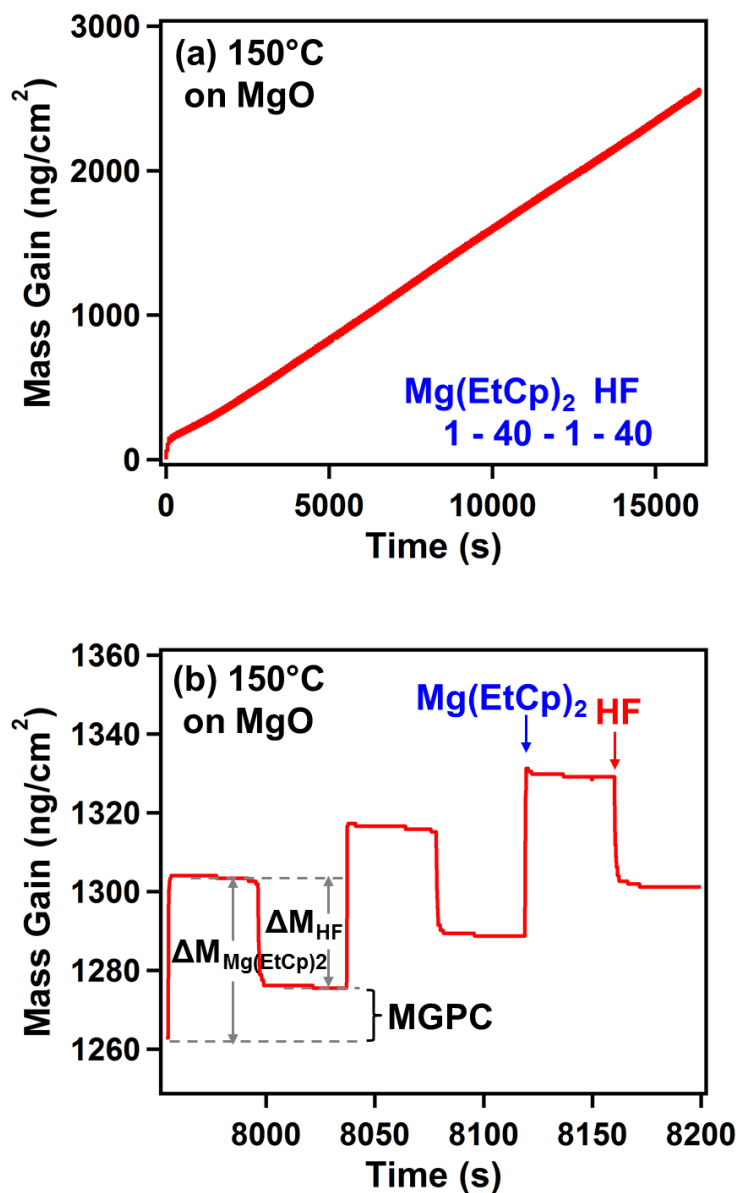
Figure 4-7. (a) Mass gain versus time during 200 MgF$_2$ ALD cycles with Mg(EtCp)$_2$ and HF as the reactants on MgO at 150 °C using the reaction sequence of (1-40-1-40); (b) Enlargement of mass gain versus time for three sequential Mg(EtCp)$_2$ and HF exposures during MgF$_2$ ALD in the steady-state, linear growth regime.

shows very distinct steps. The mass increase after the $Mg(EtCp)_2$ exposure is $\Delta M_{Mg(EtCp)2} = 39.5$ ng/(cm^2 cycle). The mass loss after the HF exposure is $\Delta M_{HF} = -27.2$ ng/(cm^2 cycle). The MGPC was 12.3 ng/(cm^2 cycle). $\Delta M_{Mg(EtCp)2}$/MGPC ratio averaged from 100-200 cycles of MgF_2 ALD using a reaction sequence of (1-40-1-40) was 3.2.

The growth rates determined from *ex situ* XRR and SE measurements. MgF_2 film was grown on Si wafer using 400 cycles of $Mg(EtCp)_2$ and HF reaction at 150°C. XRR and SE measured the film thickness of MgF_2 ALD as 154 Å and 153 Å respectively. These thicknesses were consistent with 0.39 Å / cycle and 0.38 Å / cycle. The MGPC 12.3 ng/(cm^2 cycle) obtained by *in situ* QCM can be converted to the growth rate in Å /cycle using the film density. XRR also measured the film has density of 3.1 g/cm^3. This converted growth rate was 0.40 Å / cycle. The agreement between the *in situ* and *ex situ* measurements of the growth rate is very good. This density of 3.1 g/cm^3 is ~98 % of the bulk density of 3.15 g /cm^3 for crystalline MgF_2.[31] The surface roughness was measured as 12 Å by XRR. This high surface roughness suggests the MgF_2 ALD film is crystalline.   SE determined the refractive index of n=1.40 at 589 nm and were obtained using the Sellmeier model. The measured refractive index of n=1.40 is consistent with the refractive index n=1.38-1.39[36] at 589nm for MgF_2 and n=1.38[34] at 600 nm for the MgF_2 film grown by sputtering. The MgF_2 ALD films were also stable in air. The thickness, film density, and film roughness of MgF_2 films did not change after storage in atmosphere for one month.
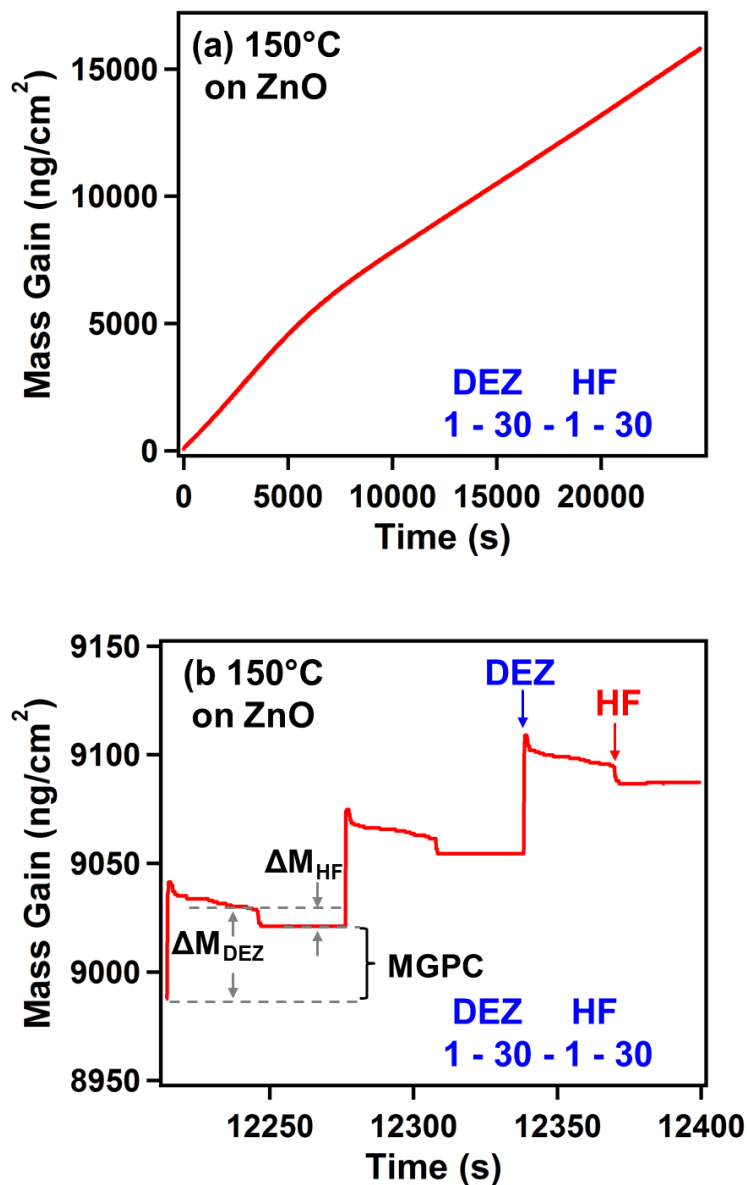
Figure 4-8. (a) Mass gain versus time during 400 ZnF_2 ALD cycles with DEZ and HF as the reactants on ZnO at 150 °C using the reaction sequence of (1-30-1-30); (b) Enlargement of mass gain versus time for three sequential DEZ and HF exposures during ZnF_2 ALD in the steady-state, linear growth regime.

sequence was (1-30-1-30). Figure 8b shows the mass gain during three sequential ZnF_2 ALD cycles at 150°C using the reaction sequence (1-30-1-30). These three cycles were the 198th, 199th, and 200th ZnF_2 ALD cycles in Figure 8a. The mass changes shows very distinct steps. The mass increase after the DEZ exposure is $\Delta M_{DEZ} = 41.4$ ng/(cm^2 cycle). The mass loss after the HF exposure is $\Delta M_{HF} = -7.9$ ng/(cm^2 cycle). The MGPC was 33.5 ng/(cm^2 cycle). ΔM_{DEZ}/MGPC ratio averaged from 200-400 cycles of ZnF_2 ALD using a reaction sequence of (1-30-1-30) was 1.2.

The growth rates determined from *ex situ* XRR and SE measurements. ZnF_2 film was grown on Si wafer using 400 cycles of DEZ and HF reaction at 150°C. XRR and SE measured the film thickness of ZnF_2 ALD as 357Å and 336Å respectively. These thicknesses were consistent with 0.89 Å / cycle and 0.84 Å / cycle. The MGPC 33.5 ng/(cm^2 cycle) obtained by *in situ* QCM can be converted to the growth rate in Å /cycle using the film density. XRR also measured the film has density of 4.9 g/cm^3. This converted growth rate was 0.68 Å / cycle. The disagreement between the *in situ* and *ex situ* measurements of the growth rate suggests the surface enhanced nucleation. This density of 4.9 g/cm^3 is ~100 % of the bulk density of 4.9 g /cm^3 for crystalline ZnF_2.[31] The surface roughness was measured as 44 Å by XRR. This high surface roughness suggests the ZnF_2 ALD film is crystalline. SE determined the refractive index of 1.49 at 589 nm and were obtained using the Sellmeier model. The refractive index of n=1.50-1.53 for ZnF_2[36] at 589nm. The ZnF_2 ALD films were stored in the desiccator until the *ex situ* measurements due to the known instability in air.

4.3G. Reaction Mechanism and Stoichiometry.

Figure 9 presents a schematic showing the proposed reaction mechanism for ZrF_4. In reaction A, TEMAZ, $Zr(NEtMe)_4$ molecules react with HF molecules adsorbed on the surface to yield $ZrF_2(NEtMe)_2$ and HNEtMe molecules as the reaction products. The $ZrF_2(NEtMe)_2$ species remain adsorbed on the surface. In reaction B, HF converts the adsorbed $ZrF_2(NEtMe)_2$ species to ZrF_4. HNEtMe is again a reaction product and additional HF molecules may remain on the surface.

The more general surface chemistry for ZrF_4ALD can be expressed by:

(A) $ZrF_4|xHF^* + Zr(NEtMe)_4 \qquad \rightarrow ZrF_4| ZrF_x(NEtMe)_{4-x}^* + x$ HNEtMe   (2)

(B) $ZrF_4| ZrF_x(NEtMe)_{4-x}^* + 4HF \rightarrow ZrF_4|ZrF_4|xHF^* + (4-x)CH_4$ (3)

The asterisks designate the surface species. The vertical lines distinguish the various surface species. The parameter x quantifies the number of HF molecules adsorbed on the surface relative to the number of ZrF_4 species deposited during one Metal fluorides ALD cycle. $x=2$ indicates one HF per ZrF_4 on the surface as shown in Figure 9.

Based on this surface chemistry, the ΔM_{TEMAZ}/MGPC ratio can be determined by:

$$\frac{\Delta M_{TEMAZ}}{MGPC} = \frac{\Delta M_{TEMAZ}}{\Delta M_{TEMAZ} + \Delta M_{HF}} = \frac{M_{TEMAZ} - x \cdot M_{HNEtMe}}{M_{ZrF4}} \qquad (4)$$

In equation 4, M_{TEMAZ}, M_{HF}, M_{NEtMe}, and M_{ZrF4} are the molar masses of TEMAZ, HF, HNEtMe, and ZrF_4 respectively. The equation for x is:

$$x = \frac{1}{M_{HNEtMe}} [M_{TEMAZ} - M_{ZrF_4}(\frac{\Delta M_{TEMAZ}}{MGPC})] = \frac{1}{59.1}[323.6 - 167.2(\frac{\Delta M_{TEMAZ}}{MGPC})] \qquad (5)$$

Figure 4-9. Proposed reaction mechanism for ZrF$_4$ ALD using TEMAZ and HF as the reactants.

The ΔM_{TEMAZ}/MGPC ratio and x can be determined from the mass changes obtained by the QCM measurements. A ΔM_{TEMAZ}/MGPC ratio of 1.1 was determined from the QCM measurements at 150°C shown in Figure 2b. This ratio of 1.1 is close to the ratio of 1.2 based on the proposed mechanism in Figure 9 where x=2. These values are summarized in Table 2. An x value of nearly x=2.0~2.4 is observed for HfF_4 and ZrF_4. An x= 0.78 for AlF_3.

ZrF_4 is strong Lewis acid.[38] The F in HF can act as a Lewis base. Together ZrF_4 and HF have a strong Lewis acid-base interaction. TEMAZ are also Lewis acids. The F in Zr-F* species on the surface can act as a Lewis base. A strong Lewis acid-base interaction is also expected between Zr-F* and either TEMAZ. HfF_4 and AlF_3 are also strong Lewis acids, which follow the same trend as ZrF_4.[23,24] ZrF_4 and HfF_4.[38] Figure 10 represents a schematic showing the proposed reaction mechanism for MnF_2. In reaction A, $Mn(EtCp)_2$ molecules adsorbed on the MnF_2 surface. In reaction B, HF converts the adsorbed $Mn(EtCp)_2$ species to MnF_2. xHCpEt is a reaction product and additional HF molecules may remain on the surface.

The more general surface chemistry for MnF_2 ALD can be expressed by:
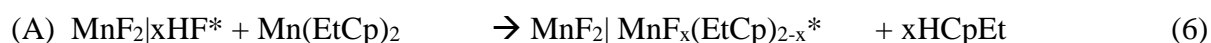
(A) $MnF_2|xHF* + Mn(EtCp)_2 \rightarrow MnF_2| MnF_x(EtCp)_{2-x}* + xHCpEt$ (6)

(B) $MnF_2| MnF_x(EtCp)_{2-x}* + 2HF \rightarrow MnF_2|MnF_2|xHF* + (2-x) HCpEt$ (7)

The asterisks designate the surface species. The vertical lines distinguish the various surface species. The parameter x quantifies the number of HF molecules adsorbed on the surface relative to the number of MnF_2 species deposited during one MnF_2 ALD cycle. x=0 indicates no HF per MnF_2 on the surface as shown in Figure 10.

Based on this surface chemistry, the $\Delta M_{Mn(EtCp)2}$/MGPC ratio can be determined by:
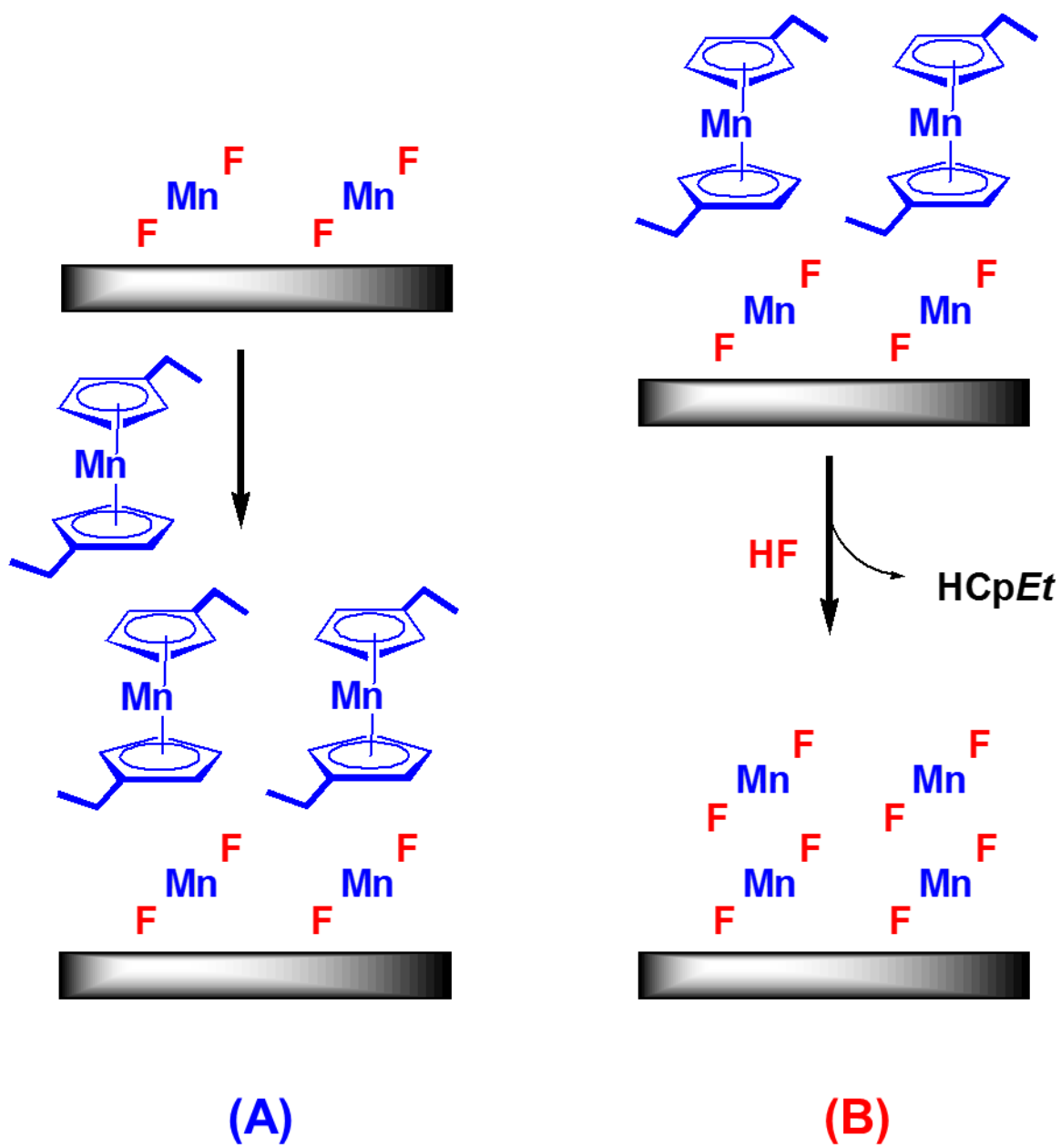
Figure 4-10. Proposed reaction mechanism for MnF$_2$ ALD using Mn(EtCp)$_2$ and HF as the reactants.

$$\frac{\Delta M_{Mn(EtCp)2}}{MGPC} = \frac{\Delta M_{Mn(EtCp)2}}{\Delta M_{Mn(EtCp)2}+\Delta M_{HF}} = \frac{M_{Mn(EtCp)2}-x\cdot M_{HCpEt}}{M_{MnF2}} \quad (8)$$

In equation 8, $M_{Mn(EtCp)2}$, M_{HF}, M_{HCpEt}, and M_{MnF2} are the molar masses of Mn(EtCp)$_2$, HF, HCpEt, and MnF$_2$ respectively.

The equation for x is:

$$x = \frac{1}{M_{HCpEt}}[M_{Mn(EtCp)2} - M_{MnF2}(\frac{\Delta M_{Mn(EtCp)2}}{MGPC})] = \frac{1}{94.2}[241.2 - 92.9(\frac{\Delta M_{Mn(EtCp)2}}{MGPC})] \quad (9)$$

The $\Delta M_{Mn(EtCp)2}$/MGPC ratio and x can be determined from the mass changes obtained by the QCM measurements. A $\Delta M_{Mn(EtCp)2}$/MGPC ratio of 2.6 was determined from the QCM measurements at 150°C. This ratio of 2.6 is close to the ratio of 2.6 based on the proposed mechanism in Figure10 where x=0. x values ≈ 0 for MgF$_2$, MnF$_2$, and ZnF$_2$, and LiF.

MnF$_2$ is a weak Lewis acid. MnF$_2$ can not interact with F in HF. The F in Mn-F* species on the surface can act as a Lewis base. A Lewis acid-base interaction is expected between Mn-F* and Mn(EtCp)$_2$.

MgF$_2$ is also weak Lewis acid.[39] Lewis acidity of ZnF$_2$ is lower than MgF$_2$:[40] LiF is weak Lewis base.[39] MgF$_2$, ZnF$_2$, and LiF have little interaction with F in HF. There is not enough room for HF coordination on metal fluorides such as MnF$_2$ and MgF$_2$, and LiF. Metal fluorides such as MnF$_2$ and MgF$_2$ do not have a strong Lewis acid-base interaction with HF. Mn(EtCp)$_2$ and Mn(EtCp)$_2$ are not strong Lewis acids. LiHMDS is a Lewis base.

4.3H. *Ex situ* Film Characterization Using XRR, SE, and XPS
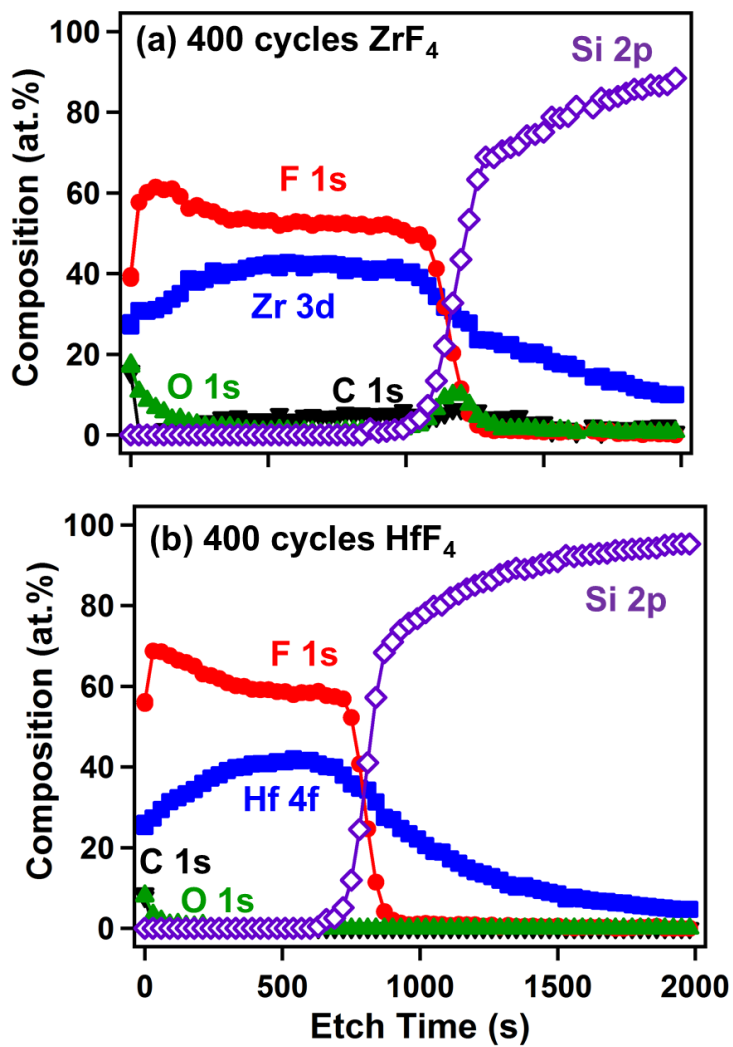
Figure 4-11. Sputter depth profile of (a) ZrF$_4$ film; (b) HfF$_4$ film measured by X-ray

photoelectron spectroscopy.

Figure 11a shows an X-ray photoelectron spectroscopy (XPS) sputter depth profile of an ZrF$_4$ ALD film grown with TEMAZ and HF. Most of the film is zirconium and fluorine after removal of the adventitious surface carbon. Some oxygen impurities >4-5% are detected at the film surface. This may indicate some strong interaction of ZrF$_4$ with the moisture.[41] Oxygen impurities in the bulk film of ~1.1% may result from water that could be produced in the reaction of HF with metal oxide inside the stainless steel reactor. Carbon impurities in the film are detected at ~3.4 at%. Nitrogen impurities are below the detection limit of XPS. The ratio between the calibrated zirconium and fluorine in XPS signals is less than 1:2. This result is consistent with the XPS result of AlF$_3$ and LiF ALD film having off stoichiometry.[23-25] Other techniques such as Rutherford backscattering spectrum (RBS) confirmed that the AlF$_3$ film was stoichiometric even though XPS of AlF$_3$ was not stoichiometric.[23,24] The preferential sputtering of fluorine may explain the low fluorine signals.[13,14,24,42]

ZrF$_4$ ALD film grown with ZTB and HF was also analyzed by XPS sputter depth profile. ZrF$_4$ ALD film grown with ZTB and HF has no carbon in the film. However, oxygen impurities are detected at ~10%. This unexpected high oxygen impurities in the ZrF$_4$ film grown with ZTB precursor may suggest that the inclusion of oxygen originated from alkoxide ligand. ZTB precursor is very moisture sensitive. This may also suggest that the film is not stable to air to form the partial oxide in the fluoride film.

Figure 11b shows an XPS sputter depth profile of an HfF$_4$ ALD film grown with TDMAH and HF. The film consists of entirely hafnium and fluorine after removal of adventitious surface carbon. Oxygen, carbon, and nitrogen impurities are not detected in the HfF$_4$ film. The ratio between the calibrated hafnium and fluorine determined by XPS signals is

less than 1:2.5 again quite off from stoichiometric HfF_4 probably due to the preferential

sputtering of F.

Other metal fluorides films were also analyzed by XPS sputter depth profile. MnF_2 ALD

film has oxygen impurities of ~0.9% in the film. Carbon impurities are not detected in the MnF_2

ALD film. The ratio between the calibrated manganese and fluorine determined by XPS signals

was 1:2.4.

MgF_2 ALD film consists of magnesium and fluorine having oxygen impurities of ~1.0 %

in the film. Carbon impurities are not detected in the MgF_2 film. The ratio between the

calibrated magnesium and fluorine determined by XPS signals was 1:1.3.

The film density of metal fluoride films are determined by XRR and are summarized in

Table 3. All densities of metal fluorides are >93% of the bulk density. More than 100% density

for ZrF_4 grown by ZTB and HF is attributed to ~10% of oxygen impurity in ZrF_4 grown using

ZTB. The density of d= 5.68 g/cm^3 for bulk ZrO_2 is much higher than the density of for bulk

ZrF_4.[31]

Figure 12 shows the refractive indices of the metal fluoride ALD films in the spectral

range between 240 and 1700 nm using the Sellmeier model. The refractive index measured by

SE at 589 nm was also summarized in Table 3. The highest refractive index n=1.55 for ZrF_4

ALD film and n=1.55 for HfF_4 ALD film were obtained grown by TEMAZ and TDMAH

respectively. ZrF_4 ALD film grown by ZTB has higher refractive index n=1.62 due to ~10%

oxygen impurity. Other fluoride films have consistent refractive indices with the reported ones.

The lowest refractive index n=1.36 for AlF_3 ALD film and n=1.37 for LiF ALD film were

obtained.

Metal Fluorides	Metal Precursor	Growth rate at 150°C (Å/cycle)	Density (g/cm^3)	n at 589nm
ZrF_4	TEMAZ	0.9	4.1	1.55
ZrF_4	ZTB	0.6	4.7	1.62
HfF_4	TDMAH	0.8	6.8	1.55
MnF_2	$Mn(EtCp)_2$	0.4	3.8	1.50
MgF_2	$Mg(EtCp)_2$	0.4	3.1	1.40
ZnF_2	DEZ	0.7	4.9	1.49
AlF_3	TMA	1.0	2.9	1.36
LiF	LiHMDS	0.5	2.6	1.37

Table 4-3. Metal fluorides, acronym of metal precursors, growth rate at 150°C, density, and the refractive index.
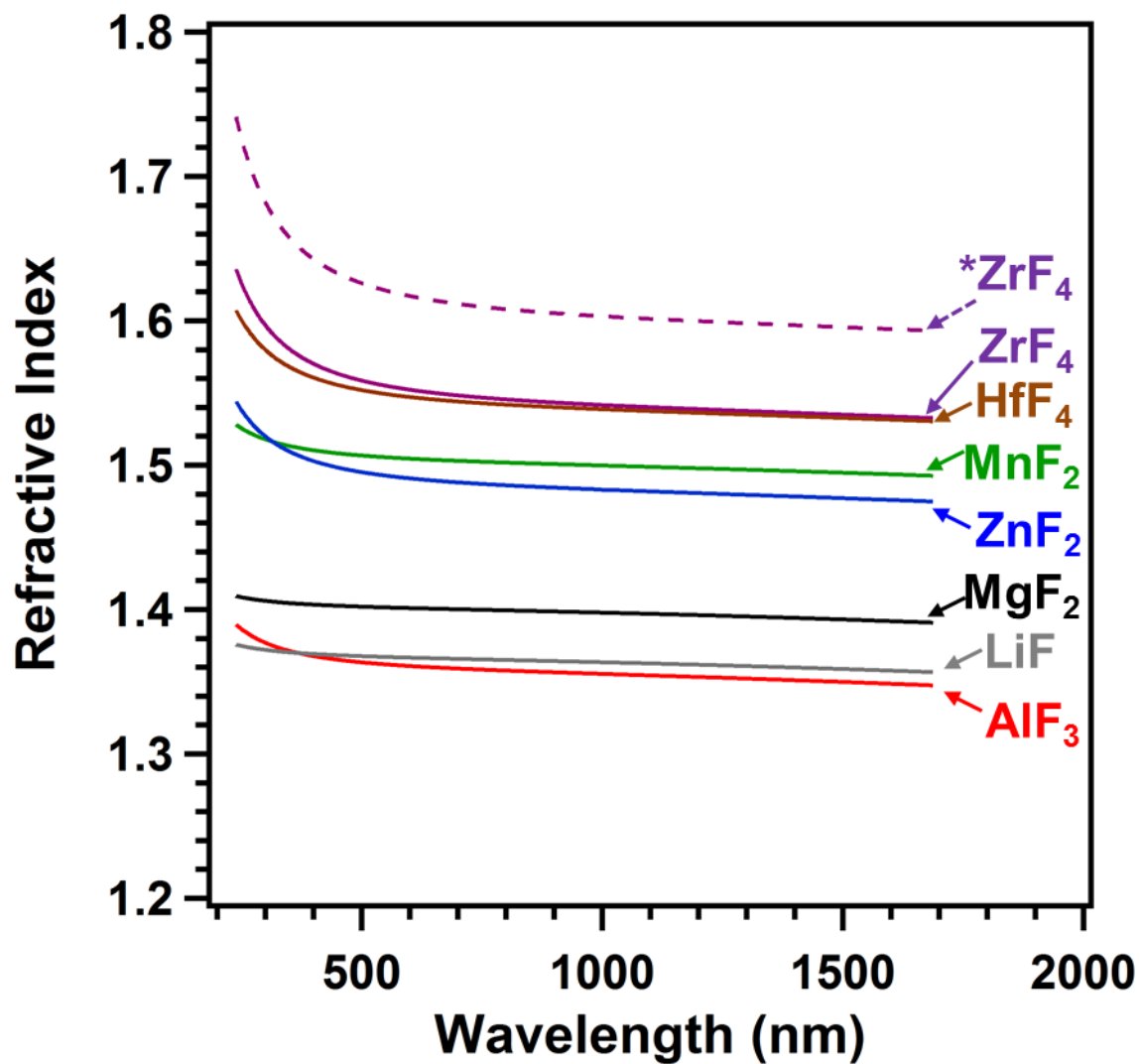
Figure 4-12. Refractive index for metal fluorides ALD films grown at 150 °C in the spectral range between 240 and 1700 nm using the Sellmeier model.

4.4. Conclusions

Metal fluorides ALD films were grown at 150°C using various metal precursors and HF from HF-pyridine as the reactants. The Metal fluorides ALD was examined using *in situ* quartz crystal microbalance (QCM). The growth rate for metal fluorides ALD obtained from *in situ* QCM and *ex situ* X-ray reflectivity (XRR) and spectroscopic ellipsometry (SE) measurements showed very good agreements. XPS measurements showed that most of the metal fluorides ALD films were pure fluoride films having little oxygen impurity of ~1 at%. Metal fluorides ALD may be useful for a number of applications such as ultraviolet optical films, and Lewis acid catalytic films.

4.5. Acknowledgements

4.6. References

(1)   Pellicori, S. F.; Colton, E. Thin Solid Films 1992, 209, 109.

(2)   Kruschwitz, J. D. T.; Pawlewicz, W. T. Appl. Opt. 1997, 36, 2157.

(3)   Niisaka, S.; Saito, T.; Saito, J.; Tanaka, A.; Matsumoto, A.; Otani, M.; Biro, R.; Ouchi, C.; Hasegawa, M.; Suzuki, Y.; Sone, K. Appl. Opt. 2002, 41, 3242.

(4)   Herron, N.; Farneth, W. E. Adv. Mater. (Weinheim, Ger.) 1996, 8, 959.

(5)   Kemnitz, E.; Gross, U.; Rudiger, S.; Shekar, C. S. Angewandte Chemie-International Edition 2003, 42, 4251.

(6)   Kemnitz, E.; Menz, D. H. Prog. Solid State Chem. 1998, 26, 97.

(7)   Taki, Y. Vacuum 2004, 74, 431.

(8)   Iwahori, K.; Furuta, M.; Taki, Y.; Yamamura, T.; Tanaka, A. Appl. Opt. 2006, 45, 4598.

(9)   Heitmann, W. Thin Solid Films 1970, 5, 61.

(10)   Lee, C. C.; Liu, M. C.; Kaneko, M.; Nakahira, K.; Takano, Y. Appl. Opt. 2005, 44, 7333.

(11)   Barriere, A. S.; Lachter, A. Appl. Opt. 1977, 16, 2865.

(12)   Bridou, F.; Cuniot-Ponsard, M.; Desvignes, J. M.; Richter, M.; Kroth, U.; Gottwald, A. Opt. Commun. 2010, 283, 1351.

(13)   Schink, H.; Kolbe, J.; Zimmermann, F.; Ristau, D.; Welling, H. In Proc. SPIE 1990; Vol. Laser-Induced Damage in Optical Materials, p 327.

(14)   Targove, J. D.; Bovard, B. G.; Lingg, L. J.; Macleod, H. A. Thin Solid Films 1988, 159, L57.

(15)   George, S. M. Chem Rev 2010, 110, 111.

(16)   Ylilammi, M.; Rantaaho, T. J. Electrochem. Soc. 1994, 141, 1278.

(17)   Pilvi, T.; Hatanpaa, T.; Puukilainen, E.; Arstila, K.; Bischoff, M.; Kaiser, U.; Kaiser, N.; Leskela, M.; Ritala, M. J. Mater. Chem. 2007, 17, 5077.

(18)   Pilvi, T.; Puukilainen, E.; Kreissig, U.; Leskela, M.; Ritala, M. Chem. Mater. 2008, 20, 5023.

(19)   Pilvi, T.; Puukilainen, E.; Arstila, K.; Leskela, M.; Ritala, M. Chem. Vap. Deposition 2008, 14, 85.

(20)   Pilvi, T.; Puukilainen, E.; Munnik, F.; Leskela, M.; Ritala, M. Chem. Vap. Deposition 2009, 15, 27.

(21)   Mantymaki, M.; Hamalainen, J.; Puukilainen, E.; Munnik, F.; Ritala, M.; Leskela, M. Chem. Vap. Deposition 2013, 19, 111.

(22)   Putkonen, M.; Szeghalmi, A.; Pippel, E.; Knez, M. J. Mater. Chem. 2011, 21, 14461.

(23)   Lee, Y.; Cavanagh, A. S.; George, S. M. Atomic Layer Deposition of AlF3 Using Trimethylaluminum and Hydrogen Fluoride-Pyridine, Proceedings of the 13th International Conference on Atomic Layer Deposition, San Diego, California, July 28-31, 2013.

(24)   Lee, Y.; DuMont, J. W.; Cavanagh, A. S.; George, S. M. Submitted to Journal of Physical Chemistry C 2015.

(25)   Lee, Y.; Piper, D. M.; Cavanagh, A. S.; Young, M. J.; Lee, S.-H.; George, S. M. Atomic Layer Deposition of Lithium Ion Conducting (AlF3)(LiF)x Alloys Using Trimethylaluminum, Lithium Hexamethyldisilazide and Hydrogen Fluoride-Pyridine, Proceedings of the 14th International Conference on Atomic Layer Deposition, Kyoto, Japan, June 15-18, 2014.

(26)   Elam, J. W.; Groner, M. D.; George, S. M. Rev. Sci. Instrum. 2002, 73, 2981.

(27)   Lee, Y.; Yoon, B.; Cavanagh, A. S.; George, S. M. Langmuir 2011, 27, 15155.

(28)   Olah, G. A.; Nojima, M.; Kerekes, I. Synthesis-Stuttgart 1973, 779.

(29)   D. Shannon, R.; Shannon, R. C.; Medenbach, O.; Fischer, R. X. J. Phys. Chem. Ref. Data 2002, 31, 931.

(30)   Hausmann, D. M.; Kim, E.; Becker, J.; Gordon, R. G. Chem. Mater. 2002, 14, 4350.

(31)   CRC Handbook of Chemistry and Physics; 85th ed.; Lide, D. R., Ed.; CRC Press: Boca Raton, FL, 2005.

(32)   Almeida, R. M.; Morais, P. J. J. Non-Cryst. Solids 1995, 184, 93.

(33)   Kukli, K.; Ritala, M.; Leskela, M. Chem. Vap. Deposition 2000, 6, 297.

(34)   Martin, P. M.; Olsen, L. C.; Johnston, J. W.; Depoy, D. M. Thin Solid Films 2002, 420, 8.

(35)   Burton, B. B.; Fabreguette, F. H.; George, S. M. Thin Solid Films 2009, 517, 5658.

(36)   Shannon, R. D.; Shannon, R. C.; Medenbach, O.; Fischer, R. X. J. Phys. Chem. Ref. Data 2002, 31, 931.

(37)   Burton, B. B.; Goldstein, D. N.; George, S. M. J. Phys. Chem. C 2009, 113, 1939.

(38)   Benjamin, S. L.; Levason, W.; Pugh, D.; Reid, G.; Zhang, W. J. Dalton Trans. 2012, 41, 12548.

(39)   Molten Salt Chemistry: An Introduction and Selected Applications; Mamantov, G.; Marassi, R., Eds., 1987; Vol. 202

(40)   Guo, Y.; Wuttke, S.; Vimont, A.; Daturi, M.; Lavalley, J. C.; Teinz, K.; Kemnitz, E. J. Mater. Chem. 2012, 22, 14587.

(41)   Waters, T. N. J. Inorg. Nucl. Chem. 1960, 15, 320.

(42)   Allen, T. H.; Lehan, J. P.; Larry C. McIntyre, J. In Proc. SPIE 1990; Vol. Optical Thin Films III: New Developments, p 277

CHAPTER 5

Atomic Layer Etching of Al₂O₃ Using Sequential, Self-Limiting Thermal Reactions with Sn(acac)₂ and HF

5.1. Introduction

Atomic layer deposition (ALD) is a thin film growth technique based on sequential, self-limiting surface reactions.[1] ALD can deposit extremely conformal thin films with atomic layer control. ALD has developed rapidly over the last 10-15 years to meet many industrial needs such as the miniaturization of semiconductor devices.[1] ALD can deposit a wide range of materials from metal oxides to metals.[2] ALD is typically accomplished using thermal chemistry. However, sometimes plasma ALD is employed to enhance the surface reactions.[3]

In contrast, atomic layer etching (ALE) is a thin film removal technique based on sequential, self-limiting surface reactions.[4-6] ALE can be viewed as the reversal of ALD. ALE should be able to remove thin films conformally and isotropically with atomic layer control. Compared with the large number of ALD processes,[2] ALE processes have not been defined for as many materials. In addition, no thermal chemical processes have been reported for ALE. The ALE processes that have been reported have used excitation such as ion-enhanced or energetic

noble gas atom-enhanced surface reactions.[4-6] Most of the reported ALE processes have adsorbed a halogen on the surface of the material. Ion or noble gas atom bombardment is then used to desorb halogen compounds that etch the material.[4-6]

Most of the reports of ALE have focused on the ALE of Si, Ge, compound semiconductors, oxides and carbon substrates. Si ALE has been accomplished using either Cl or F adsorption that is subsequently followed by the removal of silicon halides using Ar^+ ion bombardment.[5-10] Very similar approaches are employed for Ge ALE.[11-12] Alternative approaches for Si ALE utilize energetic neutral Ar beam bombardment.[13] GaAs ALE has been demonstrated using Cl adsorption followed by excitation with either Ar^+ ions,[14] 100 eV electrons,[15] or UV radiation.[16-17] InP ALE has also been accomplished using Cl adsorption and energetic neutral Ne beam bombardment.[18]

The ALE of a variety of oxides have been reported based on the adsorption of Cl using BCl_3 and the removal of chloride compounds using an energetic Ar atom neutral beam. This approach has been used for the ALE of Al_2O_3,[19] HfO_2,[20] ZrO_2,[21] and TiO_2.[22] SiO_2 ALE has also been performed using fluorocarbon adsorption followed by Ar^+ ion bombardment.[23-24] The ALE of various carbon substrates have also been accomplished using oxygen radical adsorption followed by material removal using Ar^+ ion bombardment or an energetic Ar neutral beam. This approach has been demonstrated for graphite,[25] graphene[26] and polymer material.[27]

Developing thermal self-limiting ALE reactions that are the reversal of ALD reactions will be difficult. Thermal ALD reactions are typically exothermic and extremely favorable thermochemical reactions.[1] These thermal reactions are spontaneous with negative ΔG values where G is the Gibbs free energy. Performing ALD reactions in reverse will not occur because of these thermodynamic considerations. The challenge for thermal ALE reactions is to find

alternative, self-limiting, reactions with different reactants that are exothermic and display

negative ΔG values to ensure a spontaneous reaction.

In this paper, sequential exposures of tin(II) acetylacetonate ($Sn(acac)_2$) and hydrogen

fluoride (HF) are employed for the thermal ALE of Al_2O_3. The thermal Al_2O_3 ALE reactions are

examined using quartz crystal microbalance (QCM) studies. The Al_2O_3 film thicknesses are

measured using x-ray reflectivity (XRR) analysis. The QCM and XRR measurements can

determine if the Al_2O_3 etching is linear versus the number of $Sn(acac)_2$ and HF reaction cycles.

The QCM measurements can evaluate whether the Al_2O_3 ALE is self-limiting versus the

$Sn(acac)_2$ and HF exposure times. This new method for ALE based on sequential, self-limiting,

thermal reactions with $Sn(acac)_2$ and HF as the reactants broadens the strategies for ALE

reactions.

5.2. Results & Discussion

Figure 1 shows the mass change during 100 ALE cycles of $Sn(acac)_2$ and HF reactions on

an Al_2O_3 surface at 200°C. The initial Al_2O_3 ALD film on the QCM surface was prepared by

100 cycles of Al_2O_3 ALD using TMA and H_2O at 200°C. One ALE cycle consisted of a

$Sn(acac)_2$ dose of 1 s, an N_2 purge of 30 s, a HF dose of 1 s, and a second N_2 purge of 30 s. This

reaction sequence is denoted as 1-30-1-30. Pressure transients during $Sn(acac)_2$ and HF doses

were 20 mTorr and 80 mTorr, respectively.

The etching of the Al_2O_3 film in Figure 1 is very linear and displays a mass change per

cycle (MCPC) = -8.4 $ng/(cm^2$ cycle). This MCPC corresponds to an etch rate of 0.28 Å /cycle

based on the Al_2O_3 ALD film density of 3.0 g/cm^3 measured by XRR. All ALE cycles show

mass loss resulting from the etching of the Al_2O_3 film except during the first ALE cycle. The first cycle displays mass gains of $\Delta M_{Sn} = 57$ ng/cm^2 and $\Delta M_{HF} = 13$ ng/cm^2.

The mass gain for ΔM_{Sn} on the first cycle is attributed to $Sn(acac)_2$ adsorption on the hydroxylated Al_2O_3 surface. $Sn(acac)_2$ could adsorb either molecularly as $Sn(acac)_2$* or dissociatively as $Sn(acac)$* and $(acac)$* where the asterisks designate a surface species. This adsorption would lead to a mass increase. In addition, the mass gain for ΔM_{HF} on the first cycle is attributed to the formation of AlF_3 by the reaction of HF with the underlying Al_2O_3 surface. The reaction $Al_2O_3 + 6HF \rightarrow 2AlF_3 + 3H_2O$ is spontaneous with $\Delta G= -58$ kcal at 200°C.[28] AlF_3 formation has also been confirmed by *in situ* Fourier transform infrared (FTIR) spectroscopy studies that will be presented in another publication.[29] The first cycle of $Sn(acac)_2$ and HF exposures establishes the initial $Sn(acac)_2$ and AlF_3 species on the Al_2O_3 substrate.

Figure 2 shows an enlargement of the mass losses versus time at 200°C for three cycles in the steady state linear etching regime in Figure 1. There is a gradual mass decrease after a short mass gain coinciding with the $Sn(acac)_2$ exposure. This behavior suggests $Sn(acac)_2$ adsorption followed by either $Sn(acac)_2$ desorption and/or the removal of reaction products. A mass loss of $\Delta M_{Sn} = -8.1$ ng/cm^2 was observed after 1 s of $Sn(acac)_2$ exposure. In contrast, the HF exposure leads to little mass loss. A mass loss of $\Delta M_{HF} = -0.28$ ng/cm^2 was observed after 1 s of HF exposure.
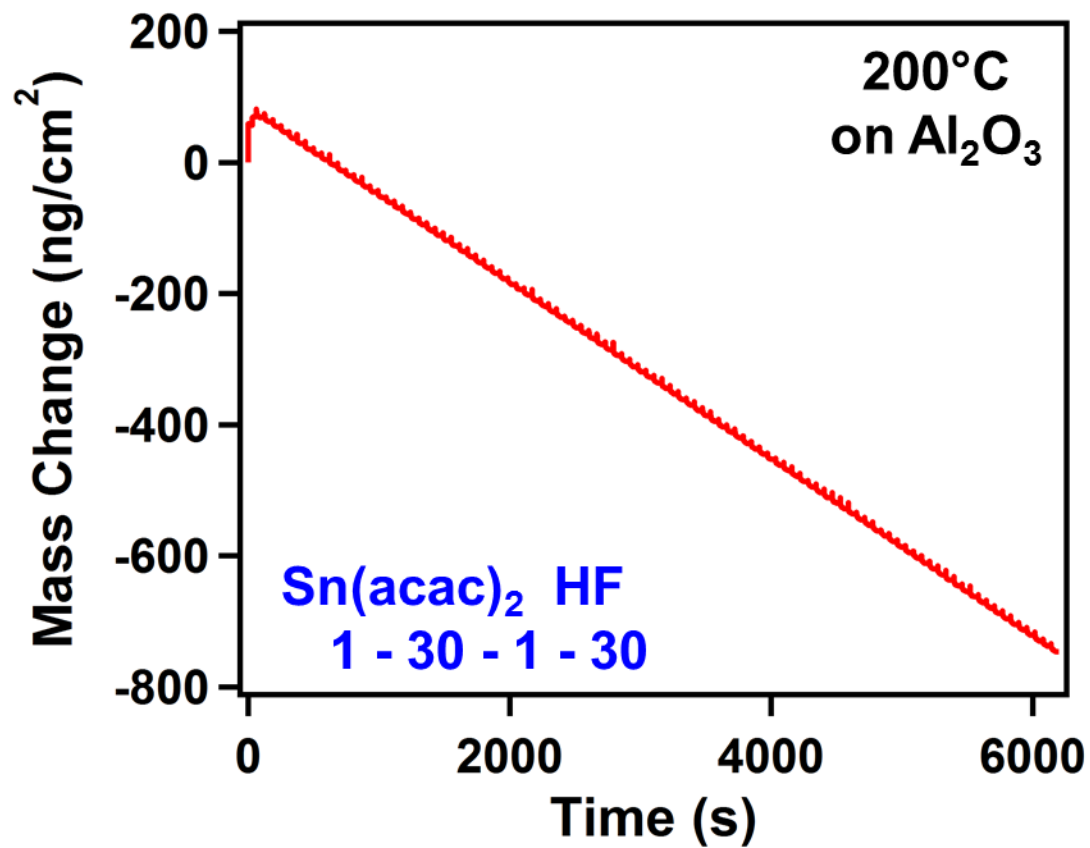
Figure 5-1   Mass change versus time for Al₂O₃ ALE using sequential Sn(acac)₂ and HF
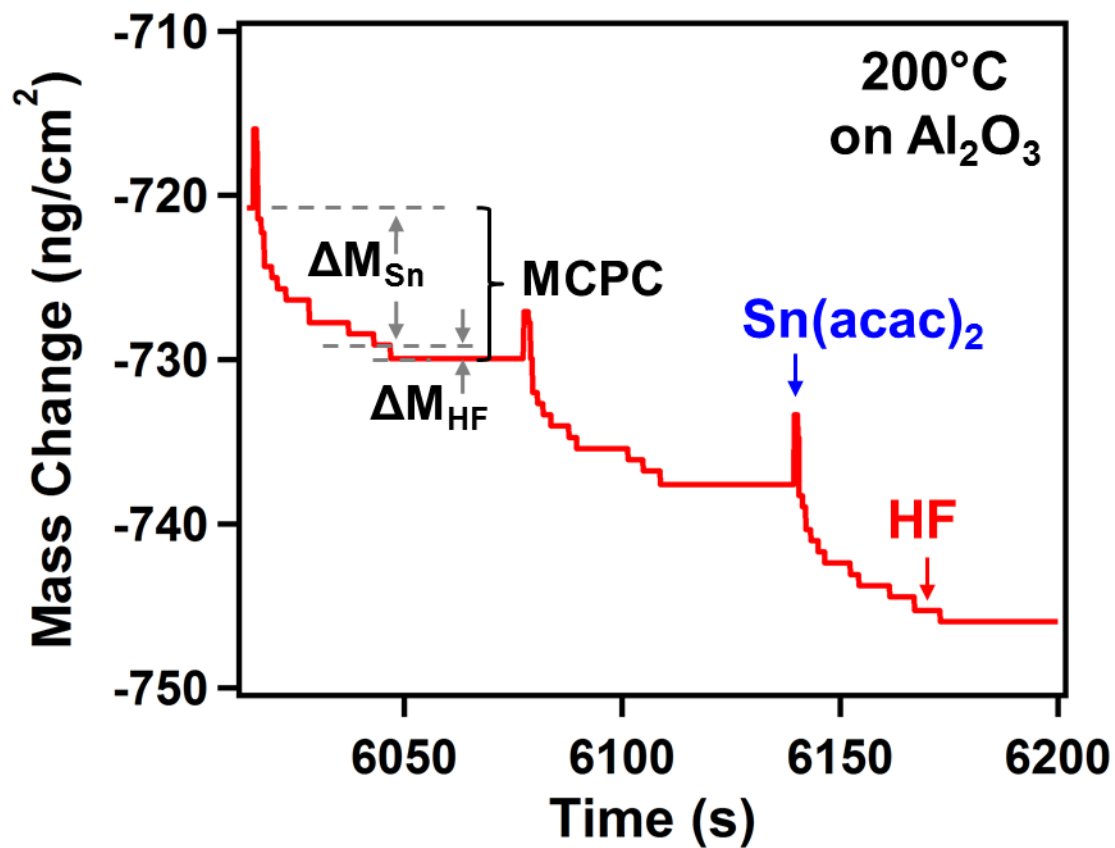
exposures at 200°C.

Figure 5-2   Expansion of linear region of Figure 5-1 showing the individual mass changes

during the sequential Sn(acac)$_2$ and HF exposures at 200°C.

Figure 3 examines the self-limiting nature of the Al_2O_3 ALE reactions at 200℃. These MCPCs were measured versus different reactant exposure times. Figure 3a shows the self-limiting behavior of the $Sn(acac)_2$ reaction using different $Sn(acac)_2$ exposure times with a single 1 s exposure of HF. A constant N_2 purge of 30 s was used after each exposure. This reaction sequence can be denoted as x-30-1-30. The MCPC versus $Sn(acac)_2$ exposure time decreases quickly and levels off at MCPC = -8 $ng/(cm^2 cycle)$.

Figure 3b examines the self-limiting behavior of the HF reaction using different HF exposure times with a single 1 s exposure of $Sn(acac)_2$. This reaction sequence can be denoted as 1-30-x-30. The MCPC versus HF exposure time deceases and then levels off. The slow change in the MCPC beyond -8 $ng/(cm^2 cycle)$ for longer HF exposures > 1 s is believed to be caused by larger HF background pressures and longer HF residence times that lead to some chemical vapor etching (CVE) during the $Sn(acac)_2$ exposures. Figures 3a and 3b together show that the $Sn(acac)_2$ and HF reactions display nearly self-limiting behavior. The MCPC = -8 $ng/(cm^2 cycle)$ for 1 s exposures of $Sn(acac)_2$ and HF was independent of purge time for purge times between 20 s and 120 s.

Figure 4 shows the mass change during 100 ALE cycles of $Sn(acac)_2$ and HF reactions on an Al_2O_3 surface at 150℃ using a reaction sequence of 1-30-1-30. The initial Al_2O_3 film was prepared by 100 cycles of Al_2O_3 ALD using TMA and H_2O at 150℃. The etching of the Al_2O_3 film is very linear with MCPC = -4.1 $ng/(cm^2 cycle)$. This MCPC corresponds to an etch rate of 0.14 Å/cycle based on the Al_2O_3 ALD film density of 3.0 g/cm^3 measured by XRR.
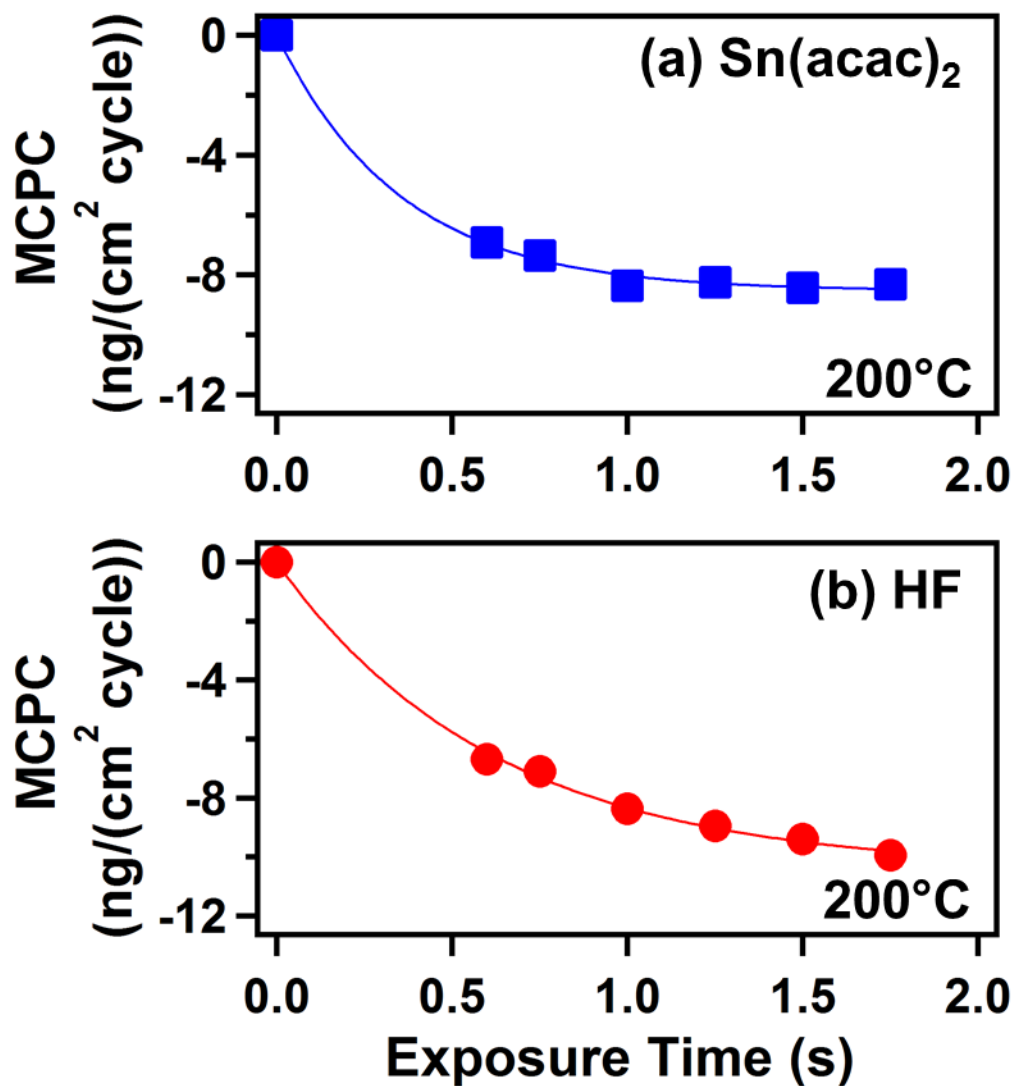
Figure 5-3   Mass change per cycle (MCPC) versus precursor exposure time at 200°C for (a)

Sn(acac)$_2$ and (b) HF.
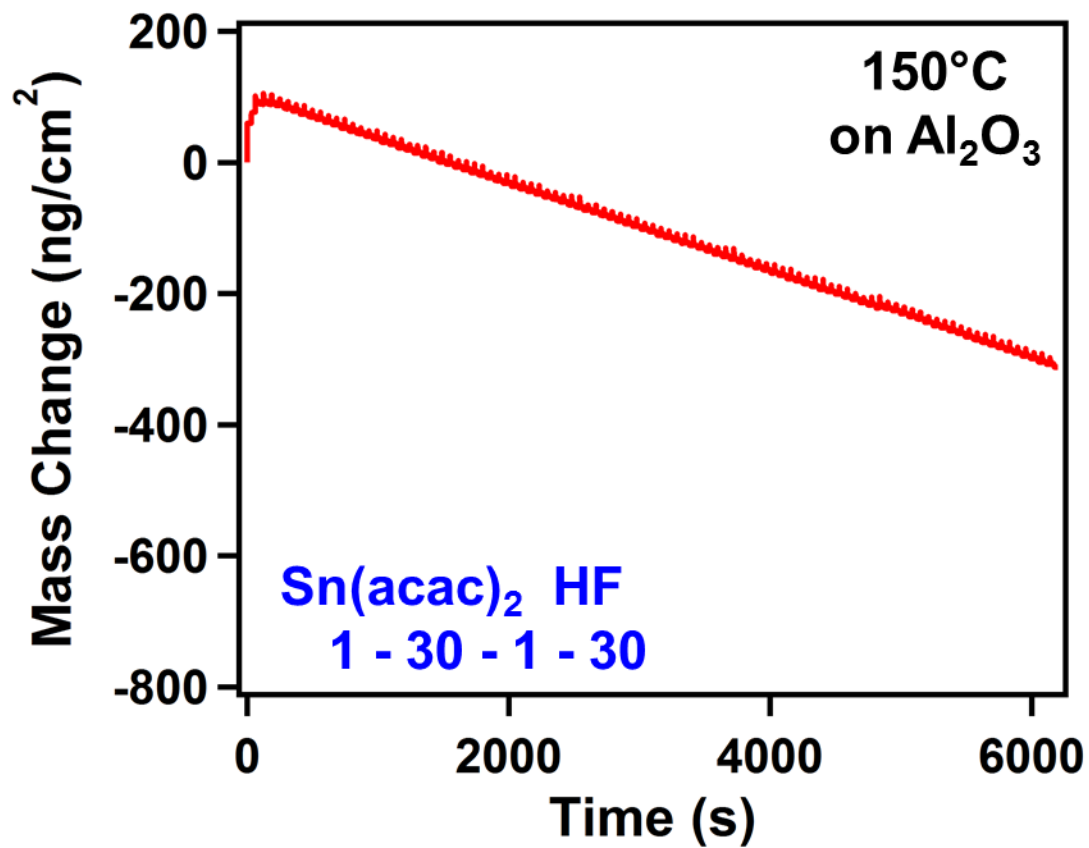
Figure 5-4   Mass change versus time for Al_2O_3 ALE using sequential $Sn(acac)_2$ and HF

exposures at 150°C.

Figure 5 shows an enlargement of the mass losses versus time at 150°C for three cycles in the steady state linear etching regime in Figure 4. There are distinct differences between the mass changes during the etching reactions at 200°C and 150°C. A mass gain of $\Delta M_{Sn} = +0.19$ ng/cm^2 was observed after the Sn(acac)$_2$ exposure for 1 s at 150°C. In contrast, a mass loss of $\Delta M_{Sn} = -8.1$ ng/cm^2 was obtained at 200°C. This difference may be attributed to more stable Sn(acac)$_2$ reaction products on the surface at 150°C.

A mass decrease of $\Delta M_{HF} = -4.3$ ng/cm^2 was observed after the HF exposure for 1 s at 150°C. This mass decrease is much larger than the mass decrease of $\Delta M_{HF} = -0.28$ ng/cm^2 at 200°C. However, if more Sn(acac)$_2$ reaction products remain on the surface following the Sn(acac)$_2$ exposure at 150°C, then more Sn(acac)$_2$ reaction products can be lost during the HF reaction. This behavior would explain the mass gain after the Sn(acac)$_2$ exposure and larger mass loss after the HF exposure at 150°C.

The ΔM_{Sn}, ΔM_{HF}, and MCPC values at all the reaction temperatures are shown in Figure 6. All ALE reactions were performed using a reaction sequence of 1-30-1-30 on initial Al$_2$O$_3$ surfaces. Figure 6a displays the ΔM_{Sn} and ΔM_{HF} values obtained at different reaction temperatures. ΔM_{Sn} displays a slight mass gain at 150°C and progressively larger mass losses at higher temperatures. In contrast, ΔM_{HF} displays a mass loss at temperatures between 150-200°C and mass gains at higher temperatures.

Figure 6b shows the MCPC where MCPC $= \Delta M_{Sn} + \Delta M_{HF}$. All the temperatures display a mass loss and the mass loss is larger at higher temperatures. The MCPC in Figure 6b correlates well with ΔM_{Sn} in Figure 6a. This correspondence shows that the mass change during the Sn(acac)$_2$ reaction is primarily responsible for the temperature dependence of the mass loss
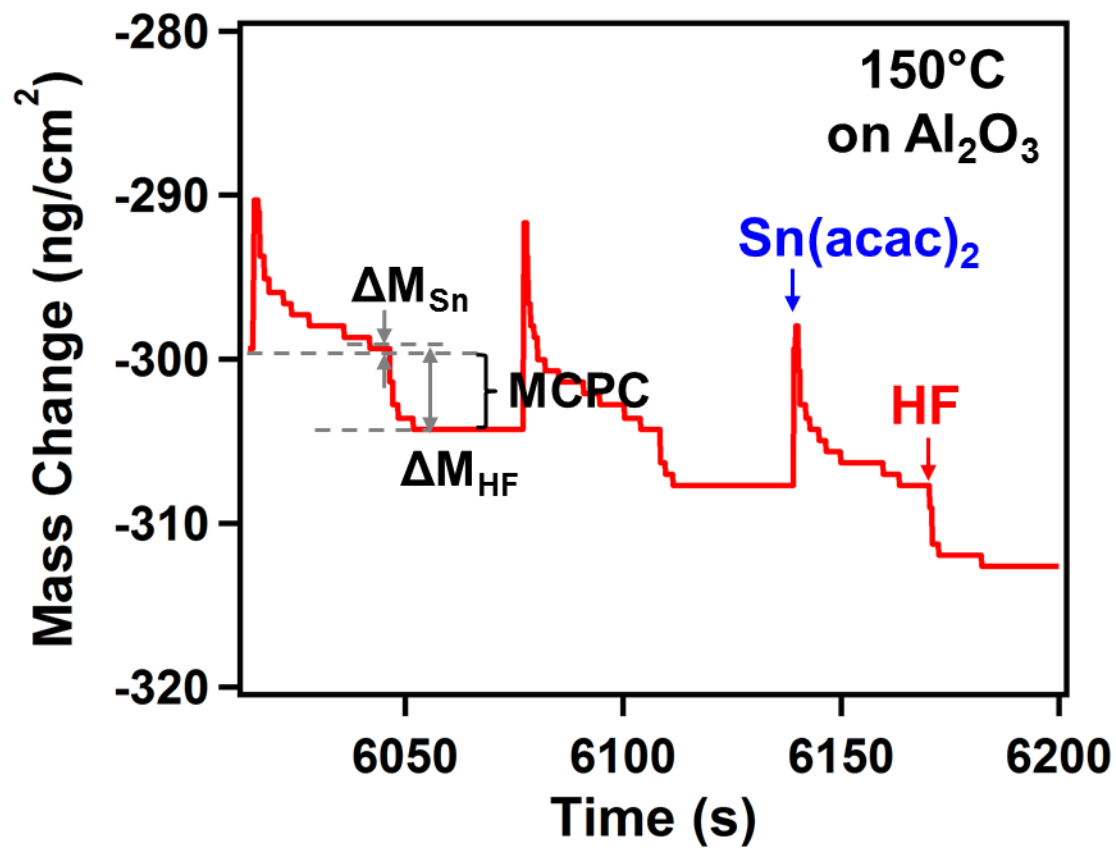
Figure 5-5   Expansion of linear region of Figure 5-4 showing the individual mass changes

during the sequential Sn(acac)$_2$ and HF exposures at 150°C.
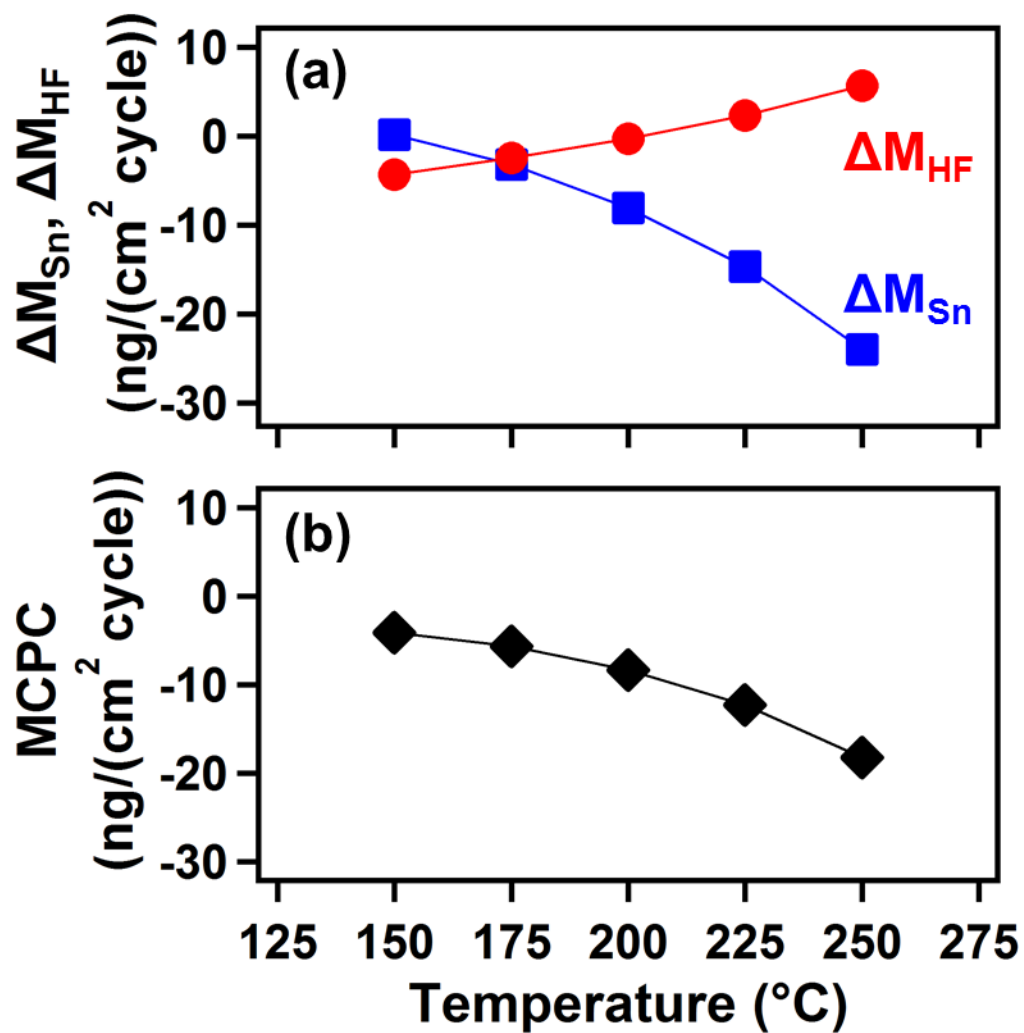
Figure 5-6   Temperature dependence of (a) ΔM_{Sn} and ΔM_{HF} and (b) MCPC for Al_2O_3 ALE.

during Al_2O_3 ALE. ΔM_{Sn}, ΔM_{HF}, and MCPC at the different reaction temperatures are summarized in Table 1.

Al_2O_3 ALE was also examined using *ex situ* XRR studies. For these experiments, Al_2O_3 ALD films with a thickness of 172 Å were grown on Si(100) wafers at 200°C. These Al_2O_3 ALD films were deposited using 150 cycles of TMA and H_2O with a reaction sequence of 1-20-1-20. Figure 7 displays XRR scans of the Al_2O_3 ALD films on the Si wafers versus number of $Sn(acac)_2$ and HF reaction cycles at 200°C. The XRR scans have been displaced from each other for clarity in presentation. These XRR scans are consistent with very uniform and smooth Al_2O_3 films.

Figure 7a shows the XRR scan of the initial Al_2O_3 ALD film grown on Si(100). The Al_2O_3 ALD film thickness of 172 Å can be obtained by fitting the reflected x-ray intensity versus incident angle. Figure 7b, 7c, 7d, and 7e show XRR scans of the etched Al_2O_3 film after 50, 100, 200, and 400 ALE cycles at 200°C, respectively. The Al_2O_3 thicknesses decrease with increasing number of ALE cycles. This decreasing film thickness is revealed by the longer modulation periods for the x-ray intensity versus angle after higher numbers of ALE cycles. The position of the critical angle of all the etched Al_2O_3 films is also constant. This constant critical angle indicates that there is no change of the film density during the ALE reactions.

The etched Al_2O_3 films are very smooth and do not roughen versus Al_2O_3 ALE. The XRR measurements yielded a roughness of the initial Al_2O_3 ALD film of ~5 Å. The surface roughness obtained by XRR analysis then decreased to ~2-3 Å after 50, 100, 200, and 400 ALE

Temperature(°C)	ΔM_{Sn} ng/(cm² cycle)	ΔM_{HF} ng/(cm² cycle)	MCPC ng/(cm² cycle)
150	0.19	-4.3	-4.1
175	-3.2	-2.4	-5.6
200	-8.1	-0.28	-8.4
225	-14.6	2.3	-12.3
250	-24.0	5.7	-18.3

Table 5-1. ΔM_{Sn}, ΔM_{HF} and MCPC for Al$_2$O$_3$ ALE at different temperatures.
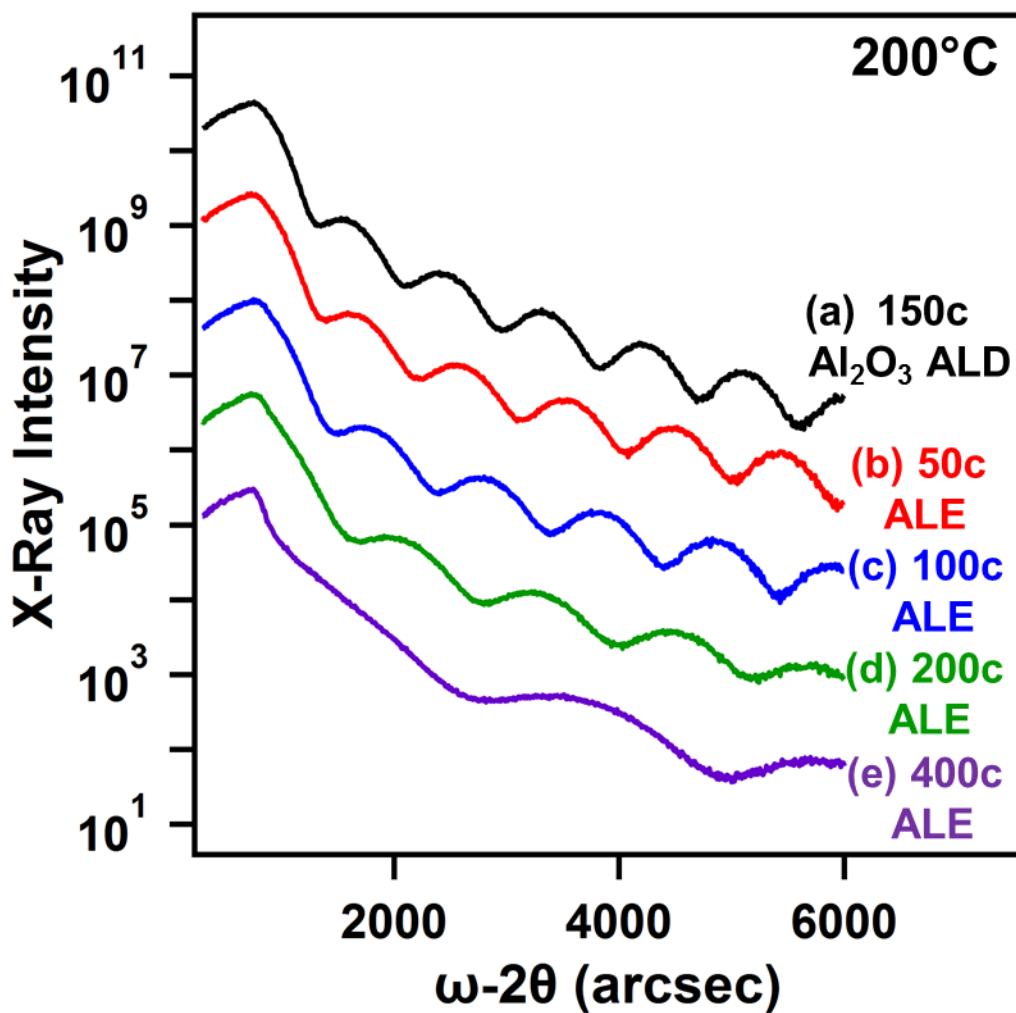
Figure 5-7 X-ray reflectivity scans showing x-ray intensity versus incident angle for Al_2O_3 films on Si(100). (a) Initial Al_2O_3 film grown using 150 Al_2O_3 ALD cycles; and Al_2O_3 films after various numbers of Al_2O_3 ALE cycles: (b) 50 cycles, (c) 100 cycles, (d) 200 cycles and (e) 400 cycles.

cycles at 200°C. The XRR measurements suggest that the ALE process is able to smooth the surface of the initial Al_2O_3 films. The error in these XRR surface roughness measurements is ~1 Å. Atomic force microscope (AFM) measurements also examined the Al_2O_3 film after Al_2O_3 ALE at 200°C. The AFM root-mean squared (RMS) surface roughness was 2.0 Å, 3.5 Å and 3.7 Å for the bare Si(100) wafer, an Al_2O_3 ALD film on Si(100) grown using 150 Al_2O_3 ALD cycles and the same Al_2O_3 film etched using 400 Al_2O_3 ALE cycles, respectively. This AFM analysis indicates that the Al_2O_3 film remains smooth during Al_2O_3 ALE.

Figure 8 shows the XRR measurements of the initial Al_2O_3 film thickness and the Al_2O_3 film thickness after 50, 100, 200, and 400 ALE cycles at 200°C. For the Al_2O_3 films with an initial thickness of 172 Å in Figure 8a, the film thickness versus number of ALE cycles is very linear and yields an etch rate of 0.27 Å/cycle. The spectroscopic ellipsometry (SE) measurements on these same samples yield an etch rate of 0.27 Å/cycle with an initial Al_2O_3 ALD film thickness of 166 Å. The initial thickness of the Al_2O_3 film is not used to obtain the etch rate because of the mass gain that occurs on the first ALE cycle.

The y-intercepts for the linear least squares fitting in Figure 8a are 176 Å and 169 Å by XRR and SE, respectively. These thicknesses are slightly higher than initial thicknesses of 172 Å and 166 Å measured by XRR and SE, respectively. These larger thicknesses originate from the mass gain that occurs during nucleation of the ALE process on the first ALE cycle. The SE analysis also determined a refractive index of n=1.70 for the Al_2O_3 film at a wavelength of 589 nm. This refractive index for the Al_2O_3 film remained at n=1.69-1.70 after 50, 100 and 200 ALE cycles.
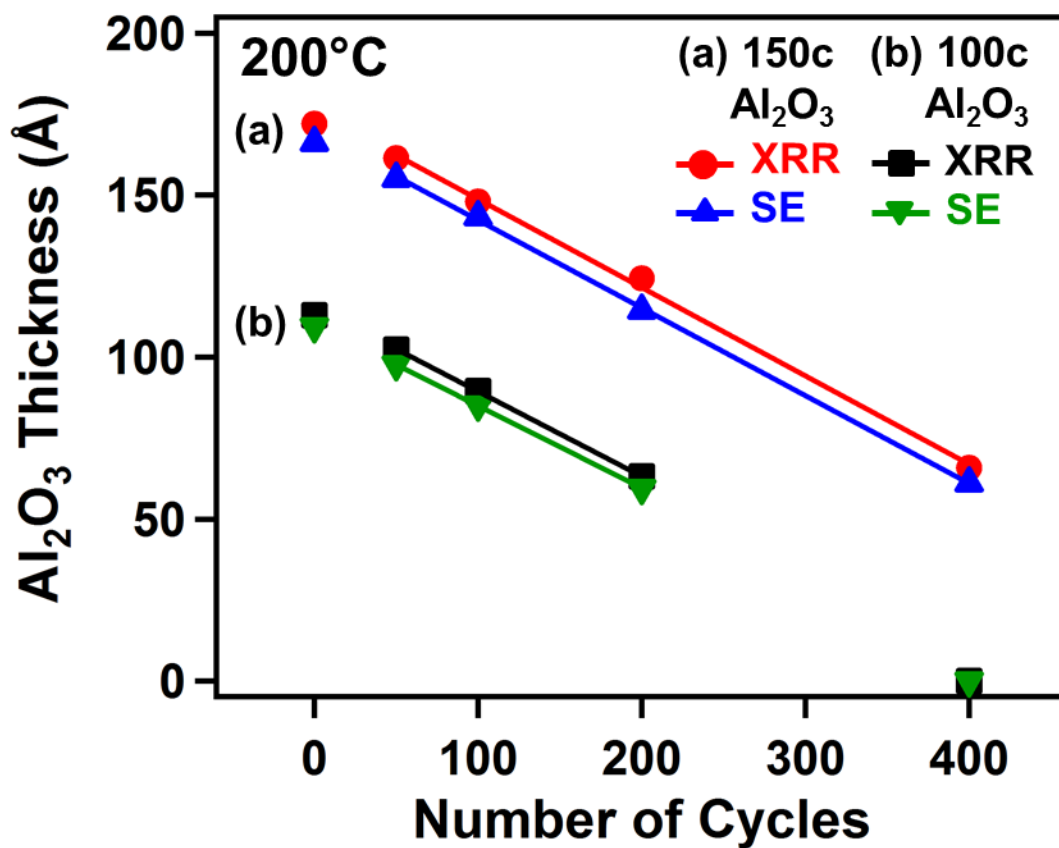
Figure 5-8   X-ray reflectivity and spectroscopic ellipsometry measurements of Al_2O_3 film

thickness versus number of Al_2O_3 ALE cycles for initial Al_2O_3 ALD films grown

using (a) 150 Al_2O_3 ALD cycles and (b) 100 Al_2O_3 ALD cycles.

XRR measurements were also performed on Al_2O_3 ALD films with a thickness of 113 Å that were grown on Si(100) wafers. These Al_2O_3 ALD films were deposited at 200°C using 100 cycles of TMA and H_2O with a reaction sequence of 1-20-1-20. Figure 8b displays the film thickness versus number of $Sn(acac)_2$ and HF reaction cycles at 200°C. The XRR measurements yield an Al_2O_3 ALE etch rate of 0.26 Å/cycle. The SE measurements also yield an etch rate of 0.25 Å/cycle with an initial Al_2O_3 ALD film thickness of 109 Å. The initial thickness of the Al_2O_3 film is again not employed to determine the etch rate because of the mass gain that occurs on the first ALE cycle.

The y-intercepts for the linear least squares fitting in Figure 8b are 116 Å and 110 Å by XRR and SE, respectively. These thicknesses are again slightly higher than the initial thicknesses of 113 Å and 109 Å measured by XRR and SE, respectively. These larger thicknesses originate from the mass gain that occurs on the first ALE cycle. After 400 ALE cycles for this thinner Al_2O_3 film, the XRR and SE measurements in Figure 8b indicate that the Al_2O_3 film is completely removed from the Si(100) wafer.

X-ray photoelectron spectroscopy (XPS) measurements were employed to determine the elements on the Al_2O_3 film after Al_2O_3 ALE. The XPS analysis measured Sn $3d_{5/2}$ XPS signals of 1 at% and F 1s XPS signals of 6 at% after 200 or 400 Al_2O_3 ALE cycles after the HF exposure. These XPS signals are consistent with AlF_3 formation and residual $Sn(acac)_2$ adsorption products. The Sn and F XPS signals were removed completely below the XPS detection limit after Ar ion sputtering for 2 minutes. This sputtering time is the time required to remove adventitious carbon from the surface.

Figure 9 shows the schematic for the proposed ALE reaction mechanism. This mechanism is based on the mass changes during the $Sn(acac)_2$ and HF exposures as determined by the QCM measurements. During the $Sn(acac)_2$ reaction (A), the $Sn(acac)_2$ reacts with the AlF_3 layer on the Al_2O_3 substrate. This AlF_3 layer is formed from the reaction of Al_2O_3 with HF after several ALE reactions on the initial Al_2O_3 surface. The $Sn(acac)_2$ reacts with the AlF_3 layer to form volatile $SnF(acac)$ and $Al(acac)_3$ reaction products and $SnF(acac)*$ surface species. The slow loss of mass in Figures 2 and 5 after the $Sn(acac)_2$ exposure is attributed to the slow desorption of acac species.[30-31] SnF_2 formation is unlikely because $Sn(acac)_2$ is expected to react with AlF_3 to form volatile $SnF(acac)$ and $Al(acac)_3$ until depleting the AlF_3 layer. After the AlF_3 layer is lost resulting from $Al(acac)_3$ and $SnF(acac)$ product formation, there may be a strong interaction between $SnF(acac)*$ surface species and the underlying Al_2O_3 substrate. This interaction may lead to $SnF(acac)*$ species adsorbed to the Al_2O_3 substrate.

During the HF reaction (B), HF reacts with the underlying Al_2O_3 surface to form a new AlF_3 layer. Figure 5 illustrates that this reaction has a rapid mass change. This fast mass change is attributed to the favorable thermochemistry for the $Al_2O_3 + 6HF \rightarrow 2AlF_3 + 3H_2O$ reaction.[28] The formation of the AlF_3 layer also leads to the removal of the $SnF(acac)*$ species. The reaction of HF with $SnF(acac)*$ species to form SnF_2 can not be ruled out. However, SnF_2 surface species would be expected to react with $Sn(acac)_2$ to form $SnF(acac)*$ again during the $Sn(acac)_2$ exposure. In addition, HF also provides hydrogen to form H_2O as a reaction product. This reaction removes the oxygen in Al_2O_3. The AlF_3 layer is then ready for the next $Sn(acac)_2$ reaction.
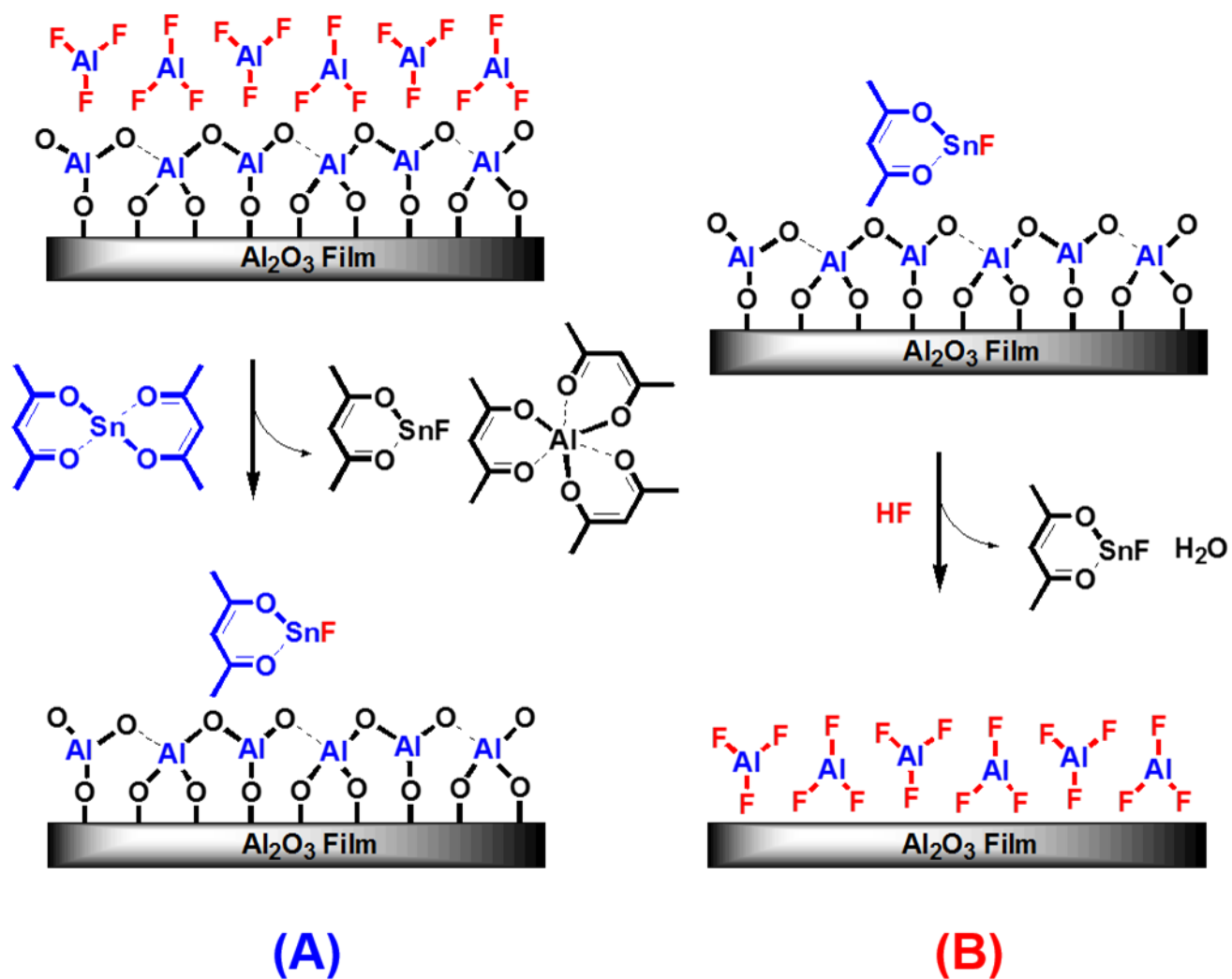
Figure 5-9 Schematic of proposed reaction mechanism for Al$_2$O$_3$ ALE showing (A) Sn(acac)$_2$ reaction and (B) HF reaction.

The overall proposed reaction can be expressed as:
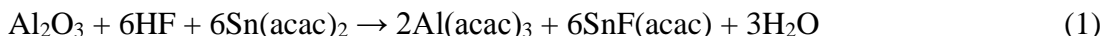
$$Al_2O_3 + 6HF + 6Sn(acac)_2 \rightarrow 2Al(acac)_3 + 6SnF(acac) + 3H_2O \quad (1)$$

This overall reaction can be divided into the $Sn(acac)_2$ and HF reactions:

(A) $Al_2O_3|2AlF_3^* + 6Sn(acac)_2 \rightarrow$

$$Al_2O_3|xSnF(acac)^* + 2Al(acac)_3 + (6-x)SnF(acac) \quad (2)$$

(B) $Al_2O_3|xSnF(acac)^* + 6HF \rightarrow 2AlF_3^* + xSnF(acac) + 3H_2O \quad (3)$
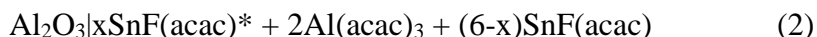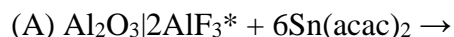
The asterisks indicate the surface species and the vertical lines are used to separate the various surface species. The Al_2O_3 shown in Equations 2 and 3 is the amount of Al_2O_3 that is etched during the ALE reactions. x is a parameter determined by the ΔM_{Sn} and ΔM_{HF} mass changes. To obtain agreement with the ΔM_{Sn} and ΔM_{HF} mass changes in Table 1, x = 0.74, 0.46, 0.29, 0.19, and 0.15 at 150, 175, 200, 225 and 250°C, respectively. Note that AlF_3 is the key reaction intermediate. The production of all the $Al(acac)_3$ is assumed to occur during reaction (A). This assumption needs to be confirmed by mass spectrometry studies. $Al(acac)_3$ is a stable metal β-diketonate with a vapor pressure of ~3-4 Torr at 150 °C.[32-34]

The temperature dependence of ΔM_{Sn} and ΔM_{HF} is believed to be dependent on the surface species present after the $Sn(acac)_2$ and HF exposures. The larger mass gains after the $Sn(acac)_2$ exposure and the larger mass losses after the HF exposure at lower temperatures can be explained by more $Sn(acac)_2$ adsorption products on the surface after the $Sn(acac)_2$ exposure at lower temperatures. The larger mass gains after the HF exposure and the larger mass losses after the $Sn(acac)_2$ exposure at higher temperatures can be explained by more AlF_3 species on the surface after the HF exposure at higher temperatures.

Equations 2 and 3 present the surface chemistry for the $Sn(acac)_2$ and HF reactions as determined by the QCM measurements. Complementary *in situ* Fourier transform infrared (FTIR) vibrational spectroscopy studies have shown that there are surface species that do not change during the $Sn(acac)_2$ and HF reactions. These surface species are not observed by the QCM measurements that only detect a change in mass. More detail on the reaction mechanism and the temperature dependence of Al_2O_3 ALE using both QCM and FTIR studies will be presented in another publication.[29]

5.3. Generality and Advantages of Thermal ALE Approach

The ALE of other materials including metal oxides, metal nitrides, metal phosphides, metal sulfides and metal arsenides should be possible using sequential, self-limiting thermal reactions with $Sn(acac)_2$ and HF as the reactants. $Sn(acac)_2$ can readily react with HF to form $SnF(acac)$. Sn-F bond formation is expected to be favorable because tin has a high affinity for fluorine.[35] The Sn-F bond enthalpy is 466.5 kJ/mole in the diatomic SnF molecule.[36] The reaction of $Sn(acac)_2$ with fluorine to form $SnF(acac)$ enables $Sn(acac)_2$ to release an acac ligand to the surface. Metals easily form complexes with acac ligands and have comparable stabilities.[37] The hydrogen from HF can combine with either oxygen, nitrogen, phosphorous, sulfur or arsenic from the metal oxide, metal nitride, metal phosphide, metal sulfide or metal arsenide to form H_2O, NH_3, PH_3, H_2S or AsH_3, respectively.

ALE reactions for various metal oxides, metal nitrides, metal phosphides, metal sulfides, and metal arsenides are given in Table 2. The ALE of many other metal oxides, metal nitrides, metal phosphides, metal sulfides and metal arsenides may also be possible using $Sn(acac)_2$ and HF. The reaction efficiency may be dependent on the volatility of the metal acetylacetonate

Metal Oxides
$Al_2O_3 + 6Sn(acac)_2 + 6HF \rightarrow 2Al(acac)_3 + 6SnF(acac) + 3H_2O$ $HfO_2 + 4Sn(acac)_2 + 4HF \rightarrow Hf(acac)_4 + 4SnF(acac) + 2H_2O$
Metal Nitrides
$GaN + 3Sn(acac)_2 + 3HF \rightarrow Ga(acac)_3 + 3SnF(acac) + NH_3$ $InN + 3Sn(acac)_2 + 3HF \rightarrow In(acac)_3 + 3SnF(acac) + NH_3$
Metal Phosphides
$AlP + 3Sn(acac)_2 + 3HF \rightarrow Al(acac)_3 + 3SnF(acac) + PH_3$ $InP + 3Sn(acac)_2 + 3HF \rightarrow In(acac)_3 + 3SnF(acac) + PH_3$
Metal Sulfides
$ZnS + 2Sn(acac)_2 + 2HF \rightarrow Zn(acac)_2 + 2SnF(acac) + H_2S$ $PbS + 2Sn(acac)_2 + 2HF \rightarrow Pb(acac)_2 + 2SnF(acac) + H_2S$
Metal Arsenides
$GaAs + 3Sn(acac)_2 + 3HF \rightarrow Ga(acac)_3 + 3SnF(acac) + AsH_3$ $InAs + 3Sn(acac)_2 + 3HF \rightarrow In(acac)_3 + 3SnF(acac) + AsH_3$

Table 5-2. Atomic Layer Etching Reactions for Various Materials

reaction product. For example, many metal oxides, in addition to Al_2O_3, should be etched by the $Sn(acac)_2$ and HF reactants including HfO_2, ZrO_2, Fe_2O_3, Co_2O_3, Cr_2O_3, Sc_2O_3 and Ga_2O_3. These metal oxides all produce etch products, $M(acac)_3$ or $M(acac)_4$, with vapor pressures of ~1 Torr at 150°C.[34,38-39]

The ALE of elemental metals could also be performed using sequential exposures of $Sn(acac)_2$ and HF. The surface of the elemental metal would first be oxidized using an oxidant such as O_2 or O_3. The metal oxide could then be etched with $Sn(acac)_2$ and HF. Alternatively, the surface of the elemental metal could be nitrided, phosphided, sulfided or arsenided prior to etching the metal nitride, metal phosphide, metal sulfide or metal arsenide, respectively, with $Sn(acac)_2$ and HF.

Other Sn β-diketonates may also serve as etching reactants besides $Sn(acac)_2$ with acac= acetylacetonate. Many other β-diketone ligands on the Sn metal center are possible such as hfac= hexafluoroacetylacetonate, tfac= trifluroacetylacetonate, and tmhd= tetramethylheptanedionate.[35,40] Different β-diketone ligands can change the physical properties of the metal β-diketonate.[37] For example, fluorine substituted β-diketone ligands generally show higher vapor pressure.[37]

Other metal β-diketonates, in addition to Sn-based compounds, could also react with HF to yield β-diketone ligands that could then form the etch products. The possible advantage of using different metal β-diketonates may be their more favorable vapor pressure, thermal stability, reaction kinetics or thermochemistry. Metal β-diketonates with metals in higher oxidation states can bind to more β-diketone ligands.[33-34] The larger number of β-diketone ligands may facilitate the etching of the metal oxide. However, $Sn(acac)_2$ with tin in the +2 oxidation state has an open

coordination sphere and a readily available electron lone-pair that may facilitate fluorine binding to tin.[35]

There is also the possibility that the ALE of metal oxides would be possible with HCl or HBr instead of HF as a reactant. For example, the reaction of HCl with $Sn(acac)_2$ could produce SnCl(acac). This Sn chloride β-diketonate compound was produced earlier by the reaction of $Sn(acac)_2$ and $SnCl_2$.[35,40] The Sn-Cl bond energy in the diatomic SnCl molecule is 414 kJ/mole.[41] This bond energy is only slightly less than the bond energy of 466.5 kJ/mole in the diatomic SnF molecule.[36,41]

The advantage of using HCl or HBr would be avoiding the use of HF and its safety concerns. However, HCl and HBr are also chemically corrosive. A possible disadvantage of HCl or HBr is the lower stability of metal chlorides and metal bromides compared with metal fluorides for metal oxides, metal nitrides, metal phosphides and metal arsenides. The AlF_3 layer plays a key role as a reaction intermediate in the proposed reaction mechanism for Al_2O_3 ALE. The stability of the metal fluoride reaction intermediate may be critical for the ALE mechanism for self-limiting reactions based on $Sn(acac)_2$ and HF.

The absolute etch rate may also differ between various metal oxides during ALE with $Sn(acac)_2$ and HF as the reactants. The etch rate may be dependent upon the residual coverage of acetylacetonate species on the metal oxide surface. Higher acetylacetonate coverages may block surface sites and prevent the adsorption of $Sn(acac)_2$ or formation of the metal fluoride layer. This site-blocking by acetylacetonate surface species may reduce the etch rate. Site-blocking by hfac and hfacH was recently demonstrated during Pt ALD and Pd ALD using $Pt(hfac)_2$ and $Pd(hfac)_2$, respectively.[30-31] The temperature dependence of the Al_2O_3 ALE may be attributed to the lower residual coverage of acetylacetonate surface species at higher temperatures. Other

ligands on the metal β-diketonate may alter the residual coverage of ligands on the metal oxide surface and change the etch rate.

There are advantages to the thermal ALE approach compared with ALE based on halogen adsorption and ion or energetic neutral noble atom bombardment. The thermal ALE approach avoids any damage to the underlying substrate resulting from high energy ions or energetic neutrals. Ions from plasmas have been implicated in the performance degradation of high-k/metal gate stacks.[42] Using neutral noble gas beams is able to mitigate the structural and electrical damage caused by ions.[8]

ALE based on ion or neutral noble atom bombardment also requires line-of-sight to the substrate. This requirement can be used advantageously to minimize undercutting with directional ions or energetic neutral atoms during ALE. However, this line-of-sight requirement is detrimental if conformality is required for the etching. The line-of-sight requirement is also limited to the relatively small surface areas that are subjected to ion or neutral noble atom bombardment. The thermal ALE approach will be particularly important for etching high surface area and high aspect ratio structures.

5.4. Conclusions

Al_2O_3 ALE was observed using $Sn(acac)_2$ and HF as the reactants. The sequential, self-limiting thermal reactions of $Sn(acac)_2$ and HF etched Al_2O_3 linearly with atomic level precision. Al_2O_3 ALE was demonstrated at temperatures from 150-250℃. The sequential $Sn(acac)_2$ and HF reactions were self-limiting versus reactant exposure as revealed by QCM studies. The QCM studies also measured MCPC values that increased with temperature from -4.1 ng/(cm^2 cycle) at

150℃ to -18.3 ng/(cm^2 cycle) at 250℃. These mass losses per cycle correspond to etch rates from 0.14 Å/cycle at 150℃ to 0.61 Å/cycle at 250℃. The linear removal of Al$_2$O$_3$ was confirmed by XRR analysis. The XRR studies measured Al$_2$O$_3$ ALE etch rates of 0.27 Å/cycle at 200℃. The Al$_2$O$_3$ films also remained smooth during Al$_2$O$_3$ ALE.

The overall etching reaction is believed to follow the reaction: Al$_2$O$_3$ + 6Sn(acac)$_2$ + 6HF → 2Al(acac)$_3$ + 6SnF(acac) + 3H$_2$O. In the proposed reaction mechanism, AlF$_3$ is the key reaction intermediate. The Sn(acac)$_2$ reactant donates acac to the AlF$_3$ layer on the Al$_2$O$_3$ substrate to produce Al(acac)$_3$. The HF reactant forms the AlF$_3$ reaction intermediate from Al$_2$O$_3$ and allows SnF(acac) and H$_2$O to leave as reaction products. The ALE of many other metal oxides besides Al$_2$O$_3$ should also be possible using Sn(acac)$_2$, or other metal β-diketonates, together with HF. This ALE reaction mechanism should also be applicable for the ALE of metal nitrides, metal phosphides, metal sulfides and metal arsenides.

5.5. Experimental Methods

5.5A. Viscous Flow Reactor Equipped for *in situ* QCM Measurements

The ALE reactions at 150-250℃ were performed in a viscous flow ALD reactor.[43-44] A proportional-integral-derivative (PID) temperature controller (2604, Eurotherm) stabilized the temperature in the reactor to within ±0.04℃. A capacitance manometer (Baratron 121A, MKS) measured the pressure in the reactor. The ALD reactor was equipped with an *in situ* quartz crystal microbalance (QCM).[43] The RC-cut quartz crystal[45] (gold coated and polished, 6 MHz, Colnatec) was placed in a sensor head (BSH-150, Inficon) and then sealed with high temperature

epoxy (Epo-Tek H21D, Epoxy technology). All *in situ* QCM measurements were recorded by a thin film deposition monitor (Maxtek TM-400, Inficon).

The Al_2O_3 ALE reactions were performed using sequential exposure of tin(II) acetylacetonate ($Sn(acac)_2$, 37-38% Sn, Gelest) and HF-pyridine (70 wt% HF, Sigma-Aldrich). HF-pyridine is a liquid at room temperature and has an equilibrium with gaseous HF.[46] The HF pressure from HF-pyridine is >2-3 Torr at room temperature. The two pneumatic valves and one metering valve used for HF dosing produced HF pressure transients of ~80 mTorr. HF-pyridine enabled the safe handling of anhydrous HF. Note that HF-pyridine can be dangerous if not utilized properly. $Sn(acac)_2$ and HF-pyridine were transferred to stainless steel bubblers in a dry N_2-filled glove bag. The stainless steel bubbler containing $Sn(acac)_2$ was held at 100°C. The one pneumatic valve used for $Sn(acac)_2$ dosing produced $Sn(acac)_2$ pressure transients of ~20 mTorr. The Al_2O_3 films were grown with Al_2O_3 ALD using TMA (97 %, Sigma-Aldrich) and H_2O (Chromasolv for HPLC, Sigma-Aldrich). The HF-pyridine, TMA, and H_2O precursors were maintained at room temperature.

The reactor was pumped using a mechanical pump (Pascal 2015SD, Alcatel). The base pressure of the reactor without any N_2 flow was ~10 mTorr. Separate mass flow controllers were used to provide N_2 carrier gas for each reactant. An additional mass flow controller streamed N_2 gas through the reactor. These three separate mass flow controllers (Type 1179A, MKS) delivered a constant total flow of 150 sccm of ultra high purity (UHP) N_2 carrier gas into the reactor. Additional N_2 gas flow of 20 sccm using a metering bellows-sealed valve (SS-4BMG, Swagelok) prevented deposition on the backside of the QCM crystal.[43] The total N_2 gas flow of 170 sccm produced a background N_2 pressure of ~1 Torr in the reactor.

5.5B. Sample Preparation and *ex situ* Film Analysis

Boron-doped Si(100) wafers (p-type, Silicon Valley Microelectronics) were cut into samples with dimensions of 2.5 cm by 2.5 cm. These substrates were used for Al_2O_3 ALD deposition. The Si wafers were first rinsed with acetone, isopropanol, and deionized water. Subsequently, the Si wafers were dried with UHP N_2 gas.

The *ex situ* x-ray reflectivity (XRR) scans were recorded by a high resolution x-ray diffractometer (Bede D1, Jordan Valley Semiconductors) using Cu Kα ($\lambda = 1.540$ Å) radiation. The filament voltage and current in the x-ray tube were 40 kV and 35 mA, respectively. A 10 arcsec step size and a 5 s acquisition time were used for recording all XRR scans with a range of 300 to 6000 arcsec. The analysis software (Bede REFS, Jordan Valley Semiconductors) fitted the XRR scans to determine film thickness, film density and surface roughness.

Spectroscopic ellipsometry (SE) determined the film thicknesses and refractive index. The measurement of Ψ and Δ were recorded using a spectroscopic ellipsometer (M-2000, J. A. Woollam) with a spectral range of 240 to 1700 nm and an incidence angle of 75°. The analysis software (CompleteEASE, J. A. Woollam) fitted Ψ and Δ based on a Sellmeier model to determine the thicknesses and refractive index of the film.[47]

X-ray photoemission spectroscopy (XPS) analysis was performed using a PHI 5600 X-ray photoelectron spectrometer using a monochromatic Al Kα source. The XPS data were collected using Auger Scan (RBD Enterprises, Inc., Bend, OR). The XPS data were analyzed in CASA XPS (Casa Software Ltd, UK). Atomic force microscope (AFM) analysis was performed using an EasyScan 2 (Nanosurf) with a dynamic force module. The scan software (EasyScan 2, Nanosurf) measured the RMS roughness using a 5 µm × 5 µm image size.

5.6. Acknowledgements

5.7. References

(1)   George, S. M. Atomic Layer Deposition: An Overview. *Chem. Rev.* **2010**, *110*, 111-131.

(2)   Miikkulainen, V.; Leskela, M.; Ritala, M.; Puurunen, R. L. Crystallinity of Inorganic Films Grown by Atomic Layer Deposition: Overview and General Trends. *J. Appl. Phys.* **2013**, *113*, 021301.

(3)   Profijt, H. B.; Potts, S. E.; van de Sanden, M. C. M.; Kessels, W. M. M. Plasma-Assisted Atomic Layer Deposition: Basics, Opportunities, and Challenges. *J. Vac. Sci. Technol. A* **2011**, *29*, 050801.

(4)   Agarwal, A.; Kushner, M. J. Plasma Atomic Layer Etching Using Conventional Plasma Equipment. *J. Vac. Sci. Technol. A* **2009**, *27*, 37-50.

(5)   Athavale, S. D.; Economou, D. J. Molecular Dynamics Simulation of Atomic Layer Etching of Silicon. *J. Vac. Sci. Technol. A* **1995**, *13*, 966-971.

(6)   Athavale, S. D.; Economou, D. J. Realization of Atomic Layer Etching of Silicon. *J. Vac. Sci. Technol. B* **1996**, *14*, 3702-3705.

(7)   Kubota, N. A.; Economou, D. J.; Plimpton, S. J. Molecular Dynamics Simulations of Low-Energy (25-200 eV) Argon Ion Interactions with Silicon Surfaces: Sputter Yields and Product Formation Pathways. *J. Appl. Phys.* **1998**, *83*, 4055-4063.

(8)   Park, S. D.; Lim, W. S.; Park, B. J.; Lee, H. C.; Bae, J. W.; Yeom, G. Y. Precise Depth Control and Low-Damage Atomic-Layer Etching of HfO_2 using BCl_3 and Ar Neutral Beam. *Electrochem. Solid State Lett.* **2008**, *11*, H71-H73.

(9)   Sakaue, H.; Iseda, S.; Asami, K.; Yamamoto, J.; Hirose, M.; Horiike, Y. Atomic Layer Controlled Digital Etching of Silicon. *Jpn. J. Appl. Phys. 1* **1990**, *29*, 2648-2652.

(10)   Yamamoto, J.; Kawasaki, T.; Sakaue, H.; Shingubara, S.; Horiike, Y. Digital Etching Study and Fabrication of Fine Si Lines and Dots. *Thin Solid Films* **1993**, *225*, 124-129.

(11)   Matsuura, T.; Sugiyama, T.; Murota, J. Atomic-Layer Surface Reaction of Chlorine on Si and Ge Assisted by an Ultraclean ECR Plasma. *Surf. Sci.* **1998**, *402*, 202-205.

(12)   Sugiyama, T.; Matsuura, T.; Murota, J. Atomic-Layer Etching of Ge Using an Ultraclean ECR Plasma. *Appl. Surf. Sci.* **1997**, *112*, 187-190.

(13)   Park, S. D.; Lee, D. H.; Yeom, G. Y. Atomic Layer Etching of Si(100) and Si(111) Using Cl_2 and Ar Neutral Beam. *Electrochem. Solid State Lett.* **2005**, *8*, C106-C109.

(14)   Lim, W. S.; Park, S. D.; Park, B. J.; Yeom, G. Y. Atomic Layer Etching of (100)/(111) GaAs with Chlorine and Low Angle Forward Reflected Ne Neutral Beam. *Surf. Coat. Tech.* **2008**, *202*, 5701-5704.

(15)   Meguro, T.; Hamagaki, M.; Modaressi, S.; Hara, T.; Aoyagi, Y.; Ishii, M.; Yamamoto, Y. Digital Etching of GaAs - New Approach of Dry Etching to Atomic Ordered Processing. *Appl. Phys. Lett.* **1990**, *56*, 1552-1554.

(16)   Meguro, T.; Ishii, M.; Sugano, T.; Gamo, K.; Aoyagi, Y. Control of the Etching Reaction of Digital Etching Using Tunable UV Laser Irradiation. *Appl. Surf. Sci.* **1994**, *82-3*, 193-199.

(17)   Maki, P. A.; Ehrlich, D. J. Laser Bilayer Etching of GaAs Surfaces. *Appl. Phys. Lett.* **1989**, *55*, 91-94.

(18)   Park, S. D.; Oh, C. K.; Bae, J. W.; Yeom, G. Y.; Kim, T. W.; Song, J. I.; Jang, J. H. Atomic Layer Etching of InP Using a Low Angle Forward Reflected Ne Neutral Beam. *Appl. Phys. Lett.* **2006**, *89*, 043109.

(19)   Min, K. S.; Kang, S. H.; Kim, J. K.; Jhon, Y. I.; Jhon, M. S.; Yeom, G. Y. Atomic Layer Etching of Al_2O_3 Using BCl_3/Ar for the Interface Passivation Layer of III-V MOS Devices. *Microelectron. Eng.* **2013**, *110*, 457-460.

(20)   Park, J. B.; Lim, W. S.; Park, B. J.; Park, I. H.; Kim, Y. W.; Yeom, G. Y. Atomic Layer Etching of Ultra-Thin HfO_2 Film for Gate Oxide in MOSFET Devices. *J. Phys. D Appl. Phys.* **2009**, *42*, 055202.

(21)   Lim, W. S.; Park, J. B.; Park, J. Y.; Park, B. J.; Yeom, G. Y. Low Damage Atomic Layer Etching of ZrO_2 by Using BCl_3 Gas and Ar Neutral Beam. *J. Nanosci. Nanotechnol.* **2009**, *9*, 7379-7382.

(22)   Park, J. B.; Lim, W. S.; Park, S. D.; Park, Y. J.; Yeom, G. Y. Etch Characteristics of TiO_2 Etched by Using an Atomic Layer Etching Technique with BCl_3 Gas and an Ar Neutral Beam. *J. Korean Phys. Soc.* **2009**, *54*, 976-980.

(23)   Metzler, D.; Bruce, R. L.; Engelmann, S.; Joseph, E. A.; Oehrlein, G. S. Fluorocarbon Assisted Atomic Layer Etching of SiO_2 using Cyclic Ar/C_4F_8 Plasma. *J. Vac. Sci. Technol. A* **2014**, *32*, 020603.

(24)   Rauf, S.; Sparks, T.; Ventzek, P. L. G.; Smirnov, V. V.; Stengach, A. V.; Gaynullin, K. G.; Pavlovsky, V. A. A Molecular Dynamics Investigation of Fluorocarbon Based Layer-by-layer Etching of Silicon and SiO_2. *J. Appl. Phys.* **2007**, *101*, 033308.

(25)   Kim, Y. Y.; Lim, W. S.; Park, J. B.; Yeom, G. Y. Layer by Layer Etching of the Highly Oriented Pyrolythic Graphite by Using Atomic Layer Etching. *J. Electrochem. Soc.* **2011**, *158*, D710-D714.

(26)   Lim, W. S.; Kim, Y. Y.; Kim, H.; Jang, S.; Kwon, N.; Park, B. J.; Ahn, J.-H.; Chung, I.; Hong, B. H.; Yeom, G. Y. Atomic Layer Etching of Graphene for Full Graphene Device Fabrication. *Carbon* **2012**, *50*, 429-435.

(27)   Vogli, E.; Metzler, D.; Oehrlein, G. S. Feasibility of Atomic Layer Etching of Polymer Material Based on Sequential O_2 Exposure and Ar Low-Pressure Plasma-Etching. *Appl. Phys. Lett.* **2013**, *102*, 253105.

(28)   *HSC Chemistry*; HSC Chemistry 5.1, Outokumpu Research Oy: Pori, Finland.

(29)   Lee, Y.; DuMont, J. W.; George, S. M. Mechanism of Thermal Al_2O_3 Atomic Layer Etching Using Sequential Reactions with $Sn(acac)_2$ and HF. *In preparation for submission to Chemistry of Materials*

(30)   Anderson, V. R.; Leick, N.; Clancey, J. W.; Hurst, K. E.; Jones, K. M.; Dillon, A. C.; George, S. M. Atomic Layer Deposition of Platinum Nanoparticles on Titanium Oxide and Tungsten Oxide Using Platinum(II) Hexafluoroacetylacetonate and Formalin as the Reactants. *J. Phys. Chem. C* **2014**, *118*, 8960-8970.

(31)   Goldstein, D. N.; George, S. M. Surface poisoning in the nucleation and growth of palladium atomic layer deposition with Pd(hfac)(2) and formalin. *Thin Solid Films* **2011**, *519*, 5339-5347.

(32)   Berg, E. W.; Truemper, J. T. Vapor Pressure-Temperature Data for Various Metal Beta-Diketone Chelates. *Anal. Chim. Acta* **1965**, *32*, 245-252.

(33)   Eisentraut, K. J.; Sievers, R. E. Thermogravimetric Studies of Metal Beta-Diketonates. *J. Inorg. Nucl. Chem.* **1967**, *29*, 1931-1936.

(34)   Fahlman, B. D.; Barron, A. R. Substituent Effects on the Volatility of Metal Beta-Diketonates. *Adv. Mater. Opt. Electr.* **2000**, *10*, 223-232.

(35)   Ewings, P. F. R.; Harrison, P. G.; Fenton, D. E. Derivatives of Divalent Germanium, Tin, and Lead. 5. Bis-(Pentane-2,4-Dionato)-Tin(II),Bis(1,1,1-Trifluoropentane-2,4-Dionato)-

Tin(II), and Bis(1,1,1,5,5,5-Hexafluoropentane-2,4-Dionato)-Tin(II). *J. Chem. Soc.-Dalton Trans.* **1975**, 821-826.

(36)   Zimbov, K.; Hastie, J. W.; Margrave, J. L. Mass Spectrometric Studies at High Temperatures. 24. Thermodynamics of Vaporization of SnF_2 and PbF_2 and Dissociation Energies of SnF and PbF. *Trans. Faraday Soc.* **1968**, *64*, 861-867.

(37)   Mehrotra, R. C.; Bohra, R.; Gaur, D. P. *Metal Beta-Diketonates and Allied Derivatives*; Academic Press: London, 1978.

(38)   Morozova, N. B.; Zherikova, K. V.; Baidina, I. A.; Sysoev, S. V.; Semyannikov, P. P.; Yakovkina, L. V.; Smirnova, T. P.; Gelfond, N. V.; Igumenov, I. K.; Carta, G.; Rossetto, G. Volatile Hafnium(IV) Compounds with Beta-Diketonate and Cyclopentadienyl Derivatives. *J. Phys. Chem. Solids* **2008**, *69*, 673-679.

(39)   Zherikova, K. V.; Morozova, N. B.; Zelenina, L. N.; Sysoev, S. V.; Chusova, T. P.; Igumenov, I. K. Thermal Properties of Hafnium(IV) and Zirconium(IV) Beta-Diketonates. *J. Therm. Anal. Calorim.* **2008**, *92*, 729-734.

(40)   Bos, K. D.; Budding, H. A.; Bulten, E. J.; Noltes, J. G. Tin(II) Bis(1,3-Diketonates) and Tin(II) 1,3-Diketonate Chlorides. *Inorg. Nucl. Chem. Lett.* **1973**, *9*, 961-963.

(41)   *CRC Handbook of Chemistry and Physics*; 85th ed.; Lide, D. R., Ed.; CRC Press: Boca Raton, FL, 2005.

(42)   Hussain, M. M.; Song, S.-C.; Barnett, J.; Kang, C. Y.; Gebara, G.; Sassman, B.; Moumen, N. Plasma-Induced Damage in High-k/Metal Gate Stack Dry Etch. *IEEE Elect. Device Lett.* **2006**, *27*, 972-974.

(43)   Elam, J. W.; Groner, M. D.; George, S. M. Viscous Flow Reactor with Quartz Crystal Microbalance for Thin Film Growth by Atomic Layer Deposition. *Rev. Sci. Instrum.* **2002**, *73*, 2981-2987.

(44)   Lee, Y.; Yoon, B.; Cavanagh, A. S.; George, S. M. Molecular Layer Deposition of Aluminum Alkoxide Polymer Films Using Trimethylaluminum and Glycidol. *Langmuir* **2011**, *27*, 15155-15164.

(45)   Riha, S. C.; Libera, J. A.; Elam, J. W.; Martinson, A. B. F. Design and Implementation of an Integral Wall-Mounted Quartz Crystal Microbalance for Atomic Layer Deposition. *Rev. Sci. Instrum.* **2012**, *83*, 094101.

(46)   Olah, G. A.; Nojima, M.; Kerekes, I. Synthetic Methods and Reactions .2.
       Hydrofluorination of Alkenes, Cyclopropane and Alkynes with (Trialkylamine)
       Reagents. *Synthesis-Stuttgart* **1973**, *12*, 779-780.

(47)   Shannon, R. D.; Shannon, R. C.; Medenbach, O.; Fischer, R. X. Refractive Index and
       Dispersion of Fluorides and Oxides. *J. Phys. Chem. Ref. Data* **2002**, *31*, 931-970.

CHAPTER 6

Mechanism of Thermal Al$_2$O$_3$ Atomic Layer Etching Using Sequential Reactions with Sn(acac)$_2$ and HF

6.1. Introduction

Atomic layer etching (ALE) is a technique that can remove thin films with atomic layer control using sequential, self-limiting surface reactions.[1-3] ALE is the opposite of atomic layer deposition (ALD) which can provide conformal and atomic layer controlled film deposition.[4] ALD and ALE are both important techniques to provide thin film engineering at the atomic level.[5-6] ALE processes have been previously reported using ion-enhanced or energetic noble gas atom-enhanced surface reactions.[1-3] During these ALE processes, a halogen is first adsorbed on the surface of the material. Ion or noble gas atom bombardment is then used to desorb halogen compounds that etch the material. Based on this process, ALE has been reported for Si,[2-3,7-11] Ge,[6,12] and compound semiconductors.[13-16] ALE has also been demonstrated for a variety of metal oxides[17-21] and various carbon substrates.[22-24]

The ALE of Al$_2$O$_3$ was recently reported using sequential, self-limiting thermal reactions with Sn(acac)$_2$ and HF as the reactants.[25] The Al$_2$O$_3$ samples were Al$_2$O$_3$ atomic layer deposition (ALD) films grown using trimethylaluminum and H$_2$O. The HF source was HF-pyridine. The

linear removal of Al_2O_3 was observed at temperatures from 150-250°C without the use of ion or noble gas atom bombardment. An Al_2O_3 ALE etch rate of 0.27 Å/cycle was measured at 200°C.[25] The ALE etch rates also increased at higher temperatures. The $Sn(acac)_2$ and HF thermal reactions were both self-limiting versus exposure. The Al_2O_3 films also did not roughen versus number of Al_2O_3 ALE cycles.[25] In addition, the ALE of HfO_2 has also been recently demonstrated using $Sn(acac)_2$ and HF as the reactants.[26]

The overall Al_2O_3 etching reaction was proposed to follow the reaction: Al_2O_3 + $6Sn(acac)_2 + 6HF \rightarrow 2Al(acac)_3 + 6SnF(acac) + 3H_2O$.[25] In the surface reactions, the $Sn(acac)_2$ reactant was suggested to donate acac to the substrate to produce $Al(acac)_3$. The HF reactant was suggested to allow $SnF(acac)$ and H_2O to leave as reaction products.[25] An adlayer of AlF_3 was proposed to exist on the Al_2O_3 surface after HF exposures.[25] $Sn(acac)_2$ adsorption products were proposed to exist on the Al_2O_3 surface after $Sn(acac)_2$ exposures.

In this study, quartz crystal microbalance (QCM) measurements determined the Al_2O_3 etch rates and the mass changes after individual $Sn(acac)_2$ and HF exposures versus temperature. The temperature-dependence of the mass change per cycle (MCPC) and the individual mass changes during the $Sn(acac)_2$ and HF exposures helped to formulate a mechanism for Al_2O_3 ALE. In addition, FTIR vibrational spectroscopy analysis was able to monitor the Al_2O_3 etching and characterize the surface species after the $Sn(acac)_2$ and HF exposures. The combination of these QCM and FTIR studies leads to the understanding of the key reaction intermediates during Al_2O_3 ALE and the reaction mechanism for thermal Al_2O_3 ALE.

6.2. Experimental

6.2A. Viscous Flow Reactor Equipped for *in situ* QCM Measurements

Al_2O_3 ALE was monitored using *in situ* QCM experiments in a viscous flow reactor.[27] The QCM sensor was an RC-cut quartz crystal[28] (gold coated and polished, 6 MHz, Colnatec). This QCM sensor was mounted in the bakeable sensor head (BSH-150, Inficon) and then sealed with high temperature epoxy (Epo-Tek H21D, Epoxy technology). All the QCM measurements were recorded by a film deposition monitor (Maxtek TM-400, Inficon). The reactor temperature was maintained by a PID temperature controller (2604, Eurotherm) at 150-250°C during the reactions. The pressure in the reactor was measured using a bakeable capacitance manometer (Baratron 121A, MKS).

The reactor was pumped using a mechanical pump (Pascal 2015SD, Alcatel). A constant N_2 carrier gas flow of 150 sccm was streamed through the reactor. This N_2 gas flow was supplied by three separate mass flow controllers (Type 1179A, MKS). An additional N_2 purge gas flow of 20 sccm passed through the QCM housing and prevented deposition on the back side of the QCM sensor. The base pressure in the reactor resulting from the total N_2 gas flow of 170 sccm was ~1 Torr.

Al_2O_3 ALE was performed using tin(II) acetylacetonate ($Sn(acac)_2$, 37-38% Sn, Gelest) and HF-pyridine (70 wt% HF, Sigma-Aldrich) as the reactants. HF-pyridine is known as "Olah's reagent" and is a convenient reservoir for anhydrous HF.[29] The HF pressure from HF-pyridine is >2-3 Torr at room temperature. $Sn(acac)_2$ and HF-pyridine were transferred to stainless steel bubblers in a dry N_2-filled glove bag. The $Sn(acac)_2$ precursor was maintained at 100°C and produced a pressure transient of 15-20 mTorr using a pneumatic valve for dosing. The HF-

pyridine precursor was held at room temperature and produced a pressure transient of 80 mTorr using a two pneumatic valves and one metering valve for dosing.

The Al_2O_3 films were grown on the QCM sensor by Al_2O_3 ALD. The Al_2O_3 ALD films were grown using at least 100 cycles of Al_2O_3 ALD using TMA (97 %, Sigma-Aldrich) and H_2O (deionized water, Chromasolv for HPLC, Sigma-Aldrich). The TMA and H_2O precursors were held at room temperature. The Al_2O_3 films were grown on the QCM sensor before each ALE reaction.

6.2B. FTIR Spectroscopy Measurements

The *in situ* FTIR studies were performed in a reactor equipped with an FTIR spectrometer that has been described previously.[30] The reactor was pumped using a mechanical pump (TRIVAC D8B , Oerlikon Leybold Vacuum). The FTIR spectrometer (Nicolet 6700 FTIR, Thermo Scientific) utilized a liquid-N_2-cooled mercury cadmium telluride (MCT-B) detector. Dry, CO_2-free air was employed to purge the spectrometer, mirror, and detector setup. Each spectrum consisted of a total of 100 scans at 4 cm^{-1} resolution from 400 to 4000 cm^{-1}.

The transmission FTIR measurements were performed on high surface area ZrO_2 nanoparticles (99.95%, US Research Nanomaterials Inc.) with an average diameter of 20 nm and high surface area SiO_2 nanoparticles (99.5%, US Research Nanomaterials Inc.) with an average diameter of 15-20 nm. The ZrO_2 nanoparticles absorb infrared radiation between ~400-800 cm^{-1}. The SiO_2 nanoparticles absorb infrared radiation between 400-650 cm^{-1}, 700-875 cm^{-1}, and 925-1400 cm^{-1}. These absorption regions leave open available windows to observe absorbance from the species in Al_2O_3 ALD and Al_2O_3 ALE. The high surface area of these nanoparticles was needed to enhance the signal-to-noise ratio.[31] Sample preparation involved pressing the ZrO_2 or

SiO_2 nanoparticles into a tungsten grid support (Tech-Etch).[31-32] The tungsten grids had dimensions of 2×3 cm^2. Each grid was 50 μm thick with 100 grid lines per inch.

The tungsten grid could be resistively heated using a DC power supply (6268B, 20V/20A, Hewlett-Packard). The voltage output of the power supply was controlled by a PID temperature controller (Love Controls 16B, Dwyer Instruments, Inc.). A type K thermocouple was attached to the bottom of the tungsten grid with epoxy (Ceramabond 571, Aremco) that attached and electrically isolated the thermocouple.

A consistent cleaning procedure of the ZrO_2 nanoparticles/grid support was used to produce a reproducible starting surface. Prior to film deposition, the temperature of the sample support was increased to 500°C for ~2 minutes to degas and clear adventitious carbon from the ZrO_2 nanoparticles. Since this procedure also depleted the hydroxyl groups from the ZrO_2 surface, a ~2 s H_2O dose was used to rehydroxylate the surface. This procedure consistently removed any carbon-related vibrational modes and resulted in a clean ZrO_2 starting surface with absorbances attributed only to the O-H stretching vibrations and bulk ZrO_2 modes. This cleaning procedure was not utilized for the SiO_2 nanoparticles because rehydroxylation of the SiO_2 surface is very difficult following dehydroxylation.[33]

The Al_2O_3 ALE reactions were performed using sequential exposures of tin(II) acetylacetonate ($Sn(acac)_2$, 37-38% Sn, Gelest) and HF-pyridine (70 wt% HF, Sigma-Aldrich). Static dosing of the ALE precursors was utilized to achieve self-limiting behavior on the high surface area particle substrates. Each $Sn(acac)_2$ exposure consisted of a ~1.0 Torr static dose for 15 s followed by a 120 s purge. Each HF-pyridine exposure consisted of a ~1.5 Torr static dose for 15 s followed by a 120 s purge. The Al_2O_3 films were grown by Al_2O_3 ALD using TMA (97 %, Sigma-Aldrich) and H_2O (Chromasolv for HPLC, Sigma-Aldrich). The HF-pyridine,

TMA, and H_2O precursors were maintained at room temperature. The stainless steel bubbler containing $Sn(acac)_2$ was held at 100℃.

For a direct comparison between the FTIR studies at different temperatures, the sample remained fixed during Al_2O_3 ALD and Al_2O_3 ALE. An Al_2O_3 film was grown using 10 cycles of Al_2O_3 ALD at 200℃. Subsequently, 10 cycles of Al_2O_3 ALE were performed at 200℃ followed by 8 cycles of Al_2O_3 ALE at both 250℃ and 300℃. The FTIR spectra monitored at 250℃ and 300℃ were recorded during the last two cycles of Al_2O_3 ALE.

6.3. Results and Discussion

6.3A. QCM Measurements versus Temperature

Figure 1 displays the mass change during 100 ALE cycles of Al_2O_3 using $Sn(acac)_2$ and HF reactions at 150℃, 175℃, 200℃, 225℃, and 250℃. A report of some of these QCM results was presented earlier.[25] The initial Al_2O_3 ALD films were grown by 100 cycles of Al_2O_3 ALD using TMA and H_2O with a sequence of 1-20-1-20. One ALE cycle consisted of a $Sn(acac)_2$ exposure of 1 s, an N_2 purge of 30 s, a HF exposure of 1 s, and a second N_2 purge of 30 s. This reaction sequence is represented as 1-30-1-30.

The mass changes versus time during Al_2O_3 ALE are very linear for all temperatures. The mass change per cycle (MCPC) increases with temperature from -4.1 ng/(cm^2 cycle) at 150℃ to -18.3 ng/(cm^2 cycle) at 250℃.[25] These MCPCs correspond to etch rates that vary from 0.14 Å/cycle at 150℃ to 0.61 Å/cycle at 250℃. The determination of these etch rates is based on the Al_2O_3 ALD film density of 3.0 g/cm^3.
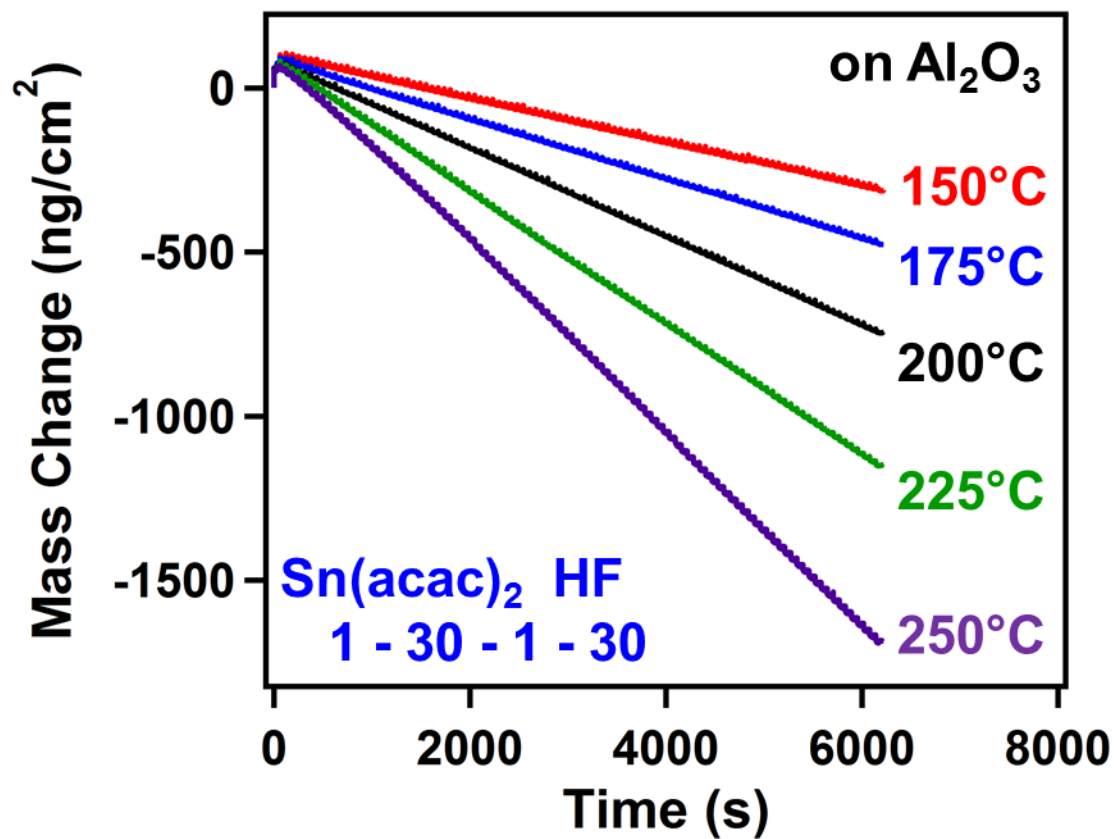
Figure 6-1   Mass change versus time for Al_2O_3 ALE using sequential $Sn(acac)_2$ and HF

exposures at 150, 175, 200, 225 and 250°C.

Figure 2a, 2b, and 2c shows an enlargement of the mass changes during three cycles in the steady state etching regime for Al_2O_3 ALE at 150°C, 200°C, and 250°C, respectively, in Figure 1. Figure 2a shows a gradual mass decrease after a small mass gain during the $Sn(acac)_2$ exposure at 150°C. A small mass gain of ΔM_{Sn} = +0.19 ng/cm^2 was observed after the $Sn(acac)_2$ exposure for 1 s at 150°C. This behavior suggests $Sn(acac)_2$ adsorption followed by either the removal of reaction products and/or $Sn(acac)_2$ desorption. In contrast, a mass decrease of ΔM_{HF} = -4.3 ng/cm^2 was observed after the HF exposure for 1 s at 150°C. This mass decrease is consistent with the removal of $Sn(acac)_2$ surface reaction products.

The mass changes are different at 200°C. After a $Sn(acac)_2$ exposure for 1 s at 200°C, Figure 2b shows a mass loss of ΔM_{Sn} = -8.1 ng/cm^2. In addition, an HF exposure for 1 s leads to a small mass loss of ΔM_{HF} = -0.28 ng/cm^2. The mass changes continue to evolve at 250°C. Figure 2c shows a larger mass loss of ΔM_{Sn} = -24.0 ng/cm^2 after 1 s of $Sn(acac)_2$ exposure at 250°C. In contrast, the HF exposure leads to a mass gain instead of a mass loss. A mass gain of ΔM_{HF} = +5.7 ng/cm^2 was observed after 1 s of HF exposure.

The differences between the mass changes at different temperatures can be qualitatively understood in terms of more stable $Sn(acac)_2$ surface reaction products at lower temperature and more AlF_3 formation at higher temperatures. If more surface species remain following $Sn(acac)_2$ exposures at lower temperatures, then there is a mass gain after the $Sn(acac)_2$ reaction and more surface species that can be lost during the HF reaction. Likewise, larger mass losses after the $Sn(acac)_2$ exposure and mass gains following the HF exposure at higher temperature can be qualitatively understood in terms of AlF_3 formation. More AlF_3 may form by the reaction of HF with Al_2O_3 at higher temperatures. This AlF_3 layer is then removed by the $Sn(acac)_2$ exposure and leads to a pronounced mass loss.
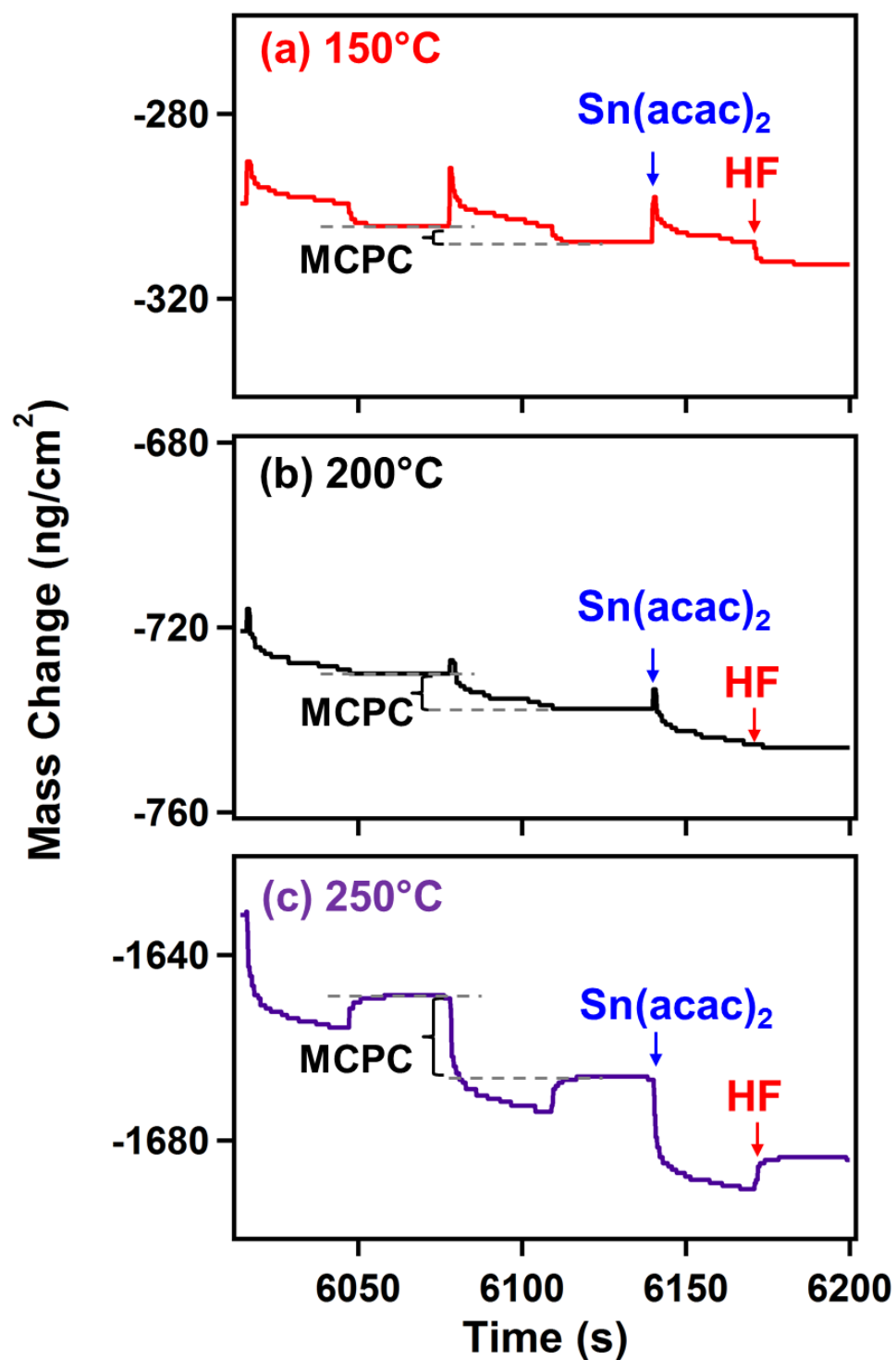
Figure 6-2   Expansion of linear region of Figure 6-1 showing the individual mass changes during the sequential Sn(acac)$_2$ and HF exposures at 150, 200 and 250°C.

Figure 3 shows the MCPC and the ΔM_{Sn}/MCPC ratio during 100 cycles at 200°C. The MCPC is defined by MCPC = $\Delta M_{Sn} + \Delta M_{HF}$. Figure 3a displays ΔM_{Sn}, ΔM_{HF} and MCPC for the same 100 cycles of Al_2O_3 ALE reaction on the Al_2O_3 surface at 200°C as shown in Figure 1. The MCPC reaches a steady-state value of -8.4 ng/(cm^2 cycle) after 3 cycles of a nucleation. Figure 3b displays the ΔM_{Sn}/MCPC ratio during the same 100 cycles. The ΔM_{Sn} /MCPC ratio reaches a steady-state value of 0.97 after 3 cycles of nucleation. The ΔM_{Sn} /MCPC ratio will be used to describe the stoichiometry of the Al_2O_3 ALE reactions.

ΔM_{Sn}, ΔM_{HF}, MCPC, and the ΔM_{Sn}/MCPC ratio at 150-250°C are summarized in Table 1. All temperatures display a mass loss and the mass loss is larger at higher temperatures. The mass change after the $Sn(acac)_2$ exposure, ΔM_{Sn}, is mostly responsible for the temperature dependence of the MCPC. An Arrhenius plot is employed to characterize this temperature dependence. Figure 4a shows the Arrhenius plot for the temperature-dependent MCPC. This Arrhenius plot yields an activation of 6.6 ± 0.4 kcal/mole for Al_2O_3 ALE.
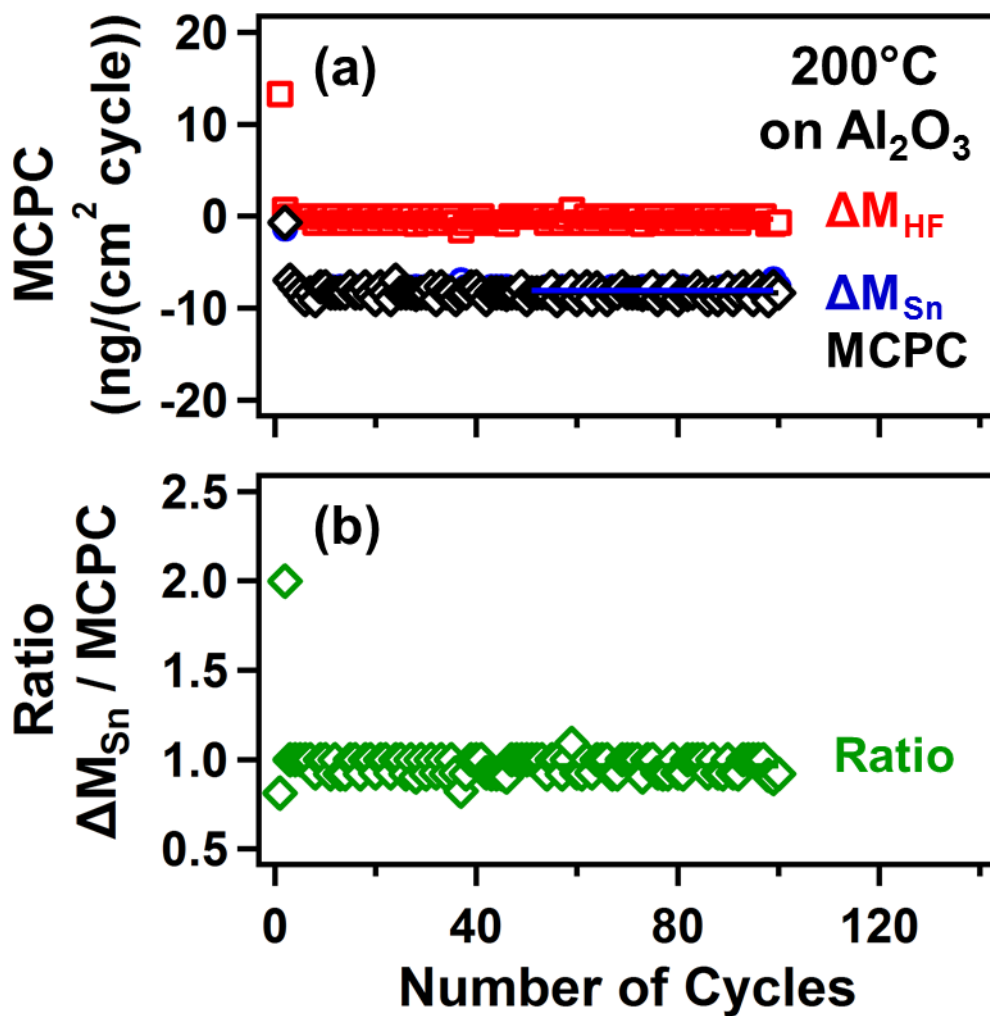
Figure 6-3   (a) Mass change after the Sn(acac)$_2$ exposure (ΔM_{Sn}), mass change after the HF

exposure (ΔM_{HF}) and mass change per cycle (MCPC) versus number of ALE

cycles at 200℃. (b) ΔM_{Sn}/MCPC ratio versus number of ALE cycles.
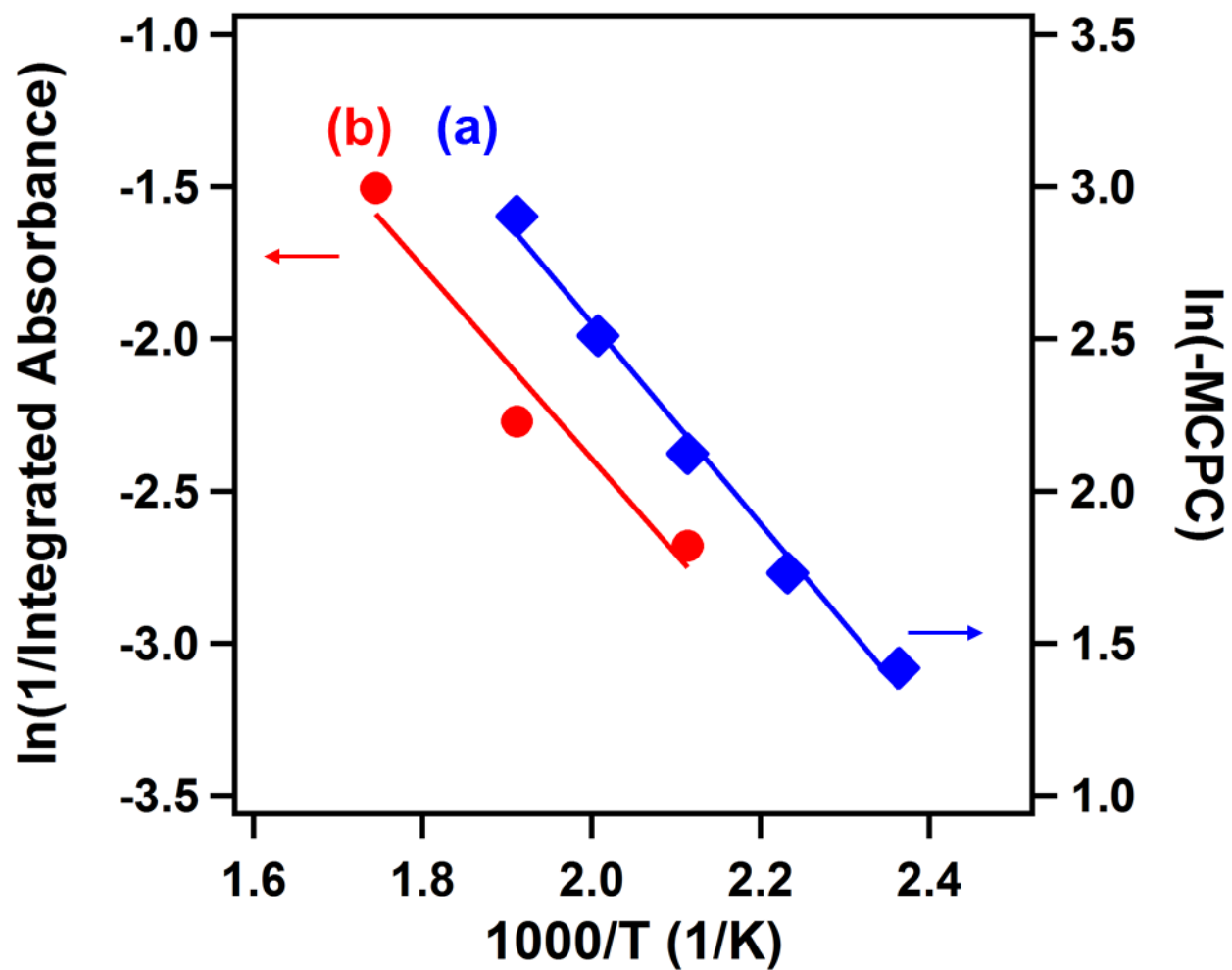
Figure 6-4   (a) Arrhenius plot of the MCPC. The slope yields an activation barrier of E= 6.6

kcal/mole. (b) Arrhenius plot of 1/(integrated absorbance) for the acetylacetonate

vibrational features. The slope yields an activation barrier of E= 6.2 kcal/mole.

Temperature (°C)	MCPC	ΔM_{Sn}	ΔM_{HF}	ΔM_{Sn}/MCPC	x	x(MCPC)
150	-4.1	0.19	-4.3	-0.067	0.74	-3.0
175	-5.6	-3.2	-2.4	0.57	0.46	-2.6
200	-8.4	-8.1	-0.28	0.97	0.29	-2.4
225	-12.3	-14.6	2.3	1.2	0.19	-2.4
250	-18.3	-24.0	5.7	1.3	0.15	-2.7

Table 6-1. ΔM_{Sn}, ΔM_{HF}, MCPC, ΔM_{Sn}/MCPC, x, and x(MCPC) for Al_2O_3 ALE at different temperatures. ΔM_{Sn}, ΔM_{HF}, MCPC, and x(MCPC) are expressed in units of ng/(cm^2 cycle).

6.3B. FTIR Studies of Al₂O₃ ALE

In situ FTIR spectra of Al_2O_3 films grown on ZrO_2 nanoparticles using 10 Al_2O_3 ALD cycles at 200°C are shown in Figure 5. These FTIR spectra are referenced to the initial ZrO_2 nanoparticles. The absorbance feature between 800-1000 cm^{-1} is attributed to the Al-O stretching vibrations in bulk Al_2O_3. The absorbance of the Al-O stretching vibrations in amorphous Al_2O_3 is broad and ranges from ~550-1030 cm^{-1}. [31,34-36] The breadth of this expected absorbance feature is not observed in Figure 5. The strong absorption from the ZrO_2 nanoparticles at $\leq$ 800 cm^{-1} partially obscures the infrared absorbance of the Al-O stretching vibrations. The absorbance feature for the Al-O stretching vibration grows progressively with the Al_2O_3 ALD cycles.

FTIR spectra during the etching of the Al_2O_3 ALD films on the ZrO_2 nanoparticles at 200°C are shown in Figure 6. These FTIR spectra were recorded after the Sn(acac)₂ exposures and are referenced to the initial ZrO_2 nanoparticles. The absorbance feature from the Al-O stretching vibrations between 800-1000 cm^{-1} decreases progressively with Al_2O_3 ALE cycles. Infrared absorbance features also appear between 1250-1650 cm^{-1} that are attributed to acetylacetonate vibrations from the Sn(acac)₂ surface reaction products.[34-35] The absorbance from these acetylacetonate vibrations remains approximately constant after the Sn(acac)₂ exposures versus number of Al_2O_3 ALE cycles.

The FTIR spectra of the absorbance from the acetylacetonate vibrations during Al_2O_3 ALE at 200, 250 and 300°C are shown after Sn(acac)₂ and HF exposures in Figure 7a and Figures 7b, respectively. The absorbance from the acetylacetonate surface species, such as SnF(acac)*, Sn(acac)* or acac*, decreases at higher temperatures after the Sn(acac)₂ exposures
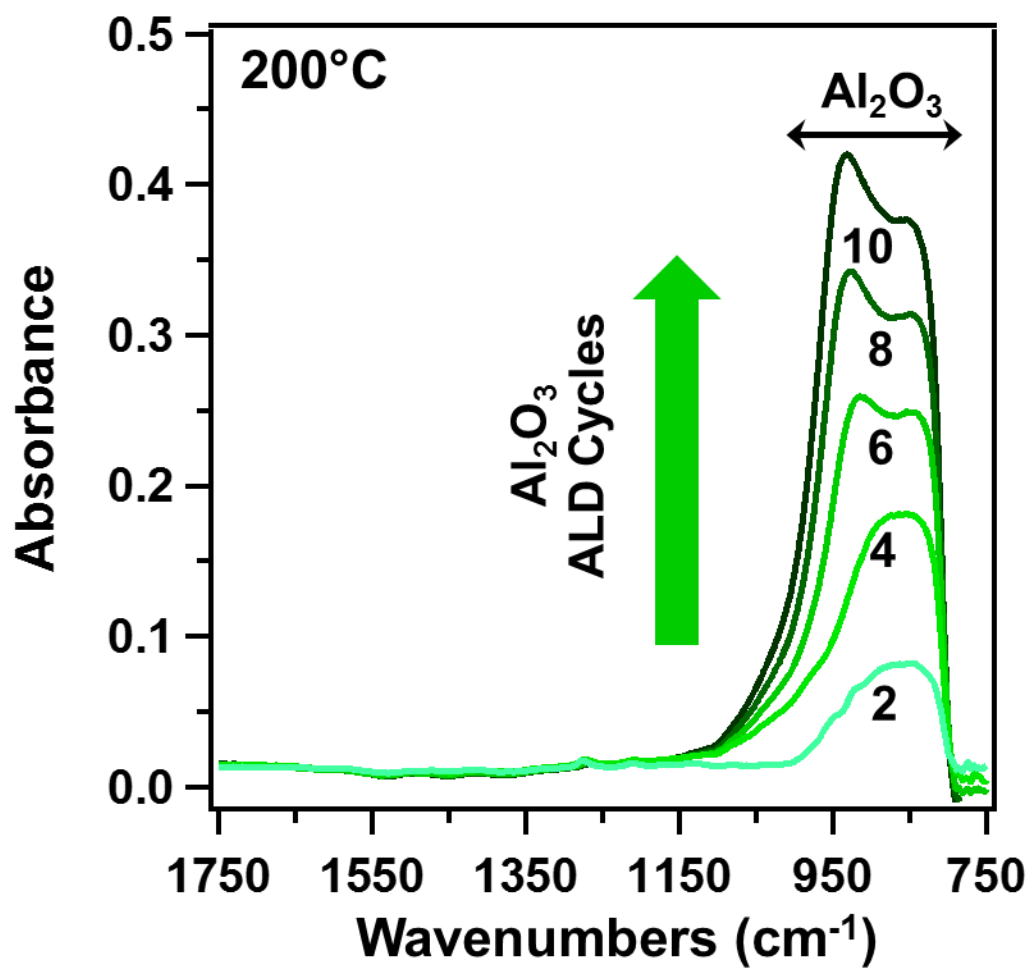
Figure 6-5   Infrared absorbance showing the growth of Al-O stretching vibrations in bulk

Al_2O_3 versus number of Al_2O_3 ALD cycles at 200°C. These FTIR spectra were

referenced to the initial ZrO_2 nanoparticles.
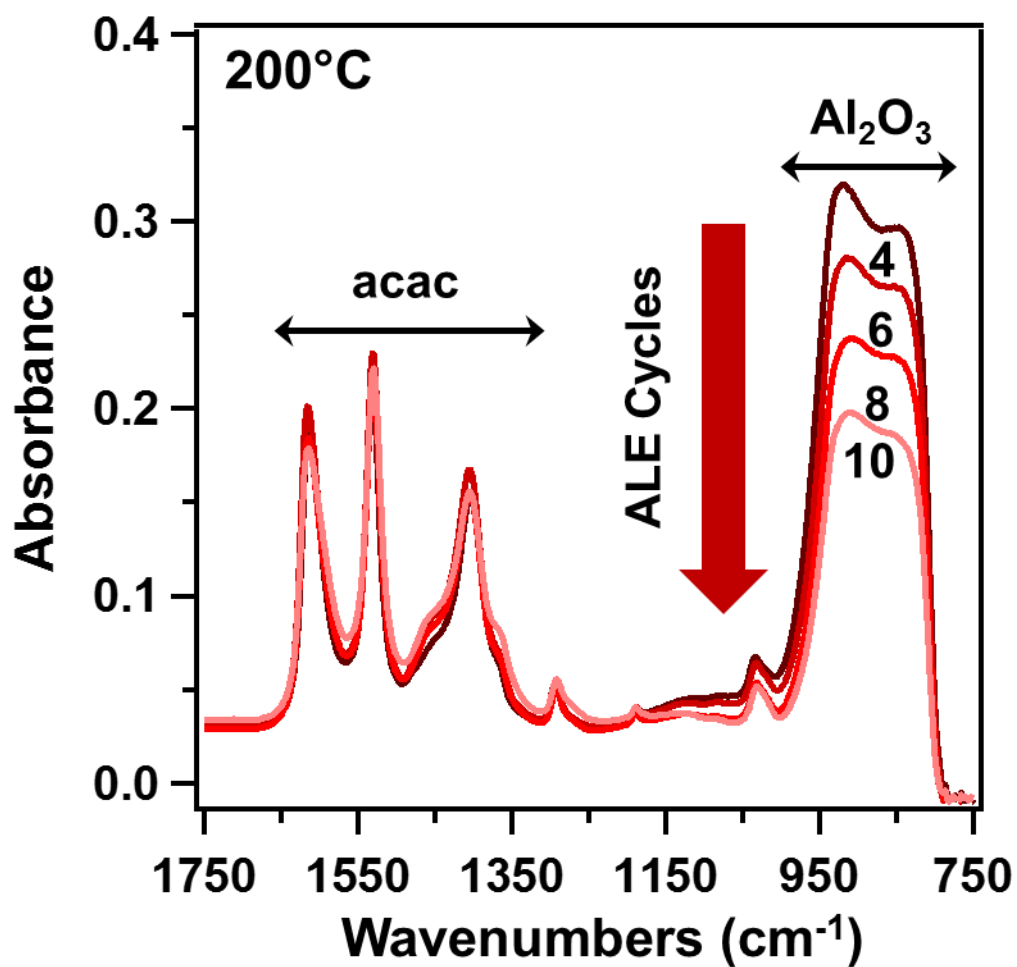
Figure 6-6   Infrared absorbance showing the loss of Al-O stretching vibration in bulk Al_2O_3

versus number of Al_2O_3 ALE cycles at 200°C. These FTIR spectra were

referenced to the initial ZrO_2 nanoparticles.
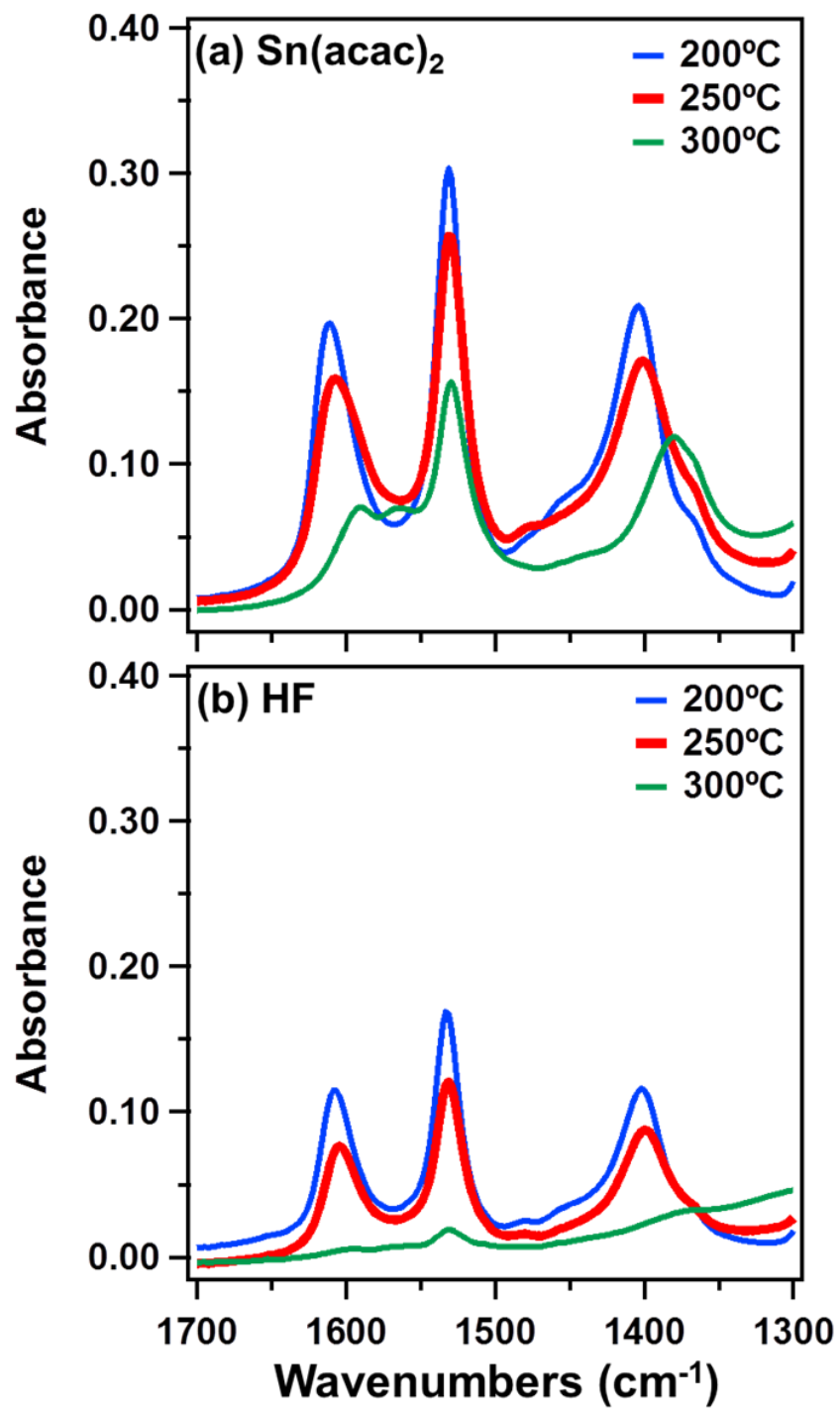
Figure 6-7   Infrared absorbance from the acetylacetonate vibrations during Al_2O_3 ALE at 200,

250 and 300°C after (a) $Sn(acac)_2$ exposures and after (b) HF exposures. These

FTIR spectra were referenced to the initial ZrO_2 nanoparticles.

in Figure 7a. The astericks are used to indicate surface species. This behavior illustrates that the Sn(acac)$_2$ surface reaction products are more stable at lower surface temperatures.

Figure 7b reveals that the absorbances from the acetylacetonate vibrational features are much lower following the HF exposures. The loss of acetylacetonate vibrational features is expected because HF is believed to react with acetylacetonate species to produce volatile reaction products such as SnF(acac). The absorbance of the remaining acetylacetonate species after HF exposures also decreases dramatically at 300°C. This behavior indicates that HF exposures are able to remove nearly all the acetylacetonate species at 300°C.

6.3C. Studies of Al$_2$O$_3$ ALE Nucleation

QCM and FTIR measurements were employed to study the nucleation of Al$_2$O$_3$ ALE during the first Sn(acac)$_2$ and HF exposures. Figure 8 shows an enlargement of mass changes during the first two Al$_2$O$_3$ ALE cycles for the various temperatures in Figure 1. The first Sn(acac)$_2$ exposure displays mass gains of ΔM_{Sn} = 52-61 ng/cm^2 at 150-250°C resulting from Sn(acac)$_2$ surface reaction products on the Al$_2$O$_3$ film such as Sn(acac)* and acac*. To estimate the coverage of Sn(acac)$_2$* species on the surface, the sites on the Al$_2$O$_3$ surface can be approximated using the density of 3.0 g/cm^3 for Al$_2$O$_3$ ALD films. This mass density is equivalent to a number density of ρ= 1.77 $\times$ 10^{22} "Al$_2$O$_3$ units"/cm^3. This number density yields an estimate for the number of "Al$_2$O$_3$ units" on the Al$_2$O$_3$ surface of $\rho^{2/3}$ = 6.80 $\times$ 10^{14} "Al$_2$O$_3$ units"/cm^2 assuming a square lattice. This coverage of "Al$_2$O$_3$ units" represents an Al$_2$O$_3$ mass of 115 ng/cm^2.
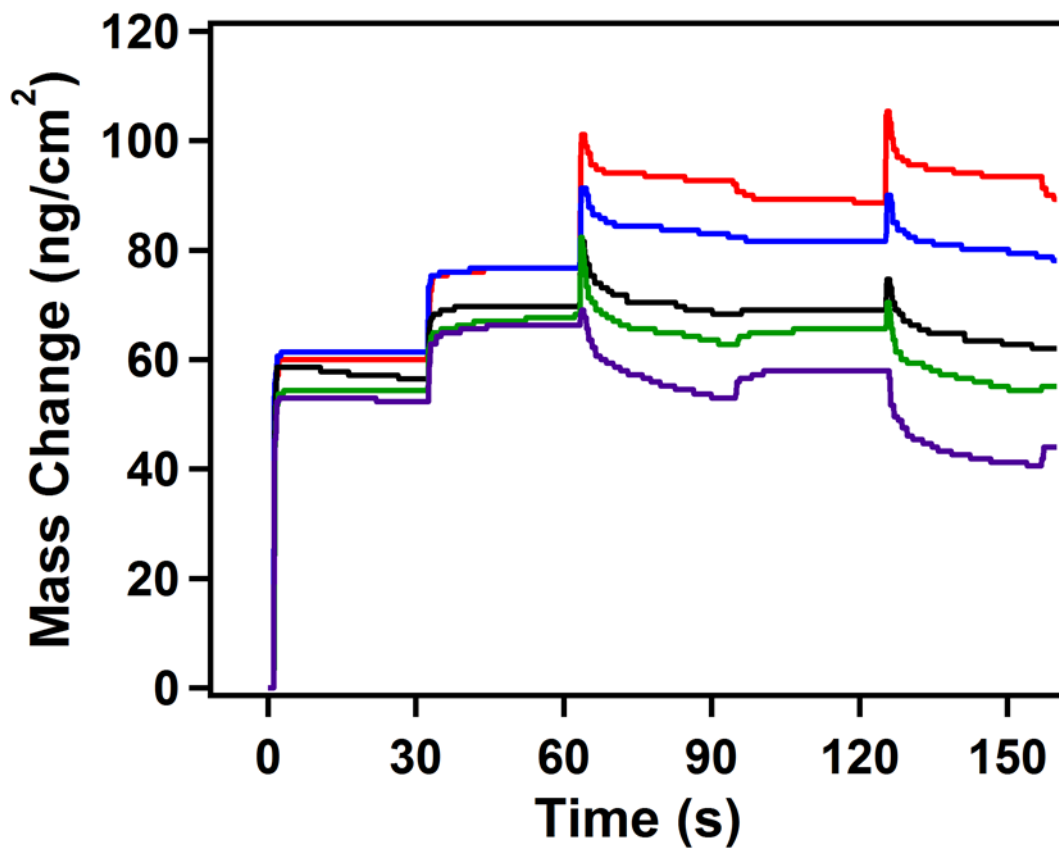
Figure 6-8 Expansion of first two ALE cycles in Figure 1 showing the individual mass

changes during the sequential Sn(acac)$_2$ and HF exposures at 150, 175, 200, 225

and 250°C.

The coverage of Sn(acac)$_2$* can then be approximated based on the mass gain of 61 ng/cm^2. This mass gain is equivalent to 1.16×10^{14} Sn(acac)$_2$ molecules/cm^2. The normalized coverage of Sn(acac)$_2$* species relative to "Al$_2$O$_3$ units" on the surface is 1.16×10^{14} Sn(acac)$_2$ molecules/cm^2 / 6.80×10^{14} "Al$_2$O$_3$ units"/cm^2 = 0.17 Sn(acac)$_2$ species/ "Al$_2$O$_3$ unit". This coverage is reasonable given that Sn(acac)$_2$ may dissociate into Sn(acac)* and acacH*. In addition, the acetylacetonate ligand is bulky and expected to occupy more than one "Al$_2$O$_3$ unit" on the Al$_2$O$_3$ surface.

The first HF exposure on the Al$_2$O$_3$ surface previously exposed to Sn(acac)$_2$ shows mass gains of ΔM_{HF} = 13-17 ng/cm^2 at 150-250°C. In contrast, the first HF exposure on a fresh Al$_2$O$_3$ surface prior to Sn(acac)$_2$ exposures shows mass gains of ΔM_{HF} = 35-38 ng/cm^2 at 150-250°C. The difference between these mass gains is caused by the amount of Sn(acac)$_2$ reaction products that are removed by the HF exposures and result in a mass loss.

The coverage of HF or HF reaction products can be approximated based on the mass gain of 38 ng/cm^2 following HF exposures on fresh Al$_2$O$_3$ surfaces. Assuming that HF is the adsorption product, the mass gain is equivalent to 1.14×10^{15} HF molecules/cm^2. The normalized coverage of HF species relative to "Al$_2$O$_3$ units" on the surface is (1.14×10^{15} HF molecules/cm^2) / (6.80×10^{14} "Al$_2$O$_3$ units"/cm^2) = 1.68 HF/"Al$_2$O$_3$ unit". This estimated HF coverage is larger than the number of "Al$_2$O$_3$ units" on the Al$_2$O$_3$ substrate.

The HF may also react with the Al$_2$O$_3$ substrate by the reaction: Al$_2$O$_3$ + 6HF → 2AlF$_3$ + 3H$_2$O. The reaction of HF with γ-Al$_2$O$_3$ to produce AlF$_3$ has been observed 250°C.[36] This reaction is predicted to be spontaneous over the temperature range from 150-250°C.[37] The Gibbs free energy changes are negative and decrease slightly in absolute magnitude from ΔG= -63.1 kcal at 150°C to ΔG = -53.8 kcal at 250°C.[37]

Assuming that AlF_3 is the reaction product, the mass gain of 38 ng/cm² is equivalent to an AlF_3 coverage of 6.93×10^{14} AlF_3 molecules/cm². The normalized coverage of AlF_3 relative to "Al_2O_3 units" on the surface is (6.93×10^{14} AlF_3 molecules/cm²) / (6.80×10^{14} "Al_2O_3 units"/cm²) = 1.02 AlF_3 / "Al_2O_3" unit. This estimated AlF_3 coverage is very similar to the number of "Al_2O_3 units" on the Al_2O_3 substrate.

After the HF exposure, the next $Sn(acac)_2$ exposure reacts with the AlF_3 or HF adlayer on the Al_2O_3 substrate. Figure 8 shows that mass losses begin with this second $Sn(acac)_2$ exposure and continue with the subsequent HF exposure. Except for the first ALE cycle shown in Figure 8, all subsequent $Sn(acac)_2$ and HF exposures lead to mass loss resulting from the etching of the Al_2O_3 film.

The nucleation of the Al_2O_3 ALE process was also observed by the FTIR studies. Figure 9 shows the FTIR spectra during the first Al_2O_3 ALE cycle. These FTIR spectra are referenced to the initial ZrO_2 nanoparticles. The infrared absorbance corresponding to the Al-O stretching vibration in bulk Al_2O_3 between 800-1000 cm^{-1} decreases slightly with the first $Sn(acac)_2$ exposure. This decrease is attributed to $Sn(acac)_2$ adsorbing on the thin Al_2O_3 film and perturbing the Al-O vibrational modes. Pronounced vibrational features associated with acetylacetonate species on the Al_2O_3 substrate at 1250-1650 cm^{-1} are also observed in Figure 9 after the $Sn(acac)_2$ exposure.[34-35]
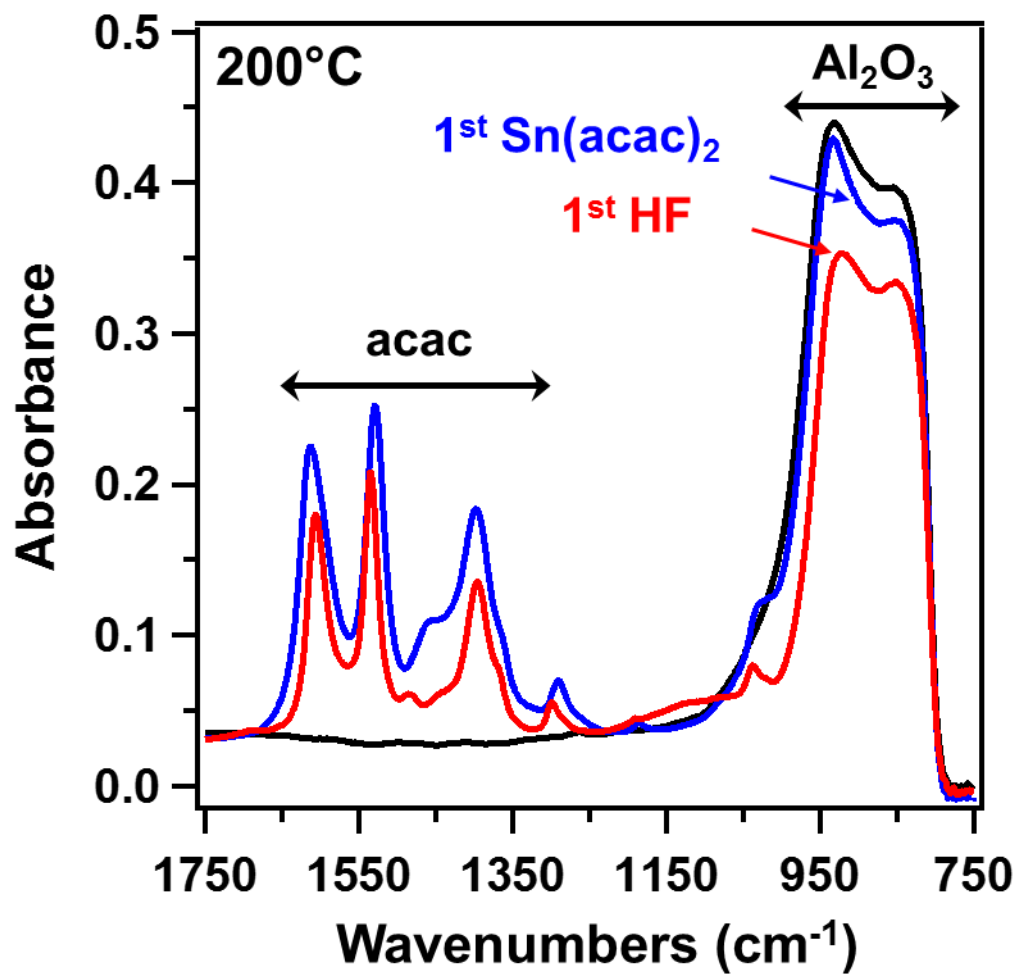
Figure 6-9   Infrared absorbance showing the Al-O stretching vibrations in bulk Al_2O_3 and the acetylacetonate vibrational features for the first $Sn(acac)_2$ and HF exposures at 200°C. These FTIR spectra were referenced to the initial ZrO_2 nanoparticles.

Figure 9 also shows that an additional reduction occurs in absorbance features corresponding to the Al-O vibrational modes after the first HF exposure. This reduction is consistent with the conversion of some Al_2O_3 to AlF_3. Figure 9 also shows that the vibrational features of the acetylacetonate species are also decreased after the first HF exposure. This decrease is consistent with HF reacting with the $Sn(acac)_2$ surface reaction products to remove some acetylacetonate species from the Al_2O_3 substrate.

Figure 10 displays the infrared absorbance spectra after the first $Sn(acac)_2$ exposure and first HF exposure on Al_2O_3 films at 200°C. In contrast to Figures 5, 6 and 9, these FTIR experiments were performed on SiO_2 nanoparticles. Unlike ZrO_2 nanoparticles that absorb infrared radiation between ~400-800 cm^{-1}, SiO_2 nanoparticles absorb infrared radiation between 925-1400 cm^{-1}, 700-875 cm^{-1}, and 400-650 cm^{-1}. The SiO_2 nanoparticles have an open window at lower frequency to observe the species involved in Al_2O_3 ALD and Al_2O_3 ALE.

The spectra in Figure 10 were referenced to the SiO_2 nanoparticles and the Al_2O_3 ALD film that coated the SiO_2 nanoparticles. The acetylacetonate features were again observed at 1250-1650 cm^{-1}. In addition, an absorbance feature at 500-800 cm^{-1} appeared after the 1st HF exposure. This feature was assigned to the Al-F stretching vibration in the AlF_3 layer that forms from Al_2O_3 during the HF exposure.[38-40] There was also an absorbance loss observed at ~1000 cm^{-1} that corresponds with the removal of some absorbance from the Al-O stretching vibration in Al_2O_3 upon AlF_3 formation.

Figure 11 displays the FTIR spectra during Al_2O_3 ALE at 200°C, 250°C and 300°C. These spectra were again referenced to the SiO_2 nanoparticles coated with the Al_2O_3 ALD film.
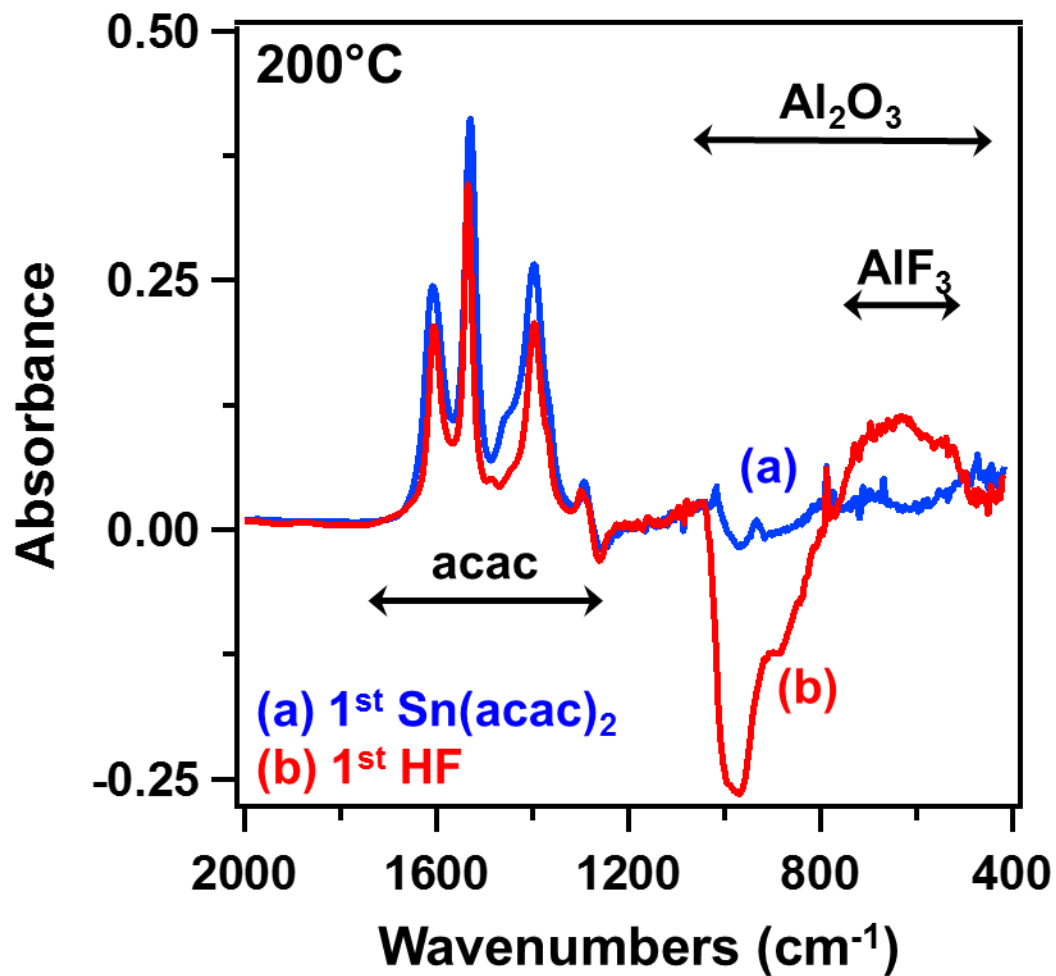
Figure 6-10 Infrared absorbance after the first Sn(acac)$_2$ exposure and first HF exposure on an

Al$_2$O$_3$ film at 200°C. These FTIR spectra were referenced to the SiO$_2$

nanoparticles coated with the Al$_2$O$_3$ film.
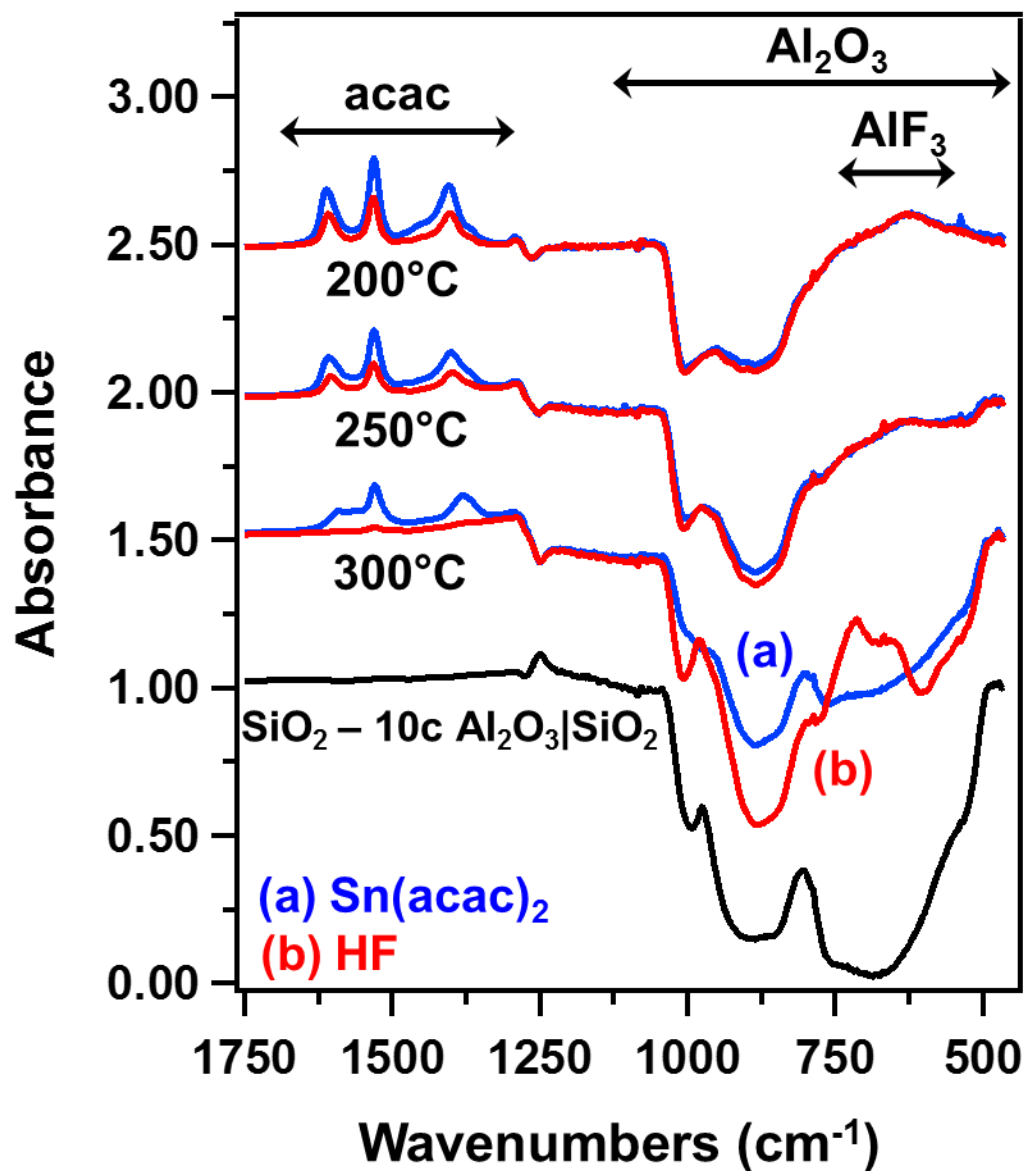
Figure 6-11   Infrared absorbance during Al_2O_3 ALE at 200°C, 250°C and 300° recorded after

the Sn(acac)₂ exposures and HF exposures. These FTIR spectra were referenced

to the SiO₂ nanoparticles coated with the Al_2O_3 film.

Spectra are shown after both the Sn(acac)$_2$ exposures and HF exposures. The absorbance feature

from acetylacetonate surface species at 1250-1650 cm^{-1} were present after all the Sn(acac)$_2$

exposures. The acetylacetonate surface species decreased with increasing temperature after both

Sn(acac)$_2$ and HF exposures. In addition, the acetylacetonate surface species were nearly

completely removed from the surface by the HF exposure at 300℃.

Figure 11 also reveals that a loss from the absorbance feature assigned to the Al-O

stretching vibration in Al$_2$O$_3$ occurs at 200℃, 250℃ and 300℃. This loss appears at 825-1050

cm^{-1} because the absorbance gain from the Al-F stretching vibrations of AlF$_3$ at 500-800 cm^{-1}

partially obscures the loss from the Al-O stretching vibrations in Al$_2$O$_3$ at lower frequencies.

The spectra after the Sn(acac)$_2$ and HF exposures in the region from 500-1050 cm^{-1} were not

substantially different at 200℃ and 250℃. In contrast, the spectra were distinctly different at

300℃ where the absorbance from the Al-F stretching vibration is nearly completely removed

after the Sn(acac)$_2$ exposure and then reappears after the HF exposure. The spectrum at the

bottom of Figure 11 is provided for reference and shows the expected absorbance loss

corresponding to 10 cycles of Al$_2$O$_3$ ALD.

Figure 12 shows the difference infrared absorbance spectra during Al$_2$O$_3$ ALE at 200℃,

250℃ and 300℃. Spectra are displayed after both the Sn(acac)$_2$ exposures and HF exposures.

These difference spectra correspond to the absolute spectra shown in Figure 11. These

difference spectra are referenced with respect to the sample after the previous reactant exposure.

The difference spectra in Figure 12 highlight the absorbance changes that occur during

the sequential ALE reactions. The absorbance changes for the acetylacetonate surface species

are nearly equal and mirror images of each other after the Sn(acac)$_2$ and HF exposures at 200℃,
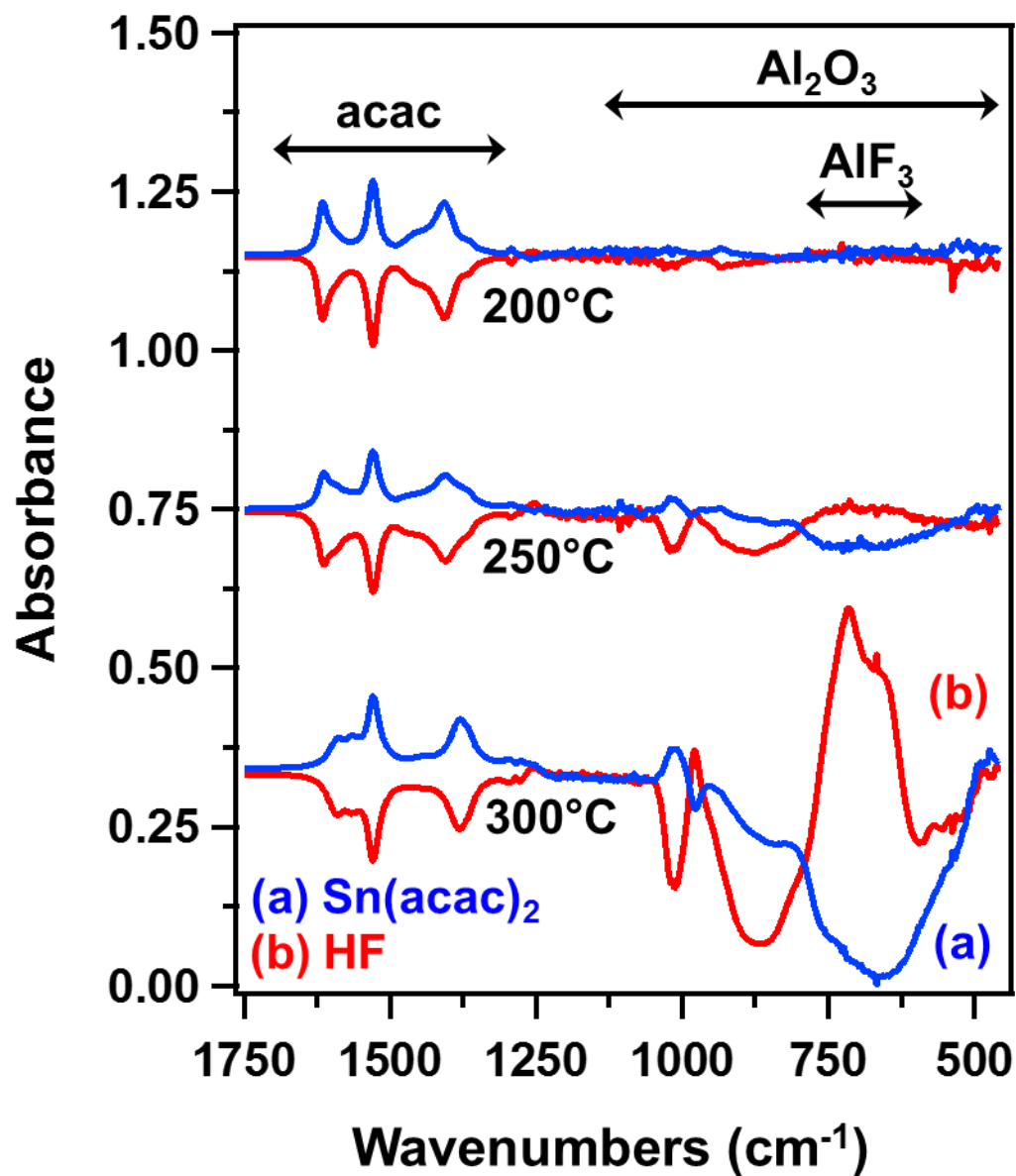
Figure 6-12 Difference infrared absorbance during Al$_2$O$_3$ ALE at 200°C, 250°C and 300°C. The difference spectra recorded after the Sn(acac)$_2$ and HF exposures were referenced using the spectra after the previous HF and Sn(acac)$_2$ exposures, respectively.

250°C and 300°C. In contrast, the absorbance from Al-F vibrations in the AlF$_3$ adlayer shows little change at 200°C and nearly mirror image changes after the Sn(acac)$_2$ and HF exposures at 250°C. At 300°C, the absorbance for the Al-F stretching vibration dramatically appears after the HF exposure and is lost after the Sn(acac)$_2$ exposure.

6.3D. Proposed Al$_2$O$_3$ ALE Reaction Mechanism

Figure 13 shows the schematic for the proposed Al$_2$O$_3$ ALE surface chemistry. This possible picture for Al$_2$O$_3$ ALE is derived from the mass changes during the Sn(acac)$_2$ and HF exposures as determined by the QCM measurements and the vibrational absorbances observed by the FTIR spectroscopy analysis. This scheme does not include species, such as possible acetylacetonate species, that do not change during the Sn(acac)$_2$ and HF exposures. This scheme also assumes that the HF reaction produces AlF$_3$ on the Al$_2$O$_3$ film.

During the Sn(acac)$_2$ reaction (A), Sn(acac)$_2$ reacts with the AlF$_3$ layer on the Al$_2$O$_3$ substrate. The reaction between Sn(acac)$_2$ and AlF$_3$ is probably facilitated by Lewis acid-base interactions. The electron lone pair on Sn(acac)$_2$ acts as a Lewis base.[41] AlF$_3$ is strong Lewis acid either as a molecule or as a molecular solid.[42-44] The reaction between Sn(acac)$_2$ and AlF$_3$ forms volatile SnF(acac) and Al(acac)$_3$ reaction products and SnF(acac)* surface species.

After the AlF$_3$ layer is lost resulting from Al(acac)$_3$ and SnF(acac) product formation, there may be a strong interaction between the SnF(acac)* surface species and the underlying Al$_2$O$_3$ substrate. The electron lone pair on SnF(acac)* can again act as a Lewis base and bind on Lewis acid sites on Al$_2$O$_3$. This interaction may lead to SnF(acac)* species adsorbed to the Al$_2$O$_3$ substrate.
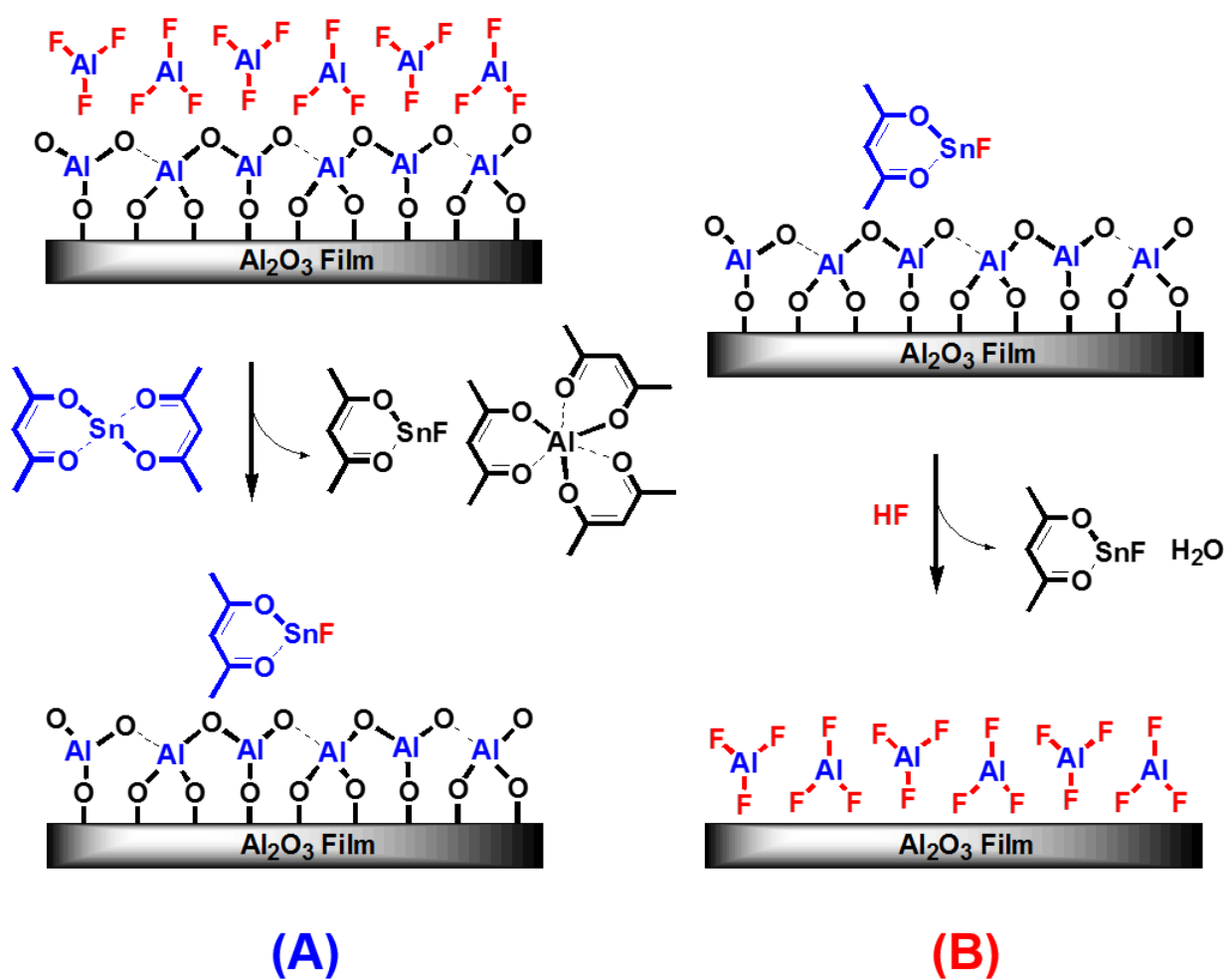
Figure 6-13   Schematic of proposed surface chemistry for Al_2O_3 ALE showing (A) $Sn(acac)_2$

reaction and (B) HF reaction.

During the HF reaction (B), HF reacts with the SnF(acac)* surface species and the underlying Al_2O_3 surface to form a AlF_3 layer. In addition, HF also provides hydrogen to form H_2O as a reaction product. This reaction removes the oxygen in Al_2O_3. The AlF_3 layer is then ready for the next $Sn(acac)_2$ reaction.

The overall reaction can be written as:

$$Al_2O_3 + 6HF + 6Sn(acac)_2 \rightarrow 2Al(acac)_3 + 6SnF(acac) + 3H_2O \tag{1}$$
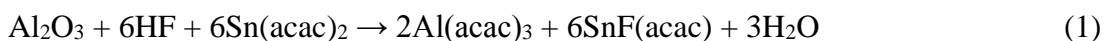
This overall reaction can be separated into the $Sn(acac)_2$ and HF reactions:

(A) $Al_2O_3|2AlF_3^* + 6Sn(acac)_2 \rightarrow$

$$Al_2O_3|xSnF(acac)^* + 2Al(acac)_3 + (6-x)SnF(acac) \tag{2}$$
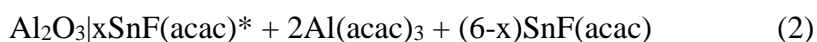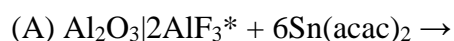
(B) $Al_2O_3|xSnF(acac)^* + 6HF \rightarrow 2AlF_3^* + xSnF(acac) + 3H_2O \tag{3}$$

These reactions include only species that change during the $Sn(acac)_2$ and HF exposures. There may be other surface species present that do not change during the $Sn(acac)_2$ and HF exposures. The asterisks indicate the surface species and the vertical lines are used to separate the various surface species. AlF_3 is the key reaction intermediate. The production of all the $Al(acac)_3$ is assumed to occur during reaction (A). $Al(acac)_3$ is a stable metal β-diketonate with a vapor pressure of ~3-4 Torr at 150°C.[45-47]

The Al_2O_3 shown in Equations 2 and 3 is the amount of Al_2O_3 that is etched during the ALE reactions. Table 1 shows that the amount of Al_2O_3 that is etched during one Al_2O_3 ALE cycle increases with temperature. The Arrhenius plot of the temperature dependence of the MCPCs in Figure 4 yielded an activation barrier of E= 6.6 ± 0.4 kcal/mole. $2AlF_3^*$ and SnF(acac)* are also the amounts added during the HF and $Sn(acac)_2$ reactions, respectively. x

quantifies SnF(acac)* after the Sn(acac)$_2$ exposures relative to the amount of Al$_2$O$_3$ that is etched in one Al$_2$O$_3$ ALE cycle.

The parameter x in Equations 2 and 3 is determined by the ΔM_{Sn}, ΔM_{HF} and MCPC values. x can be calculated from the ΔM_{Sn}/MCPC ratio using the equation:

$$x = (2\times84.0 - 102.0(\Delta M_{Sn}/MCPC))/236.8 \tag{4}$$

where 84.0, 102.0 and 236.8 are the molecular weights for AlF$_3$, Al$_2$O$_3$ and SnF(acac), respectively. The temperature dependence of the x values is x= 0.74, 0.46, 0.29, 0.19, and 0.15 at 150, 175, 200, 225 and 250°C, respectively. These x values are included in Table 1.

The parameter x defines the SnF(acac)* species after the Sn(acac)$_2$ exposures relative to the amount of Al$_2$O$_3$ that is etched in one Al$_2$O$_3$ ALE cycle. Consequently, the product x(MCPC) provides a measure of the SnF(acac)* species on the surface after the Sn(acac)$_2$ exposures. The x(MCPC) values are included in Table 1. These x(MCPC) values are fairly constant at all the temperatures. This behavior indicates that the SnF(acac)* coverage is nearly constant at the different temperatures.

The difference infrared absorbance spectra in the acetylacetonate region of the spectra in Figure 12 are consistent with a constant coverage of SnF(acac)* species at the different temperatures. Figure 12 shows that the changes in the absorbance in the acetylacetonate region after Sn(acac)$_2$ and HF exposures are very similar at 200, 250 and 300°C. This constant absorbance change can be identified with the SnF(acac)* surface species that are added and then removed during the Sn(acac)$_2$ and HF exposures, respectively, as described by Equations 2 and 3.

The SnF(acac)* coverage after the Sn(acac)$_2$ exposures can be determined from the amount of Al$_2$O$_3$ that is etched in one Al$_2$O$_3$ ALE cycle. For example, the MCPC of -5.6 ng/cm^2 at 175°C represents a coverage of 3.3×10^{13} "Al$_2$O$_3$ units"/cm^2. This conversion is based on 1.69×10^{-22} g/"Al$_2$O$_3$ unit". This coverage of "Al$_2$O$_3$ units" multiplied by the x value of 0.46 at 175°C yields a SnF(acac)* coverage of 1.52×10^{13} SnF(acac)*/cm^2. The MCPC and x values at the other temperatures also yield similar SnF(acac)* coverages that vary from 1.38-1.77×10^{13} SnF(acac)*/cm^2.

The nearly constant SnF(acac)* coverage of $\sim1.5 \times 10^{13}$ SnF(acac)*/cm^2 can be compared with the number of "Al$_2$O$_3$ units" on the Al$_2$O$_3$ surface of 6.80×10^{14} "Al$_2$O$_3$ units"/cm^2 assuming a square lattice. The normalized coverage of SnF(acac)* relative to "Al$_2$O$_3$ units" on the surface is $(\sim1.5 \times 10^{13}$ SnF(acac)*/cm$^2) / (6.80 \times 10^{14}$ "Al$_2$O$_3$ units"/cm$^2) = \sim0.022$ SnF(acac)*/ "Al$_2$O$_3$" unit. This normalized coverage is $\sim2.2\%$ of an "Al$_2$O$_3$ unit" monolayer. This coverage may represent a saturated monolayer of SnF(acac)* species on the Al$_2$O$_3$ surface. The normalized coverage of $\sim2.2\%$ is somewhat low. However, perhaps the SnF(acac)* species bind only on particular Lewis acid sites on the Al$_2$O$_3$ surface.

Although the absolute SnF(acac)* coverage after the Sn(acac)$_2$ exposures is very similar at the different temperatures, the FTIR experiments reveal that the total coverage of acetylacetonate species has a large change with temperature as shown in Figure 7. Figure 4b shows the effective Arrhenius dependence of 1/(integrated absorbance) for the acetylacetonate vibrational features at 200, 250 and 300°C in Figure 7a after the HF exposures. This effective Arrhenius plot yields an activation barrier of E= 6.2 ± 1.5 kcal/mole. This activation barrier is close to the activation barrier derived from the temperature-dependent MCPC values in Figure 4.

Nearly identical results were obtained from the effective Arrhenius analysis of the coverage of acetylacetonate species after the $Sn(acac)_2$ exposure.

The correlation between the Arrhenius plots in Figure 4 suggests that the MCPC is inversely dependent on the coverage of acetylacetonate species remaining on the surface after the HF or $Sn(acac)_2$ exposures. An inverse dependence between MCPC and the coverage of acetylacetonate species would be expected if there is a site-blocking effect of acetylacetonate species on Al_2O_3 ALE. Similar site-blocking effects of acetylacetonate species were observed for Pt ALD and Pd ALD.[48-49]

The proposed reactions for Al_2O_3 ALE are very similar to the reactions proposed earlier for HfO_2 ALE.[26] Both Al_2O_3 ALE and HfO_2 ALE display etching rates that increase at higher temperatures. These temperature dependent etching rates are both believed to be correlated inversely with the acetylacetonate coverage on the substrate after the HF or $Sn(acac)_2$ exposures. The $Al(acac)_3$ and $Hf(acac)_4$ etching products are both volatile. Both Al_2O_3 and HfO_2 form stable fluorides upon exposure to HF. The etching rates for Al_2O_3 ALE are somewhat higher than the etching rates for HfO_2 ALE. These differences may be related to the more favorable thermochemistry for Al_2O_3 ALE. The ΔG for the HF reaction with HfO_2 is not as favorable as the ΔG for the HF reaction with Al_2O_3.[37]

6.4. Conclusions

In situ quartz crystal microbalance (QCM) and Fourier transform infrared (FTIR) spectroscopy measurements were used to explore the mechanism of thermal Al_2O_3 atomic layer etching (ALE) using $Sn(acac)_2$) and HF as the reactants. The mass change per cycle (MCPC) for

Al_2O_3 ALE varied with temperature from -4.1 ng/(cm^2 cycle) at 150°C to -18.3 ng/(cm^2 cycle) at 250°C. These temperature dependent etch rates yielded an activation barrier for Al_2O_3 ALE of E= 6.6 ± 0.4 kcal/mole. The mass changes after the $Sn(acac)_2$ and HF exposures were also dependent on temperature. The mass changes after the $Sn(acac)_2$ exposures indicated that more $Sn(acac)_2$ surface reaction products were present at lower temperatures. The mass changes after the HF exposures indicated that more AlF_3 species were present at higher temperatures.

FTIR spectroscopy measurements monitored the Al_2O_3 ALE and quantified the acetylacetonate surface species versus temperature. A connection was observed between the MCPC values and the absorbance from the acetylacetonate species. The Al_2O_3 ALE rate was inversely dependent on the acetylacetonate surface species. This behavior suggested that the acetylacetonate surface species may have a site-blocking effect on Al_2O_3 ALE. Difference infrared absorbance spectra also revealed that there was a constant absorbance change in the acetylacetonate spectral region at all temperatures. This constant absorbance change may be attributed to the constant coverage of $SnF(acac)^*$ species after the $Sn(acac)_2$ exposures at all temperatures determined by the QCM analysis.

The nucleation of the Al_2O_3 ALE was also explored using QCM and FTIR measurements. The conversion of Al_2O_3 to AlF_3 was consistent with a large mass gain and loss of infrared absorbance of Al-O stretching vibrations after the initial HF exposure on the Al_2O_3 film. The formation of AlF_3 after the initial HF exposure and the presence of AlF_3 on the surface after each HF exposure during Al_2O_3 ALE was also observed by FTIR experiments. These results suggest that AlF_3 is the key reactive intermediate during Al_2O_3 ALE. The HF exposure converts Al_2O_3 to AlF_3 and then the AlF_3 is removed by $Sn(acac)_2$.

6.5. Acknowledgements

6.6. References

(1)   Agarwal, A.; Kushner, M. J. Plasma Atomic Layer Etching Using Conventional Plasma Equipment. *J. Vac. Sci. Technol. A* **2009**, *27*, 37-50.

(2)   Athavale, S. D.; Economou, D. J. Molecular Dynamics Simulation of Atomic Layer Etching of Silicon. *J. Vac. Sci. Technol. A* **1995**, *13*, 966-971.

(3)   Athavale, S. D.; Economou, D. J. Realization of Atomic Layer Etching of Silicon. *J. Vac. Sci. Technol. B* **1996**, *14*, 3702-3705.

(4)   George, S. M. Atomic Layer Deposition: An Overview. *Chem. Rev.* **2010**, *110*, 111-131.

(5)   Leskela, M.; Ritala, M. Atomic layer deposition chemistry: Recent developments and future challenges. *Angew. Chem. Int. Ed.* **2003**, *42*, 5548-5554.

(6)   Marchack, N.; Chang, J. P. Perspectives in nanoscale plasma etching: what are the ultimate limits? *J. Phys. D Appl. Phys.* **2011**, *44*, 174011.

(7)   Kubota, N. A.; Economou, D. J.; Plimpton, S. J. Molecular Dynamics Simulations of Low-Energy (25-200 eV) Argon Ion Interactions with Silicon Surfaces: Sputter Yields and Product Formation Pathways. *J. Appl. Phys.* **1998**, *83*, 4055-4063.

(8)   Park, S. D.; Lee, D. H.; Yeom, G. Y. Atomic Layer Etching of Si(100) and Si(111) Using Cl_2 and Ar Neutral Beam. *Electrochem. Solid State Lett.* **2005**, *8*, C106-C109.

(9)   Park, S. D.; Lim, W. S.; Park, B. J.; Lee, H. C.; Bae, J. W.; Yeom, G. Y. Precise Depth Control and Low-Damage Atomic-Layer Etching of HfO_2 using BCl_3 and Ar Neutral Beam. *Electrochem. Solid State Lett.* **2008**, *11*, H71-H73.

(10)   Sakaue, H.; Iseda, S.; Asami, K.; Yamamoto, J.; Hirose, M.; Horiike, Y. Atomic Layer Controlled Digital Etching of Silicon. *Jpn. J. Appl. Phys. 1* **1990**, *29*, 2648-2652.

(11)   Yamamoto, J.; Kawasaki, T.; Sakaue, H.; Shingubara, S.; Horiike, Y. Digital Etching Study and Fabrication of Fine Si Lines and Dots. *Thin Solid Films* **1993**, *225*, 124-129.

(12)   Sugiyama, T.; Matsuura, T.; Murota, J. Atomic-Layer Etching of Ge Using an Ultraclean ECR Plasma. *Appl. Surf. Sci.* **1997**, *112*, 187-190.

(13)   Lim, W. S.; Park, S. D.; Park, B. J.; Yeom, G. Y. Atomic Layer Etching of (100)/(111) GaAs with Chlorine and Low Angle Forward Reflected Ne Neutral Beam. *Surf. Coat. Tech.* **2008**, *202*, 5701-5704.

(14)   Meguro, T.; Hamagaki, M.; Modaressi, S.; Hara, T.; Aoyagi, Y.; Ishii, M.; Yamamoto, Y. Digital Etching of GaAs - New Approach of Dry Etching to Atomic Ordered Processing. *Appl. Phys. Lett.* **1990**, *56*, 1552-1554.

(15)   Meguro, T.; Ishii, M.; Sugano, T.; Gamo, K.; Aoyagi, Y. Control of the Etching Reaction of Digital Etching Using Tunable UV Laser Irradiation. *Appl. Surf. Sci.* **1994**, *82-3*, 193-199.

(16)   Park, S. D.; Oh, C. K.; Bae, J. W.; Yeom, G. Y.; Kim, T. W.; Song, J. I.; Jang, J. H. Atomic Layer Etching of InP Using a Low Angle Forward Reflected Ne Neutral Beam. *Appl. Phys. Lett.* **2006**, *89*, 043109.

(17)   Lim, W. S.; Park, J. B.; Park, J. Y.; Park, B. J.; Yeom, G. Y. Low Damage Atomic Layer Etching of ZrO_2 by Using BCl_3 Gas and Ar Neutral Beam. *J. Nanosci. Nanotechnol.* **2009**, *9*, 7379-7382.

(18)   Metzler, D.; Bruce, R. L.; Engelmann, S.; Joseph, E. A.; Oehrlein, G. S. Fluorocarbon Assisted Atomic Layer Etching of SiO_2 using Cyclic Ar/C_4F_8 Plasma. *J. Vac. Sci. Technol. A* **2014**, *32*, 020603.

(19)   Min, K. S.; Kang, S. H.; Kim, J. K.; Jhon, Y. I.; Jhon, M. S.; Yeom, G. Y. Atomic Layer Etching of Al_2O_3 Using BCl_3/Ar for the Interface Passivation Layer of III-V MOS Devices. *Microelectron. Eng.* **2013**, *110*, 457-460.

(20)   Park, J. B.; Lim, W. S.; Park, B. J.; Park, I. H.; Kim, Y. W.; Yeom, G. Y. Atomic Layer Etching of Ultra-Thin HfO_2 Film for Gate Oxide in MOSFET Devices. *J. Phys. D Appl. Phys.* **2009**, *42*, 055202.

(21)   Park, J. B.; Lim, W. S.; Park, S. D.; Park, Y. J.; Yeom, G. Y. Etch Characteristics of TiO_2 Etched by Using an Atomic Layer Etching Technique with BCl_3 Gas and an Ar Neutral Beam. *J. Korean Phys. Soc.* **2009**, *54*, 976-980.

(22)   Kim, Y. Y.; Lim, W. S.; Park, J. B.; Yeom, G. Y. Layer by Layer Etching of the Highly Oriented Pyrolythic Graphite by Using Atomic Layer Etching. *J. Electrochem. Soc.* **2011**, *158*, D710-D714.

(23)   Lim, W. S.; Kim, Y. Y.; Kim, H.; Jang, S.; Kwon, N.; Park, B. J.; Ahn, J.-H.; Chung, I.; Hong, B. H.; Yeom, G. Y. Atomic Layer Etching of Graphene for Full Graphene Device Fabrication. *Carbon* **2012**, *50*, 429-435.

(24)   Vogli, E.; Metzler, D.; Oehrlein, G. S. Feasibility of Atomic Layer Etching of Polymer Material Based on Sequential O_2 Exposure and Ar Low-Pressure Plasma-Etching. *Appl. Phys. Lett.* **2013**, *102*, 253105.

(25)   Lee, Y.; George, S. M. Atomic Layer Etching of Al2O3 Using Sequential, Self-Limiting Thermal Reactions with Sn(acac)2 and HF. *Submitted to ACS Nano*

(26)   Lee, Y.; DuMont, J. W.; George, S. M. Atomic Layer Etching of HfO2 Using Sequential, Self-Limiting Thermal Reactions with Sn(acac)2 and HF. *Submitted to Journal of Solid State Science & Technology*

(27)   Elam, J. W.; Groner, M. D.; George, S. M. Viscous Flow Reactor with Quartz Crystal Microbalance for Thin Film Growth by Atomic Layer Deposition. *Rev. Sci. Instrum.* **2002**, *73*, 2981-2987.

(28)   Riha, S. C.; Libera, J. A.; Elam, J. W.; Martinson, A. B. F. Design and Implementation of an Integral Wall-Mounted Quartz Crystal Microbalance for Atomic Layer Deposition. *Rev. Sci. Instrum.* **2012**, *83*, 094101.

(29)   Olah, G. A.; Nojima, M.; Kerekes, I. Synthetic Methods and Reactions .2. Hydrofluorination of Alkenes, Cyclopropane and Alkynes with (Trialkylamine) Reagents. *Synthesis-Stuttgart* **1973**, *12*, 779-780.

(30)   DuMont, J. W.; George, S. M. Pyrolysis of Alucone Molecular Layer Deposition Films Studied Using In Situ Transmission Fourier Transform Infrared Spectroscopy. *Submitted to Journal of Physical Chemistry C*

(31)   Ferguson, J. D.; Weimer, A. W.; George, S. M. Atomic layer deposition of ultrathin and conformal Al2O3 films on BN particles. *Thin Solid Films* **2000**, *371*, 95-104.

(32)   Ballinger, T. H.; Wong, J. C. S.; Yates, J. T. Transmission Infrared-Spectroscopy of High Area Solid-Surfaces - A Useful Method for Sample Preparation. *Langmuir* **1992**, *8*, 1676-1678.

(33)   Sneh, O.; George, S. M. THERMAL-STABILITY OF HYDROXYL-GROUPS ON A WELL-DEFINED SILICA SURFACE. *J. Phys. Chem.* **1995**, *99*, 4639-4647.

(34)   Nakamoto, K.; Martell, A. E.; McCarthy, P. J. INFRARED SPECTRA OF METAL CHELATE COMPOUNDS .3. INFRARED SPECTRA OF ACETYLACETONATES OF DIVALENT METALS. *J. Am. Chem. Soc.* **1961**, *83*, 1272-&.

(35) Tayyari, S. F.; Milani-nejad, F. Vibrational assignment of acetylacetone. *Spectrochim. Acta A* **2000**, *56*, 2679-2691.

(36) Jia, W.-Z.; Lu, J.-Q.; Chen, P.; Wang, Y.-J.; Luo, M.-F. A novel method for the synthesis of well-crystallized beta-AlF3 with high surface area derived from gamma-Al2O3. *J. Mater. Chem.* **2011**, *21*, 8987-8990.

(37) *HSC Chemistry*; HSC Chemistry 5.1, Outokumpu Research Oy: Pori, Finland.

(38) Gross, U.; Ruediger, S.; Kemnitz, E.; Brzezinka, K.-W.; Mukhopadhyay, S.; Bailey, C.; Wander, A.; Harrison, N. Vibrational analysis study of aluminum trifluoride phases. *J. Phys. Chem. A* **2007**, *111*, 5813-5819.

(39) Koenig, R.; Scholz, G.; Scheurell, K.; Heidemann, D.; Buchem, I.; Unger, W. E. S.; Kemnitz, E. Spectroscopic characterization of crystalline AlF3 phases. *J. Fluorine Chem.* **2010**, *131*, 91-97.

(40) Utkin, A. N.; Girichev, G. V.; Giricheva, N. I.; Khaustov, S. V. STRUCTURE AND VIBRATIONAL FREQUENCIES OF ALUMINUM TRIFLUORIDE AND GALLIUM TRIFLUORIDE. *J. Struct. Chem.* **1986**, *27*, 212-215.

(41) Ewings, P. F. R.; Harrison, P. G.; Fenton, D. E. Derivatives of Divalent Germanium, Tin, and Lead. 5. Bis-(Pentane-2,4-Dionato)-Tin(II),Bis(1,1,1-Trifluoropentane-2,4-Dionato)-Tin(II), and Bis(1,1,1,5,5,5-Hexafluoropentane-2,4-Dionato)-Tin(II). *J. Chem. Soc.-Dalton Trans.* **1975**, 821-826.

(42) Ball, D. W. AB-INITIO STUDIES OF ALH3-H2O, ALF3-H2O, AND ALCL3-H2O COMPLEXES. *J. Phys. Chem.* **1995**, *99*, 12786-12789.

(43) Krahl, T.; Vimont, A.; Eltanany, G.; Daturi, M.; Kemnitz, E. Determination of the acidity of high surface AlF3 by IR spectroscopy of adsorbed CO probe molecules. *J. Phys. Chem. C* **2007**, *111*, 18317-18325.

(44) Wander, A.; Bailey, C. L.; Searle, B. G.; Mukhopadhyay, S.; Harrison, N. M. Identification of possible Lewis acid sites on the beta-AlF3(100) surface: an ab initio total energy study. *Phys. Chem. Chem. Phys.* **2005**, *7*, 3989-3993.

(45) Berg, E. W.; Truemper, J. T. Vapor Pressure-Temperature Data for Various Metal Beta-Diketone Chelates. *Anal. Chim. Acta* **1965**, *32*, 245-252.

(46) Eisentraut, K. J.; Sievers, R. E. Thermogravimetric Studies of Metal Beta-Diketonates. *J. Inorg. Nucl. Chem.* **1967**, *29*, 1931-1936.

(47)   Fahlman, B. D.; Barron, A. R. Substituent Effects on the Volatility of Metal Beta-Diketonates. *Adv. Mater. Opt. Electr.* **2000**, *10*, 223-232.

(48)   Anderson, V. R.; Leick, N.; Clancey, J. W.; Hurst, K. E.; Jones, K. M.; Dillon, A. C.; George, S. M. Atomic Layer Deposition of Platinum Nanoparticles on Titanium Oxide and Tungsten Oxide Using Platinum(II) Hexafluoroacetylacetonate and Formalin as the Reactants. *J. Phys. Chem. C* **2014**, *118*, 8960-8970.

(49)   Goldstein, D. N.; George, S. M. Surface poisoning in the nucleation and growth of palladium atomic layer deposition with Pd(hfac)(2) and formalin. *Thin Solid Films* **2011**, *519*, 5339-5347.

Chapter 7

Atomic Layer Etching of HfO₂ Using Sequential, Self-Limiting Thermal Reactions with Sn(acac)₂ and HF

7.1. Introduction

Atomic layer etching (ALE) is a thin film removal technique based on sequential, self-limiting surface reactions.[1-3] ALE can be viewed as the reverse of atomic layer deposition (ALD).[4] ALE is able to remove thin films with atomic layer control. ALD and ALE are able to provide the necessary processing techniques for surface engineering at the atomic level.[5, 6] This atomic level control is needed for the nanofabrication of a wide range of nanoscale devices.[7]

Until recently, ALE processes have been reported using only ion-enhanced or energetic noble gas atom-enhanced surface reactions.[1-3] In these ALE processes, a halogen is adsorbed on the surface of the material. Subsequently, ion or noble gas atom bombardment is used to desorb halogen compounds that etch the material. Using this approach, ALE has been reported for Si,[2, 3, 8-12] Ge,[6, 13] and compound semiconductors.[14-17] ALE has also been demonstrated for a variety of metal oxides.[7, 18-20] Additional ALE studies have been conducted on various carbon substrates.[21-23]

The ALE of Al₂O₃ was recently reported using sequential, self-limiting thermal reactions with Sn(acac)₂ and HF as the reactants.[24] The linear removal of Al₂O₃ was observed at temperatures from 150-250°C without the use of ion or noble gas atom bombardment. Al₂O₃

ALE etch rates varied with temperature from 0.14 Å /cycle at 150°C to 0.61 Å /cycle at 250°C.[24] The Sn(acac)$_2$ and HF thermal reactions were both self-limiting versus reactant exposure. In addition, the Al$_2$O$_3$ films were smoothed by Al$_2$O$_3$ ALE cycles.[24] The overall Al$_2$O$_3$ etching reaction was proposed to be: Al$_2$O$_3$ + 6Sn(acac)$_2$ + 6HF $\rightarrow$ 2Al(acac)$_3$ + 6SnF(acac) + 3H$_2$O.[24]

HfO$_2$ is an important high k dielectric material that is a replacement for SiO$_2$ in gate oxides in metal oxide semiconductor field effect transistors (MOSFET).[25, 26] The HfO$_2$ films used in the gate stack have been grown using ALD.[27] The HfO$_2$-based gate oxide was introduced in 2007 for the 45 nm node in complementary MOSFET technology.[28] HfO$_2$ is also being employed as the gate dielectric in FinFET structures.[29, 30] Etching of HfO$_2$ films may be needed to define the gate dielectric thickness.[7] To meet these needs, HfO$_2$ ALE has been previously developed using BCl$_3$ to adsorb chlorine on the HfO$_2$ substrate and then energetic Ar beams to desorb Cl-containing compounds that etch the HfO$_2$ material.[7]

In this study, a new approach for HfO$_2$ ALE is demonstrated using sequential, self-limiting thermal reactions with Sn(acac)$_2$ and HF as the reactants. Quartz crystal microbalance (QCM) measurements are used to study HfO$_2$ ALE. The QCM analysis obtains the HfO$_2$ etch rates and the mass changes after individual Sn(acac)$_2$ and HF exposures. The mass change per cycle (MCPC) and the individual mass changes during the Sn(acac)$_2$ and HF exposures are used to develop a mechanism for HfO$_2$ ALE. In addition, Fourier transform infrared (FTIR) analysis is able to monitor HfO$_2$ ALE and characterize the Sn(acac)$_2$ and HF reaction products on the surface. This new approach for HfO$_2$ ALE offers an alternative and may have advantages relative to ALE methods based on ions or energetic neutrals.

7.2. Experimental

7.2A. Viscous Flow Reactor Equipped for *in situ* QCM Measurements

The ALE reactions were performed in a viscous flow ALD reactor.[31] The reaction temperatures varied from 150-250°C. A proportional-integral-derivative (PID) temperature controller (2604, Eurotherm) maintained the temperature to within ±0.04°C. The pressure was measured in the reactor using a capacitance manometer (Baratron 121A, MKS). The ALD reactor was equipped with an *in situ* QCM.[31] An RC-cut quartz crystal[32] (gold coated and polished, 6 MHz, Colnatec) was positioned in a sensor head (BSH-150, Inficon). The sensor head was then sealed with high temperature epoxy (Epo-Tek H21D, Epoxy technology). A thin film deposition monitor (Maxtek TM-400, Inficon) was used to record the QCM measurements.

Sequential exposure of tin(II) acetylacetonate ($Sn(acac)_2$, 37-38% Sn, Gelest) and HF-pyridine (70 wt% HF, Sigma-Aldrich) were employed for the HfO_2 ALE reactions. These precursors are shown in Figure 1. Use of gaseous HF from HF-pyridine enables the safe handling of anhydrous HF. HF-pyridine is a liquid at room temperature and is known as Olah's reagent.[33] The HF-pyridine solution has an equilibrium with gaseous HF. Our mass spectrometer analysis has shown that HF dominates the vapor pressure of HF-pyridine. Our measurement of the vapor pressure of HF-pyridine was 90-100 Torr at room temperature.

$Sn(acac)_2$ and HF-pyridine were transferred to stainless steel bubblers in a dry N_2-filled glove bag. The $Sn(acac)_2$ precursor was held at 100°C to produce a vapor pressure of 15-20 mTorr. The HF-pyridine precursor was maintained at room temperature. The HfO_2 films were grown by HfO_2 ALD using tetrakisdimethylamido hafnium (TDMAH) (≥99.99%, Sigma-Aldrich) and H_2O (Chromasolv for HPLC, Sigma-Aldrich) at 200°C. TDMAH was transferred
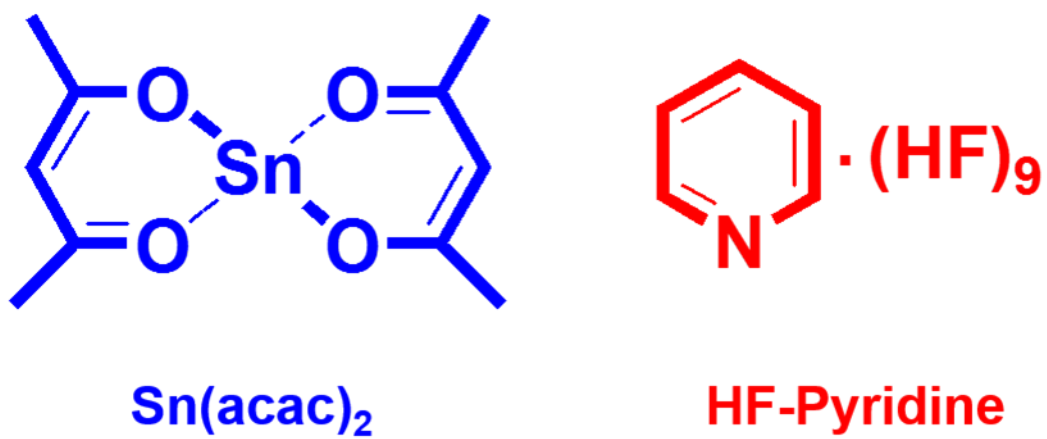
Figure 7-1   Pictures of Sn(acac)₂ and HF-pyridine precursors.

to a stainless steel bubbler and maintained at 67°C to produce a vapor pressure of 20 mTorr. The H_2O precursor was held at room temperature.

A mechanical pump (Pascal 2015SD, Alcatel) was used to pump the reactor. A constant total flow of 150 sccm of ultra high purity (UHP) N_2 carrier gas into the reactor was delivered by three separate mass flow controllers (Type 1179A, MKS). Additional N_2 gas flow of 20 sccm was provided using a metering bellows-sealed valve (SS-4BMG, Swagelok) to prevent deposition on the backside of the QCM crystal.[31] A base pressure of ~1 Torr in the reactor was produced by the total N_2 gas flow of 170 sccm.

7.2B. Si Wafers, X-ray Reflectivity, X-ray Photoelectron Spectroscopy and Spectroscopic Ellipsometry

The x-ray reflectivity (XRR), x-ray photoelectron spectroscopy (XPS) and spectroscopic ellipsometry (SE) experiments were performed on boron-doped Si (100) wafers (p-type, Silicon Valley Microelectronics). These wafers were cut into samples with dimensions of 2.5 cm by 2.5 cm. These substrates were used for HfO_2 ALD deposition and then for subsequent HfO_2 ALE experiments. Prior to HfO_2 ALD, the Si wafers were rinsed with acetone, isopropanol, and deionized water and then dried with UHP N_2 gas.

The *ex situ* XRR scans were recorded using a high resolution x-ray diffractometer (Bede D1, Jordan Valley Semiconductors) employing Cu Kα (λ = 1.540 Å) radiation. The filament voltage and current in the x-ray tube were 40 kV and 35 mA, respectively. A 10 arcsec step size and a 5 s acquisition time were used for recording all XRR scans with a range of 300 to 6000 arcsec. The analysis software (Bede REFS, Jordan Valley Semiconductors) fitted the XRR scans to determine film thickness, film density and surface roughness.

X-ray photoemission spectroscopy (XPS) analysis was performed using a PHI 5600 X-ray photoelectron spectrometer using a monochromatic Al Kα source. The XPS data were collected using Auger Scan (RBD Instruments). The XPS data were analyzed in CASA XPS (Casa Software Ltd.).

SE analysis determined the film thicknesses and refractive index. The measurement of Ψ and Δ were recorded using a spectroscopic ellipsometer (M-2000, J. A. Woollam) with a spectral range of 240 to 1700 nm and an incidence angle of 75°. The analysis software (CompleteEASE, J. A. Woollam) fitted Ψ and Δ based on a Sellmeier model to determine the thicknesses and refractive index of the film.[34]

7.2C. FTIR Spectroscopy Measurements

The *in situ* transmission FTIR measurements of HfO_2 ALE were performed in a reactor equipped with an FTIR spectrometer.[35] The FTIR spectrometer (Nicolet 6700 FTIR from Thermo Scientific) utilized a high-sensitivity liquid-N_2-cooled mercury cadmium telluride (MCT-B) detector. The spectrometer, mirror, and detector were purged with dry, CO_2-free air. A total of 100 scans at 4 cm^{-1} resolution from 400 to 4000 cm^{-1} were recorded for each collected spectrum.

The transmission FTIR measurements were performed on high surface area SiO_2 nanoparticles (99.5%, US Research Nanomaterials Inc.) with an average diameter of 15-20 nm. The high surface area of these particles improved the signal-to-noise ratio compared with a flat sample.[36] Sample preparation involved pressing the SiO_2 nanoparticles into a tungsten grid support (Tech-Etch).[36, 37] The tungsten grids were 2 x 3 cm^2. Each grid was 50 µm thick with 100 grid lines per inch.

The tungsten grid could be resistively heated using a DC power supply (6268B, 20V/ 20A, Hewlett-Packard). The voltage output of the power supply was controlled by a PID temperature controller (Love Controls 16B, Dwyer Instruments, Inc.). A type K thermocouple was attached to the bottom of the tungsten grid with Epoxy (Ceramabond 571, Aremco) that served to attach and electrically isolate the thermocouple during the experiment.

The HfO_2 films were grown with HfO_2 ALD using TDMAH and H_2O. The HfO_2 ALE reactions were performed using sequential exposures of $Sn(acac)_2$ and HF-pyridine. Static dosing of both the ALD and ALE precursors was utilized to achieve self-limiting behavior on the high surface area SiO_2 particles. During HfO_2 ALD, each TDMAH exposure consisted of a ~1.0 Torr static dose for 30 s followed by a 240 s purge. For the H_2O reaction, each exposure consisted of a ~1.0 Torr static dose for 30 s followed by a 240 s purge.

During HfO_2 ALE, each $Sn(acac)_2$ exposure consisted of a ~1.0 Torr static dose for 30 s followed by a 240 s purge. For the HF reaction, each HF-pyridine exposure consisted of a ~1.0 Torr static dose for 30 s followed by a 240 s purge. For these FTIR experiments, the HF-pyridine and H_2O precursors were maintained at room temperature. The stainless steel bubbler containing $Sn(acac)_2$ was held at 100°C. The stainless steel bubbler containing TDMAH was held at 70°C.

HfF_4 films were deposited using HfF_4 ALD with sequential exposures of TDMAH and HF-pyridine. The HfF_4 films were grown on a fresh HfO_2 ALD film that was prepared using three HfO_2 ALD cycles with TDMAH and H_2O as the reactants. Static dosing of the reactants was utilized to achieve self-limiting behavior of the surface reactions on the high surface area SiO_2 particles. During HfF_4 ALD, each TDMAH exposure consisted of a ~1.0 Torr static dose

for 30 s followed by a 240 s purge. Each HF exposure consisted of a ~1.0 Torr static dose for 30

s followed by a 240 s purge.

7.3. Results & Discussion

7.3A. QCM Measurements

Figure 2 displays the mass change during 100 ALE cycles of sequential $Sn(acac)_2$ and HF

reactions on an HfO_2 surface at 200°C. The initial HfO_2 film on the QCM sensor was deposited

using 100 cycles of HfO_2 ALD with TDMAH and H_2O as the reactants at 200°C. One ALE

cycle was defined by a $Sn(acac)_2$ dose of 1.0 s, an N_2 purge of 30 s, a HF dose of 1.0 s, and a

second N_2 purge of 30 s. This reaction sequence is designated as 1-30-1-30. The pressure

transients during the $Sn(acac)_2$ and HF-pyridine exposures were 20 mTorr and 80 mTorr,

respectively.

The etching of the HfO_2 film in Figure 2 is linear and is consistent with a mass change

per cycle (MCPC) = 11.1 ng/(cm^2 cycle). This MCPC corresponds to an etch rate of 0.116

Å/cycle based on the HfO_2 ALD film density of 9.6 g/cm^3 that was measured by XRR analysis.

All of the ALE cycles display a mass loss as a result of etching the HfO_2 film except during the

first ALE cycle. The first cycle shows mass gains of $\Delta M_{Sn} = 71$ ng/cm^2 and $\Delta M_{HF} = 6$ ng/cm^2.

The mass gain for ΔM_{Sn} on the first cycle is assigned to $Sn(acac)_2$ adsorption on the HfO_2

surface. The $Sn(acac)_2$ could either adsorb associatively as $Sn(acac)_2$* or dissociatively as

$Sn(acac)$* and $(acac)$*. The asterisks designate a surface species. The mass gain for ΔM_{HF} on

the first cycle is explained by HF adsorption or the formation of HfF_4 or HfF_x species by the

reaction of HF with the underlying HfO_2 surface. The reaction $HfO_2 + 4HF \rightarrow HfF_4 + 2H_2O$ is
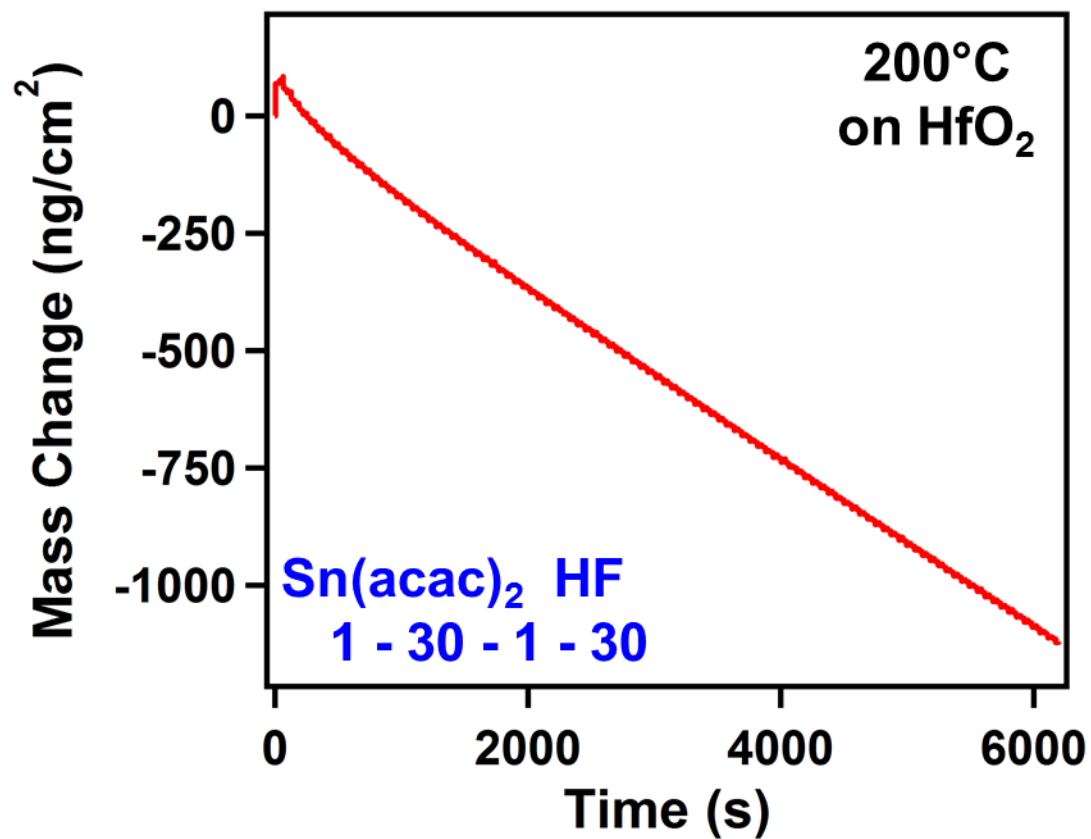
Figure 7-2   Mass change versus time for HfO$_2$ ALE using sequential Sn(acac)$_2$ and HF

exposures at 200°C.

spontaneous with ΔG= -19 kcal at 200°C.[38] This first cycle establishes the initial $Sn(acac)_2$ and

HF, HfF_4 or HfF_x species on the HfO_2 substrate.

Figure 3 displays an enlargement of the mass changes versus time at 200°C for three

cycles in the steady state linear etching regime in Figure 2. There is a gradual mass decrease

after a small mass gain coinciding with the $Sn(acac)_2$ exposure. This behavior suggests

$Sn(acac)_2$ adsorption followed by either $Sn(acac)_2$ desorption and/or the removal of reaction

products. A mass change of ΔM_{Sn} = -4.8 ng/cm^2 was observed after 1.0 s of $Sn(acac)_2$ exposure.

A mass change of ΔM_{HF} = -6.3 ng/cm^2 was observed after 1.0 s of HF exposure. The

experimental variation of these mass changes was measured over 50 HfO_2 ALE cycles. The

standard deviation on the ΔM_{Sn} and ΔM_{HF} mass changes was <0.1 ng/cm^2.

Figure 4 shows the MCPC and the ΔM_{Sn}/MCPC ratio during 100 cycles of HfO_2 ALE at

200°C. The MCPC is defined by MCPC = ΔM_{Sn} + ΔM_{HF}. The standard deviation on the MCPC

was also <0.1 ng/cm^2. Figure 4a displays ΔM_{Sn}, ΔM_{HF} and MCPC for the same 100 cycles of

HfO_2 ALE on the HfO_2 film at 200 °C as shown in Figure 2. The MCPC varies from -26

ng/(cm^2 cycle) to -17 ng/(cm^2 cycle) over the second to fifth ALE cycles. The MCPC decreases

to a steady-state value of -11.1 ng/(cm^2 cycle) after ~20 HfO_2 ALE cycles. These first 20 HfO_2

ALE cycles prior to reaching the steady state values define the nucleation regime.

Figure 4b displays the ΔM_{Sn}/MCPC ratio during the same 100 cycles as shown in Figure

4a. This ΔM_{Sn}/MCPC ratio varies from 0.78 to 0.64 over the second to fifth ALE cycles. The

ratio then slowly decreases to a steady-state value of 0.43 after the first ~20 HfO_2 ALE cycles in

the nucleation regime. This ΔM_{Sn}/MCPC ratio will be used to determine the stoichiometry of the

ALE surface reactions. The standard deviations on the ΔM_{Sn}/MCPC ratio was <0.005.
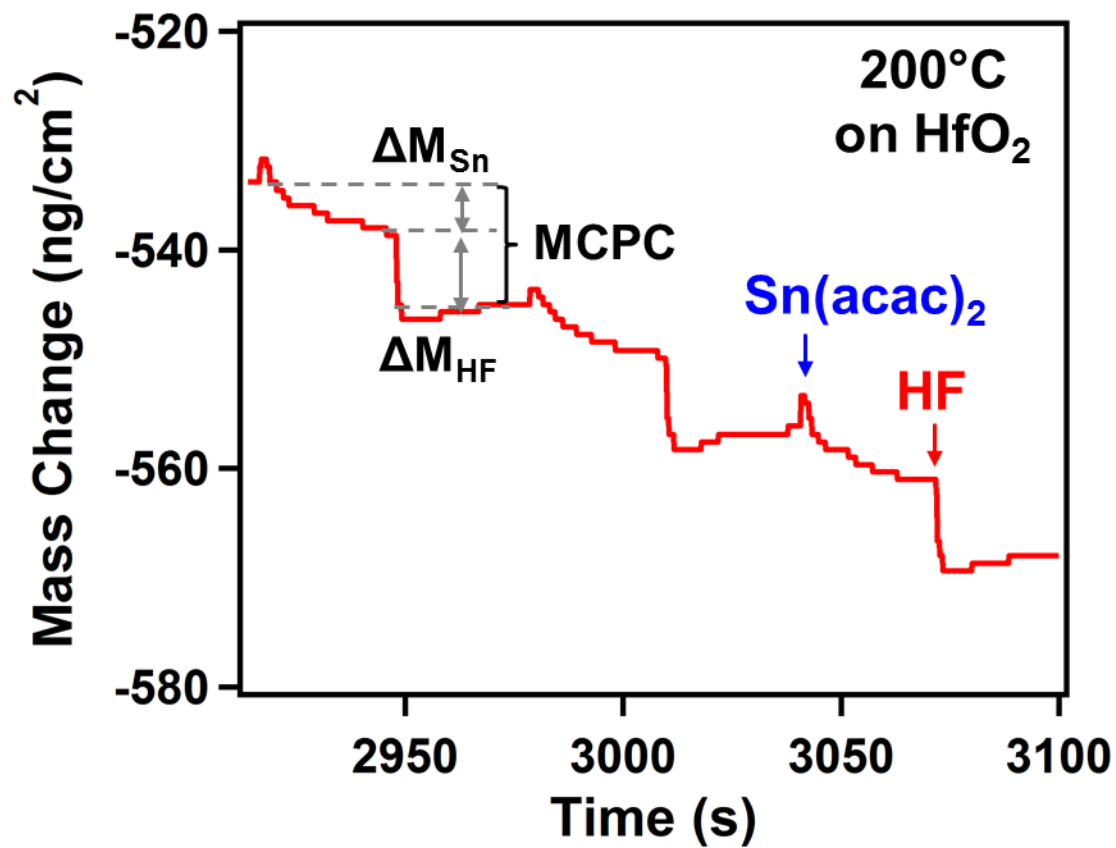
Figure 7-3   Expansion of linear region of Figure 2 showing the individual mass changes

during the sequential Sn(acac)$_2$ and HF exposures at 200°C.
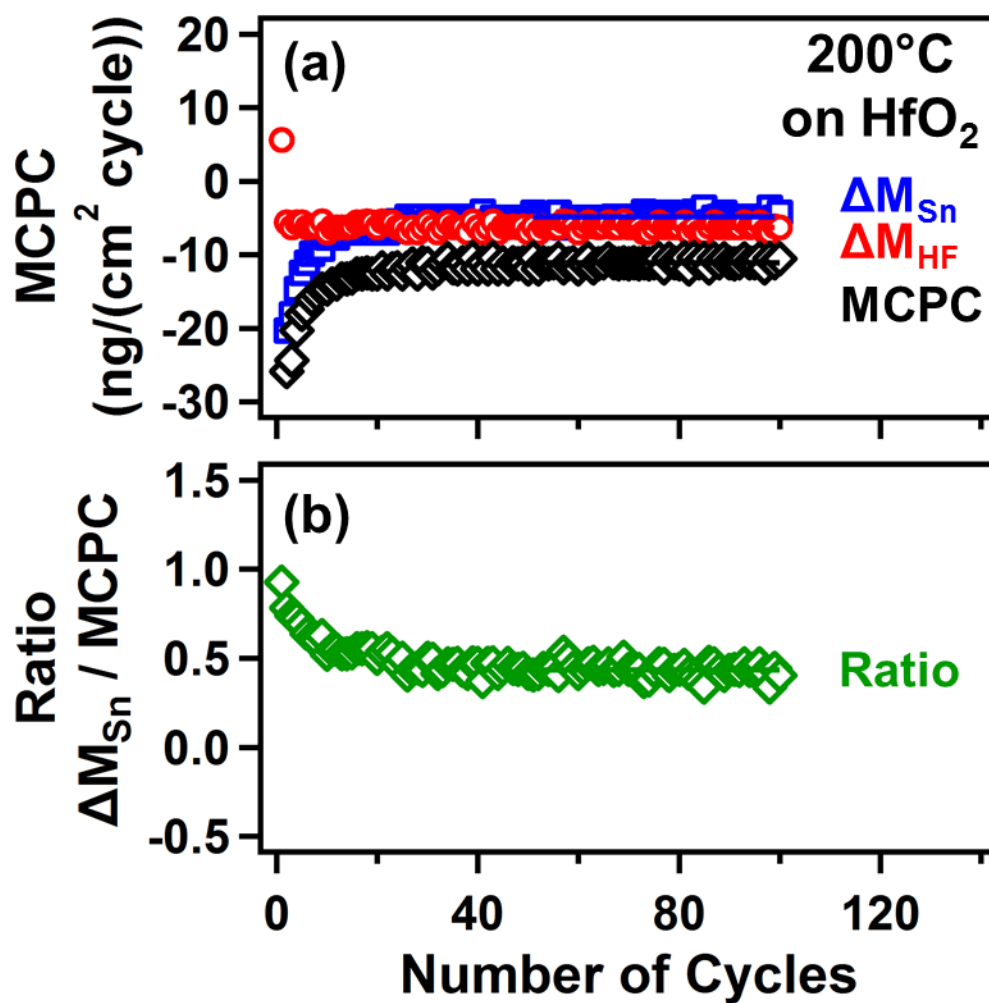
Figure 7-4   (a) Mass change after the Sn(acac)$_2$ exposure (ΔM_{Sn}), mass change after the HF exposure (ΔM_{HF}) and mass change per cycle (MCPC) versus number of ALE cycles at 200°C. (b) ΔM_{Sn}/MCPC ratio versus number of ALE cycles.

Figure 5 examines the self-limiting nature of the $Sn(acac)_2$ and HF reactions during HfO_2 ALE at 200°C. These MCPC values were measured versus different reactant exposure times. Figure 5a shows the self-limiting behavior of the $Sn(acac)_2$ reaction using different $Sn(acac)_2$ exposure times with a single 1.0 s exposure of HF. A constant N_2 purge of 30 s was used after each exposure. This reaction sequence can be denoted as x-30-1-30. The MCPC versus $Sn(acac)_2$ exposure time decreases quickly and levels off at MCPC = -11 ng/(cm^2 cycle).

Figure 5b examines the self-limiting behavior of the HF reaction using different HF exposure times with a single 1.0 s exposure of $Sn(acac)_2$. This reaction sequence can be denoted as 1-30-x-30. The MCPC versus HF exposure time decreases and does not level off after longer HF exposure times. The HF reaction does not appear to be self-limiting versus HF exposure. The lack of self-limiting behavior for the HF exposure may indicate that the HF reaction has not reached saturation. Much larger HF exposures may be necessary to complete the surface reaction.

Another possibility is that the larger HF exposures lead to larger HF background pressures and longer HF residence times in the reactor. If some HF residual pressure remains during the $Sn(acac)_2$ exposure, then the HfO_2 substrate can be continuously etched with HF and $Sn(acac)_2$ by chemical vapor etching (CVE). CVE is the reverse of chemical vapor deposition (CVD) and occurs when the two precursors required for ALE are present at the same time.[39]

Additional experiments were performed to understand the lack of self-limiting behavior for the HF exposure. Figure 6a shows five cycles of HfO_2 ALD followed by ten individual HF exposures at 200°C. The first HF exposure displays a mass gain of ΔM_{HF} = 37.8 ng/cm^2. Subsequent HF exposures display no additional mass change. These results indicate that the HF
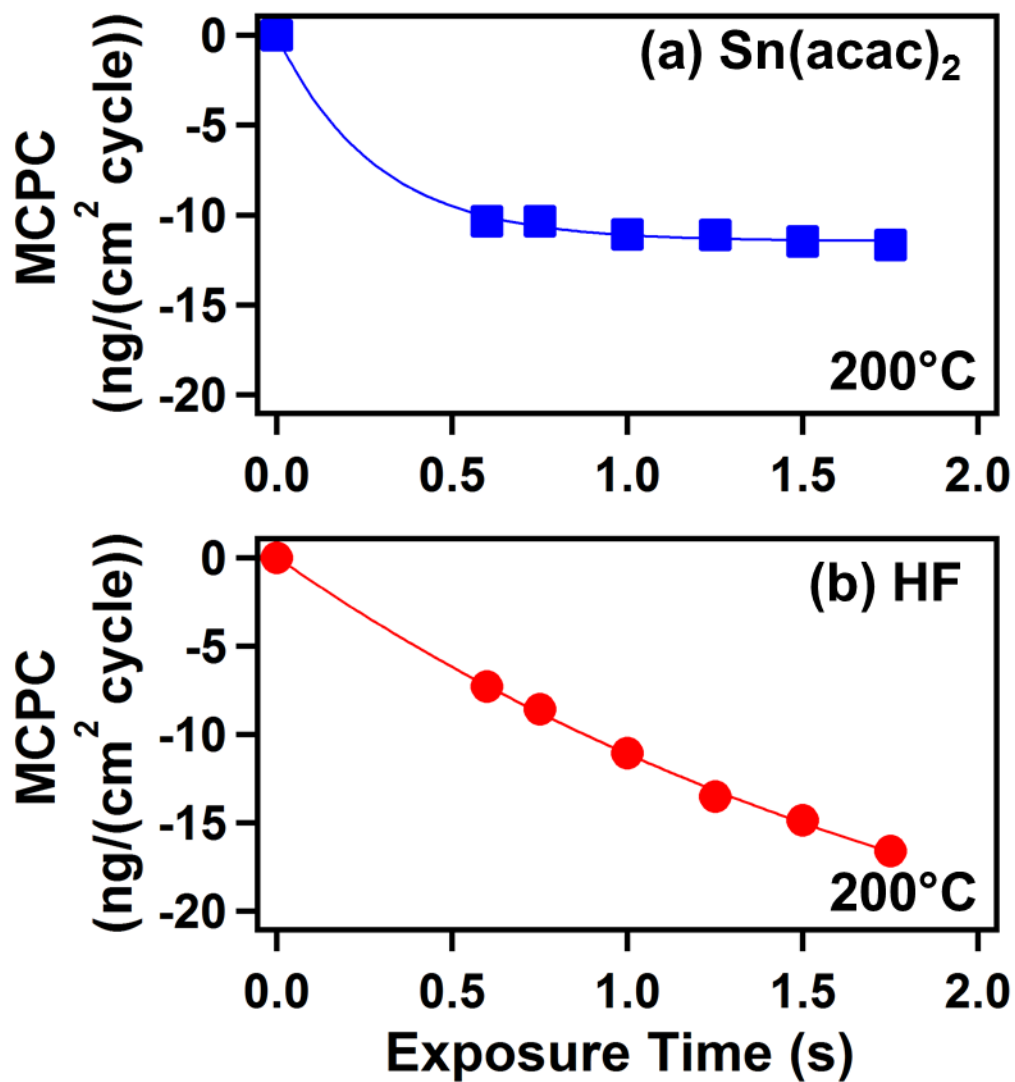
Figure 7-5   Mass change per cycle (MCPC) versus exposure time for (a) $Sn(acac)_2$ and (b) HF.
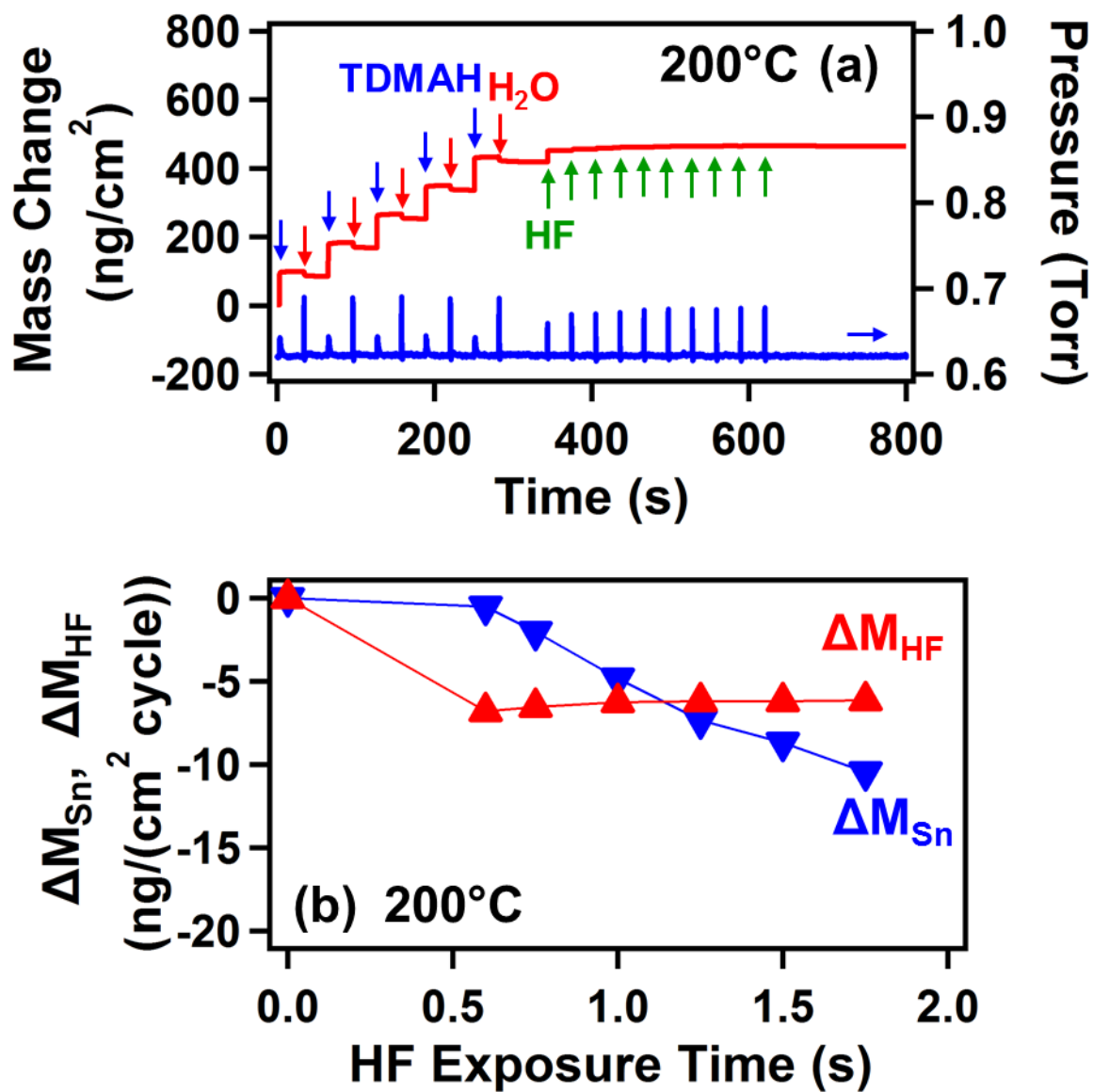
Figure 7-6 (a) Mass change versus time during five cycle of HfO_2 ALD and then ten HF exposures on the HfO_2 ALD film. (b) ΔM_{Sn} and ΔM_{HF} during HfO_2 ALE for a $Sn(acac)_2$ exposure of 1.0 s and variable HF exposure.

reaction has reached saturation. This behavior is consistent with the self-limiting adsorption of HF on HfO_2. In addition, HF does not spontaneously etch HfO_2.

Figure 6b shows the ΔM_{Sn} and ΔM_{HF} values for variable HF exposure times with a $Sn(acac)_2$ exposure time of 1.0 s. The ΔM_{HF} values are fairly constant at approximately -6 ng/(cm^2 cycle). This behavior indicates that the ΔM_{HF} values are not responsible for the lack of self-limiting behavior observed in Figure 5b. In contrast, the ΔM_{Sn} values increase progressively with HF exposure time for a fixed $Sn(acac)_2$ exposure time of 1.0 s. This increasing mass loss during the $Sn(acac)_2$ exposure is attributed to HfO_2 CVE caused by the presence of both HF and $Sn(acac)_2$. At longer HF exposure times, more HF residual pressure is believed to be present during the $Sn(acac)_2$ exposure. This HF residual pressure together with the fixed $Sn(acac)_2$ exposure time of 1.0 s leads to HfO_2 CVE.

Additional experiments performed at longer purge times than 30 s after the HF exposures did lead to more self-limiting behavior. However, the MCPC continued to increase versus HF exposure time. HF is difficult to purge completely after long HF exposures. The results in Figure 5b should be self-limiting with effective HF purging after HF exposures.

Figure 7 displays the mass change during 100 HfO_2 ALE cycles using sequential $Sn(acac)_2$ and HF reactions at 150℃, 175℃, 200℃, 225℃, and 250℃. The initial HfO_2 films were grown before HfO_2 ALE at the same temperatures. These HfO_2 films were deposited by 100 cycles of HfO_2 ALD using TDMAH and H_2O with a sequence of 1-20-1-20. Using the same reaction conditions as employed for the results in Figures 2 and 3, one HfO_2 ALE cycle consisted of a $Sn(acac)_2$ exposure of 1.0 s, an N_2 purge of 30 s, a HF exposure of 1.0 s, and a second N_2 purge of 30 s.
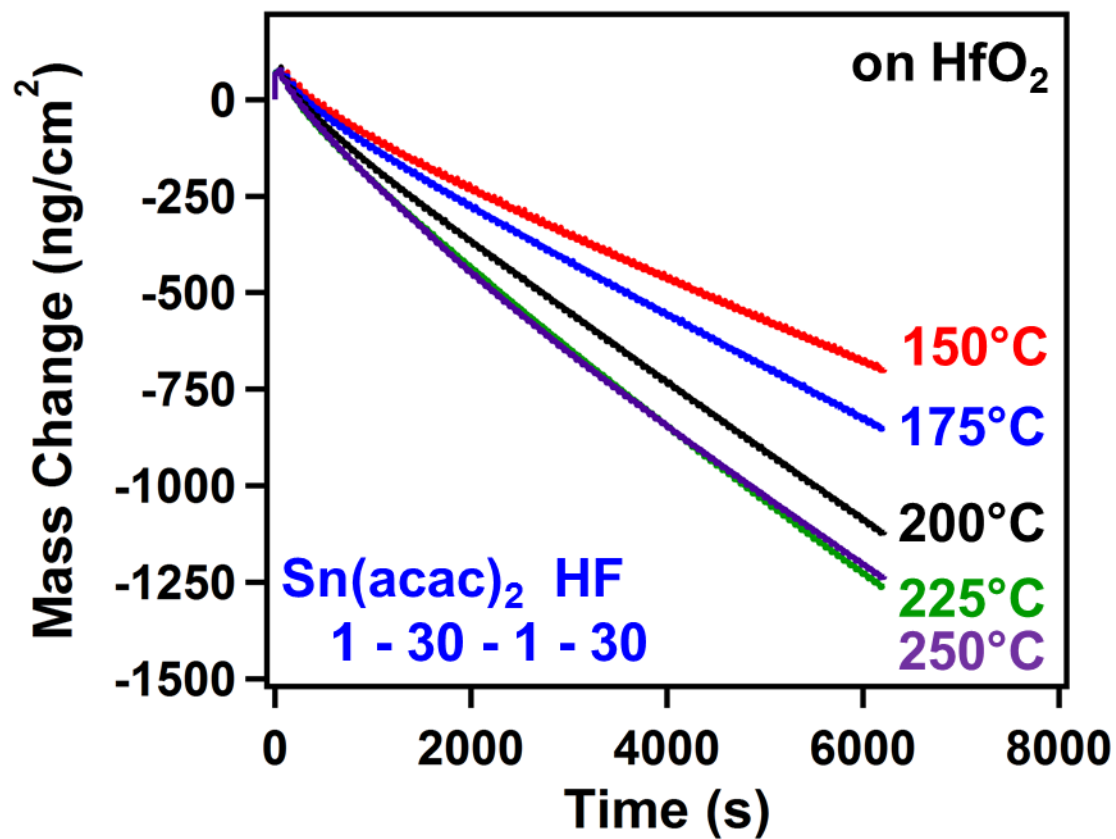
Figure 7-7   Mass change versus time for HfO_2 ALE using sequential $Sn(acac)_2$ and HF

exposures at 150, 175, 200, 225 and 250°C.

The HfO$_2$ ALE mass changes are linear for all temperatures. The MCPC was determined at steady state after the first 20 HfO$_2$ ALE cycles. The MCPC increases at higher temperatures. The MCPC was -6.7, -8.3, -11.1, -11.9, and -11.2 ng/(cm^2 cycle) at 150, 175, 200, 225, and 250°C, respectively. These MCPCs correspond to etch rates of 0.070, 0.087, 0.116, 0.124, and 0.117 Å /cycle at 150, 175, 200, 225 and 250°C, respectively. These etch rates in Å /cycle are based on the HfO$_2$ ALD film density of 9.6 g/cm^3. The MCPC values are essentially equivalent at 200, 225 and 250°C. The differences in the mass change after 100 cycles for these temperatures are determined mostly by the mass changes in the nucleation regime during the first 20 HfO$_2$ ALE cycles.

The ΔM_{Sn}, ΔM_{HF}, and MCPC values at the various reaction temperatures are shown in Figure 8. All HfO$_2$ ALE reactions were performed using a reaction sequence of 1-30-1-30 on initial HfO$_2$ films. Figure 8a shows that ΔM_{Sn} displays a slight mass gain at 150°C and progressively larger mass losses at higher temperatures. In contrast, ΔM_{HF} displays mass losses over the entire temperature range. The mass losses are slightly less at higher temperatures.

Figure 8b reveals that the MCPC increases with temperature between 150 and 200°C. The MCPC values are nearly equivalent at 200, 225 and 250°C. The MCPC in Figure 8b correlates with ΔM_{Sn} in Figure 8a. This correspondence indicates that the mass change during the Sn(acac)$_2$ reaction is primarily responsible for the temperature dependence of the mass loss during HfO$_2$ ALE. The ΔM_{Sn}, ΔM_{HF}, MCPC and ΔM_{sn}/MCPC values at the different reaction temperatures are summarized in Table 1. Based on previous results for Al$_2$O$_3$ ALE,[24, 40] the temperature dependence of the MCPC values is believed to be dependent on the amount of acetylacetonate surface species remaining after the Sn(acac)$_2$ and HF exposures.
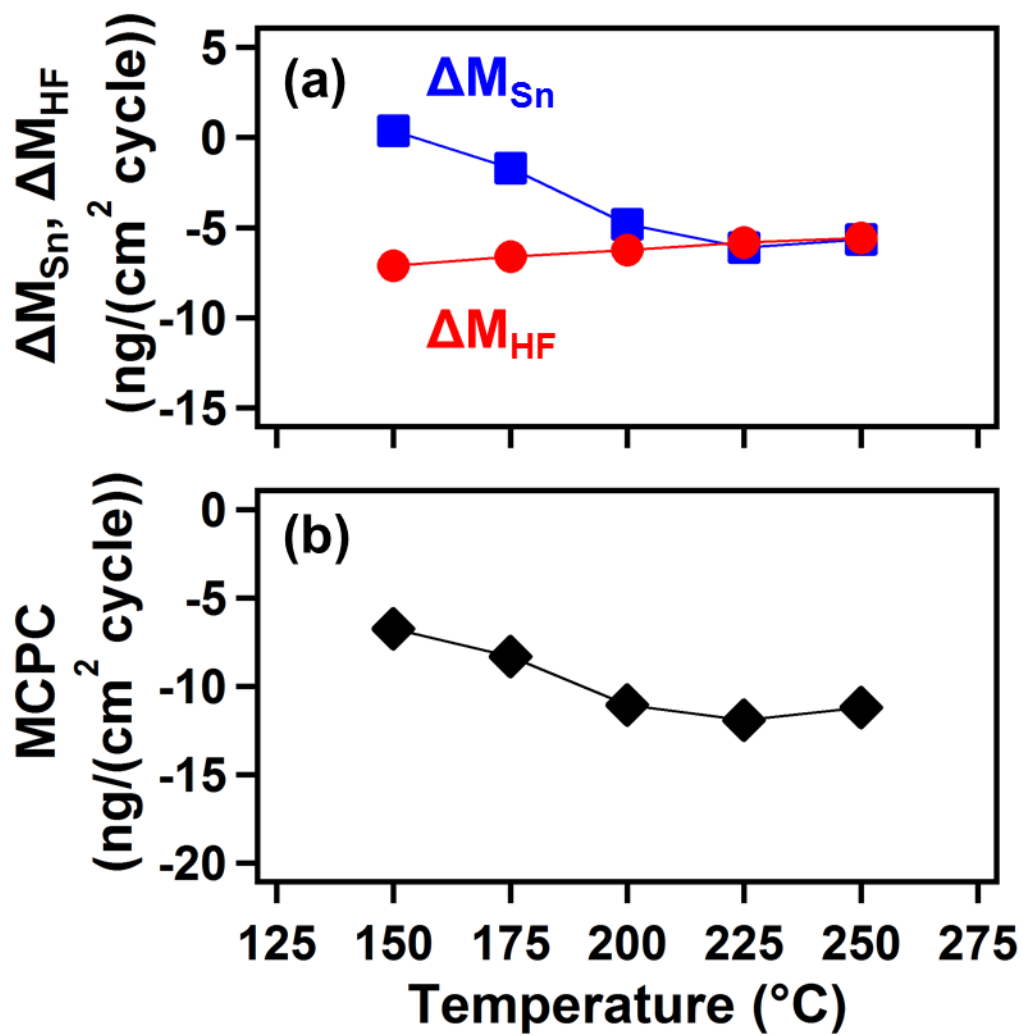
Figure 7-8   Temperature dependence of (a) ΔM_{Sn} and ΔM_{HF} and (b) MCPC for HfO_2 ALE.

Temperature (°C)	MCPC	ΔM_{Sn}	ΔM_{HF}	$\Delta M_{Sn}/$ MCPC	x	x(MCPC)
150	-6.7	0.37	-7.1	-0.058	1.1	-7.6
175	-8.3	-1.7	-6.6	0.20	0.90	-7.4
200	-11.1	-4.8	-6.3	0.43	0.69	-7.7
225	-11.9	-6.1	-5.8	0.51	0.62	-7.4
250	-11.2	-5.6	-5.6	0.50	0.63	-7.0

Table 7-1. ΔM_{Sn}, ΔM_{HF}, MCPC, $\Delta M_{Sn}/$MCPC, x, and x(MCPC) for HfO_2 ALE at different temperatures. ΔM_{Sn}, ΔM_{HF}, MCPC and x(MCPC) are expressed in units of ng/(cm^2 cycle).

7.3B. XRR, XPS and SE Measurements

Ex situ XRR studies also examined HfO_2 ALE. These XRR experiments employed HfO_2 ALD films with a thickness of 144 Å that were grown on Si(100) wafers. These HfO_2 ALD films were deposited using 150 cycles of TDMAH and H_2O at 200°C with a reaction sequence of 1-20-1-20. Figure 9 shows XRR scans of the HfO_2 ALD films on the Si wafers versus number of $Sn(acac)_2$ and HF reaction cycles at 200°C. The XRR scans have been displaced from each other for clarity. These XRR scans reveal uniform and smooth HfO_2 films.

Figure 9a displays the XRR scan of the initial HfO_2 ALD film grown on Si(100) wafers. The HfO_2 ALD film thickness of 144 Å can be obtained by fitting the reflected x-ray intensity versus incident angle. Figure 9b, 9c, 9d, and 9e show XRR scans of the etched HfO_2 film after 50, 100, 200, and 400 ALE cycles at 200°C, respectively. The HfO_2 thicknesses decrease with increasing number of ALE cycles. This decreasing film thickness leads to the decrease in the modulation of the x-ray intensity versus angle with higher numbers of ALE cycles.

The etched HfO_2 films are smooth and do not roughen versus HfO_2 ALE. The XRR measurements yielded a roughness of the initial HfO_2 ALD film of ~6 Å . The surface roughness then decreased to ~3-4 Å after 50, 100, 200, and 400 ALE cycles. The ALE process is able to smooth the surface of the initial HfO_2 films. The error in these XRR surface roughness measurements is ~1 Å . The position of the critical angle of all the etched HfO_2 films is also constant. This constant critical angle indicates that there is no change of the film density during the ALE reactions.
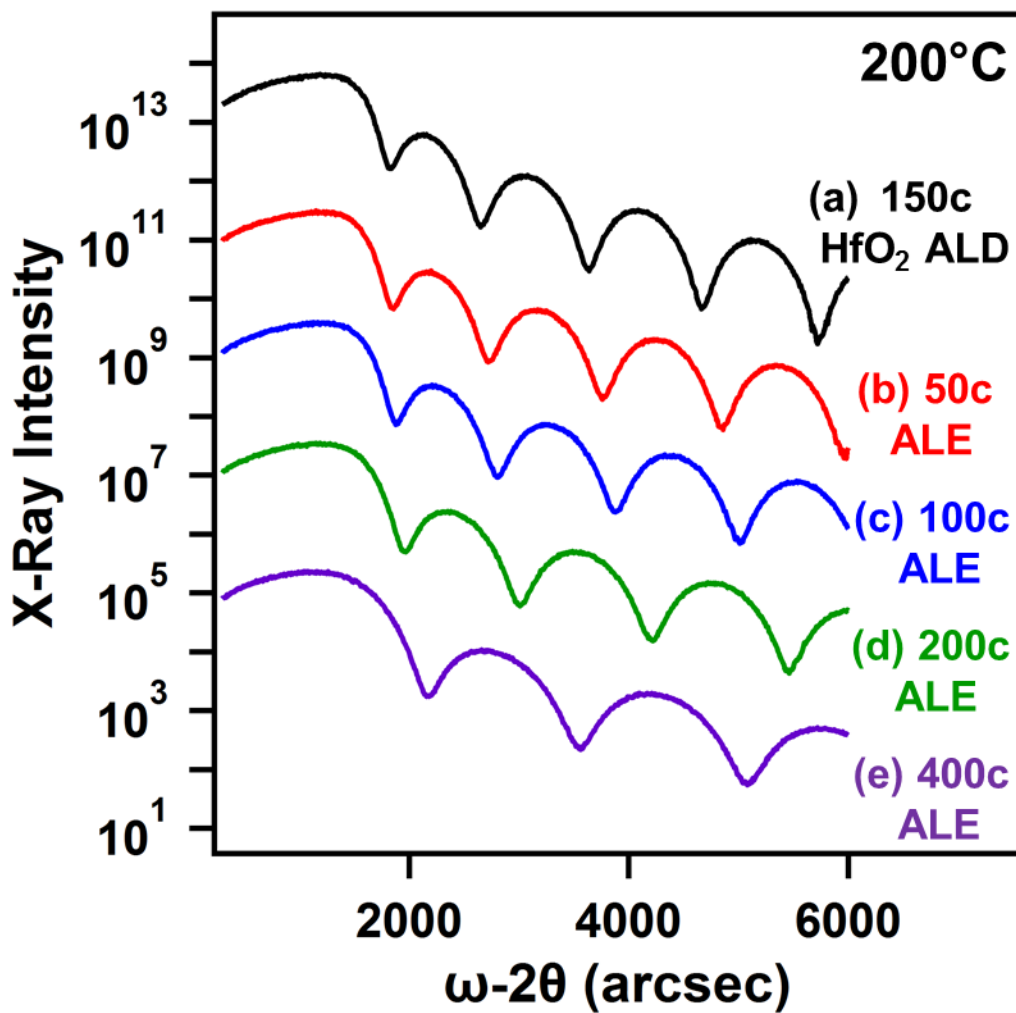
Figure 7-9   X-ray reflectivity scans showing x-ray intensity versus incident angle for HfO_2

films on Si(100). (a) Initial HfO_2 film grown using 150 HfO_2 ALD cycles; and

HfO_2 films after various numbers of HfO_2 ALE cycles: (b) 50 cycles, (c) 100

cycles, (d) 200 cycles and (e) 400 cycles.

Figure 10 shows the XRR measurements of the initial HfO_2 film thickness and the HfO_2 film thicknesses after 50, 100, 200, and 400 ALE cycles at 200°C. For the HfO_2 films with an initial thickness of 144 Å in Figure 10a, the film thickness versus number of ALE cycles is linear and yields an etch rate of 0.11 Å/cycle. The SE measurements on these same samples yield an etch rate of 0.11 Å/cycle with an initial HfO_2 ALD film thickness of 143 Å. The initial thickness of the HfO_2 film was not used to obtain the etch rate because of the mass gain on the first cycle and the nucleation regime that occurs during first 20 ALE cycles. The SE analysis also determined a refractive index of n=2.07 for the HfO_2 film at a wavelength of 589 nm. This refractive index for the HfO_2 film remained at n=2.07-2.09 after 50, 100, 200, and 400 ALE cycles.

XRR measurements were also performed on HfO_2 ALD films with a thickness of 87 Å that were grown on Si(100) wafers. These HfO_2 ALD films were deposited at 200°C using 100 cycles of TDMAH and H_2O with a reaction sequence of 1-20-1-20. Figure 10b displays the film thickness versus number of $Sn(acac)_2$ and HF reaction cycles at 200°C. The XRR measurements yield an HfO_2 ALE etch rate of 0.11 Å/cycle. The SE measurements also yield an etch rate of 0.12 Å/cycle with an initial HfO_2 ALD film thickness of 87 Å. The initial thickness of the HfO_2 film is again not employed to determine the etch rate because of the mass gain that occurs on the first ALE cycle and the nucleation regime that occurs during the first 20 ALE cycles.

X-ray photoelectron spectroscopy (XPS) analysis was used to determine the elements on the HfO_2 film after HfO_2 ALE. The XPS analysis measured Sn $3d_{5/2}$ XPS signals of 0.47-0.61 at% and F 1s XPS signals of 4.0-4.1 at% after 200 or 400 Al_2O_3 ALE cycles after the HF
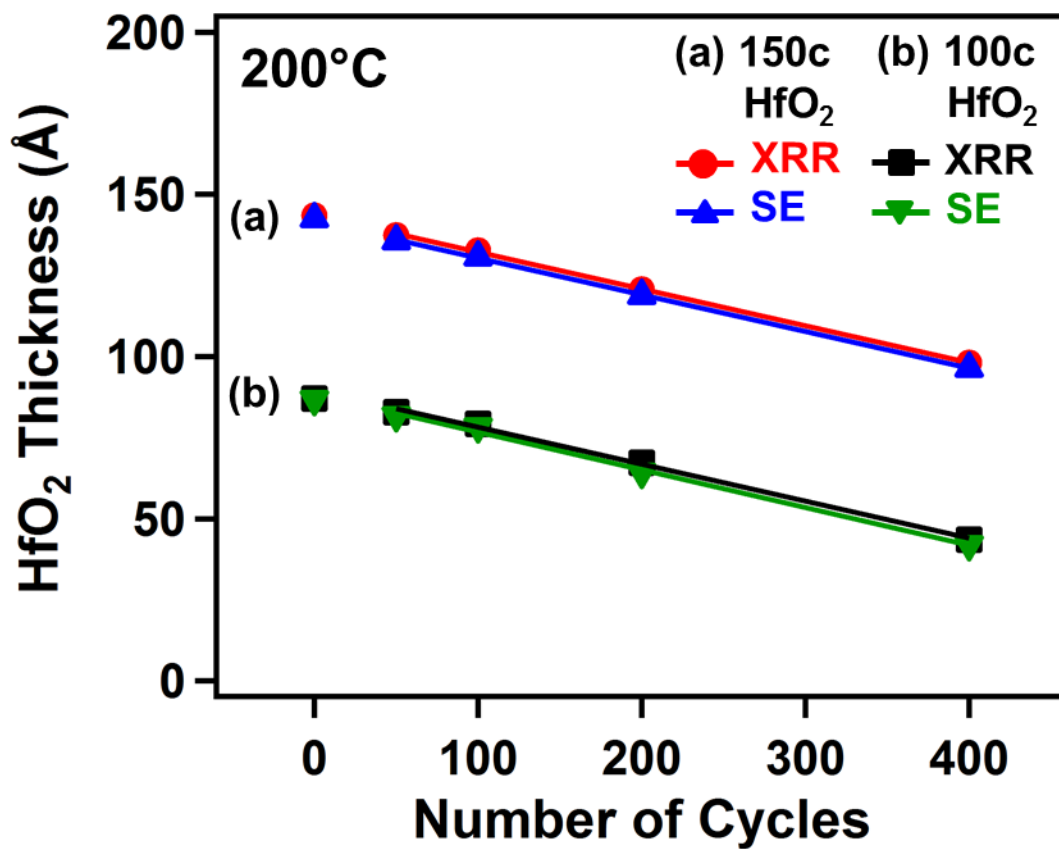
Figure 7-10   X-ray reflectivity (XRR) and spectroscopic ellipsometry (SE) measurements of

HfO$_2$ film thickness versus number of HfO$_2$ ALE cycles for initial HfO$_2$ ALD

films grown using (a) 150 HfO$_2$ ALD cycles and (b) 100 HfO$_2$ ALD cycles.

exposure. These XPS signals are consistent with residual Sn(acac)$_2$ adsorption products and the formation of HfF$_4$ or HfF$_x$ surface species. The Sn and F XPS signals were removed to below the XPS detection limit after Ar ion sputtering for 2 minutes. This sputtering time also removes adventitious carbon from the surface.

7.3C. FTIR Spectroscopy Measurements

In situ FTIR spectra of HfO$_2$ ALD films grown using 10 cycles of TDMAH and H$_2$O at 200°C are shown in Figure 11. These FTIR spectra are difference spectra referenced to the initial SiO$_2$ nanoparticle substrate. The prominent absorbance feature between 500–800 cm^{-1} is attributed to the Hf-O stretching vibrations in bulk HfO$_2$.[41, 42] The absorbance of the Hf-O stretching vibrations in amorphous HfO$_2$ is broad and ranges from ~200-750 cm^{-1}.[41-43] The breadth of this expected absorbance feature is not observed in Figure 11. The strong absorption from the SiO$_2$ nanoparticles at ≤500 cm^{-1} obscures the infrared absorbance of the Hf-O stretching vibrations at ≤500 cm^{-1}.

The infrared absorbance of the Hf-O stretching vibration between 500–800 cm^{-1} increases progressively versus number of HfO$_2$ ALD cycles. In addition to these Hf-O vibrational features, a negative absorption feature appears in Figure 11 at ~1250 cm^{-1} along with the positive absorption feature at ~1000 cm^{-1}. The negative absorption feature at ~1250 cm^{-1} is assigned to the loss of absorbance from Si-O-Si stretching vibrations in the SiO$_2$ substrate.[44] The positive absorption feature at ~1000 cm^{-1} is attributed to the gain of absorbance from Si-O-Hf stretching
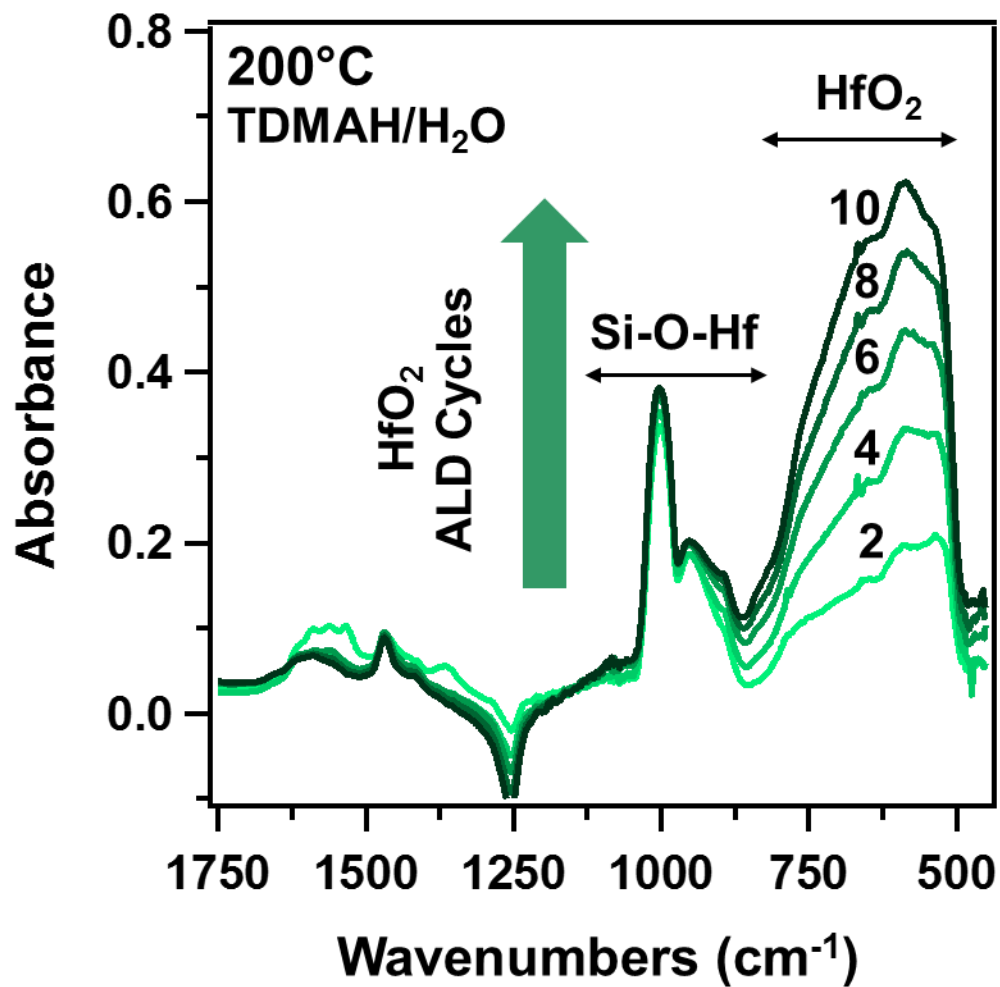
Figure 7-11   Absolute infrared absorbance showing the growth of Hf-O stretching vibrations in

bulk HfO_2 versus number of HfO_2 ALD cycles at 200°C. These FTIR spectra

were referenced to the initial SiO_2 particles.

vibrations in hafnium silicate.[41, 44, 45] The hafnium silicate forms almost entirely during the first two HfO_2 ALD cycles on the SiO_2 nanoparticles at 200°C.

Figure 12 shows the FTIR spectra after 4, 6, 8, and 10 ALE cycles at 200 °C. These spectra were recorded after the $Sn(acac)_2$ exposures. Decreasing absorbance for the Hf-O stretching vibration at 500–800 cm^{-1} versus ALE cycles is consistent with HfO_2 etching. There is also a corresponding decrease in absorbance of the Si-O-Hf vibrations in hafnium silicate at ~1000 cm^{-1}. Infrared absorbance for the $Sn(acac)_2$ adsorption products is also observed in Figure 12 in the range between 1250-1750 cm^{-1}. These vibrational features are derived from the acetylacetonate (acac) constituents.[46, 47] These features are consistent with either $Sn(acac)_2$*, $SnF(acac)$* or acac* adsorbed on the HfO_2 substrate

7.3D. Nucleation Behavior and Proposed HfF₄ Formation

Figure 13 displays an enlargement of the mass changes from Figure 7 during the first two ALE cycles on HfO_2 films. The first $Sn(acac)_2$ exposure shows mass gains of $\Delta M_{Sn} = 68\text{-}72$ ng/cm^2 at 150-250°C resulting from adsorption products of $Sn(acac)_2$ such as $Sn(acac)$* and acacH*. To estimate the coverage of $Sn(acac)_2$* species on the surface, the sites on the HfO_2 surface can be approximated using the HfO_2 density of 9.6 g/cm^3. This mass density is equivalent to a number density of $\rho = 2.7 \times 10^{22}$ "HfO_2 units"/cm^3. This number density yields an estimate for the number of "HfO_2 units" on the HfO_2 surface of $\rho^{2/3} = 9.10 \times 10^{14}$ "HfO_2 units"/cm^2 assuming a square lattice. This coverage of "HfO_2 units" represents an HfO_2 mass of 320 ng/cm^2.
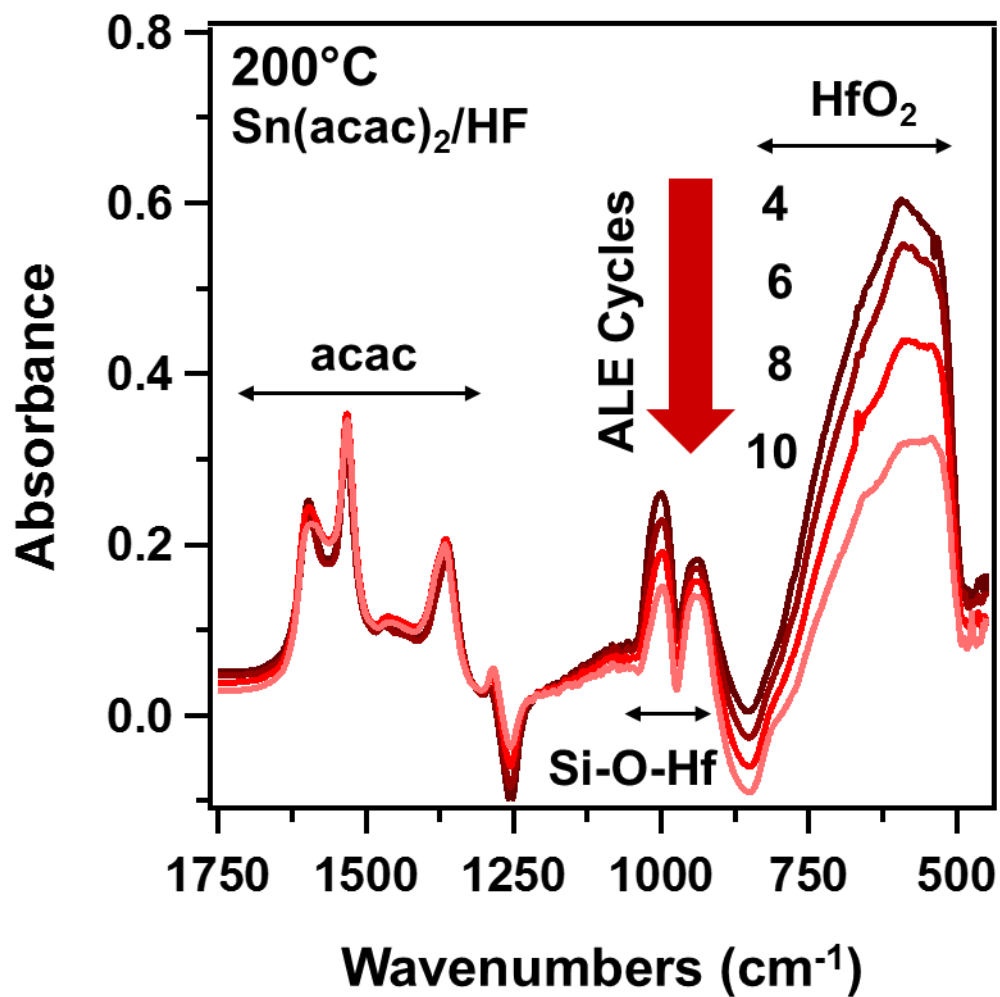
Figure 7-12 Absolute infrared absorbance showing the loss of Hf-O stretching vibration in

bulk HfO_2 versus number of HfO_2 ALE cycles at 200°C. These FTIR spectra

were referenced to the initial SiO_2 particles.
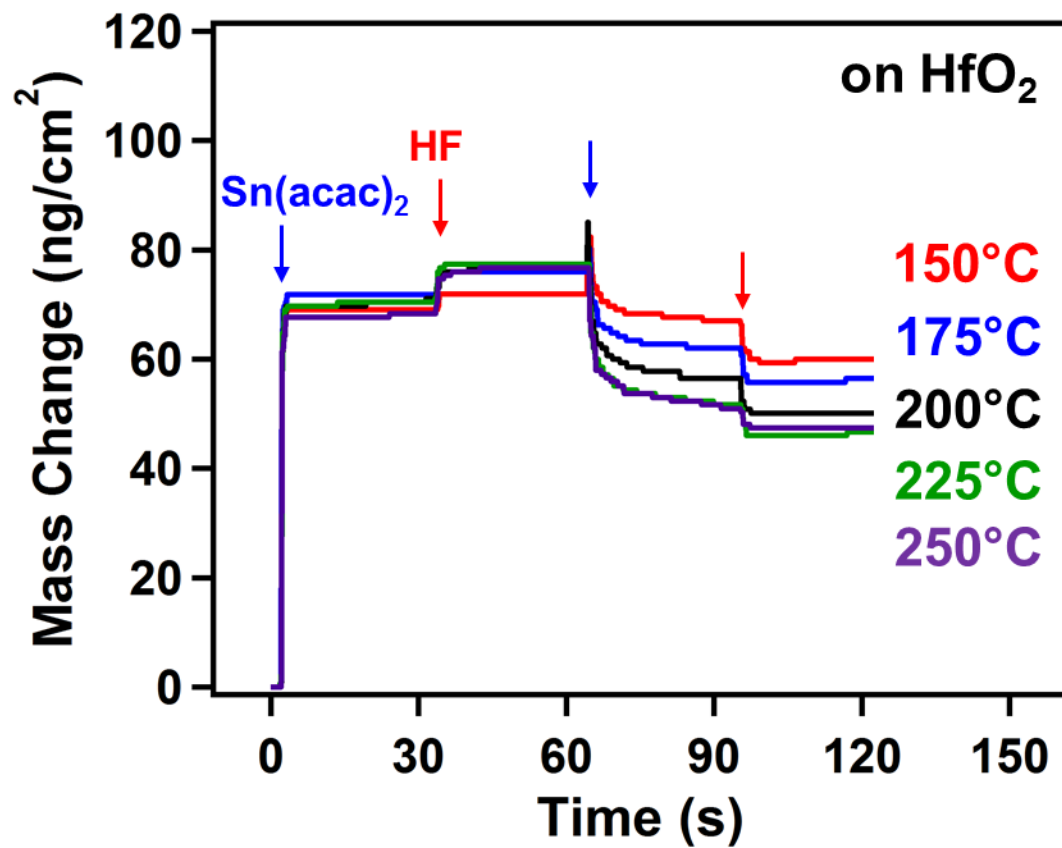
Figure 7-13   Expansion of first two ALE cycles in Figure 6 showing the individual mass

changes during the sequential Sn(acac)$_2$ and HF exposures at 150, 175, 200, 225

and 250°C.

The coverage of $Sn(acac)_2$* can then be approximated based on the mass gain of 72 ng/cm^2. This mass gain is equivalent to 1.37×10^{14} $Sn(acac)_2$ molecules/cm^2. The normalized coverage of $Sn(acac)_2$* species relative to "HfO_2 units" on the surface is 1.37×10^{14} $Sn(acac)_2$ molecules/cm^2 / 9.10×10^{14} "HfO_2 units"/cm^2 = 0.15 $Sn(acac)_2$ species/HfO_2 unit. This coverage is reasonable given that $Sn(acac)_2$ may dissociate into $Sn(acac)$* and acacH*. In addition, the acac ligand is bulky and expected to occupy more than one "HfO_2 unit" on the HfO_2 surface.

The first HF exposure on the surface previously exposed to $Sn(acac)_2$ shows mass gains of ΔM_{HF} = 3-8 ng/cm^2 at 150-250°C. These mass gains may be affected by the loss of $Sn(acac)_2$ adsorption products. The mass gains following HF exposures on an initial HfO_2 film can be used to estimate the coverage of HF or HF reaction products. A mass gain of 37.8 ng/cm^2 is observed after HF exposures on an initial HfO_2 film at 200°C in Figure 6a. Assuming that HF is the adsorption product, this mass gain is equivalent to 1.14×10^{15} HF molecules/cm^2. The normalized coverage of HF species relative to "HfO_2 units" on the surface is 1.14×10^{15} HF molecules/cm^2 / 9.10×10^{14} "HfO_2 units"/cm^2 = 1.25 HF/HfO_2 unit.

The HF may also react with the HfO_2 substrate by the reaction: $HfO_2 + 4HF \rightarrow HfF_4 + 2H_2O$. This reaction is predicted to be spontaneous over the temperature range from 150-250°C. The Gibbs free energy changes are negative and decrease slightly in absolute magnitude from ΔG= -22 kcal at 150 °C to ΔG = -16 kcal at 250°C.[38] Assuming that HfF_4 is the reaction product, the mass gain of 37.8 ng/cm^2 on an initial HfO_2 film at 200°C is equivalent to a HfF_4 coverage of 5.17×10^{14} HfF_4 molecules/cm^2. The normalized coverage of HfF_4 relative to "HfO_2 units" on the surface is 5.17×10^{14} HfF_4 molecules/cm^2 / 9.10×10^{14} "HfO_2 units"/cm^2 = 0.57 HfF_4/HfO_2 unit.

Assuming either HF or HfF_4 products, the estimated coverages after the HF exposure are comparable with the number of "HfO_2 units" on the HfO_2 substrate. These coverages are consistent with the rapid and self-limiting fluorination of the HfO_2 surface. In contrast, slow fluorination kinetics of bulk HfO_2 were observed during HF exposures.[48] Thermogravimetric studies showed that bulk HfO_2 did not begin fluorination under HF exposure until >350°C.[48] In addition, HfF_4 was not observed as a product by x-ray diffraction analysis until higher temperatures between 450-580°C.[48] The fluorination of the HfO_2 surface occurs much more readily than the fluorination of bulk HfO_2 substrates.

After the HF exposure, the next $Sn(acac)_2$ exposure reacts with the HfF_4 or HF adlayer on the HfO_2 substrate. Figure 13 shows that mass losses begin with this second $Sn(acac)_2$ exposure and continue with the subsequent HF exposure. Except for the first ALE cycle shown in Figure 13, all subsequent $Sn(acac)_2$ and HF exposures lead to mass loss resulting from the etching of the HfO_2 film.

The nucleation of the HfO_2 ALE process was also observed by the FTIR studies. Figure 14 shows FTIR spectra that are referenced to the starting SiO_2 substrate during the first HfO_2 ALE cycle. For these FTIR spectra, HF was exposed first to the initial HfO_2 film to monitor the surface fluorination to form HfF_4 or HfF_x surface species. With the first HF exposure, a portion of the Hf-O absorbance feature decreases between 625 - 800 cm^{-1}. There is also another absorbance decrease between ~800-900 cm^{-1}. These changes may correspond with the conversion of Hf-O stretching vibrations to Hf-F stretching vibrations.
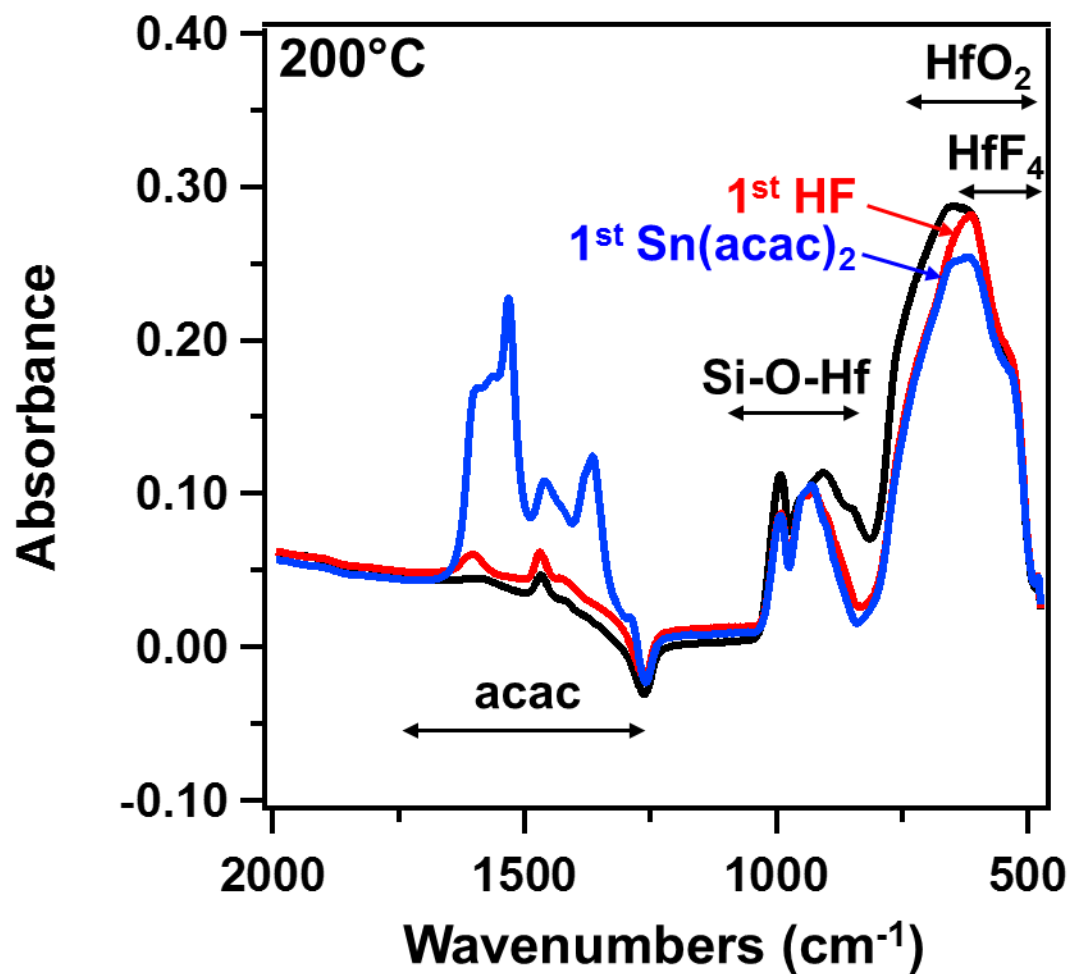
Figure 7-14   Absolute infrared absorbance showing the Hf-O stretching vibrations in bulk

HfO_2 and the acac vibrational features for the first $Sn(acac)_2$ and HF exposures at

200°C. These FTIR spectra were referenced to the initial SiO_2 particles.

The infrared absorbance between 500-650 cm^{-1} decreases after the first Sn(acac)$_2$ exposure. This decrease is attributed to the removal of HfF$_4$ or HfF$_x$ surface species. For an HfF$_4$ adlayer, this removal may occur by the reaction HfF$_4$ + 4Sn(acac)$_2$ $\rightarrow$ Hf(acac)$_4$ + 4SnF(acac). Sn(acac)$_2$ may also adsorb on the thin HfO$_2$ film and perturb the Hf-O vibrational modes. In addition, pronounced vibrational features associated with acac species on the HfO$_2$ substrate at 1250-1750 cm^{-1} are observed in Figure 14 after the Sn(acac)$_2$ exposure.

Because the loss in absorbance from HfO$_2$ and the gain in absorbance from HfF$_4$ or HfF$_x$ surface species occur in the same frequency range, difference FTIR spectra were recorded during the first HF and first Sn(acac)$_2$ exposures on the initial HfO$_2$ film to distinguish the HfF$_4$ or HfF$_x$ surface species produced by the first HF exposure. Figure 15a shows the difference spectra after the first HF exposure. The first HF exposure produces a gain in absorbance between 500 – 650 cm^{-1} and a loss in absorbance between 650 - 925 cm^{-1}. The reference spectrum for this FTIR spectrum was the initial HfO$_2$ film on the SiO$_2$ nanoparticles. The gain in absorbance between 500 – 650 cm^{-1} that is centered at ~585 cm^{-1} is attributed to the HfF$_4$ or HfF$_x$ surface species.

Figure 15a also shows that the subsequent Sn(acac)$_2$ exposure removes the absorbance feature associated with the HfF$_4$ or HfF$_x$ surface species. The reference spectrum for this FTIR spectrum was the previous FTIR spectrum recorded after the HF exposure. This loss of absorbance is expected from the Sn(acac)$_2$ reaction with the HfF$_4$ or HfF$_x$ surface species. There is also much less absorbance loss at 650 - 925 cm^{-1} associated with the higher frequency portion of the absorbance for the Hf-O stretching vibration. The Sn(acac)$_2$ removes the HfF$_4$ or HfF$_x$ surface species without significantly perturbing the underlying HfO$_2$ film. For comparison, Figure 15b displays the absorbance loss expected after the removal of an HfO$_2$ ALD film that was grown using ten HfO$_2$ ALD cycles.
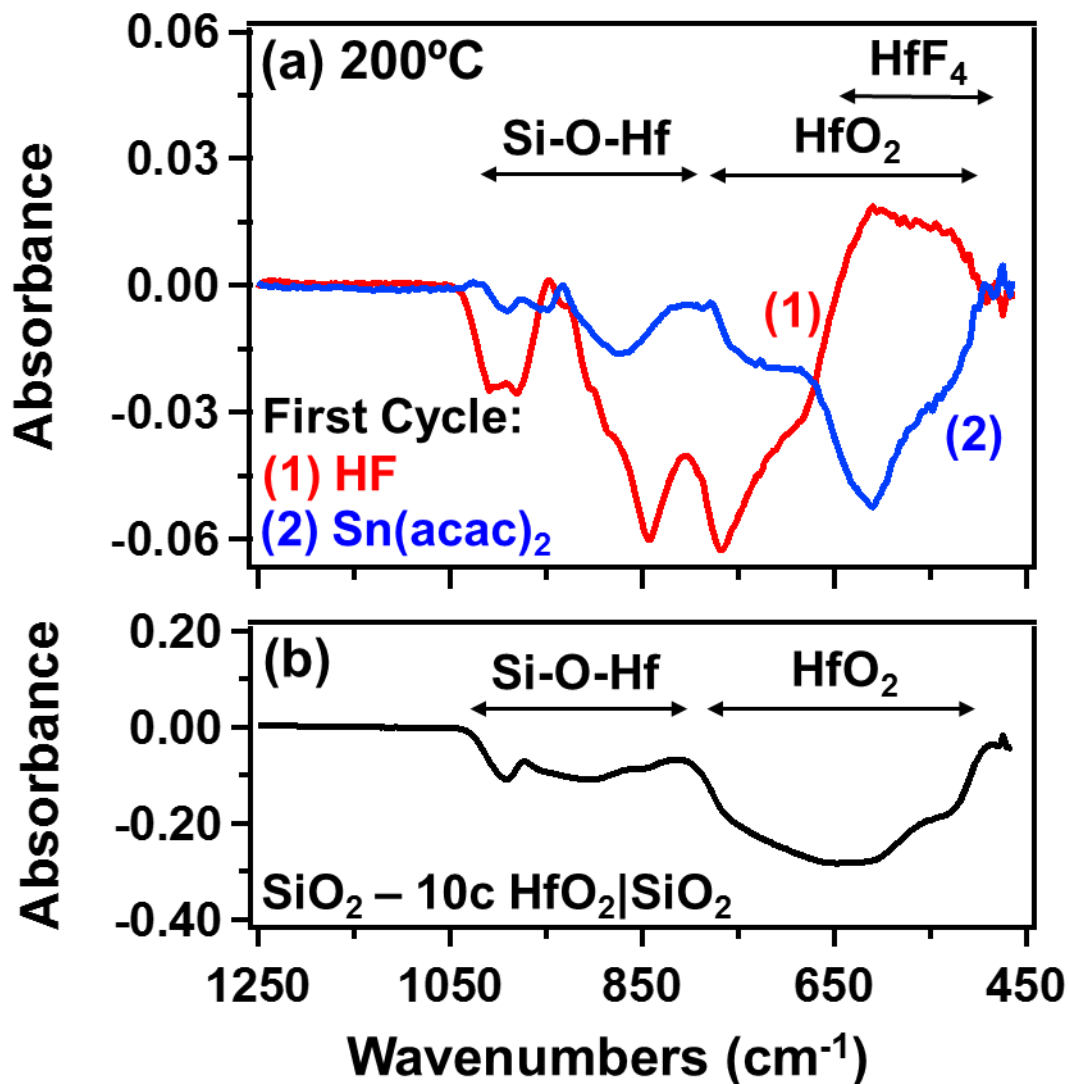
Figure 7-15 (a) 1. Difference spectrum after HF exposure on an initial HfO_2 film. The reference spectrum was the initial HfO_2 film on the SiO_2 nanoparticles. 2. Difference spectrum after the subsequent $Sn(acac)_2$ exposure. The reference spectrum was the previous FTIR spectrum after the HF exposure. (b) Difference spectrum after removal of 10 cycles of HfO_2 ALD from the SiO_2 nanoparticles. The reference spectrum was the FTIR spectrum after 10 cycles of HfO_2 ALD on the SiO_2 nanoparticles.

The absorbance feature between 500 – 650 cm^{-1} that is centered at ~585 cm^{-1} is attributed to HfF$_4$ or HfF$_x$ surface species. The frequency of this absorbance feature is slightly lower than the expected frequency of 645 - 650 cm^{-1} for Hf-F stretching vibrations in HfF$_4$.[49, 50] To determine the Hf-F stretching vibrational frequency in ultrathin HfF$_4$ films, HfF$_4$ ALD films were grown on a thin HfO$_2$ ALD film on SiO$_2$ nanoparticles using TDMAH and HF. The FTIR spectra versus number of HfF$_4$ ALD cycles are displayed in Figure 16. These FTIR spectra are referenced to the initial HfO$_2$ film on the SiO$_2$ nanoparticles.

The initial HfF$_4$ ALD film after two HfF$_4$ ALD cycles displays increased absorbance in a broad peak centered at ~585 cm^{-1}. The absorbance from these Hf-F stretching vibrations then shifts to higher frequencies with increasing number of HfF$_4$ ALD cycles. After ~20 HfF$_4$ ALD cycles, the absorbance peak shifts to ~640 cm^{-1}. This frequency is very close to the frequency of 645-650 cm^{-1} for the Hf-F stretching vibrations in HfF$_4$.[49, 50] These results argue that the absorbance feature in Figure 15a between 500 – 650 cm^{-1} that is centered at ~585 cm^{-1} is derived from HfF$_4$ or HfF$_x$ surface species. The Hf-F stretching vibration has a lower frequency in HfF$_x$ surface species or in ultrathin HfF$_4$ films.

7.3E. Proposed HfO$_2$ ALE Reactions

Figure 17 shows the schematic for the proposed HfO$_2$ ALE surface chemistry. This possible picture for HfO$_2$ ALE is derived from the mass changes during the Sn(acac)$_2$ and HF exposures as determined by the QCM measurements and the vibrational absorbances observed
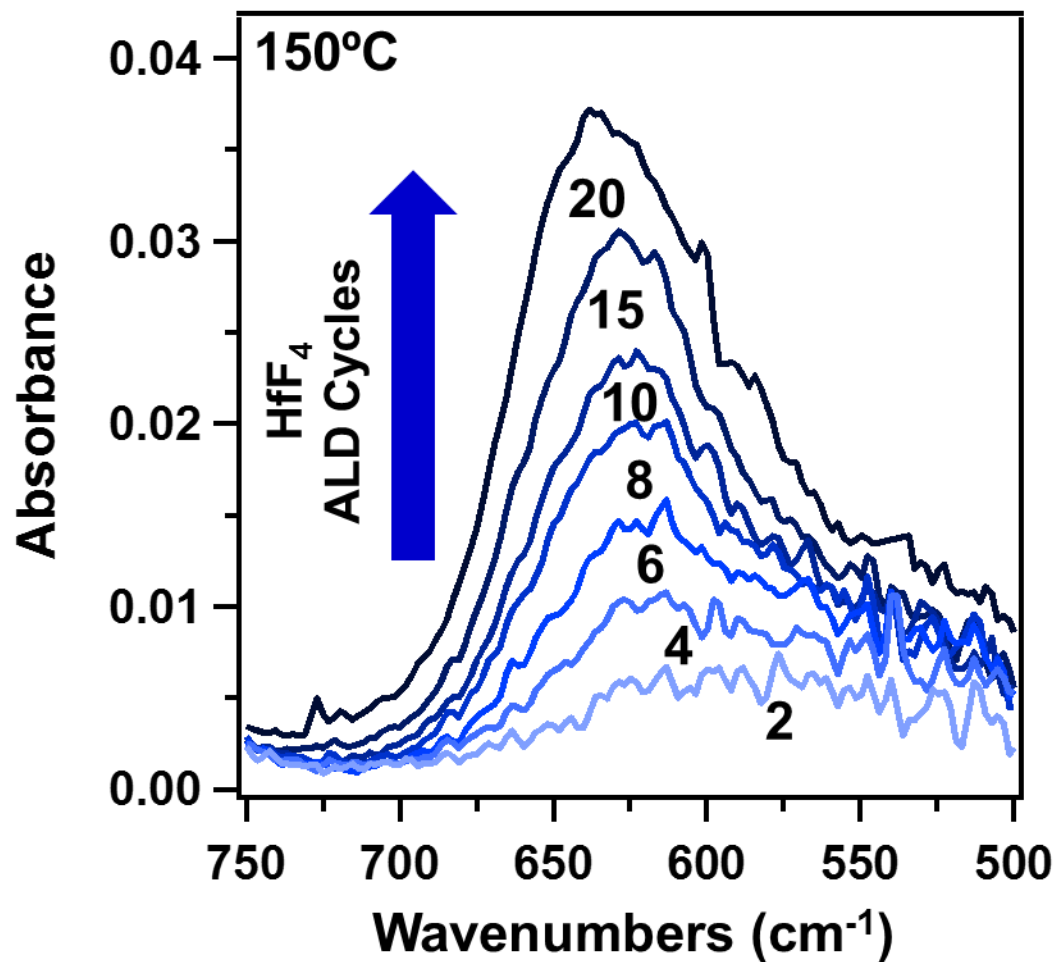
Figure 7-16   Absolute infrared absorbance showing the growth of Hf-F stretching vibrations in

HfF$_4$ films versus number of HfF$_4$ ALD cycles at 150°C. These FTIR spectra are

referenced to the initial HfO$_2$ film on the SiO$_2$ nanoparticles after the first HF
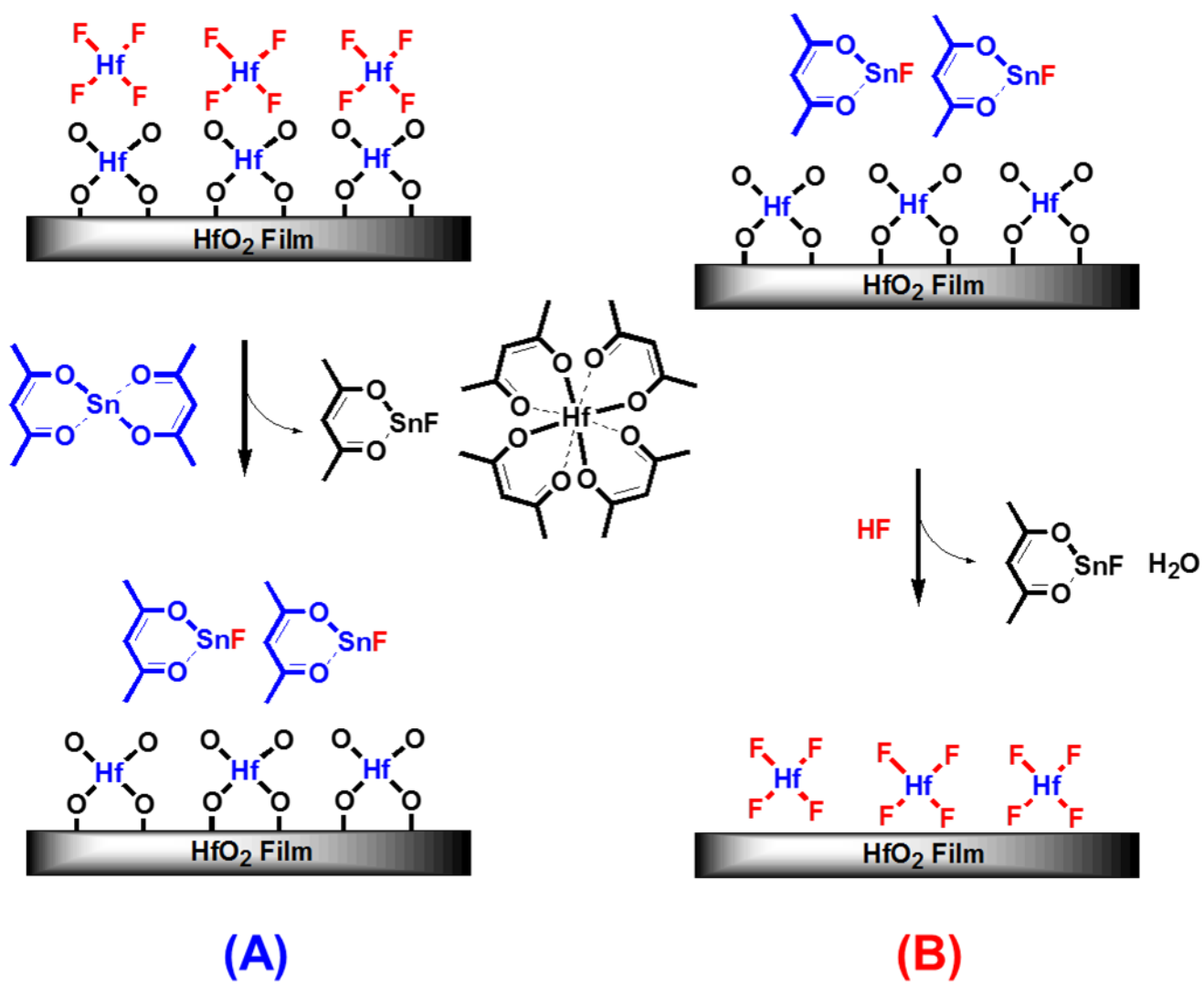
exposure.

Figure 7-17 Schematic of proposed surface chemistry for HfO$_2$ ALE showing (A) Sn(acac)$_2$ reaction and (B) HF reaction.

by the FTIR spectroscopy analysis. This scheme includes only surface species that change during the $Sn(acac)_2$ and HF exposures. This scheme also assumes that the HF reaction produces HfF_4 on the HfO_2 film.

During the $Sn(acac)_2$ reaction (A), $Sn(acac)_2$ reacts with the HfF_4 layer on the HfO_2 substrate to form volatile $SnF(acac)$ and $Hf(acac)_4$ reaction products and $SnF(acac)*$ surface species. After the HfF_4 layer is lost resulting from $Hf(acac)_4$ and $SnF(acac)$ product formation, there may be a strong interaction between $SnF(acac)*$ surface species and the underlying HfO_2 substrate. This interaction may lead to some $SnF(acac)*$ species adsorbed to the HfO_2 substrate.

During the HF reaction (B), HF reacts with some of the $SnF(acac)*$ surface species and the underlying HfO_2 surface to form a HfF_4 layer. In addition, HF also provides hydrogen to form H_2O as a reaction product. This reaction removes the oxygen in HfO_2. The HfF_4 layer is then ready for the next $Sn(acac)_2$ reaction.

The overall proposed reaction can be expressed as:

$$HfO_2 + 4HF + 4Sn(acac)_2 \rightarrow Hf(acac)_4 + 4SnF(acac) + 2H_2O \qquad (1)$$

This overall reaction can be divided into the $Sn(acac)_2$ and HF reactions:

(A) $HfO_2|HfF_4* + 4Sn(acac)_2 \rightarrow$

$$HfO_2|xSnF(acac)* + Hf(acac)_4 + (4\text{-}x)SnF(acac) \qquad (2)$$

(B) $HfO_2|xSnF(acac)* + 4HF \rightarrow HfF_4* + xSnF(acac) + 2H_2O \qquad (3)$
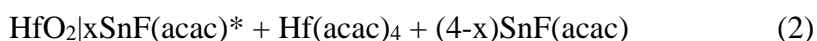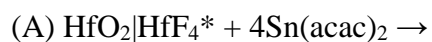
These reactions include only the species that change during the $Sn(acac)_2$ and HF exposures. The asterisks indicate the surface species and the vertical lines are used to separate the various surface species. Note that HfF_4 is the key reaction intermediate. The production of all the

Hf(acac)$_4$ is assumed to occur during reaction (A). Hf(acac)$_4$ is a stable metal β-diketonate with a vapor pressure of ~0.1 Torr at 150 °C.[51, 52]

The HfO$_2$ shown in Equations 2 and 3 is the amount of HfO$_2$ that is etched in one HfO$_2$ ALE cycle. x quantifies the coverage of SnF(acac)* on the surface after the Sn(acac)$_2$ exposures relative to the amount of HfO$_2$ that is etched in on HfO$_2$ ALE cycle. x can be determined from the ΔM_{Sn}/MCPC ratio using the equation:

$$x = (254.5 - 210.5(\Delta M_{Sn}/MCPC))/236.8 \tag{4}$$

where 254.5, 210.5 and 236.8 are the molecular weights for HfF$_4$, HfO$_2$ and SnF(acac), respectively. The x values are 1.1, 0.90, 0.69, 0.62, and 0.63 at 150, 175, 200, 225 and 250°C, respectively. Table 1 lists all the x and MCPC values.

x defines the SnF(acac)* species after the Sn(acac)$_2$ exposures relative to the amount of HfO$_2$ that is etched in one HfO$_2$ ALE cycle. Consequently, the product x(MCPC) provides a measure of the SnF(acac)*surface species after the Sn(acac)$_2$ exposures. The x(MCPC) values are included in Table 1. These x(MCPC) values are fairly constant at all the temperatures. This behavior indicates that the SnF(acac)* coverage is nearly constant at all the temperatures after the Sn(acac)$_2$ exposures. This coverage may represent a saturated monolayer for SnF(acac)* on the HfO$_2$ surface.

The proposed reactions for HfO$_2$ ALE are similar to the reactions proposed earlier for Al$_2$O$_3$ ALE.[24] Both HfO$_2$ ALE and Al$_2$O$_3$ ALE display etching rates that increase at higher temperatures. These temperature dependent etching rates are believed to be correlated inversely with the acetylacetonate coverage remaining on the substrate after the Sn(acac)$_2$ exposure.[24, 40] The Hf(acac)$_4$ and Al(acac)$_3$ etching products are both volatile. The vapor pressure of Hf(acac)$_4$

at 150°C is ~0.1 Torr.[51, 52] The vapor pressure of Al(acac)$_3$ at 150°C is ~3-4 Torr.[53-55] Both

HfO$_2$ and Al$_2$O$_3$ form stable fluorides upon exposure to HF. However, the Hf(acac)$_4$ etching

product may become unstable at >100°C.[52] The ΔG for the HF reaction with HfO$_2$ is also not as

favorable as the ΔG for the HF reaction with Al$_2$O$_3$.[38] These factors may lead to etching rates for

Al$_2$O$_3$ ALE that are higher than the etching rates for HfO$_2$ ALE.

7.3F. Extensions to Other Materials and Advantages of Thermal ALE

The ALE of other materials should be possible using sequential, self-limiting thermal

reactions with Sn(acac)$_2$ and HF as the reactants.[24] The prospective materials include other

metal oxides, metal nitrides, metal phosphides, metal sulfides and metal arsenides.[24] The

Sn(acac)$_2$ and HF reactants should be generally useful because Sn(acac)$_2$ can readily react with

fluorine to form SnF(acac). Sn-F bond formation is favorable because tin has a high affinity for

fluorine.[56] The Sn-F bond enthalpy is 466.5 kJ/mole in the diatomic SnF molecule.[57]

The reaction of Sn(acac)$_2$ with fluorine to form SnF(acac) enables Sn(acac)$_2$ to release an

acac ligand to the surface. Metals easily form complexes with acac ligands and have comparable

stabilities.[58] The hydrogen from HF can also combine with either oxygen, nitrogen,

phosphorous, sulfur or arsenic from the metal oxide, metal nitride, metal phosphide, metal

sulfide or metal arsenide to form H$_2$O, NH$_3$, PH$_3$, H$_2$S or AsH$_3$, respectively.[24] The ALE of

elemental metals should also be possible by first oxidizing the metal and then etching the

resulting metal oxide.[24] Alternatively, elemental metals could be directly fluorinated to form the

metal fluoride and then the metal fluoride could be removed by Sn(acac)$_2$.

There are advantages to the thermal ALE approach compared with ALE based on halogen adsorption and ion or energetic neutral noble atom bombardment. The thermal ALE approach avoids any damage to the underlying substrate resulting from high energy ions or energetic neutrals.[59] ALE based on ion or neutral noble atom bombardment requires line-of-sight to the substrate. This requirement can be used advantageously to minimize undercutting with directional ions or energetic neutral atoms during ALE. However, this line-of-sight requirement is limited to the small surface areas that are subjected to ion or neutral noble atom bombardment. In contrast, the thermal ALE approach will be useful for etching larger samples. The thermal ALE approach will also be important for etching high surface area samples and high aspect ratio structures.

7.4. Conclusions

HfO_2 ALE was demonstrated using $Sn(acac)_2$ and HF as the reactants. The sequential, self-limiting thermal reactions of $Sn(acac)_2$ and HF etched HfO_2 linearly with atomic level precision. HfO_2 ALE was observed at temperatures from 150-250℃. The $Sn(acac)_2$ reaction was self-limiting versus reactant exposure as revealed by QCM studies. However, the HF reaction was weakly self-limiting presumably because of a high residence time for HF and chemical vapor etching (CVE) caused by the presence of both $Sn(acac)_2$ and HF in the reactor.

The QCM studies measured MCPC values of -6.7, -8.3, -11.1, -11.9, and -11.2 $ng/(cm^2$ cycle) at 150, 175, 200, 225, and 250℃, respectively. These mass changes per cycle correspond to etch rates of 0.070, 0.087, 0.116, 0.124, and 0.117 Å/cycle at 150, 175, 200, 225 and 250℃, respectively. The linear removal of HfO_2 was confirmed by XRR analysis. The XRR studies measured HfO_2 ALE etch rates of 0.11 Å/cycle at 200℃. The HfO_2 films also were smoothed

by HfO_2 ALE. HfO_2 ALE was also observed by FTIR spectroscopy analysis that monitored the loss of the Hf-O stretching vibration of bulk HfO_2 versus number of $Sn(acac)_2$ and HF reaction cycles. FTIR analysis also monitored absorbance features that were consistent with HfF_4 or HfF_x surface species as a reaction intermediate.

The HfO_2 etching is believed to follow the reaction: $HfO_2 + 4Sn(acac)_2 + 4HF \rightarrow Hf(acac)_4 + 4SnF(acac) + 2H_2O$. In the proposed reaction mechanism, HfF_4 or HfF_x is the key reaction intermediate. The $Sn(acac)_2$ reactant donates acac to the HfF_4 or HfF_x adlayer on the HfO_2 substrate to produce $Hf(acac)_4$. The HF reactant forms the HfF_4 or HfF_x reaction intermediate from HfO_2 and allows $SnF(acac)$ and H_2O to leave as reaction products. The ALE of many other metal oxides besides HfO_2 should also be possible using sequential $Sn(acac)_2$ and HF exposures. This ALE reaction mechanism should also be applicable for the ALE of metal nitrides, metal phosphides, metal arsenides and elemental metals.

7.5. Acknowledgements

7.6. References

1.   A. Agarwal and M. J. Kushner, *J. Vac. Sci. Technol. A*, **27**, 37 (2009).

2.   S. D. Athavale and D. J. Economou, *J. Vac. Sci. Technol. A*, **13**, 966 (1995).

3.   S. D. Athavale and D. J. Economou, *J. Vac. Sci. Technol. B*, **14**, 3702 (1996).

4.   S. M. George, *Chem. Rev.*, **110**, 111 (2010).

5.   M. Leskela and M. Ritala, *Angew. Chem. Int. Ed.*, **42**, 5548 (2003).

6.   N. Marchack and J. P. Chang, *J. Phys. D Appl. Phys.*, **44**, 174011 (2011).

7.   J. B. Park, W. S. Lim, B. J. Park, I. H. Park, Y. W. Kim and G. Y. Yeom, *J. Phys. D Appl. Phys.*, **42**, 055202 (2009).

8.   N. A. Kubota, D. J. Economou and S. J. Plimpton, *J. Appl. Phys.*, **83**, 4055 (1998).

9.   S. D. Park, D. H. Lee and G. Y. Yeom, *Electrochem. Solid State Lett.*, **8**, C106 (2005).

10.   S. D. Park, W. S. Lim, B. J. Park, H. C. Lee, J. W. Bae and G. Y. Yeom, *Electrochem. Solid State Lett.*, **11**, H71 (2008).

11.   H. Sakaue, S. Iseda, K. Asami, J. Yamamoto, M. Hirose and Y. Horiike, *Jpn. J. Appl. Phys. 1*, **29**, 2648 (1990).

12.   J. Yamamoto, T. Kawasaki, H. Sakaue, S. Shingubara and Y. Horiike, *Thin Solid Films*, **225**, 124 (1993).

13.   T. Sugiyama, T. Matsuura and J. Murota, *Appl. Surf. Sci.*, **112**, 187 (1997).

14.   W. S. Lim, S. D. Park, B. J. Park and G. Y. Yeom, *Surf. Coat. Tech.*, **202**, 5701 (2008).

15.   T. Meguro, M. Hamagaki, S. Modaressi, T. Hara, Y. Aoyagi, M. Ishii and Y. Yamamoto, *Appl. Phys. Lett.*, **56**, 1552 (1990).

16.   T. Meguro, M. Ishii, T. Sugano, K. Gamo and Y. Aoyagi, *Appl. Surf. Sci.*, **82-3**, 193 (1994).

17.   S. D. Park, C. K. Oh, J. W. Bae, G. Y. Yeom, T. W. Kim, J. I. Song and J. H. Jang, *Appl. Phys. Lett.*, **89**, 043109 (2006).

18.   J. B. Park, W. S. Lim, S. D. Park, Y. J. Park and G. Y. Yeom, *J. Korean Phys. Soc.*, **54**, 976 (2009).

19.   D. Metzler, R. L. Bruce, S. Engelmann, E. A. Joseph and G. S. Oehrlein, *J. Vac. Sci. Technol. A*, **32**, 020603 (2014).

20.   K. S. Min, S. H. Kang, J. K. Kim, Y. I. Jhon, M. S. Jhon and G. Y. Yeom, *Microelectron. Eng.*, **110**, 457 (2013).

21.   Y. Y. Kim, W. S. Lim, J. B. Park and G. Y. Yeom, *J. Electrochem. Soc.*, **158**, D710 (2011).

22.   W. S. Lim, Y. Y. Kim, H. Kim, S. Jang, N. Kwon, B. J. Park, J.-H. Ahn, I. Chung, B. H. Hong and G. Y. Yeom, *Carbon*, **50**, 429 (2012).

23.   E. Vogli, D. Metzler and G. S. Oehrlein, *Appl. Phys. Lett.*, **102**, 253105 (2013).

24.   Y. Lee and S. M. George, *ACS Nano*, **9**, 2061 (2015).

25.   J. H. Choi, Y. Mao and J. P. Chang, *Mater. Sci. Eng., R*, **72**, 97 (2011).

26.   J. Robertson, *Eur. Phys. J. Appl. Phys.*, **28**, 265 (2004).

27.   M. H. Cho, Y. S. Roh, C. N. Whang, K. Jeong, S. W. Nahm, D. H. Ko, J. H. Lee, N. I. Lee and K. Fujihara, *Appl. Phys. Lett.*, **81**, 472 (2002).

28.   K. Mistry, C. Allen, C. Auth, B. Beattie, D. Bergstrom, M. Bost, M. Brazier, M. Buehler, A. Cappellani, R. Chau, C. H. Choi, G. Ding, K. Fischer, T. Ghani, R. Grover, W. Han, D. Hanken, M. Hatttendorf, J. He, J. Hicks, R. Huessner, D. Ingerly, P. Jain, R. James, L. Jong, S. Joshi, C. Kenyon, K. Kuhn, K. Lee, H. Liu, J. Maiz, B. McIntyre, P. Moon, J. Neirynck, S. Pei, C. Parker, D. Parsons, C. Prasad, L. Pipes, M. Prince, P. Ranade, T. Reynolds, J. Sandford, L. Schifren, J. Sebastian, J. Seiple, D. Simon, S. Sivakumar, P. Smith, C. Thomas, T. Troeger, P. Vandervoorn, S. Williams and K. Zawadzki, *2007 IEEE International Electron Devices Meeting, Vols. 1 and 2*, 247 (2007).

29.   T. Rudenko, N. Collaert, S. De Gendt, V. Kilchytska, M. Jurczak and D. Flandre, *Microelectron. Eng.*, **80**, 386 (2005).

30.   A. Tsormpatzoglou, D. H. Tassis, C. A. Dimitriadis, M. Mouis, G. Ghibaudo and N. Collaert, *Semicond. Sci. Technol.*, **24** (2009).

31.   J. W. Elam, M. D. Groner and S. M. George, *Rev Sci Instrum*, **73**, 2981 (2002).

32.   S. C. Riha, J. A. Libera, J. W. Elam and A. B. F. Martinson, *Rev Sci Instrum*, **83**, 094101 (2012).

33.   G. A. Olah, M. Nojima and I. Kerekes, *Synthesis-Stuttgart*, **12**, 779 (1973).

34.   R. D. Shannon, R. C. Shannon, O. Medenbach and R. X. Fischer, *J. Phys. Chem. Ref. Data* **31**, 931 (2002).

35.   J. W. DuMont and S. M. George, *Journal of Physical Chemistry C (In Press)*

36.   J. D. Ferguson, A. W. Weimer and S. M. George, *Thin Solid Films*, **371**, 95 (2000).

37.   T. H. Ballinger, J. C. S. Wong and J. T. Yates, *Langmuir*, **8**, 1676 (1992).

38.   M. Putkonen, A. Szeghalmi, E. Pippel and M. Knez, *J Mater Chem*, **21**, 14461 (2011).

39.   R. Steger and R. Masel, *Thin Solid Films*, **342**, 221 (1999).

40.   Y. Lee, J. W. DuMont and S. M. George, *Submitted to Chemistry of Materials*.

41.   D. A. Neumayer and E. Cartier, *J. Appl. Phys.*, **90**, 1801 (2001).

42.   Y. Wang, M. T. Ho, L. V. Goncharova, L. S. Wielunski, S. Rivillon-Amy, Y. J. Chabal, T. Gustafsson, N. Moumen and M. Boleslawski, *Chem. Mater.*, **19**, 3127 (2007).

43.   D. Ceresoli and D. Vanderbilt, *Phys. Rev. B*, **74** (2006).

44.   V. Cosnier, M. Olivier, G. Theret and B. Andre, *J. Vac. Sci. Technol.*, **19**, 2267 (2001).

45.   L. Khomenkova, *Physica B*, **453**, 19 (2014).

46.   K. Nakamoto, A. E. Martell and P. J. McCarthy, *J. Am. Chem. Soc.*, **83**, 1272 (1961).

47.   S. F. Tayyari and F. Milani-nejad, *Spectrochim. Acta A*, **56**, 2679 (2000).

48.   B. M. Vilakazi, O. S. Monnahela, J. B. Wagener, P. A. B. Carstens and T. Ntsoane, *J. Fluorine Chem.*, **141**, 64 (2012).

49.   A. Buechler, D. H. Dugre and J. B. Berkowitz, *J. Chem. Phys.*, **34**, 2202 (1961).

50.   V. N. Bukhmarina, S. L. Dobychin, Y. B. Predtechenskii and V. G. Shklyarik, *Zhurnal Fizicheskoi Khimii*, **60**, 1775 (1986).

51.   N. B. Morozova, K. V. Zherikova, I. A. Baidina, S. V. Sysoev, P. P. Semyannikov, L. V. Yakovkina, T. P. Smirnova, N. V. Gelfond, I. K. Igumenov, G. Carta and G. Rossetto, *J. Phys. Chem. Solids*, **69**, 673 (2008).

52.   K. V. Zherikova, N. B. Morozova, L. N. Zelenina, S. V. Sysoev, T. P. Chusova and I. K. Igumenov, *J. Therm. Anal. Calorim.*, **92**, 729 (2008).

53.   E. W. Berg and J. T. Truemper, *Anal. Chim. Acta*, **32**, 245 (1965).

54.   K. J. Eisentraut and R. E. Sievers, *J. Inorg. Nucl. Chem.*, **29**, 1931 (1967).

55.   B. D. Fahlman and A. R. Barron, *Adv. Mater. Opt. Electr.*, **10**, 223 (2000).

56.   P. F. R. Ewings, P. G. Harrison and D. E. Fenton, *J Chem Soc Dalton*, 821 (1975).

57.   K. Zimbov, J. W. Hastie and J. L. Margrave, *T Faraday Soc*, **64**, 861 (1968).

58.   R. C. Mehrotra, R. Bohra and D. P. Gaur, *Metal Beta-Diketonates and Allied Derivatives*, p. viii, Academic Press, London (1978).

59.   M. M. Hussain, S.-C. Song, J. Barnett, C. Y. Kang, G. Gebara, B. Sassman and N. Moumen, *IEEE Elect. Device Lett.*, **27**, 972 (2006).

Chapter 8

BIBLIOGRAPHY

1.	HSC Chemistry. HSC Chemistry 5.1, Outokumpu Research Oy: Pori, Finland.

2.	Agarwal, A.; Kushner, M. J., Plasma Atomic Layer Etching Using Conventional Plasma Equipment. *Journal of Vacuum Science & Technology A* **2009**, 27 (1), 37-50.

3.	Ahmed, K.; Schuegraf, K., Transistor Wars. *IEEE Spectrum* **2011**, 48 (11), 50-66.

4.	Allen, T. H.; Lehan, J. P.; McIntyre, J. L. C. Ion-Beam-Sputtered Metal Fluorides, *Proc. SPIE* December 1, 1990; **1990**; p 277

5.	Almeida, R. M.; Morais, P. J., Preparation and Characterization of Amorphous ZrF_4 Thin-Films. *Journal of Non-Crystalline Solids* **1995**, 184, 93-97.

6.	Anderson, V. R.; Leick, N.; Clancey, J. W.; Hurst, K. E.; Jones, K. M.; Dillon, A. C.; George, S. M., Atomic Layer Deposition of Platinum Nanoparticles on Titanium Oxide and Tungsten Oxide Using Platinum(II) Hexafluoroacetylacetonate and Formalin as the Reactants. *The Journal of Physical Chemistry C* **2014**, 118 (17), 8960-8970.

7.	Athavale, S. D.; Economou, D. J., Molecular Dynamics Simulation of Atomic Layer Etching of Silicon. *Journal of Vacuum Science & Technology A* **1995**, 13 (3), 966-971.

8.	Athavale, S. D.; Economou, D. J., Realization of Atomic Layer Etching of Silicon. *Journal of Vacuum Science & Technology B* **1996**, 14 (6), 3702-3705.

9.	Atkins, P. W., Physical Chemistry, 5th Edition. Oxford University Press: Oxford 1994.

10.	Auth, C. et al., A 22nm High Performance and Low-Power CMOS Technology Featuring Fully-Depleted Tri-Gate Transistors, Self-Aligned Contacts and High Density MIM Capacitors. *Symposium on VLSI Technology Digest of Technical Papers* **2012**.

11.	Ayotte, P.; Hebert, M.; Marchand, P., Why Is Hydrofluoric Acid a Weak Acid? *Journal of Chemical Physics* **2005**, 123 (18).

12. Bailey, C. L.; Mukhopadhyay, S.; Wander, A.; Searle, B. G.; Harrison, N. M., Structure and Stability of alpha-AlF_3 Surfaces. *Journal of Physical Chemistry C* **2009**, 113 (12), 4976-4983.

13. Bailey, C. L.; Wander, A.; Mukhopadhyay, S.; Searle, B. G.; Harrison, N. M., Adsorption of HF and HCl on the beta-AlF_3 (100) Surface. *Physical Chemistry Chemical Physics* **2008**, 10 (20), 2918-2924.

14. Ball, D. W., Ab Initio Studies of AlH_3-H_2O, AlF_3-H_2O, and $AlCl_3$-H_2O Complexes. *Journal of Physical Chemistry* **1995**, 99 (34), 12786-12789.

15. Ballinger, T. H.; Wong, J. C. S.; Yates, J. T., Transmission Infrared-Spectroscopy of High Area Solid-Surfaces - A Useful Method for Sample Preparation. *Langmuir* **1992**, 8 (6), 1676-1678.

16. Barriere, A. S.; Lachter, A., Optical-Transitions in Disordered Thin-Films of Ionic Compounds MgF_2 and AlF_3 as a Function of Their Conditions of Preparation. *Applied Optics* **1977**, 16 (11), 2865-2871.

17. Benjamin, S. L.; Levason, W.; Pugh, D.; Reid, G.; Zhang, W. J., Preparation and Structures of Coordination Complexes of the Very Hard Lewis Acids ZrF_4 and HfF_4. *Dalton Transactions* **2012**, 41 (40), 12548-12557.

18. Berg, E. W.; Truemper, J. T., Vapor Pressure-Temperature Data for Various Metal beta-Diketone Chelates. *Analytica Chimica Acta* **1965**, 32 (3), 245-252.

19. Bohr, M. T.; Chau, R. S.; Ghani, T.; Mistry, K., The High-k Solution. *IEEE Spectrum* **2007**, 44 (10), 29-35.

20. Bos, K. D.; Budding, H. A.; Bulten, E. J.; Noltes, J. G., Tin(II) Bis(1,3-Diketonates) and Tin(II) 1,3-Diketonate Chlorides. *Inorganic and Nuclear Chemistry Letters* **1973**, 9 (9), 961-963.

21. Bridou, F.; Cuniot-Ponsard, M.; Desvignes, J. M.; Richter, M.; Kroth, U.; Gottwald, A., Experimental Determination of Optical Constants of MgF_2 and AlF_3 Thin Films in the Vacuum Ultra-violet Wavelength Region (60-124 nm), and Its Application to Optical Designs. *Optics Communications* **2010**, 283 (7), 1351-1358.

22. Buechler, A.; Dugre, D. H.; Berkowitz, J. B., Infrared Spectra of Some Group IV Halides. *Jouranl of Chemical Physics* **1961**, 34 (6), 2202-&.

23. Bukhmarina, V. N.; Dobychin, S. L.; Predtechenskii, Y. B.; Shklyarik, V. G., Infrared-Spectra and Raman-Scattering Spectra of ZrF_4 and HfF_4 Mmolecules Isolated in Ne and Ar Matrices. *Zhurnal Fizicheskoi Khimii* **1986**, 60 (7), 1775-1777.

24. Burton, B. B.; Fabreguette, F. H.; George, S. M., Atomic Layer Deposition of MnO Using Bis(ethylcyclopentadienyl)manganese and H_2O. *Thin Solid Films* **2009**, 517 (19), 5658-5665.

25. Burton, B. B.; Goldstein, D. N.; George, S. M., Atomic Layer Deposition of MgO Using Bis(ethylcyclopentadienyl)magnesium and H_2O. *Journal of Physical Chemistry C* **2009**, 113 (5), 1939-1946.

26. Buslov, D. K.; Sushko, N. I.; Yukhnevich, G. V., The IR Spectrum of Liquid Hydrogen Fluoride. *Journal of Optical Technology* **2003**, 70 (1), 28-30.

27. Carver, C. T.; Plombon, J. J.; Romero, P. E.; Suri, S.; Tronic, T. A.; Turkot Jr., R. B., Atomic Layer Etching: An Industry Perspective. *ECS Journal of Solid State Science and Technology*, **2015**, 4 (6), N5005-N5009.

28. Ceresoli, D.; Vanderbilt, D., Structural and Dielectric Properties of Amorphous ZrO_2 and HfO_2. *Physical Review B* **2006**, 74 (12) 125108.

29. Cho, M. H.; Roh, Y. S.; Whang, C. N.; Jeong, K.; Nahm, S. W.; Ko, D. H.; Lee, J. H.; Lee, N. I.; Fujihara, K., Thermal Stability and Structural Characteristics of HfO_2 Films on Si (100) Grown by Atomic Layer Deposition. *Applied Physics Letters* **2002**, 81 (3), 472-474.

30. Choi, J. H.; Mao, Y.; Chang, J. P., Development of Hafnium Based High-k Materials-A Review. *Materials Science and Engineering*, R **2011**, 72 (6), 97-136.

31. Cosnier, V.; Olivier, M.; Theret, G.; Andre, B., HfO_2-SiO_2 Interface in PVD Coatings. *Journal of Vacuum Science & Technology* **2001**, 19 (5), 2267-2271.

32. Ding, F.; Xu, W.; Choi, D. W.; Wang, W.; Li, X. L.; Engelhard, M. H.; Chen, X. L.; Yang, Z. G.; Zhang, J. G., Enhanced Performance of Graphite Anode Materials by AlF_3 Coating for Lithium-ion Batteries. *Journal of Materials Chemistry* **2012**, 22 (25), 12745-12751.

33. Dippel, K.; Klingebiel, U.; Sheldrick, G. M.; Stalke, D., 4-Membered (Sinsio) Rings by Lif Elimination - Crystal-Structure of an 8-Membered (Flinsi) Ring. *Chemische Berichte-Recueil* **1987**, 120 (4), 611-616.

34. DuMont, J. W.; George, S. M., Pyrolysis of Alucone Molecular Layer Deposition Films Studied Using In Situ Transmission Fourier Transform Infrared Spectroscopy. *Journal of Physical Chemistry C* (In Press) **2015**.

35. Eisentraut, K. J.; Sievers, R. E., Thermogravimetric Studies of Metal Beta-Diketonates. *Journal of Inorganic and Nuclear Chemistry* **1967**, 29 (8), 1931-1936.

36. Elam, J. W.; Groner, M. D.; George, S. M., Viscous Flow Reactor with Quartz Crystal Microbalance for Thin Film Growth by Atomic Layer Deposition. *Review of Scientific Instruments* **2002**, 73 (8), 2981-2987.

37. Ewings, P. F. R.; Harrison, P. G.; Fenton, D. E., Derivatives of Divalent Germanium, Tin, and Lead. 5. Bis-(Pentane-2,4-Dionato)-Tin(II),Bis(1,1,1-Trifluoropentane-2,4-Dionato)-Tin(II), and Bis(1,1,1,5,5,5-Hexafluoropentane-2,4-Dionato)-Tin(II). *Journal of the Chemical Society, Dalton Transactions* **1975**, (9), 821-826.

38. Fahlman, B. D.; Barron, A. R., Substituent Effects on the Volatility of Metal Beta-Diketonates. *Advanced Materials for Optics and Electronics* **2000**, 10 (3-5), 223-232.

39. Ferguson, J. D.; Weimer, A. W.; George, S. M., Atomic Layer Deposition of Ultrathin and Conformal Al_2O_3 Films on BN particles. *Thin Solid Films* **2000**, 371 (1-2), 95-104.

40. Ferguson, J. D.; Weimer, A. W.; George, S. M., Atomic Layer Deposition of Al_2O_3 Films on Polyethylene Particles. *Chemistry of Materials* **2004**, 16 (26), 5602-5609.

41. George, S. M., Atomic Layer Deposition: An Overview. *Chemical Reviews* **2010**, 110 (1), 111-131.

42. Giguere, P. A.; Zengin, N., SPECTRE INFRAROUGE DE HF A LETAT CRISTALLIN. *Canadian Journal of Chemistry-Revue Canadienne De Chimie* **1958**, 36 (6), 1013-1019.

43. Goldstein, D. N.; George, S. M., Surface Poisoning in the Nucleation and Growth of Palladium Atomic Layer Deposition with $Pd(hfac)_2$ and Formalin. *Thin Solid Films* **2011**, 519 (16), 5339-5347.

44. Goldstein, D. N.; McCormick, J. A.; George, S. M., Al_2O_3 Atomic Layer Deposition with Trimethylaluminum and Ozone Studied by in Situ Transmission FTIR Spectroscopy and Quadrupole Mass Spectrometry. *Journal of Physical Chemistry C* **2008**, 112 (49), 19530-19539.

45.   Groner, M. D.; Elam, J. W.; Fabreguette, F. H.; George, S. M., Electrical Characterization of Thin Al_2O_3 Films Grown by Atomic Layer Deposition on Silicon and Various Metal Substrates. *Thin Solid Films* **2002**, 413 (1-2), 186-197.

46.   Gross, U.; Ruediger, S.; Kemnitz, E.; Brzezinka, K.-W.; Mukhopadhyay, S.; Bailey, C.; Wander, A.; Harrison, N., Vibrational Analysis Study of Aluminum Trifluoride Phases. *Journal of Physical Chemistry A* **2007**, 111 (26), 5813-5819.

47.   Guo, Y.; Wuttke, S.; Vimont, A.; Daturi, M.; Lavalley, J. C.; Teinz, K.; Kemnitz, E., Novel Sol-Gel Prepared Zinc Fluoride: Synthesis, Characterisation and Acid-Base Sites Analysis. *Journal of Materials Chemistry* **2012**, 22 (29), 14587-14593.

48.   Gusev, E. P.; Cabral, C.; Copel, M.; D'Emic, C.; Gribelyuk, M., Ultrathin HfO_2 Films Grown on Silicon by Atomic Layer Deposition for Advanced Gate Dielectrics Applications. *Microelectronic Engineering* **2003**, 69 (2-4), 145-151.

49.   Hausmann, D. M.; Kim, E.; Becker, J.; Gordon, R. G., Atomic Layer Deposition of Hafnium and Zirconium Oxides Using Metal Amide Precursors. *Chemistry of Materials* **2002**, 14 (10), 4350-4358.

50.   Heitmann, W., Vacuum Evaporated Films of Aluminum Fluoride. *Thin Solid Films* **1970**, 5 (1), 61.

51.   Henley, S. J.; Ashfold, M. N. R.; Pearce, S. R. J., The Structure and Composition of Lithium Fluoride Films Grown by Off-axis Pulsed Laser Ablation. *Applied Surface Science* **2003**, 217 (1-4), 68-77.

52.   Herron, N.; Farneth, W. E., The Design and Synthesis of Heterogeneous Catalyst Systems. *Advanced Materials* **1996**, 8 (12), 959-968.

53.   Horiike, Y.; Tanaka, T.; Nakano, M.; Iseda, S.; Sakaue, H.; Nagata, A.; Shindo, H.; Miyazaki, S.; Hirose, M., Digital Chemical Vapor-Deposition and Etching Technologies for Semiconductor Processing. *Journal of Vacuum Science & Technology A-Vacuum Surfaces and Films* **1990**, 8 (3), 1844-1850.

54.   Hung, L. S.; Tang, C. W.; Mason, M. G., Enhanced Electron Injection in Organic Electroluminescence Devices Using an Al/LiF Electrode. *Applied Physics Letters* **1997**, 70 (2), 152-154.

55.   Hussain, M. M.; Song, S.-C.; Barnett, J.; Kang, C. Y.; Gebara, G.; Sassman, B.; Moumen, N., Plasma-Induced Damage in High-k/Metal Gate Stack Dry Etch. *IEEE Electron Device Letters* **2006**, 27 (12), 972-974.

56.   Iwahori, K.; Furuta, M.; Taki, Y.; Yamamura, T.; Tanaka, A., Optical Properties of Fluoride Thin Films Deposited by RF Magnetron Sputtering. *Applied Optics* **2006**, 45 (19), 4598-4602.

57.   Jabbour, G. E.; Kippelen, B.; Armstrong, N. R.; Peyghambarian, N., Aluminum Based Cathode Structure for Enhanced Electron Injection in Electroluminescent Organic Devices. *Applied Physics Letters* **1998**, 73 (9), 1185-1187.

58.   Jia, W.-Z.; Lu, J.-Q.; Chen, P.; Wang, Y.-J.; Luo, M.-F., A Novel Method for the Synthesis of Well-Crystallized beta-AlF_3 with High Surface Area Derived from gamma-Al_2O_3. *Journal of Materials Chemistry* **2011**, 21 (25), 8987-8990.

59.   Jung, Y. S.; Cavanagh, A. S.; Dillon, A. C.; Groner, M. D.; George, S. M.; Lee, S. H., Enhanced Stability of $LiCoO_2$ Cathodes in Lithium-Ion Batteries Using Surface Modification by Atomic Layer Deposition. *Journal of the Electrochemical Society* **2010**, 157 (1), A75-A81.

60.   Jung, Y. S.; Cavanagh, A. S.; Riley, L. A.; Kang, S. H.; Dillon, A. C.; Groner, M. D.; George, S. M.; Lee, S. H., Ultrathin Direct Atomic Layer Deposition on Composite Electrodes for Highly Durable and Safe Li-Ion Batteries. *Advanced Materials* **2010**, 22 (19), 2172-2176.

61.   Kemnitz, E.; Gross, U.; Rudiger, S.; Shekar, C. S., Amorphous Metal Fluorides with Extraordinary High Surface Areas. *Angewandte Chemie-International Edition* **2003**, 42 (35), 4251-4254.

62.   Kemnitz, E.; Menz, D. H., Fluorinated Metal Oxides and Metal Fluorides as Heterogeneous Catalysts. *Progress in Solid State Chemistry* **1998**, 26 (2), 97-153.

63.   Khomenkova, L., Analysis of PL Spectrum Shape of Si-based Materials as a Tool for Determination of Si Crystallites' Distribution. *Physica B* **2014**, 453, 19-25.

64.   Kim, H.; King, A. H., Grain Growth and Texture Development in Lithium Fluoride Thin Films. *Journal of Materials Research* **2008**, 23 (2), 452-462.

65. Kim, J. Y.; George, S. M., Tin Monosulfide Thin Films Grown by Atomic Layer Deposition Using Tin 2,4-Pentanedionate and Hydrogen Sulfide. *Journal of Physical Chemistry C* **2010**, 114 (41), 17597-17603.

66. Kim, Y. Y.; Lim, W. S.; Park, J. B.; Yeom, G. Y., Layer by Layer Etching of the Highly Oriented Pyrolythic Graphite by Using Atomic Layer Etching. *Journal of the Electrochemical Society* **2011**, 158 (12), D710-D714.

67. Koenig, R.; Scholz, G.; Scheurell, K.; Heidemann, D.; Buchem, I.; Unger, W. E. S.; Kemnitz, E., Spectroscopic Characterization of Crystalline AlF$_3$ Phases. *Journal of Fluorine Chemistry* **2010**, 131 (1), 91-97.

68. Konig, D.; Scholz, R.; Zahn, D. R. T.; Ebest, G., Band Diagram of the AlF$_3$/SiO$_2$/Si System. *Journal of Applied Physics* **2005**, 97 (9).

69. Krahl, T.; Vimont, A.; Eltanany, G.; Daturi, M.; Kemnitz, E., Determination of the Acidity of High Surface AlF$_3$ by IR Spectroscopy of Adsorbed CO Probe Molecules. *Journal of Physical Chemistry C* **2007**, 111 (49), 18317-18325.

70. Krouse, I. H.; Wenthold, P. G., Fluorotrimethylsilane Affinities of Anionic Nucleophiles: A Study of Fluoride-induced Desilylation. *Journal of the American Society for Mass Spectrometry* **2005**, 16 (5), 697-707.

71. Kruschwitz, J. D. T.; Pawlewicz, W. T., Optical and Durability Properties of Infrared Transmitting Thin Films. *Applied Optics* **1997**, 36 (10), 2157-2159.

72. Kubota, N. A.; Economou, D. J.; Plimpton, S. J., Molecular Dynamics Simulations of Low-Energy (25-200 eV) Argon Ion Interactions with Silicon Surfaces: Sputter Yields and Product Formation Pathways. *Journal of Applied Physics* **1998**, 83 (8), 4055-4063.

73. Kuhn, K. J., Considerations for Ultimate CMOS Scaling. *IEEE Transactions on Electron Devices* **2012**, 59 (7), 1813-1828.

74. Kukli, K.; Ritala, M.; Leskela, M., Low-Temperature Deposition of Zirconium Oxide-Based Nanocrystalline Films by Alternate Supply of Zr[OC(CH$_3$)$_3$]$_4$ and H$_2$O. *Chemical Vapor Deposition* **2000**, 6 (6), 297-302.

75. Kumar, M.; Khan, S. A.; Rajput, P.; Singh, F.; Tripathi, A.; Avasthi, D. K.; Pandey, A. C., Size Effect on Electronic Sputtering of LiF Thin Films. *Journal of Applied Physics* **2007**, 102 (8).

76.   Kumar, M.; Rajput, P.; Khan, S. A.; Avasthi, D. K.; Pandey, A. C., Substrate Effect on Electronic Sputtering Yield in Polycrystalline Fluoride (LiF, CaF$_2$ and BaF$_2$) Thin Films. *Applied Surface Science* **2010**, 256 (7), 2199-2204.

77.   Laermer, F.; Schilp, A. Plasma Polymerizing Temporary Etch Atop *U.S. Patent No. 5,501,893* **1996**.

78.   Lapianosmith, D. A.; Eklund, E. A.; Himpsel, F. J.; Terminello, L. J., Epitaxy of LiF on Ge(100). *Applied Physics Letters* **1991**, 59 (17), 2174-2176.

79.   Lee, C. C.; Liu, M. C.; Kaneko, M.; Nakahira, K.; Takano, Y., Characterization of AlF$_3$ Thin Films at 193 nm by Thermal Evaporation. *Applied Optics* **2005**, 44 (34), 7333-7338.

80.   Lee, C. G. N.; Kanarik, K. J.; Gottscho, R. A., The Grand Challenges of Plasma Etching: A Manufacturing Perspective. *Journal of Physics D-Applied Physics* **2014**, 47 (27).

81.   Lee, Y.; Cavanagh, A. S.; George, S. M., Atomic Layer Deposition of AlF$_3$ Using Trimethylaluminum and Hydrogen Fluoride-Pyridine, *Proceedings of the 13th International Conference on Atomic Layer Deposition,* San Diego, California, July 28-31, **2013**.

82.   Lee, Y.; DuMont, J. W.; Cavanagh, A. S.; George, S. M., Atomic Layer Deposition of AlF3 Using Trimethylaluminum and Hydrogen Fluoride. *Submitted to Journal of Physical Chemistry C* **2015**.

83.   Lee, Y.; DuMont, J. W.; George, S. M., Mechanism of Thermal Al$_2$O$_3$ Atomic Layer Etching Using Sequential Reactions with Sn(acac)$_2$ and HF. *Submitted to Chemistry of Materials* **2015**.

84.   Lee, Y.; DuMont, J. W.; George, S. M., Atomic Layer Etching of HfO2 Using Sequential, Self-Limiting Thermal Reactions with Sn(acac)$_2$ and HF. *ECS Journal of Solid State Science and Technology* **2015**, 4 (6), N5013-N5022.

85.   Lee, Y.; George, S. M., Atomic Layer Etching of Al$_2$O$_3$ Using Sequential, Self-Limiting Thermal Reactions with Sn(acac)$_2$ and HF. *ACS Nano* **2015**, 9, 2061-2070.

86.   Lee, Y.; Piper, D. M.; Cavanagh, A. S.; Young, M. J.; Lee, S.-H.; George, S. M., . Atomic Layer Deposition of Lithium Ion Conducting (AlF$_3$)(LiF)$_x$ Alloys Using Trimethylaluminum, Lithium Hexamethyldisilazide and Hydrogen Fluoride-Pyridine, *Proceedings of the 14th International Conference on Atomic Layer Deposition*, Kyoto, Japan, June 15-18, **2014**.

87.   Lee, Y.; Yoon, B.; Cavanagh, A. S.; George, S. M., Molecular Layer Deposition of Aluminum Alkoxide Polymer Films Using Trimethylaluminum and Glycidol. *Langmuir* **2011**, 27 (24), 15155-15164.

88.   Lennard, W. N., QUARK ver. 1.3, 2001 http://www.physics.uwo.ca/~wlennard.

89.   Leskela, M.; Ritala, M., Atomic Layer Deposition Chemistry: Recent Developments and Future Challenges. *Angewandte Chemie-International Edition* **2003**, 42 (45), 5548-5554.

90.   Li, C. L.; Gu, L.; Maier, J., Enhancement of the Li Conductivity in LiF by Introducing Glass/Crystal Interfaces. *Advanced Functional Materials* **2012**, 22 (6), 1145-1149.

91.   Li, C. L.; Guo, X. X.; Gu, L.; Samuelis, D.; Maier, J., Ionic Space-Charge Depletion in Lithium Fluoride Thin Films on Sapphire (0001) Substrates. *Advanced Functional Materials* **2011**, 21 (15), 2901-2905.

92.   Li, H. H., Refractive Index of Alkali Halides and Its Wavelength and Temperature Derivatives. *Journal of Physical and Chemical Reference Data* **1976**, 5 (2), 329-528.

93.   Lide, D. R., CRC Handbook of Chemistry and Physics. 85th ed.; CRC Press: Boca Raton, FL, 2005.

94.   Lim, W. S.; Kim, Y. Y.; Kim, H.; Jang, S.; Kwon, N.; Park, B. J.; Ahn, J.-H.; Chung, I.; Hong, B. H.; Yeom, G. Y., Atomic Layer Etching of Graphene for Full Graphene Device Fabrication. *Carbon* **2012**, 50 (2), 429-435.

95.   Lim, W. S.; Park, J. B.; Park, J. Y.; Park, B. J.; Yeom, G. Y., Low Damage Atomic Layer Etching of ZrO_2 by Using BCl_3 Gas and Ar Neutral Beam. *Journal of Nanoscience and Nanotechnology* **2009**, 9 (12), 7379-7382.

96.   Lim, W. S.; Park, S. D.; Park, B. J.; Yeom, G. Y., Atomic Layer Etching of (100)/(111) GaAs with Chlorine and Low Angle Forward Reflected Ne Neutral Beam. *Surface and Coatings Technology* **2008**, 202 (22-23), 5701-5704.

97.   Linstrom, P. J.; Mallard, W. G., NIST Chemistry WebBook, NIST Standard Reference Database Number 69, National Institute of Standards and Technology, Gaithersburg MD, 20899 (http://webbook.nist.gov).

98.   Maki, P. A.; Ehrlich, D. J., Laser Bilayer Etching of GaAs Surfaces. *Applied Physics Letters* **1989**, 55 (2), 91-94.

99.   Mamantov, G.; Marassi, R., Molten Salt Chemistry: An Introduction and Selected Applications. 1987; Vol. 202

100. Mantymaki, M.; Hamalainen, J.; Puukilainen, E.; Munnik, F.; Ritala, M.; Leskela, M., Atomic Layer Deposition of LiF Thin Films from Lithd and TiF_4 Precursors. *Chemical Vapor Deposition* **2013**, 19 (4-6), 111-116.

101. Mantymaki, M.; Hamalainen, J.; Puukilainen, E.; Sajavaara, T.; Ritala, M.; Leskela, M., Atomic Layer Deposition of LiF Thin Films from Lithd, Mg(thd)$_2$, and TiF_4 Precursors. *Chemistry of Materials* **2013**, 25 (9), 1656-1663.

102. Mäntymäki, M.; Heikkilä, M. J.; Puukilainen, E.; Mizohata, K.; Marchand, B.; Räisänen, J.; Ritala, M.; Leskelä, M., Atomic Layer Deposition of AlF_3 Thin Films Using Halide Precursors *Chemistry of Materials* **2014**, 27, 604-611.

103. Marchack, N.; Chang, J. P., Perspectives in Nanoscale Plasma Etching: What Are the Ultimate Limits? *Journal of Physics D: Applied Physics* **2011**, 44 (17), 174011.

104. Martin, P. M.; Olsen, L. C.; Johnston, J. W.; Depoy, D. M., Investigation of Sputtered HfF_4 Films and Application to Interference Filters for Thermophotovoltaics. *Thin Solid Films* **2002**, 420, 8-12.

105. Matsuura, T.; Murota, J.; Sawada, Y.; Ohmi, T., Self-Limited Layer-by-Layer Etching of Si by Alternated Chlorine Adsorption and Ar^+ Ion Irradiation. *Applied Physics Letters* **1993**, 63 (20), 2803-2805.

106. Matsuura, T.; Sugiyama, T.; Murota, J., Atomic-Layer Surface Reaction of Chlorine on Si and Ge Assisted by an Ultraclean ECR Plasma. *Surface Science* **1998**, 402 (1-3), 202-205.

107. McCormick, J. A.; Cloutier, B. L.; Weimer, A. W.; George, S. M., Rotary Reactor for Atomic Layer Deposition on Large Quantities of Nanoparticles. *Journal of Vacuum Science & Technology A* **2007**, 25 (1), 67-74.

108. Meguro, T.; Hamagaki, M.; Modaressi, S.; Hara, T.; Aoyagi, Y.; Ishii, M.; Yamamoto, Y., Digital Etching of GaAs - New Approach of Dry Etching to Atomic Ordered Processing. *Applied Physics Letters* **1990**, 56 (16), 1552-1554.

109. Meguro, T.; Ishii, M.; Sugano, T.; Gamo, K.; Aoyagi, Y., Control of the Etching Reaction of Digital Etching Using Tunable UV Laser Irradiation. *Applied Surface Science* **1994**, 82-3, 193-199.

110. Mehrotra, R. C.; Bohra, R.; Gaur, D. P., Metal Beta-Diketonates and Allied Derivatives. Academic Press: London, 1978; p viii, 382 p.

111. Metzler, D.; Bruce, R. L.; Engelmann, S.; Joseph, E. A.; Oehrlein, G. S., Fluorocarbon Assisted Atomic Layer Etching of SiO_2 using Cyclic Ar/C_4F_8 Plasma. *Journal of Vacuum Science & Technology A* **2014**, 32 (2), 020603.

112. Miikkulainen, V.; Leskela, M.; Ritala, M.; Puurunen, R. L., Crystallinity of Inorganic Films Grown by Atomic Layer Deposition: Overview and General Trends. *Journal of Applied Physics* **2013**, 113 (2), 021301.

113. Min, K. S.; Kang, S. H.; Kim, J. K.; Jhon, Y. I.; Jhon, M. S.; Yeom, G. Y., Atomic Layer Etching of Al_2O_3 Using BCl3/Ar for the Interface Passivation Layer of III-V MOS Devices. *Microelectronic Engineering* **2013**, 110, 457-460.

114. Mistry, K. e. a., A 45nm logic technology with high-k plus metal gate transistors, strained silicon, 9 Cu interconnect layers, 193nm dry patterning, and 100% Pb-free packaging. *2007 IEEE International Electron Devices Meeting*, *Vols 1 and 2* **2007**, 247-250.

115. Montereali, R. M.; Baldacchini, G.; Martelli, S.; Docarmo, L. C. S., LiF Films - Production and Characterization. *Thin Solid Films* **1991**, 196 (1), 75-83.

116. Moore, G., Cramming More Components onto Integrated Circuits. *Electronics Letters* **1965**, 38 (8).

117. Morozova, N. B.; Zherikova, K. V.; Baidina, I. A.; Sysoev, S. V.; Semyannikov, P. P.; Yakovkina, L. V.; Smirnova, T. P.; Gelfond, N. V.; Igumenov, I. K.; Carta, G.; Rossetto, G., Volatile Hafnium(IV) Compounds with Beta-Diketonate and Cyclopentadienyl Derivatives. *Journal of Physics and Chemistry of Solids* **2008**, 69 (2-3), 673-679.

118. Myung, S. T.; Lee, K. S.; Yoon, C. S.; Sun, Y. K.; Amine, K.; Yashiro, H., Effect of AlF_3 Coating on rhermal Behavior of Chemically Delithiated $Li_{0.35}[Ni_{1/3}Co_{1/3}Mn_{1/3}]O_2$. *Journal of Physical Chemistry C* **2010**, 114 (10), 4710-4718.

119. Nakamoto, K.; Martell, A. E.; McCarthy, P. J., Infrared Sectra of Metal Chelate Compounds .3. Infrared Spectra of Acetylacetonates of Divalent Metals. *Journal of the American Chemical Society* **1961**, 83 (6), 1272-&.

120. Neumayer, D. A.; Cartier, E., Materials Characterization of ZrO_2-SiO_2 and HfO_2-SiO_2 Binary Oxides Deposited by Chemical Solution Deposition. *Journal of Applied Physics* **2001**, 90 (4), 1801-1808.

121. Niisaka, S.; Saito, T.; Saito, J.; Tanaka, A.; Matsumoto, A.; Otani, M.; Biro, R.; Ouchi, C.; Hasegawa, M.; Suzuki, Y.; Sone, K., Development of Optical Coatings for 157-nm Lithography. I. Coating Materials. *Applied Optics* **2002**, 41 (16), 3242-3247.

122. Oi, T. Amorphous Lithium Fluoaluminate. *U.S. Patent No. 4,367,267* **1983**.

123. Oi, T., Ionic-Conductivity of LiF Thin-Films Containing Divalent or Trivalent Metal Fluorides. *Materials Research Bulletin* **1984**, 19 (4), 451-457.

124. Oi, T.; Miyauchi, K., Amorphous Thin-Film Ionic Conductors of mLiF.nAlF$_3$. *Materials Research Bulletin* **1981**, 16 (10), 1281-1289.

125. Olah, G. A.; Nojima, M.; Kerekes, I., Synthetic Methods and Reactions .2. Hydrofluorination of Alkenes, Cyclopropane and Alkynes with (Trialkylamine) Reagents. *Synthesis-Stuttgart* **1973**, (12), 779-780.

126. Ott, A. W.; Klaus, J. W.; Johnson, J. M.; George, S. M., Al$_2$O$_3$ Thin Film Growth on Si(100) Using Binary Reaction Sequence Chemistry. *Thin Solid Films* **1997**, 292 (1-2), 135-144.

127. Park, J. B.; Lim, W. S.; Park, B. J.; Park, I. H.; Kim, Y. W.; Yeom, G. Y., Atomic Layer Etching of Ultra-Thin HfO$_2$ Film for Gate Oxide in MOSFET Devices. *Journal of Physics D: Applied Physics* **2009**, 42 (5), 055202.

128. Park, J. B.; Lim, W. S.; Park, S. D.; Park, Y. J.; Yeom, G. Y., Etch Characteristics of TiO$_2$ Etched by Using an Atomic Layer Etching Technique with BCl$_3$ Gas and an Ar Neutral Beam. *Journal of the Korean Physical Society* **2009**, 54 (3), 976-980.

129. Park, S. D.; Lee, D. H.; Yeom, G. Y., Atomic Layer Etching of Si(100) and Si(111) Using Cl$_2$ and Ar Neutral Beam. *Electrochemical and Solid-State Letters* **2005**, 8 (8), C106-C109.

130. Park, S. D.; Lim, W. S.; Park, B. J.; Lee, H. C.; Bae, J. W.; Yeom, G. Y., Precise Depth Control and Low-Damage Atomic-Layer Etching of HfO$_2$ using BCl$_3$ and Ar Neutral Beam. *Electrochemical and Solid-State Letters* **2008**, 11 (4), H71-H73.

131. Park, S. D.; Oh, C. K.; Bae, J. W.; Yeom, G. Y.; Kim, T. W.; Song, J. I.; Jang, J. H., Atomic Layer Etching of InP Using a Low Angle Forward Reflected Ne Neutral Beam. *Applied Physics Letters* **2006**, 89 (4), 043109.

132. Peled, E.; Golodnitsky, D.; Ardel, G., Advanced Model for Solid Electrolyte Interphase Electrodes in Liquid and Polymer Electrolytes. *Journal of the Electrochemical Society* **1997**, 144 (8), L208-L210.

133. Pellicori, S. F.; Colton, E., Fluoride Compounds for IR Coatings. *Thin Solid Films* **1992**, 209 (1), 109-115.

134. Perea, A.; Gonzalo, J.; Afonso, C. N.; Martelli, S.; Montereali, R. M., On the Growth of LiF Films by Pulsed Laser Deposition. *Applied Surface Science* **1999**, 138, 533-537.

135. Pilvi, T.; Hatanpaa, T.; Puukilainen, E.; Arstila, K.; Bischoff, M.; Kaiser, U.; Kaiser, N.; Leskela, M.; Ritala, M., Study of a Novel ALD Process for Depositing MgF_2 Thin Films. *Journal of Materials Chemistry* **2007**, 17 (48), 5077-5083.

136. Pilvi, T.; Puukilainen, E.; Arstila, K.; Leskela, M.; Ritala, M., Atomic Layer Deposition of LaF_3 Thin Films Using $La(thd)_3$ and TiF_4 as Precursors. *Chemical Vapor Deposition* **2008**, 14 (3-4), 85-91.

137. Pilvi, T.; Puukilainen, E.; Kreissig, U.; Leskela, M.; Ritala, M., Atomic Layer Deposition of MgF_2 Thin Films Using TaF_5 as a Novel Fluorine Source. *Chemistry of Materials* **2008**, 20 (15), 5023-5028.

138. Pilvi, T.; Puukilainen, E.; Munnik, F.; Leskela, M.; Ritala, M., ALD of YF_3 Thin Films from TiF_4 and $Y(thd)_3$ Precursors. *Chemical Vapor Deposition* **2009**, 15 (1-3), 27-32.

139. Prada, S.; Martinez, U.; Pacchioni, G., Work Function Changes Induced by Deposition of Ultrathin Dielectric Films on Metals: A Theoretical Analysis. *Physical Review B* **2008**, 78 (23).

140. Profijt, H. B.; Potts, S. E.; van de Sanden, M. C. M.; Kessels, W. M. M., Plasma-Assisted Atomic Layer Deposition: Basics, Opportunities, and Challenges. *Journal of Vacuum Science & Technology A* **2011**, 29 (5), 050801.

141. Pulker, H. K., Characterization of Optical Thin Films. *Applied Optics* **1979**, 18 (12), 1969-1977.

142. Putkonen, M.; Szeghalmi, A.; Pippel, E.; Knez, M., Atomic Layer Deposition of Metal Fluorides Through Oxide Chemistry. *Journal of Materials Chemistry* **2011**, 21 (38), 14461-14465.

143. Rauf, S.; Sparks, T.; Ventzek, P. L. G.; Smirnov, V. V.; Stengach, A. V.; Gaynullin, K. G.; Pavlovsky, V. A., A Molecular Dynamics Investigation of Fluorocarbon Based

Layer-by-layer Etching of Silicon and SiO$_2$. *Journal of Applied Physics* **2007**, 101 (3), 033308.

144. Riha, S. C.; Libera, J. A.; Elam, J. W.; Martinson, A. B. F., Design and Implementation of an Integral Wall-Mounted Quartz Crystal Microbalance for Atomic Layer Deposition. *Review of Scientific Instruments* **2012**, 83 (9), 094101.

145. Ritala, M.; Leskela, M.; Dekker, J. P.; Mutsaers, C.; Soininen, P. J.; Skarp, J., Perfectly Conformal TiN and Al$_2$O$_3$ Films Deposited by Atomic Layer Deposition. *Chemical Vapor Deposition* **1999**, 5 (1), 7-9.

146. Robertson, J., High Dielectric Constant Oxides. *European Physical Journal - Applied Physics* **2004**, 28 (3), 265-291.

147. Roessler, D. M.; Walker, W. C., Electronic Spectrum of Crystalline Lithium Fluoride. *Journal of Physics and Chemistry of Solids* **1967**, 28 (8), 1507-&.

148. Rudenko, T.; Collaert, N.; De Gendt, S.; Kilchytska, V.; Jurczak, M.; Flandre, D., Effective Mobility in FinFET Structures with HfO$_2$ and SiON Gate Dielectrics and TaN Gate Electrode. *Microelectronic Engineering* **2005**, 80, 386-389.

149. Sakaue, H.; Iseda, S.; Asami, K.; Yamamoto, J.; Hirose, M.; Horiike, Y., Atomic Layer Controlled Digital Etching of Silicon. *Japanese Journal of Applied Physics Part 1* **1990**, 29 (11), 2648-2652.

150. Schink, H.; Kolbe, J.; Zimmermann, F.; Ristau, D.; Welling, H. Reactive Ion-Beam-Sputtering of Fluoride Coatings for the UV/VUV Range, *Proceedings of SPIE June 1,* **1991**; p 327.

151. Schulz, L. G., The Structure and Growth of Evaporation LiF and NaCl Films on Amorphous Substrates. *Journal of Chemical Physics* **1949**, 17 (11), 1153-1162.

152. Shannon, R. D.; Shannon, R. C.; Medenbach, O.; Fischer, R. X., Refractive Index and Dispersion of Fluorides and Oxides. *Journal of Physical and Chemical Reference Data* **2002**, 31 (4), 931-970.

153. Smith, J. L.; Budenste, P. P., Dielectric Breakdown in Thin Evaporated Films of CaF$_2$, MgF$_2$, NaF, and LiF. *Journal of Applied Physics* **1969**, 40 (9), 3491-&.

154. Sneh, O.; George, S. M., Thermal Stability of Hydroxyl Groups on a Well-Defined Silica Surface. *Journal of Physical Chemistry* **1995**, 99 (13), 4639-4647.

155.   Stalke, D.; Keweloh, N.; Klingebiel, U.; Noltemeyer, M.; Sheldrick, G. M., From Lithiated Aminofluorosilanes to Monomeric and Dimeric Iminosilanes. *Zeitschrift Fur Naturforschung Section B-a Journal of Chemical Sciences* **1987**, 42 (10), 1237-1244.

156.   Staritzky, E.; Asprey, L. B., Aluminum Trifluoride, AlF₃. *Analytical Chemistry* **1957**, 29 (6), 984-984.

157.   Steger, R.; Masel, R., Chemical Vapor Etching of Copper Using Oxygen and 1,1,1,5,5,5-Hexafluoro-2,4-Pentanedione. *Thin Solid Films* **1999**, 342 (1-2), 221-229.

158.   Sugiyama, T.; Matsuura, T.; Murota, J., Atomic-Layer Etching of Ge Using an Ultraclean ECR Plasma. *Applied Surface Science* **1997**, 112, 187-190.

159.   Sun, Y. K.; Lee, M. J.; Yoon, C. S.; Hassoun, J.; Amine, K.; Scrosati, B., The Role of AlF₃ Coatings in Improving Electrochemical Cycling of Li-Enriched Nickel-Manganese Oxide Electrodes for Li-Ion Batteries. *Advanced Materials* **2012**, 24 (9), 1192-1196.

160.   Suntola, T.; Antson, J. Method for Producing Compound Thin Films. *U.S. Patent No. 4,058,430* **1977**.

161.   Taki, Y., Film Structure and Optical Constants of Magnetron-Sputtered Fluoride Films for Deep Ultraviolet Lithography. *Vacuum* **2004**, 74 (3-4), 431-435.

162.   Targove, J. D.; Bovard, B. G.; Lingg, L. J.; Macleod, H. A., Densification of Aluminum Fluoride Thin-Films by Ion-Assisted Deposition. *Thin Solid Films* **1988**, 159, L57-L59.

163.   Tayyari, S. F.; Milani-nejad, F., Vibrational Assignment of Acetylacetone. *Spectrochimica Acta Part A* **2000**, 56 (14), 2679-2691.

164.   Tsormpatzoglou, A.; Tassis, D. H.; Dimitriadis, C. A.; Mouis, M.; Ghibaudo, G.; Collaert, N., Electrical Characterization and Design Optimization of FinFETs with a TiN/HfO₂ Gate Stack. *Semiconductor Science and Technology* **2009**, 24 (12).

165.   Utkin, A. N.; Girichev, G. V.; Giricheva, N. I.; Khaustov, S. V., Structure and Vibrational Frequencies of Aluminum trifluoride and Gallium Trifluoride. *Journal of Structural Chemistry* **1986**, 27 (2), 212-215.

166.   van der Meulen, P. A.; Mann, R. F., The Vapor Pressure of Pyridine. *Journal of the American Chemical Society* **1931**, 53, 451-453.

167.   Verma, P.; Maire, P.; Novak, P., A Review of the Features and Analyses of the Solid Electrolyte Interphase in Li-ion Batteries. *Electrochimica Acta* **2010**, 55 (22), 6332-6341.

168. Vilakazi, B. M.; Monnahela, O. S.; Wagener, J. B.; Carstens, P. A. B.; Ntsoane, T., A Thermogravimetric Study of the Fluorination of Zirconium and Hafnium Oxides with Anhydrous Hydrogen Fluoride Gas. *Journal of Fluorine Chemistry* **2012**, 141, 64-68.

169. Vogli, E.; Metzler, D.; Oehrlein, G. S., Feasibility of Atomic Layer Etching of Polymer Material Based on Sequential O_2 Exposure and Ar Low-Pressure Plasma-Etching. *Applied Physics Letters* **2013**, 102 (25), 253105.

170. Walter, S.; Klingebiel, U.; Noltemeyer, M., Insertion, Isomerization, and Cycloaddition Reactions of Lithiated Aminofluorosilanes. *Chemische Berichte-Recueil* **1992**, 125 (4), 783-788.

171. Wander, A.; Bailey, C. L.; Searle, B. G.; Mukhopadhyay, S.; Harrison, N. M., Identification of Possible Lewis Acid Sites on the beta-AlF_3(100) surface: An Ab initio Total Energy Study. *Physical Chemistry Chemical Physics* **2005**, 7 (23), 3989-3993.

172. Wang, Y.; Ho, M. T.; Goncharova, L. V.; Wielunski, L. S.; Rivillon-Amy, S.; Chabal, Y. J.; Gustafsson, T.; Moumen, N.; Boleslawski, M., Characterization of Ultra-Thin Hafnium Oxide Films Grown on Silicon by Atomic Layer Deposition Using Tetrakis(ethylmethyl-amino)hafnium and Water Precursors. *Chemistry of Materials* **2007**, 19 (13), 3127-3138.

173. Waters, T. N., Some Investigations in the Zirconium Tetrafluoride-Water System. *Journal of Inorganic & Nuclear Chemistry* **1960**, 15 (3-4), 320-328.

174. Weidlein, J.; Krieg, V., Vibrational Spectra of Dimethyl- and Diethylaluminium Fluoride. *Journal of Organometallic Chemistry* **1968**, 11 (1), 9.

175. Yamamoto, J.; Kawasaki, T.; Sakaue, H.; Shingubara, S.; Horiike, Y., Digital Etching Study and Fabrication of Fine Si Lines and Dots. *Thin Solid Films* **1993**, 225 (1-2), 124-129.

176. Ylilammi, M.; Rantaaho, T., Metal Fluoride Thin-Films Prepared by Atomic Layer Deposition. *Journal of the Electrochemical Society* **1994**, 141 (5), 1278-1284.

177. Yoder, M. N. Flooding Diamond Surface with Pulse of Nitrogen Dioxide, Impacting with Pulse of Ions of Noble and Hydrogen Gases *U.S. Patent No. 4,756,794 A* **1987**.

178. Zherikova, K. V.; Morozova, N. B.; Zelenina, L. N.; Sysoev, S. V.; Chusova, T. P.; Igumenov, I. K., Thermal Properties of Hafnium(IV) and Zirconium(IV) Beta-Diketonates. *Journal of Thermal Analysis and Calorimetry* **2008**, 92 (3), 729-734.

179. Zimbov, K.; Hastie, J. W.; Margrave, J. L., Mass Spectrometric Studies at High Temperatures. 24. Thermodynamics of Vaporization of SnF_2 and PbF_2 and Dissociation Energies of SnF and PbF. *Transactions of the Faraday Society* **1968**, 64 (544P), 861-867.